



Dipartimento di Matematica e Fisica

Ph.D. Thesis

**X-ray polarization properties of accreting
black holes in soft state: theory and first
observations**

Ph.D. Candidate:
Lorenzo Marra

Supervisor:
Giorgio Matt

A.A. 2022/2023

*To Ilaria.
I love you.*

Abstract

The X-ray spectra of stellar mass black holes observed in soft state is dominated by a thermal emission originating in the inner regions of the accretion disk. The polarization properties of this emission are affected by several effects, including the scattering and absorption processes influencing the radiative transfer of photons within the disk atmosphere and the relativistic effects modifying the polarization properties of the radiation during its propagation towards the observer. Since these effects depend on the black hole spin and on the accretion disk inclination, which can therefore be estimated by X-ray polarimetric observations, these sources are considered as prime targets for the observations performed by the Imaging X-ray Polarimeter Explorer (*IXPE*).

In the first part of this thesis we present a detailed analysis of these effects, introducing a model for the polarized radiative transfer in a partially ionized disk atmosphere accounting for both photoelectric absorption and scattering effects. Relativistic effects affecting the Stokes parameters of the radiation propagating in a strong gravity regime are also accounted for, obtaining the expected accretion disk spectro-polarimetric properties. Our results show that absorption plays a crucial role in determining the polarization properties of the X-ray emission, as the polarization degree of radiation tends to be higher whenever the contribution of photoelectric absorption is relevant. The inclusion of relativistic effects induces a rotation of the polarization angle and a consequent net depolarization of the global disk emission, while not modifying the local energy dependence of the polarization degree.

In the second part of this thesis we report on the observations of stellar mass black holes in soft state performed by *IXPE* in its first two years of operation, presenting a detailed spectro-polarimetric analysis of the data and a possible interpretation of the results. While showing similar spectral properties, the sources present very different polarization features. In one source (LMC X-1) the low detected polarization was considered as an upper limit, not allowing for an estimate of the source parameters from the spectro-polarimetric analysis. In two cases (4U 1957+115 and LMC X-3) the polarimetric data are well described using the standard thin disk model. Finally, the source 4U 1630-47 presented a very large polarization degree, that could not be explained in the standard disk scenario without significant modifications.

List of publications

Journal articles

- Marra L., et al. (Apr 2024). "IXPE observation confirms a high spin in the accreting black hole 4U 1957+115", A&A 684, id.A95, 12 pp., DOI: [10.1051/0004-6361/202348277](https://doi.org/10.1051/0004-6361/202348277)
- Podgorný J., Marra L., et al. (Dec 2023). "The first X-ray polarimetric observation of the black hole binary LMC X-1", MNRAS 526.4, pp. 5964-5975, DOI: [10.1093/mnras/stad3103](https://doi.org/10.1093/mnras/stad3103)
- Rodriguez Cavero N., Marra L., et al. (Nov 2023). "The First X-ray Polarization Observation of the Black Hole X-ray Binary 4U 1630-47 in the Steep Power Law State", ApJL 958.1, p.L8, DOI: [10.3847/2041-8213/acfd2c](https://doi.org/10.3847/2041-8213/acfd2c)
- Taverna R., Marra L., et al. (Mar 2021). "Spectral and polarization properties of black hole accretion disc emission: including absorption effects", MNRAS 501.3, pp. 3393-3405, DOI: [10.1093/mnras/staa3859](https://doi.org/10.1093/mnras/staa3859)
- Ingram A., ..., Marra L., ..., et al. (Nov 2023). "Tracking the X-ray Polarization of the Black Hole Transient Swift J1727.8-1613 during a State Transition", Accepted for publication in ApJ.
- Rankin J., ..., Marra L., ..., et al. (Jan 2024). "X-ray Polarimetry as a Tool to Constrain Orbital Parameters in X-Ray Binaries", ApJ 962.1, p. 34, DOI: [10.3847/1538-4357/ad1991](https://doi.org/10.3847/1538-4357/ad1991)
- Ratheesh A., ..., Marra L., ..., et al. (Mar 2024). "The high polarisation of the X-rays from the Black Hole X-ray Binary 4U 1630-47 challenges standard thin accretion disc scenario", ApJ 964.1 p. 77, DOI: [10.3847/1538-4357/ad226e](https://doi.org/10.3847/1538-4357/ad226e)
- Svoboda J., ..., Marra L., ..., et al. (Jan 2024). "First X-Ray Polarization Measurement Confirms the Low Black Hole Spin in LMC X-3", ApJ 960.1, p. 3, DOI: [10.3847/1538-4357/ad0842](https://doi.org/10.3847/1538-4357/ad0842)
- Veledina A., ..., Marra L., ..., et al. (Nov 2023). "Discovery of X-ray Polarization from the Black Hole Transient Swift J1727.8-1613", ApJL 958.1, p. L16, DOI: [10.3847/2041-8213/ad0781](https://doi.org/10.3847/2041-8213/ad0781)

- Svoboda J.,..., Marra L., ..., et al. (Mar 2024). "Dramatic Drop in the X-Ray Polarization of Swift J1727.8–1613 in the Soft Spectral State", Submitted to ApJL.

Conference proceedings

- Marra L., et al. (Sept 2022). "Spectral and polarization properties of black hole accretion disc emission: including absorption and general relativistic effects", 31st Texas Symposium on Relativistic Astrophysics.

Acknowledgements

This thesis represents the culmination of a rich and challenging journey, one that would not have been possible without the incredible individuals who accompanied me along the way.

First and foremost, I extend my deepest gratitude to my supervisor, Professor Giorgio Matt, who has been my guide during these years. His mentorship has provided me with invaluable opportunities to learn and grow, equipping me with a wealth of skills and knowledge, and showing me the importance of dedication and communication. This work has been possible thanks to him.

A heartfelt thanks to exceptional researchers and professors with whom I had the privilege of collaborating during my Ph.D. journey. Special thanks to Roberto Taverna, Stefano Bianchi and Michal Dovciak, that gave me the opportunity to learn from them and share my ideas with them.

Furthermore, I would like to express my appreciation to all the talented individuals I had the pleasure of meeting over the years, including fellow Ph.D. students, postdocs, and especially the members of the Room 81 group. In particular I want to thank Andrea Gnarini, Romana Mikušincová and Jakub Podgorný for the numerous discussions and the exchange of ideas.

Finally, words cannot express how grateful I am to the people that have always been there. To my parents, for their unwavering support and guidance through every challenge. To Andrea, Lorenzo and Luca, for the laughs and the support, for being the friends I can always rely on. To Francesco, for his invaluable moral encouragement. And to Ilaria, the better half of my Universe, for being my source of joy, for always believing in me when I did not. The best that is in this thesis is for you.

Contents

Introduction	2
I Theory	5
1 Black holes	6
1.1 From the first models to the first observations	6
1.2 Space-time metrics	8
1.2.1 Schwarzschild metric	9
1.2.2 Kerr metric	10
1.3 Accretion disks	13
1.3.1 Shakura & Sunyaev disk model	14
1.4 Accreting stellar mass black holes	17
1.4.1 X-ray Spectra	19
1.4.2 X-ray Timing	21
1.4.3 Outflows	22
1.4.4 Spectral states	23
1.4.5 Observational Techniques	28
2 Polarization	33
2.1 Stokes parameters	33
2.2 Detecting Polarization	38
2.2.1 Photoelectric absorption and Gas Pixel Detectors	40
2.2.2 IXPE	42
2.3 Polarization in black hole binaries	44
2.3.1 Scattering	44
2.3.2 Scattering in the disk and the corona	52
2.3.3 Relativistic effects	55
3 Accretion disk emission polarization properties	62
3.1 Numerical implementation	63
3.1.1 CLOUDY and TITAN	63
3.1.2 STOKES	66
3.1.3 KYN	68
3.2 Transmission through a partially ionized slab	70
3.3 Direct emission from the whole disk	78
3.4 Future projects	88

II	Observations	90
4	4U 1630-47	93
4.1	Introduction	93
4.2	Datasets	93
4.3	Spectral analysis	98
4.4	Polarimetric analysis and theoretical modeling	103
4.4.1	Thermal component	104
4.4.2	Comptonized component	110
4.5	Discussion	112
5	4U 1957+115	115
5.1	Introduction	115
5.2	Datasets	116
5.2.1	Polarization measurement	118
5.3	Spectral analysis	119
5.4	Polarimetric analysis	122
5.5	Discussion	129
6	LMC X-1	130
6.1	Introduction	130
6.2	Datasets	131
6.2.1	Polarization measurement	134
6.3	Spectral analysis	136
6.4	Polarimetric analysis	139
6.4.1	Slab-Corona modeling	142
6.5	Discussion	144
7	LMC X-3	145
7.1	Introduction	145
7.2	Datasets	146
7.2.1	Polarization measurement	147
7.3	Spectral analysis	148
7.4	Polarimetric analysis	151
7.5	Discussion	154
8	Conclusions	156
A	Data Reduction	160
A.1	IXPE	160
A.2	NICER	161
A.3	NuSTAR	163
A.4	Other facilities	163
A.4.1	ART-XC	163
A.4.2	Neil Gehrels <i>Swift</i> Observatory	164

Introduction

Throughout history, our primary means of exploring the Universe has been through the observation of radiation emitted by celestial objects. This emitted radiation holds a wealth of information about the source’s position in the sky, whether within our galaxy or beyond, its distance from Earth, and the inherent characteristics of the source itself. The spectra of radiation emitted by different sources vary, showcasing distinct intensity distributions across wavelengths. Moreover, this emission can exhibit fluctuations over various timescales. By delving into the spectral and temporal features of astrophysical sources, we have gained the ability to differentiate between a star and a planet, a supernova remnant and a galaxy, a neutron star and a black hole.

Each source predominantly emits radiation in a specific wavelength range, necessitating observations across various segments of the electromagnetic spectrum to study these phenomena comprehensively. The segments where the most energetic and violent phenomena in the Universe emit radiation are the X-ray and the γ -ray bands. However, observing X-ray and γ -ray radiation directly from the Earth’s surface is not feasible due to the protective layer of the atmosphere. Consequently, the window for these observations opened relatively late compared to other, more easily accessible wavelengths. Academic fascination with X-ray astronomy ignited with the detection of Sco X-1, marking the first discovery of an X-ray source beyond our solar system, along with the identification of the isotropic extra-galactic X-ray background [Giacconi et al., 1962]. Riding the wave of this newfound curiosity, a significant milestone took place on December 12, 1970, with the launch of the inaugural mission exclusively devoted to celestial X-ray astronomy—the satellite *Uhuru* (Swahili for *freedom*). This satellite conducted the first comprehensive and uniform all-sky survey, unveiling the presence of over 339 sources in the X-ray domain [Giacconi et al., 1972]. Following that milestone, a succession of missions joined the pursuit of exploring the X-ray sky, each introducing novel capabilities surpassing its forerunners. The *Einstein X-ray observatory* (HEAO-1), launched on the 13th of November 1978, has been the first fully imaging focusing X-ray telescope, with an angular resolution of a few arc seconds [Giacconi et al., 1979]; *ROSAT*, launched in 1990, expanded the number of known X-ray sources to more than 60000 [Voges et al., 1999]; the *Rossi X-ray Timing Explorer* (RXTE), launched in 1995, which had the unique capability of studying rapid time variability in the emission of cosmic X-ray sources over a wide band of X-ray energies [Swank, 1999]; *BeppoSAX*, launched in 1996, the first X-ray mission capable of simultaneously observing targets over more than 3 decades of energy, from 0.1 to 300 keV [Boella et al., 1997].

In 1999, the narrative of X-ray astronomy took a monumental leap with the launch of two significant satellites that, as of the time of this thesis, remain in operation: the *Chandra X-ray Observatory*, which entered orbit on July 23, and *XMM-Newton*

(*X-ray Multi-Mirror Mission*), launched on December 10. These instruments, boasting an order-of-magnitude or greater enhancement in spectral and spatial resolution coupled with heightened sensitivity, have not only illuminated existing problems but also opened new research areas. The combined capabilities of *Chandra* and *XMM-Newton* have clarified the nature of X-ray radiation from comets [Bhardwaj et al., 2007] and improved our understanding of the nature of X-ray emissions from stars of all ages [Güdel and Nazé, 2009, Wolk et al., 2005]. These observatories have resolved the diffuse emission from the Galactic plane [Revnivtsev et al., 2009] into discrete points and the diffuse extra-galactic X-ray background [Brandt and Hasinger, 2005]. Moreover, they have identified several stellar mass black holes in our galaxy and hundreds of supermassive black holes at the cores of other galaxies, acquiring high-resolution spectra that offer profound insights into the accretion processes fueling their activity [Turner and Miller, 2009, Miller et al., 2009]. Over the past two decades, numerous missions have followed the path set by these two satellites (*INTEGRAL*, *Suzaku*, *NuSTAR*, *MAXI*, *NICER*, *XRISM*, to name a few). However, a common characteristic unites all these instruments: their inability to detect the *polarization* of the observed radiation.

Polarization in transverse waves is defined as the geometric orientation of the oscillations. In the context of an electromagnetic wave, it conventionally refers to the direction of oscillation of the electric field. Consequently, polarization adds another layer of information to the radiation we observe, complementing data on radiation intensity, energy, and temporal variability. The interest in observing and studying X-ray radiation polarization traces back to the 1962 observation of Sco X-1 [Giacconi et al., 1962]. However, this curiosity was met with several challenges [Costa, 2022]. The first two satellites equipped with X-ray polarimeters, namely *Ariel-5* and *OSO-8*, remained the sole pioneers for the subsequent 45 years after their launch in 1974 and 1975, respectively, only 5 and 6 years after the *Uhuru* mission. Both polarimeters operated by utilizing reflection at a Bragg angle of 45° [Schnopper and Kalata, 1969]. Nevertheless, this technique encountered severe limitations due to the narrow band of diffracted radiation, resulting in a small effective area of the instrument. Among the two, *OSO-8* was the sole mission capable of detecting a polarized signal. During a six-day observation of the Crab Nebula, it recorded polarization degrees of $15.7\% \pm 1.5\%$ and $18.3\% \pm 4.2\%$ at 2.6 and 5.2 keV, respectively [Weisskopf et al., 1976]. This finding constituted crucial evidence for a non-thermal component in X-ray emission of this source, likely attributed to synchrotron emission. Additionally, *OSO-8* imposed stringent constraints on the polarization of Sco X-1 [Long et al., 1979]. However, the impact of other results from these missions remained notably low, and are generally considered disappointing in nature.

Due to the technical challenges in creating more efficient polarimeters and the growing focus on X-ray imaging and spectroscopy, proposed missions dedicated to observing X-ray polarization faced years of rejection. However, the landscape began shifting in the past three decades, spurred by the advancement of Gas Pixel Detectors, which departed from Bragg diffraction and instead relied on photoelectric absorption [Soffitta et al., 1995]. This paved the way for the inaugural mission solely devoted to X-ray polarimetry—the *Imaging X-Ray Polarimetry Explorer (IXPE)*, that was selected for launch in 2017, and finally took flight on December 9, 2021 [Weisskopf et al., 2016, 2022]. In its two years of operation, *IXPE* has met its expectations and plans. In

certain instances, it has reaffirmed findings suggested by spectroscopic analysis, while in numerous other cases, it has presented researchers with unparalleled data, posing new challenges and questions.

In this thesis, I will present the initial observational findings of the *IXPE*, focusing on a distinct category of sources: stellar-mass black holes observed in their soft state. This work includes an in-depth exploration of the characteristics exhibited by these sources, accompanied by the introduction of a model implemented to describe the spectral and polarization features of their emissions.

This thesis follows the structure outlined below:

- Part I provides an introduction to stellar mass black holes and outlines the theoretical model we developed for studying the spectral and polarization properties of the accretion disk emission. In particular, Chapter 1 offers a comprehensive overview of black holes, encompassing metrics describing the curved space-time around these objects, the fundamental characteristics of the accretion mechanism, and a detailed classification of stellar-mass black hole properties. In Chapter 2, a theoretical description of electromagnetic wave polarization and its detection mechanism is presented. This chapter also delves into the main processes influencing the polarization of observed radiation in stellar-mass black holes. Finally, Chapter 3 introduces the model describing the properties of accretion disk emission in these sources, including processes occurring as radiation interacts with the accretion disk atmospheric layer and general relativity effects that impact the polarization properties of observed radiation.
- Part II presents the results obtained by *IXPE* during its initial two years of observation on various sources. Chapter 4 focuses on the two observations of the transient source 4U 1630-47, providing the first-ever modelization of this source's unprecedented polarimetric data. In Chapter 5, the observation of 4U 1957+115 is described, highlighting the first polarimetric evidence suggesting the presence of returning radiation. Chapter 6 details the observation of LMC X-1, the first discovered extragalactic X-ray binary system. Finally, in Chapter 7, the observation of LMC X-3 is discussed, exploring its possible implications regarding the source's spin.

Part I

Theory

Chapter 1

Black holes

1.1 From the first models to the first observations

Black holes (BHs) are one of the most mysterious and puzzling, and thus fascinating, objects in the Universe. This fascination was also due to their apparent simplicity, since contrary to other compact objects BHs were first postulated long before the advent of modern astrophysics. As early as the 1770s John Michell was investigating the attraction of light by gravity, and in 1783 produced a paper that can be considered as the first theorization of a BH [named *dark star* by [Michell, 1784](#)]. Michell's primary argument was rooted in computing the escape velocity from the Sun, calculated to be 497 times slower than the speed of light. From this, he posited that any star with equivalent density to the Sun but with a radius 497 times larger would capture all emitted light, rendering it invisible. Moreover, Michell conjectured that these entities would perpetually evade observation, save for potential gravitational interactions with their observable satellites

The foundational understanding of the interplay between light and gravity, originating from Michell and passed on to Herschel and Laplace [[Schaffer, 1979](#)], encountered a pivotal shift when the wave-like behavior of light emerged in the early nineteenth century. This transition raised uncertainties regarding the potential impact of gravity on escaping light waves. This historical narrative underwent a transformative shift with the advent of the two main theories in the twentieth century: the theory of relativity and quantum mechanics. In 1915, Albert Einstein formulated his theory of general relativity, demonstrating that gravity indeed influences the motion of light. Shortly thereafter Karl Schwarzschild derived a solution to the Einstein field equations, delineating the gravitational field of a point mass and a spherical mass [[Schwarzschild, 1916](#)]. This solution will be described in [section 1.2](#), as well as the exact solution for a rotating black hole found by Roy [Kerr \[1963\]](#).

Simultaneous with the development of a theoretical framework explaining the existence of black holes, several scientists directed their focus toward discerning plausible mechanisms capable of forming these enigmatic objects. In 1931, Subrahmanyan Chandrasekhar, employing special relativity, established that a non-rotating body of electron-degenerate matter surpassing a critical mass (now named the *Chandrasekhar limit* at $1.4 M_{\odot}$), lacks stable solutions [[Chandrasekhar, 1931](#)]. This paved the way for the introduction of the *neutron stars*, which are stable structures where the grav-

itational collapse is opposed by the neutron degeneracy pressure. However, in 1939, Robert Oppenheimer and collaborators postulated that neutron stars surpassing another threshold (the *Tolman–Oppenheimer–Volkoff limit*) would succumb to further collapse, echoing Chandrasekhar’s earlier reasoning. They concluded that no known physical law would likely intervene to prevent some stars from collapsing into black holes [Oppenheimer and Volkoff, 1939]. The precise value of this limit has varied over time with the refinement of theory and through new observational data. More recent estimates place this limit at no less than $\sim 2.17 M_{\odot}$, owing to gravitational wave observations from the neutron star merger event GW170817. This event is believed to have resulted in the subsequent formation of a black hole [Margalit and Metzger, 2017].

Detecting black holes posed a considerable challenge due to their inherent nature. The first celestial object widely accepted as a black hole candidate was Cygnus X-1. Initially discovered in 1964 during a survey using Aerobee suborbital rockets, it was later observed in 1971 by the *Uhuru* satellite. This enigmatic source exhibited substantial X-ray variability, suggesting energy generation within a compact region. In 1972, the companion star to Cygnus X-1 was detected [Bolton, 1972]. Through the study of its orbital motion, estimates of the mass of the compact object were made. The high predicted mass strongly indicated a black hole, although this evidence was not definitive [remarkably, a bet was even placed by Stephen Hawking and Kip Thorne on the black hole nature of Cygnus X-1 in 1975, Hawking, 1988]. Despite the lack of irrefutable evidence, the scientific community gradually embraced Cygnus X-1 as the first observed black hole. Over 60 years later, several measurements continue to support this interpretation.

Concurrently, the identification of the first extragalactic black hole sources began to emerge. Observations in the early twentieth century revealed nearby galaxies with notably bright nuclei emitting unusually broad emission lines [Seyfert, 1943]. Simultaneously, the development of Radio astronomy led to the identification of objects emitting strong radio signals with a point-like or quasi-stellar appearance, later abbreviated as *quasars*. A pivotal breakthrough occurred when Maarten Schmidt measured the redshift of quasar 3C 273 [Schmidt, 1963]. Recognizing its extragalactic nature, Schmidt noted its significant redshift of 0.158, indicating that it was the nuclear region of a galaxy far more powerful than previously identified radio galaxies. The extraordinary luminosities and distinct spectral properties of these quasars hinted at a power source distinct from ordinary stars. The prevailing theory proposed that these sources were powered by gas accretion onto supermassive black holes, a model widely accepted today. Further support for this concept came from X-ray astronomy, which revealed that Seyfert galaxies and quasars were robust sources of X-ray emissions from the inner regions of black hole accretion disks. Initially perceived as disparate phenomena, these objects are now categorized under the umbrella term of *Active Galactic Nuclei* (AGN) [Antonucci, 1993]. Figure 1.1 displays a NASA image depicting these two pivotal astrophysical sources instrumental in discovering the existence of galactic and extragalactic black holes.

AGN remain an open and thrilling area of study. However, this thesis will concentrate solely on galactic black holes. In this chapter, we will introduce the most important characteristics of these sources. First, the metrics describing the space-time around BHs will be introduced (section 1.2), as well as the the basis of the accretion



Figure 1.1: *Left:* Chandra X-ray Observatory image of Cygnus X-1 (Credits: NASA/CXC). *Right:* Quasar 3C 273 observed by the Hubble Space Telescope. The relativistic jet of 3C 273 appears to the left of the bright quasar, and the four straight lines pointing outward from the central source are diffraction spikes caused by the telescope optics (Credit: ESA/Hubble & NASA).

mechanism responsible for this source's emission (section 1.3). Finally, in section 1.4 we will describe the most important properties of galactic black holes, as their emission states and the techniques implemented to estimate their mass and spin.

1.2 Space-time metrics

A BH is, by definition, a region in space-time in which the gravitational field is so strong that it precludes even light from escaping to infinity. This object is formed when a body of mass M contracts to a size less than the so-called *Schwarzschild radius* $r_S = 2GM/c^2 = 2r_g$, where $r_g = GM/c^2$ is also known as the *gravitational radius* of the object. From a classical perspective, this represents the distance at which the required escape velocity to overcome the object's gravitational pull equals the speed of light. Consequently, signals or particles within this critical radius are unable to escape, leading to the delineation of an isolated region from the rest of the universe, characterized by a boundary surface called the *event horizon*.

Describing the space-time surrounding a black hole requires a treatment in general relativity. Despite the complexity of the equations governing their properties, black holes are remarkably simple entities. They swiftly reach a stationary state post-formation, and their attributes are uniquely determined by a small set of parameters: namely, their *mass* and *angular momentum*, and their electric charge (if any). However, owing to the high conductivity of the interstellar medium, black holes are unlikely to retain a net charge for extended periods. As a result, the only pertinent parameters to consider are the mass M and the spin a (with $a_s = a/M$).

1.2.1 Schwarzschild metric

The Schwarzschild metric represents the most basic form of a black hole solution. It emerges as a vacuum solution of the Einstein field equations in the static, spherically symmetric scenario; in natural units ($G = c = 1$), this takes the following form in polar coordinates:

$$ds^2 = -\left(1 - \frac{2M}{r}\right)dt^2 + \left(1 - \frac{2M}{r}\right)^{-1}dr^2 + r^2(d\theta^2 + \sin^2\theta d\phi^2), \quad (1.1)$$

This metric is both *static*, indicating no change over time, and *irrotational*. At distances far from the center of gravity ($r \gg r_S$), spacetime approaches the flat *Minkowski spacetime* characterized by the metric:

$$ds^2 = -dt^2 + dr^2 + r^2(d\theta^2 + \sin^2\theta d\phi^2). \quad (1.2)$$

Approaching the black hole, spacetime curvature occurs due to the presence of the mass source M . At the critical radius $r = r_S$, the metric signifies a pivotal point where the free-fall acceleration concerning the Schwarzschild frame becomes infinite. This, however, does not denote an actual singularity of infinite curvature within the four-dimensional space-time geometry. Instead, it signifies the impossibility of extending this reference frame into the region $r \leq r_S$, inside the event horizon. To further explore this inner region, alternative reference frames such as the *Lemaitre* or *Eddington-Finkelstein* frames are introduced. However, these will not be covered in the scope of this thesis [for an in-depth analysis, see e.g. [Chandrasekhar, 1983](#)].

A useful astrophysical application of the Schwarzschild metric is how point-like particles and photons move in it. In general relativity, particles move on geodesics of the metric, i.e. the paths with an extremal lapse of proper time (for a massive particle) or ‘affine parameter’ (for a massless particle), along the worldline. Specifically, in the context of high energy astrophysics, it is particularly important the study of circular orbits in Schwarzschild geometry, since these will be approximately the orbits of material accreting onto BHs from accretion disks (see section 1.3). To analyze these orbits, we can examine the effective potential experienced by a particle with angular momentum h per unit mass of the black hole. This potential takes the form as described by [[Fabian and Lasenby, 2019](#)]:

$$U_S(r) = \frac{h^2}{2r^2} \left(1 - \frac{2M}{r}\right) - \frac{M}{r}. \quad (1.3)$$

This is shown in Figure 1.2 for several values of the angular momentum h . When $h < \sqrt{3}r_S$, the curve is monotonic, signifying that motion on circular orbits is viable only if $h \geq \sqrt{3}r_S$. For $h > \sqrt{3}r_S$, two critical points emerge: one denotes an unstable orbit, while the other indicates a stable one. The smallest stable circular orbit becomes accessible solely for particles with $h = \sqrt{3}r_S$, situated at:

$$r_{ISCO} = 6M = 6r_g. \quad (1.4)$$

This orbit is known as the *Innermost Stable Circular Orbit* (ISCO) of a non-rotating BH, and it results to be stable for perturbation towards greater radii and is unstable for perturbation towards the singularity at $r = 0$. Particles that go beyond that radius are forced to fall radially toward the BH, eventually crossing its event horizon.

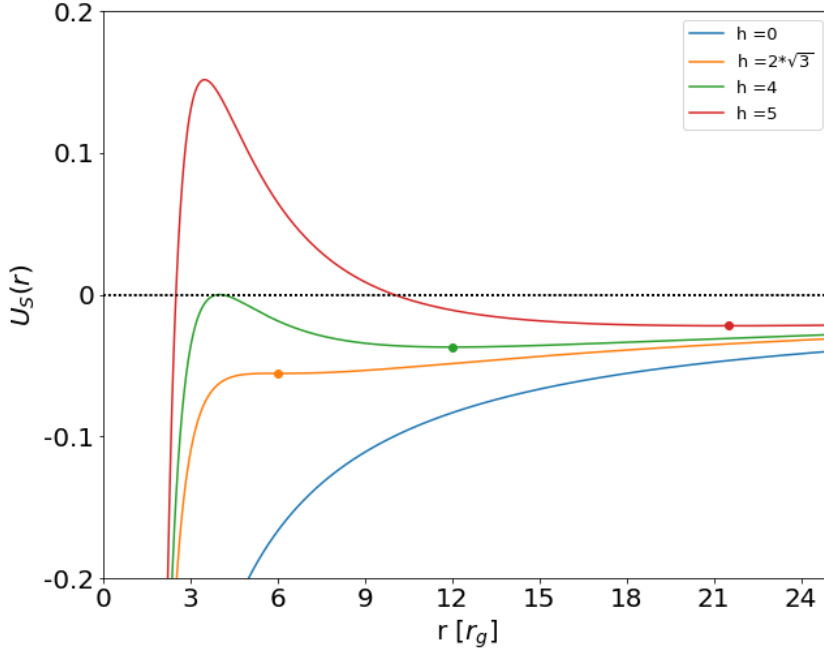


Figure 1.2: The effective potential $U_S(r)$ plotted against the radial distance r for different angular momentum values h , considering a particle in the vicinity of a black hole with a mass of $M = 10 M_\odot$. The marked points indicate the positions of stable circular orbits corresponding to each value $h > \sqrt{3}r_S$; notably, the orange point highlights the location of the ISCO.

1.2.2 Kerr metric

The gravitational collapse of a spherical, non-rotating mass produces a spherically symmetric BH when the radius of the collapsing body becomes less than its Schwarzschild radius. However, when the collapsing body deviates significantly from spherical symmetry or possesses substantial angular momentum, the spin of the resulting black hole becomes a crucial factor. In such cases, neglecting the spin of the resultant black hole is no longer viable. To describe the space-time around a BH with non-zero angular momentum we can use the Kerr metric, the form of which, in the reference frame developed by Boyer and Lindquist [1967], is:

$$ds^2 = -\left(1 - \frac{2Mr}{\rho}\right)dt^2 + \left[-\frac{4Mra \sin^2 \theta}{\rho} dt d\phi + \frac{\rho}{\Delta} dr^2 + \rho d\theta^2 + \left(r^2 + a^2 + \frac{2Mra^2 \sin^2 \theta}{\rho}\right) \sin^2 \theta d\phi^2\right], \quad (1.5)$$

where $a = J/M$ is the angular momentum of the BH, $\Delta = r^2 - 2Mr + a^2$ and $\rho = r^2 + a^2 \cos^2 \theta$.

In the absence of rotation ($a = 0$) the Kerr metric naturally reduces to the Schwarzschild metric (1.1). On the other hand, because of the counteracting torque felt by the hole in

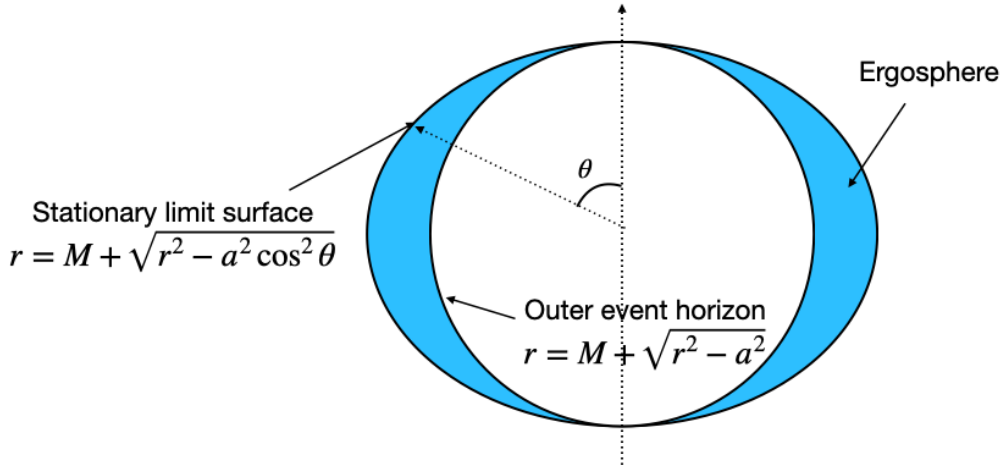


Figure 1.3: An illustration of the stationary limit and outer horizon surfaces for the Kerr solution.

absorbing radiation from the accretion disk, the maximum value that can be reached by the BH spin is $a = 0.998 M$ [Thorne, 1974].

The geometry of spacetime around a rotating black hole differs significantly from that of a Schwarzschild black hole. Illustrated in Figure 1.3, outside a Kerr black hole, two distinct surfaces are delineated: the external surface, termed the *stationary limit surface*, and the surface lying within it, referred to as the *outer event horizon*. Additionally, there exist further surfaces closer to the black hole center, named the inner stationary limit and inner horizon, yet these are obscured by the outer horizon, bearing no immediate astrophysical significance. The stationary limit surface designates the boundary beyond which an observer can no longer maintain a stationary position within the (r, θ, ϕ) coordinate system due to the gravitational pull exerted by the black hole rotation. Mathematically, this surface is characterized by the points where g_{tt} (the coefficient of the dt^2 term in Equation 1.5) equals zero, necessitating $R = M \pm \sqrt{M^2 - a^2 \cos^2 \theta}$. Conversely, the event horizon refers to the positions where the g_{rr} component of the metric (1.5) becomes infinite, identified by $R = M \pm \sqrt{M^2 - a^2}$. These locations denote points from which no particle can escape regardless of its mass or motion state. Very close to a spinning black hole, inside the stationary limit surface, frame-dragging effects become extreme, forcing any matter or even photons to rotate in the same sense as the black hole as seen by a distant observer. Penrose [1969] demonstrated via a series of thought experiments that within the static limit, physical phenomena such as particle-particle scattering can extract the spin energy of the black hole. This area is named the *ergosphere*, derived from the Ancient Greek *ergon*, meaning *work*. Considerations based on black hole thermodynamics indicate that the (extractable) energy associated with the black hole rotation is [Misner et al., 1973]:

$$E_{Spin} = \left\{ 1 - \frac{1}{2} \left[\left(1 + \sqrt{1 - a_s^2} \right)^2 + a_s^2 \right]^{1/2} \right\} M c^2 \quad (1.6)$$

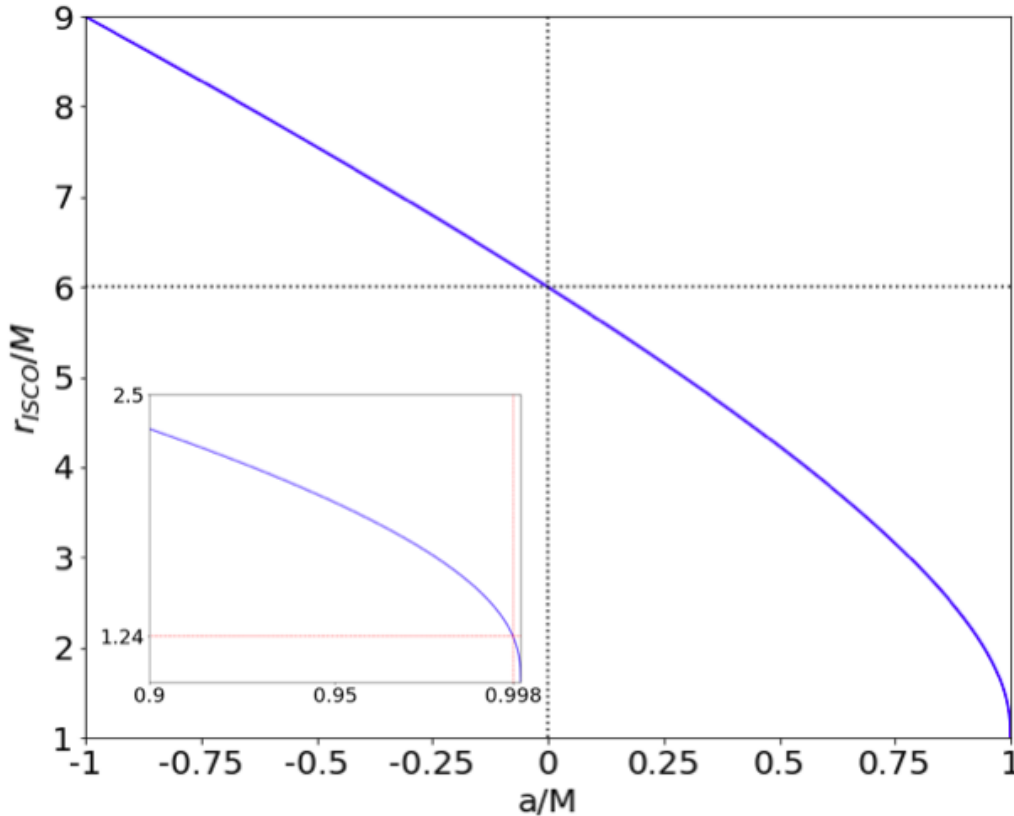


Figure 1.4: Radius of the innermost stable circular orbit plotted as a function of the BH spin. Negative values of the BH spin correspond to an opposite circulation of the particle compared to the BH angular momentum. The black dotted lines, and the red dotted lines in the zoomed panel, highlight the ISCO location for a non rotating BH and a maximally rotating BH, respectively.

For a maximally rotating black hole ($a_s = 0.998$), equation 1.6 results in a noteworthy 27% of the rest mass energy of the black hole. This establishes BHs as an astrophysically important energy source. The processes discussed in Penrose’s original work require quite violent particle interactions within the ergosphere [Bardeen et al., 1972] and may produce high-energy particle acceleration and γ -ray emission [Williams, 1995]. Particular attention was gained by the possible interaction of this process with the source magnetic field [e.g. Blandford and Znajek, 1977]; in fact, the standard paradigm for the relativistic jets seen from many black hole systems is that they are powered by the magnetic extraction of black hole spin energy [Begelman et al., 1984].

As previously observed with the Schwarzschild metric, studying particle motion around a Kerr black hole proves valuable. The effective potential experienced by a massive particle within the equatorial plane under this metric is formulated as:

$$U_K(r) = -\frac{M}{r} + \frac{1}{2r^2}(h^2 - a^2(k^2 - 1)) - \frac{M}{r^3}(h - ak)^2, \quad (1.7)$$

Here, k and h represent the specific energy and specific angular momentum of the particle per unit of black hole mass. Determining the radius of the ISCO around the

black hole involves ensuring the positivity of the second derivative of the potential (1.7) where the first derivative vanishes. The possible values for r_{ISCO} depend on the BH spin and on whether the disk is co- or counter-rotating with the BH (see Figure 1.4), as described by:

$$r_{ISCO} = 3 + Z_2 \pm [(3 - Z_1)(3 + Z_1 + 2Z_2)]^{\frac{1}{2}}, \quad (1.8)$$

where $Z_1 = 1 + (1 - a_s^2)^{1/3}[(1 + a_s)^{1/3} + (1 - a_s)^{1/3}]$ and $Z_2 = (3a_s^2 + Z_1^2)^{1/2}$, and $a_s = a/M$ in the BH spin per unit mass [Matt, 2006]. The sign - (+) applies to co- (counter-) rotating disk. In the scenario, if $a = 0$ we get a single solution, $r_{ISCO} = 6M = 6r_g$, aligning with the Schwarzschild case. Conversely, with $a = M$, indicating an extreme black hole, the solutions manifest as $r_{ISCO} = M = r_g$ when both the black hole and the particle rotate in the same direction, and $r = 9M = 9r_g$ if their rotations oppose each other. For a maximally rotating black hole ($a = 0.998 M$), $r_{ISCO} = 1.24M$, which is the minimum attainable value for the innermost stable orbit around a Kerr BH.

1.3 Accretion disks

The energy production and the radiation emission around BHs are fueled by the *accretion* mechanism, i.e. the accumulation of diffuse gas or matter onto some object under the influence of gravity. The main result of this process is the conversion of gravitational energy into heat, and thus luminosity, directly correlated to the accretion rate (i.e. the mass falling per unit time) through an efficiency parameter $L = \xi \dot{M}$. In a state of equilibrium, the generated luminosity cannot grow without bounds; an excessive luminosity would lead to radiation pressure capable of pushing away the infalling matter. This sets an upper limit on the accretion luminosity, achieved by balancing the inward gravitational force against the outward pressure of radiation. Originally derived by Sir Arthur Eddington for a steady, spherical accretion flow, this upper limit is known as the *Eddington luminosity*:

$$L_{EDD} = \frac{4\pi G m_p c}{\sigma_T} M \simeq 1.26 \times 10^{38} \left(\frac{M}{M_\odot} \right) \text{ erg s}^{-1}. \quad (1.9)$$

When matter approaches a massive object, however, its angular momentum prevents it from getting too close to the object surface. To get closer, infalling matter must dissipate its rotational energy. To do so, matter tends to collapse perpendicularly to the radial coordinate, and forms an axisymmetric structure around the massive object, known as *accretion disk*. The process that causes infalling matter to lose angular momentum in these objects is the friction caused by turbulent viscosity working between adjacent gas layers in the disk. The faster inner layer loses angular momentum and infalls slightly, while the (slower) outer layer close to it gains angular momentum, which is given away to the next outer layer, and so on, resulting in a continuous flow toward the center whereas angular momentum is transported to the outer region. Meanwhile, the friction of the disk heats up the gas, resulting in a continuous radiation emission; therefore, also in the case of objects which are not endowed with a solid surface like BHs, radiation can be emitted through accretion mechanisms, and in such case the maximum energy that can be released is given by the energy which has to be

dissipated in order to reach the last stable orbit around the BH. This means that the maximum efficiency of the accretion mechanism is $\xi \approx 0.06$ for a Schwarzschild BH, whilst for a maximally rotating Kerr BH it reaches $\xi \approx 0.426$.

Although several models of accretion disk do exist, the commonly used one, which is also the one mainly considered throughout this thesis, is the [Shakura and Sunyaev \[1973\]](#) model, also known as the *standard accretion disk model* or the *thin disk model*, as well as its general relativistic expansion described by [Novikov and Thorne \[1973\]](#).

1.3.1 Shakura & Sunyaev disk model

The *standard disk model* describes a geometrically thin, non-self-gravitating disk through hydrodynamic equations averaged over the disk thickness. The main assumptions of this model are that the scale height of the disk H (thickness) is much smaller than its radial dimension r (i.e. $H/r \ll 1$) and that the mass of the disk M_{disk} is much smaller than the mass of the central object M_* (i.e. $M_{disk} \ll M_*$) so that the gravitational influence of the disk is negligible. From the geometrically thin condition, the hydrostatic equilibrium equation on the direction perpendicular to the disk plane implies that the rotation velocity of the disk must be much greater than the sound speed in the plasma (i.e. $v_\phi \gg v_s$). To express this condition in other words, internal pressure gradients should not inflate the disk.

Considering an xyz reference frame with the disk center as the origin and the disk plane in the xy plane, we can define the shear viscosity η for a fluid moving on the disk plane in the x direction, encountering a velocity gradient in the y direction towards the central object. This results in a force per unit area in the $x - z$ vertical plane, termed the shear stress, given by:

$$f_x(y) = \eta \frac{\partial v_x(y)}{\partial y}. \quad (1.10)$$

A useful way to estimate these viscosity effects in a fluid in motion is introducing the *Reynolds number*, which is used to describe the ratio of inertial forces (resistance to change or motion) to viscous forces (glue) and thus also to define whether a fluid is laminar or turbulent. This can be defined as $\mathcal{R} \approx VL/\nu$, where L and V are typical dimensions of length and velocity of the flow, while $\nu = \eta/\rho$ is known as the *kinematic viscosity*. For a laminar flow, the Reynolds number should be less than unity; on the other hand, at large Reynolds numbers (e.g. $\mathcal{R} \geq 10^3$) the flow becomes turbulent [[Feynman et al., 1965](#), [Landau and Lifshitz, 1987](#)]. In some astrophysical applications, this second situation is expected; for example, if we consider the case of an accretion disk around an object of mass $1 M_\odot$ radiating at the Eddington limit, the Reynolds number turns out to be of the order of 10^{12} .

To describe these turbulent viscosity effects inside the disk, Shakura & Sunyaev introduced a new parameter (α), which is defined in terms of the kinematic viscosity (ν) as [[Shakura and Sunyaev, 1973](#)]:

$$\nu = \alpha v_s H, \quad (1.11)$$

and it is supposed to take values between 0 (case with no accretion) and 1. With this parametrization, they imposed that the typical dimension of the turbulent vortexes must be of the same order as the scale height of the disk and that turbulent motion

cannot be supersonic ($v_t < v_s$). The advantage of this formalism is that analytic solutions can be found for the structure of thin accretion disks in terms of the α parameter. Moreover, the model serves as a useful comparative tool for observations. Typically quoted values for α range from ~ 0.01 for protostellar disks [Hartmann et al., 1998] to ~ 0.1 for galactic binaries [Lasota, 2001].

The disk is usually assumed to be *optically thick* to radiation, so that sufficient scatterings occur to ensure that the emission can be approximated as black-body radiation at each point in the disk. This model also allows a simple estimate of the disk temperature distribution [see e.g. Longair, 2011, for the complete computations]. Assuming the disk is in steady state, the mass flowing through a ring of radius r and width dr centered on the BH does not depend on the radial coordinate, and assuming that matter in the accretion disk follows a Keplerian orbit around the star, it is possible to find that the luminosity of the disk annulus between radii r and $r + dr$ can be expressed as:

$$L(r)dr = -\left(\frac{dE}{dt}\right)2\pi r dr = \frac{3G\dot{m}M_*}{2r^2} \left[1 - \left(\frac{r_*}{r}\right)^{1/2}\right] dr. \quad (1.12)$$

To evaluate the effective temperature of the disk surface we can consider that the disk radiates as a black body from its top and bottom surfaces, so luminosity between r and $r + dr$ (1.12) can be equated to the black-body emission from these surfaces:

$$\begin{aligned} L(r)dr &= \frac{3G\dot{m}M_*}{2r^2} \left[1 - \left(\frac{r_*}{r}\right)^{1/2}\right] dr = 2 \cdot 2\pi r dr \cdot \sigma T^4 \\ &\rightarrow T^4(r) = \frac{3M_*\dot{m}}{8\pi\sigma r^3} \left[1 - \left(\frac{r_*}{r}\right)^{1/2}\right]. \end{aligned} \quad (1.13)$$

This temperature relation illustrates a scaling law where, for regions far from the disk inner radius, temperature varies as $T \propto r^{-3/4}$, indicating higher temperatures closer to the center and a cooling trend moving away from it.

This temperature profile has been extended by Novikov and Thorne [1973] into its general relativistic form, that is [Wang, 2000, Taverna et al., 2020]:

$$T(\chi, r, a_s) = 571 f_{col} \left(\frac{M}{M_\odot}\right)^{-1/2} \left(\frac{\dot{M}}{M_\odot \text{yr}^{-1}}\right)^{1/4} [f(\chi, a_s)]^{1/4} \text{keV}, \quad (1.14)$$

where $\chi = (r/r_g)^{1/2}$ and [see Page and Thorne, 1974]:

$$\begin{aligned} f(\chi, a_s) &= \frac{1}{\chi^4(\chi^3 - 3\chi + 2a_s)} \left[\chi - \chi_{ISCO} - \frac{3}{2}a_s \ln\left(\frac{\chi}{\chi_{ISCO}}\right) \right. \\ &- \frac{3(\chi_1 - a_s)^2}{\chi_1(\chi_1 - \chi_2)(\chi_1 - \chi_3)} \ln\left(\frac{\chi - \chi_1}{\chi_{ISCO} - \chi_1}\right) - \frac{3(\chi_2 - a_s)^2}{\chi_2(\chi_2 - \chi_1)(\chi_2 - \chi_3)} \ln\left(\frac{\chi - \chi_2}{\chi_{ISCO} - \chi_2}\right) \\ &\left. - \frac{3(\chi_3 - a_s)^2}{\chi_3(\chi_3 - \chi_1)(\chi_3 - \chi_2)} \ln\left(\frac{\chi - \chi_3}{\chi_{ISCO} - \chi_3}\right) \right], \end{aligned} \quad (1.15)$$

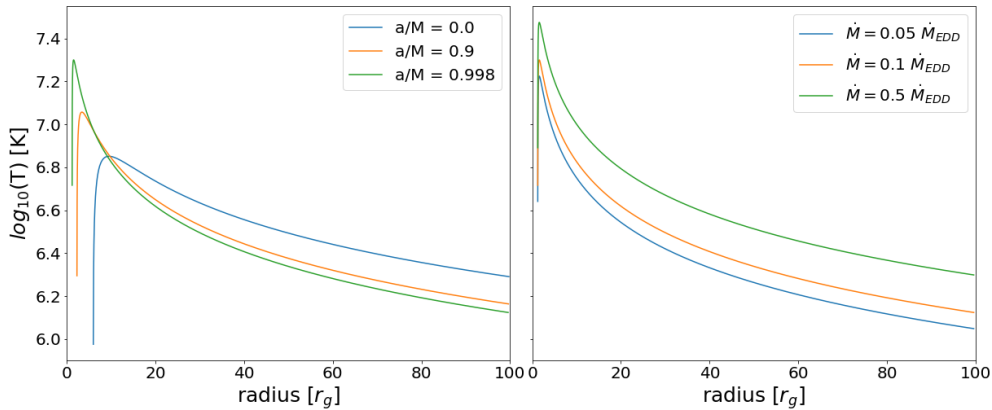


Figure 1.5: Radial temperature profile given by Equation (1.14). The left panel shows the profiles for three different spin values, assuming an accretion luminosity $L = 0.1L_{EDD}$. The right panel illustrates the variation of the temperature profile for different accretion rate values, in this case for a BH with spin $a/M = 0.998$

where $\chi_{ISCO} = (r_{ISCO}/r_g)^{1/2}$, $\chi_1 = 2 \cos(1/3 \arccos a_s - \pi/3)$, $\chi_2 = 2 \cos(1/3 \arccos a_s + \pi/3)$ and $\chi_3 = -2 \cos(1/3 \arccos a_s)$.

The hardening factor f_{col} is used to shift the energy of the thermal photons emerging from the disk to account (in a simplified way) for the effects of scatterings they undergo with disk particles [Shimura and Takahara, 1995, Dovčiak et al., 2008, Davis and El-Abd, 2019]. The temperature profile of the inner region of the disk at given a is not monotonic, since it has a peak value (r_{peak}) near the ISCO. For $r > r_{peak}$ the temperature decreases with increasing r ; on the other hand in the inner region of the disk ($r_{ISCO} < r < r_{peak}$) temperature increases steeply with r forming a cooling region with a large temperature gradient. Changing the spin of the central BH modifies the temperature profile, in fact, both the temperature peak value and the average temperature gradient increase monotonically with increasing a , while both r_{peak} and the radial width of the cooling region decrease monotonically. This behavior is shown in the left panel of Figure 1.5; the right panel, instead, shows the variation of the radial temperature profile with the accretion rate for a fixed spin value. In this case, the peak of the temperature profile does not change, but the temperature shows an increase with increasing accretion rates.

The radiation emitted from the optically thick accretion disk can be described as the superposition of several black body components, due to the temperature variation with radius; an example of the expected spectrum is shown in Figure 1.6. At the high-energy end, the spectrum shows a distinct black body exponential decline ($\propto e^{-h\nu/kT_{Max}}$), which is contingent on the maximum temperature, T_{Max} , achieved on the accretion disk surface [Ghisellini, 2013]. This value is influenced by various factors such as the accretion rate, the mass and spin of the black hole, and the disk hardening factor. The dependency on mass is particularly intriguing as the peak frequency of the disk black body emission is proportional to $M^{-1/4}$. This fundamental characteristic sets apart stellar mass black holes (with $M \sim 10M_\odot$), whose accretion disk emission peaks in the X-ray band, from supermassive black holes (with $M \sim 10^9M_\odot$), where this peak occurs

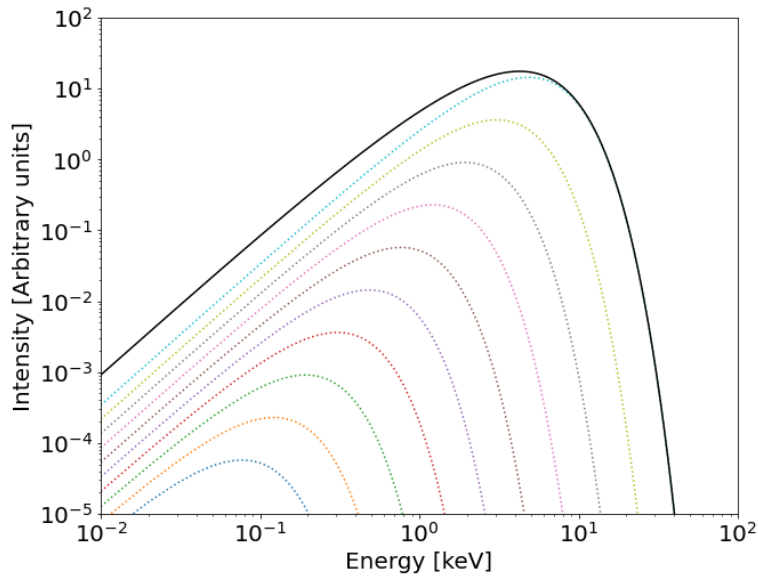


Figure 1.6: Multi-color black body radiation emitted by an accretion disk (black solid line), shown as the sum of the individual black body components (dotted lines).

in the UV band.

The spectral shape of the thermal disk emission is further influenced by the object distance and the inclination angle between the symmetry axis of the disk and the observer's line of sight. This creates a significant degeneracy among various parameters that collectively determine the spectral form of the thermal disk emission. This degeneracy is somewhat mitigated by considering general relativistic effects, such as relativistic beaming and gravitational lensing. In the realm of strong gravity, these effects can profoundly alter the observed properties of the disk emission. Additionally, they are expected to exert a substantial influence on the polarization characteristics of the observed radiation [Connors and Stark, 1977, Connors et al., 1980]. For this reason, we will provide a more detailed exploration of these effects in Chapter 3.

1.4 Accreting stellar mass black holes

Accreting stellar mass black holes are found in binary systems displaying intense X-ray emissions, commonly known as *X-ray Binaries*. These systems exhibit high X-ray luminosity due to the accretion of matter from a normal star (referred to as the *donor*) onto a collapsed star, either a neutron star or a black hole. While the donor star serves as the primary optical source in the system, the compact object is responsible for the system X-ray emissions.

X-ray binaries have been traditionally classified based on the mass of the donor star into two categories: *Low Mass X-ray Binaries* (LMXBs) and *High Mass X-ray Binaries* (HMXBs). LMXBs are sustained by accretion disks supplied by a star with a mass of approximately $\lesssim 1M_{\odot}$, which fills its *Roche lobe*, i.e. the gravitational equipotential

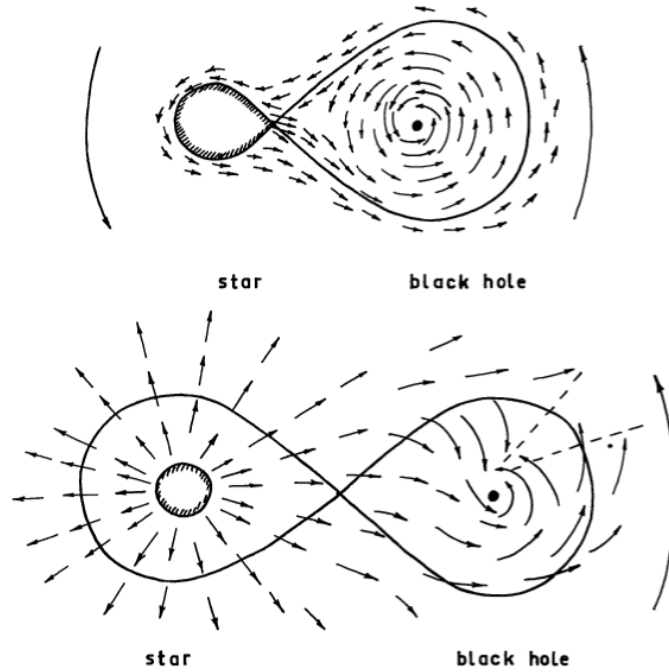


Figure 1.7: Two regimes of matter capture by a BH: (*top row*) a normal companion fills up its Roche lobe, and the outflow goes, in the main, through the inner lagrangian point; (*bottom row*) the companion size is much less than the Roche lobe and the outflow is connected with a stellar wind [Shakura and Sunyaev, 1973].

surface encompassing both objects. Conversely, HMXBs are predominantly fueled by the winds of a companion star with a mass typically $\gtrsim M_{BH}$ [e.g. Tetarenko et al., 2016], as illustrated schematically in Figure 1.7.

While some black hole binaries (BHBs), like the well-known Cygnus X-1 system [consistently accreting at a high rate and emitting luminosities above 10^{37} erg/s, Di Salvo et al., 2001, Zdziarski et al., 2002, Del Santo et al., 2013], and such as 4U1957-11, LMC X-1, and LMC X-3 (which will be extensively discussed in sections 5, 6, and 7, respectively), remain as persistent sources, the majority are transient. They spend most of their time in a low-accretion regime ($L < 10^{33}$ erg/s), where observations are still limited by the low number of counts (see [Plotkin et al., 2015] and references therein). With recurrence periods spanning from several months to decades, these binaries undergo drastic accretion rate variations, initiating outbursts lasting from a few days to, more commonly, several months. Their X-ray luminosity increases, peaks, and then decreases and can roughly be adopted as a proxy for accretion rate, while the detailed properties of the energy spectra and fast variability change, at times in a very abrupt way.

The mechanism commonly attributed to triggering outbursts, known as the *Disk Instability Model* [see, e.g., Meyer and Meyer-Hofmeister, 1981, Huang and Wheeler, 1989], can be succinctly summarized as follows. During the quiescent phase, the accretion disk medium is expected to maintain a cool, neutral state. This quiescent disk forms through a steady mass transfer from the companion star, whether as a result of Roche lobe overflow in Low-Mass X-ray Binaries (LMXBs) or via winds in the case

of High-Mass X-ray Binaries (HMXBs). Over a variable time scale across different sources, the disk temperature begins to rise. Due to the steep temperature dependence of opacity, the outer region of the disk eventually reaches temperatures high enough to initiate hydrogen ionization. This partial ionization interacts with the local magnetic field, effectively locking the magnetic field lines into the disk. The differential rotation of the disk leads to a stretching of these field lines along the radial dimension. This action tends to decelerate particles closer to the black hole (thus hastening their inward fall) while accelerating those farther away (leading them to move outward). This entire process, known as the *Magneto-Rotational Instability* initially proposed by Balbus and Hawley [1991] [see also Balbus and Hawley, 1998], essentially triggers a significant increase in turbulent viscosity within the disk, subsequently amplifying the accretion rate. As the outburst reaches its peak, and the disk is eaten away, the temperature and mass accretion rate decrease to a point that allows hydrogen recombination, triggering the thermal instability in reverse. This sequence allows the disk to revert to its cool, neutral state once again. It is however important to note that while the predictions of the disk instability model can explain many observable phenomena [Maccarone, 2014], there are a few observed phenomena that provide strong arguments against it, as the quick flux variability observed in certain BHB outbursts [e.g. XTE J1819-254 Hjellming et al., 2000].

1.4.1 X-ray Spectra

BHBs frequently display a composite spectral structure comprising both optically thick thermal emission and a Comptonization component. The thermal segment originates from the inner accretion disk and finds a fitting model in a multi-temperature black body (see section 1.3). The peak of this emission varies in energy depending on the spectral state of the source, a topic that will be further elaborated on in section 1.4.4. Typically, it ranges from approximately 0.1 – 0.3 keV for sources in hard state to around 1 keV for sources in soft state [Remillard and McClintock, 2006]. Meanwhile, the non-thermal aspect commonly takes the form of a power-law, characterized by a photon index Γ defining the photon spectrum as $N(E) \propto E^{-\Gamma}$. The origin of this component, which often extends to significantly higher energies compared to the thermal one, is widely attributed to Compton up-scattering of soft photons by high-energy electrons located in a very hot and optically thin region denominated *corona* [Zdziarski and Gierliński, 2004, Remillard and McClintock, 2006, Done et al., 2007]. In hard state sources, the power-law component typically displays an exponential cutoff at high energy, which is commonly attributed to Comptonization from an electron population featuring a Maxwellian distribution, with typical temperatures around 100 keV [Zdziarski and Gierliński, 2004]. On the other hand, this cutoff is not observed in sources in soft state, where the power-law can extend to higher energies (up to 1 MeV) with a steeper slope [Done et al., 2007]. Although the nature of this emission remains a subject of debate, it is frequently explained in terms of hybrid Comptonization, resulting from two distinct electron populations in the corona: a colder thermal population and a hotter population characterized by a power-law distribution [see e.g. Poutanen and Coppi, 1998, Coppi, 2000]. The geometry of the corona is hard to distinguish with spectral information alone and thus remains heavily debated [although see Krawczyn-

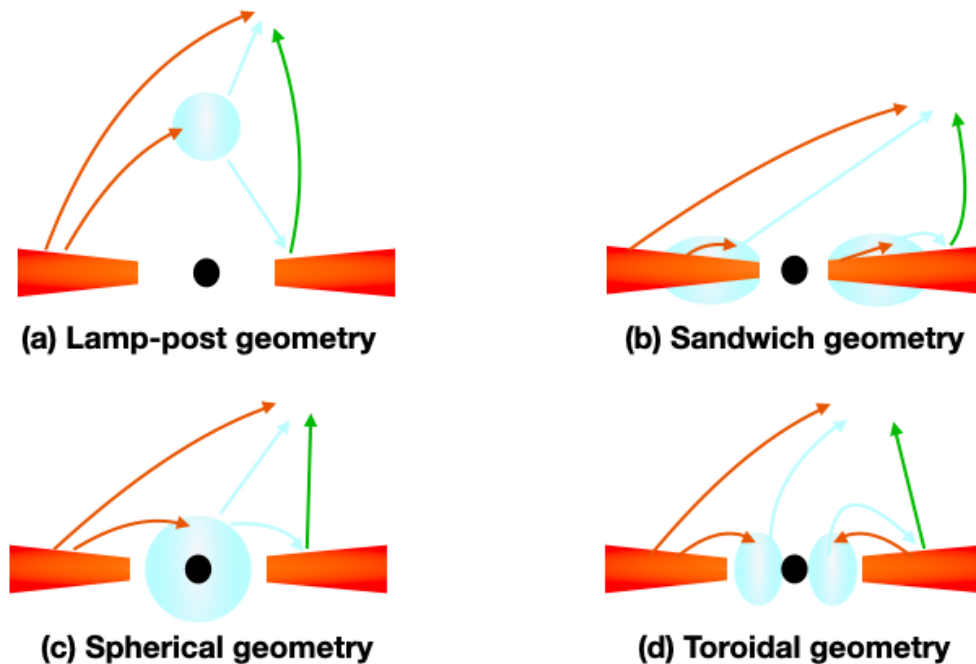


Figure 1.8: Simplified illustration of some corona geometry models: lamppost model (a), sandwich model (b), spherical model (c), and toroidal model (d). The red, light blue and green arrows indicate the thermal, comptonized and reflected component.

ski et al., 2022, for recent X-ray polarization constraints]. A simplified illustration of the most debated corona configurations is shown in Figure 1.8.

Moreover, X-ray spectra of BHBs, particularly those with inclinations that allow us to view the disk largely face-on, present an additional disk reflection component. In this case, the accretion disk reflects the X-ray powerlaw and produces a spectral bump at roughly 10 to 30 keV [see e.g. Remillard and McClintock, 2006, and references therein]. If the elements of the disk are not fully ionized the photoionization of electrons in the ions' inner shells, and the subsequent emission of fluorescent lines, can deeply modify the emitted radiation spectrum. Among these lines, the most prominent is the Fe $K\alpha$ line emitted at 6.4 keV [Matt et al., 1997]. This line arises due to the high cross-section for photoelectric absorption by iron K-shell, coupled with the large iron cosmic abundance. The energy threshold for electron photoionization in the iron K-shell stands at 7.1 keV for neutral iron and ascends with increased electron stripping in ions. The process following the L-electron filling the K-shell vacancy leads to either emitting an X-ray photon of energy 6.4 keV via a permitted electromagnetic transition or expending the energy to eject an electron from the L-shell (Auger effect). The 6.4 keV fluorescent iron line serves as a velocity field indicator in the accretion disk, its profile profoundly influenced by both special and general relativistic effects, namely gravitational redshift and the transverse Doppler effect. These effects tend to shift the line towards lower frequencies, depending on the proximity of the emitting region to the central black hole and its spin. In contrast, the longitudinal Doppler effect depends on the disk inclination concerning the observer's line of sight, particularly relevant for highly inclined disks. The analysis of these reflection features will be further explored

in section 1.4.5.

1.4.2 X-ray Timing

Black hole binaries (BHBs) are recognized for their rapid time variability, characterized by aperiodic or quasi-periodic fluctuations. The analysis of this variability is commonly conducted through the examination of power density spectra (PDS) [van der Klis, 1989]. Within the PDS of BHBs, most power spectral components exhibit broad characteristics, manifesting themselves as either a widespread power distribution spanning several frequency decades or as more localized peaks known as Quasi-Periodic Oscillations (QPOs). These QPOs are categorized into two main groups:

- Low-frequency QPOs (LFQPOs): These QPOs typically range from a few millihertz to approximately 30 Hz and represent a prevalent feature across nearly all transient BHBs. They are further classified based on their intrinsic properties, delineated by centroid frequency and width [Belloni and Motta, 2016]:
 - Type-A QPOs: Displaying a weak and broad peak around 6 – 8 Hz.
 - Type-B QPOs: Exhibiting a relatively strong and narrow peak, often concentrated around 6 Hz or within the range of 1 – 3 Hz [Motta et al., 2011].
 - Type-C QPOs: Characterized by a strong, narrow peak that exhibits variability in both centroid frequency and intensity by several percent over just a few days, typically occurring at frequencies between 0.1 and 15 Hz [Motta et al., 2015].
- High-frequency QPOs (HFQPOs): These QPOs can reach higher frequencies, up to around 450 Hz, yet their detection is limited as they appear primarily during observations at elevated flux or accretion rates [Belloni and Motta, 2016]. Notably, only in one instance, observed in the black hole GRO J1655-40 [Motta et al., 2014], have two distinct HFQPOs been firmly identified, as illustrated in Figure 1.9.

A modelization of this phenomenon was given in the *Relativistic Precession Model* [RPM, Stella et al., 1999, see also Motta et al. 2014], which associates the frequency of certain QPOs observed in accreting compact objects with certain combinations of the fundamental frequencies of motion in the strong gravitational field regime. This model offers an interpretation of type-C LFQPOs in terms of nodal precession occurring in a narrow region near the inner edge of the disk, primarily influenced by the Lense-Thirring effect [Lense and Thirring, 1918]. The higher-frequency HFQPO is identified with the orbital frequency, while the lower HFQPO is associated with the periastron precession frequency. By assuming that the perturbations generating these three QPOs originate at an identical radial distance from the black hole, the RPM establishes three independent equations linking the QPO frequencies to the radius, mass, and spin of the black hole, thereby enabling estimations of these parameters. However, the applicability of this technique hinges upon the detection of the two distinct HFQPOs and has thus far been successfully utilized in only one source, shown in Figure 1.9.

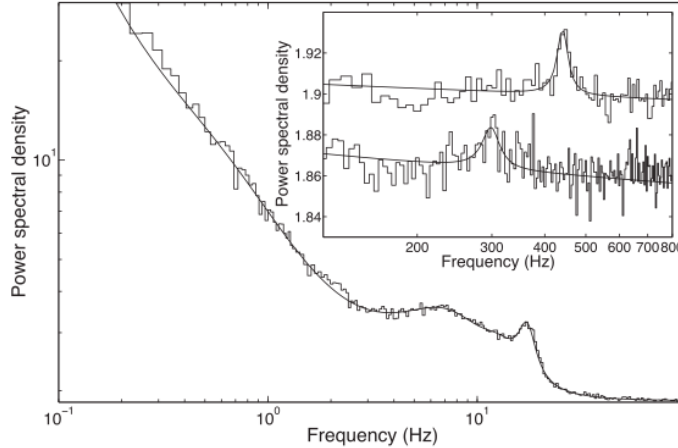


Figure 1.9: PDS obtained averaging the observations of the BH GRO J1655-40. The figure shows the three simultaneous QPOs detected in the PDS. In the large panel, we show the type-C QPO, while in the two insets we show the lower (top panel) and upper (bottom panel) HFQPOs [Figure 2 from [Motta et al., 2014](#)].

1.4.3 Outflows

While the accretion process onto stellar-mass black holes has primarily been studied in X-rays, observations at longer wavelengths have contributed to unveiling additional phenomena, notably the ejection of relativistic jets and wind outflows.

Radio emission from black-hole binaries had been detected since the early seventies [see e.g. [Tananbaum et al., 1972](#)]; however it was only in the early nineties, thanks to coordinated radio campaigns, that relativistic jets in the radio band were discovered [[Mirabel et al., 1992](#)]. These powerful ejections produce synchrotron radiation in the radio band while expanding outward at moderately relativistic speeds [[Corbel et al., 2000](#), [Fender et al., 2000](#), [Corbel and Fender, 2002](#)]. Present observational understanding strongly associates the presence of jets with the spectral state of the source, as elaborated in section 1.4.4. While the mechanisms behind jet launch have long been a focal point of investigation and conjecture, the prevailing consensus revolves around a synergy between large-scale magnetic fields and the rotation of either the central black hole, the accretion disk, or both [[Beckwith et al., 2008](#)]. Two particular Magneto Hydro-Dynamics (MHD) models have received considerable attention: the Blandford-Znajek mechanism [[Blandford and Znajek, 1977](#)] and the Blandford-Payne mechanism [[Blandford and Payne, 1982](#)]. In the Blandford-Payne model, a large-scale vertical magnetic field anchored in the disk rotates at the orbital frequency. Above and below the disk, magnetic tension dominates, compelling matter to rotate at the same frequency along the field lines. If these field lines are angled outward sufficiently, an outward force can accelerate matter along the rotating field lines. Meanwhile, the Blandford-Znajek model hinges on rotating field lines powered by the black hole itself, where field lines connecting the immediate vicinity of the black hole to infinity are forced into rotation due to frame dragging, resulting in Poynting flux carrying off energy. However, the precise contributions of these mechanisms in forming the overall accretion-ejection structure remain a subject of intense debate. Relativistic jets play a pivotal role in

the new frontier of X-ray polarimetry, standing as one of the few indicators of a source orientation in the plane of the sky. Consequently, they serve as crucial data for direct comparisons with observed polarization angles [see e.g., Figure 2 of [Krawczynski et al., 2022](#)], significantly helping the interpretation of *IXPE* data.

On the other hand, winds manifest as plasma outflows, identified by the presence of blueshifted absorption features, primarily Fe **XXV** $K\alpha$ and Fe **XXVI** $K\alpha$ transitions, displaying various stages of ionization and velocity [[Ponti et al., 2016](#), [Fukumura et al., 2021](#), [Parra et al., 2023](#)]. Such a component, almost necessarily required for continuous accretion, can efficiently transport excessive angular momentum and energy of plasma outwards [[Blandford and Begelman, 1999](#)]. Their detection often seems mutually exclusive with jet signatures [[Neilsen and Lee, 2009](#)]. Historically observed mainly in highly inclined LMXBs, indicating significant detections along the equatorial line of sight [[Ponti et al., 2012](#)], recent observations challenge this assumption. Winds are now depicted as state-independent outflows, yet their complete understanding remains elusive [see [Parra et al., 2023](#), for a recent review]. The driving mechanism behind these winds is a topic of ongoing debate, primarily categorized into thermal and magnetic driving models. The thermal driving model envisions the central spectral energy distribution (SED) heating the disk surface until the material surpasses its escape velocity [[Done et al., 2018](#)]. Conversely, the magnetic driving model involves material being lifted by large-scale magnetic fields threading the disk [[Fukumura et al., 2021, 2022](#)]. These distinct mechanisms predict contrasting absorption line properties. Thermal driving, effective further from the black hole, results in lower outflow velocities (approximately a few thousand km/s), densities, and longer-term variability. In contrast, MHD winds, generated throughout the disk with sufficient magnetization, are associated with strong signatures marked by high blueshifts, densities, and rapid variability. Current datasets might not distinctly differentiate between these MHD and thermal-radiative wind solutions due to subtle differences, even in high-quality observations [[Tomaru et al., 2023](#)]. However, MHD winds have been invoked to explain the fast velocities (between 0.03 c and 0.1 c) derived by lines detection in a number of BHB systems, e.g., IGR J17091-3624 [[King et al., 2012](#)], 4U 1630-472 [[King et al., 2014](#)], GRS 1915+105 [[Miller et al., 2016](#)], MAXI J1810-222 [[Del Santo et al., 2023](#)].

1.4.4 Spectral states

The prevailing depiction of accreting galactic BHs portrays them as sources characterized by diverse emitting regions, each contributing variably to the observed spectra. Consequently, the spectra from different BHBs can markedly differ from one another. Even within the same source, spectra can exhibit vastly distinct shapes at different times, as illustrated in Figure 1.10. A clearer understanding of these sources began emerging through the study of outbursting systems, eventually leading to the development of a unified model for BHBs initially proposed by [Fender et al. \[2005\]](#). While the evolutions of outbursts from different systems, or even multiple outbursts within the same object, can considerably differ from one another, representing the outburst evolution on a *Hardness-Intensity Diagram* (HID) reveals strong regularities. The HID, being both source-dependent due to interstellar absorption and instrument-dependent, portrays the ratio of counts in two distinct bands (hard/soft) on the abscissa, provid-

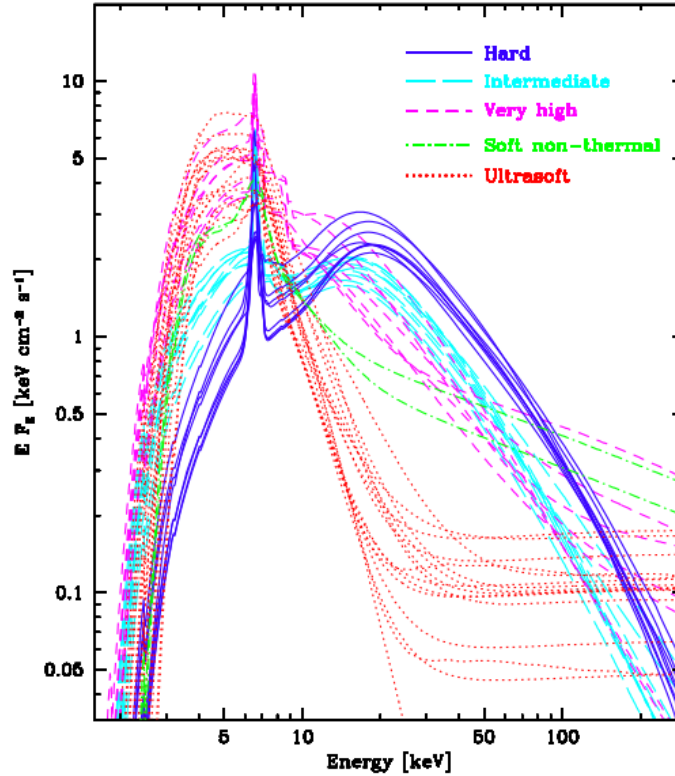


Figure 1.10: The absorbed spectral shapes of Cyg X-3 from Szostek and Zdziarski [2004]. The 42 observations are averaged into five groups, the hard state (blue solid line), the intermediate state (cyan long-dashed line), the very high state (magenta short-dashed line), the soft non-thermal state (green dot-dashed line) and the ultrasoft state (red dotted line). [Figure 1 from Hjalmarsdotter et al., 2009].

ing a rough indication of the energy spectrum hardness. On the ordinate, it illustrates the total count rate across a broad energy band, serving as a proxy for luminosity and accretion rate. The general evolution of an outburst traces a q -shaped path on the HID, typically traveled counterclockwise from the bottom-right corner. It is worth noting that a number of unusual outbursts, in which the source does not reach the soft state, have been observed. In some cases, the system never leaves the hard state and returns to quiescence after having reached a peak [Brocksopp et al., 2004, 2010]; in others, it proceeds to an intermediate state before returning to the hard state and quiescence [Capitanio et al., 2009, Ferrigno et al., 2012, Soleri et al., 2013, Del Santo et al., 2016, Bassi et al., 2019]. A qualitative representation of an HID diagram is depicted in Figure 1.11. This evolution can be summarized as follows:

- **Quiescent state (A):** Transient X-ray Binaries predominantly spend extended periods in a quiescent state lasting from a few months to decades. This phase is characterized by extreme faintness [$\sim 10^{30-33}$ erg s^{-1} ; Tetarenko et al., 2016], with minimal material transfer from the accretion disk to the compact object [McClintock and Remillard, 2006].

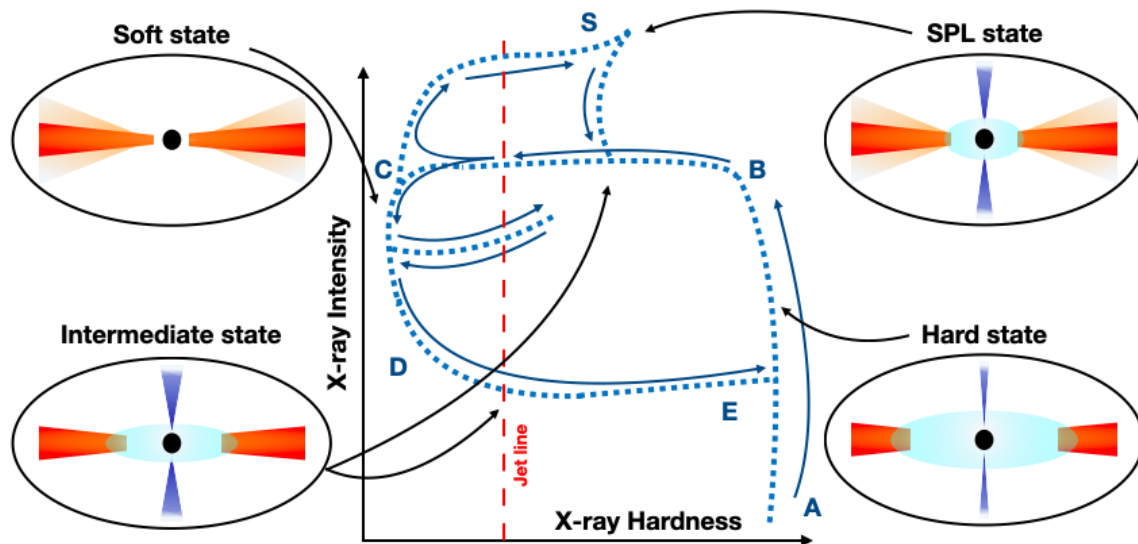


Figure 1.11: Schematic HID showing the typical path followed by a BHB source during an outburst. A simplified representation of the source geometry believed to generate the observed emission in each spectral state is also presented.

- Low/Hard state (A → B):** Transitioning from the quiescent state, the source enters the *Low/Hard State* (LHS), with a transition characterized by a rise of the X-ray luminosity of several orders of magnitude. This state is observed at the start and the end of an outburst only, never in the middle [Belloni and Motta, 2016]. In this phase the optically thick, geometrically thin disk is believed to truncate at large radii, replaced in the inner regions, possibly through evaporation [e.g., Meyer and Meyer-Hofmeister, 1994], by a hot inner flow (corona), potentially the site of jet launch. The inner flow, receiving minimal illumination from the disk, generates a hard comptonized spectrum characterized by a power-law component with a stiff photon index ($\Gamma \sim 1.5 - 1.7$) and a high energy cutoff around ~ 100 keV. This component dominates the observed spectra of LHS sources, occasionally accompanied by a weak thermal component [Done, 2010]. A reflection component is sometimes observed in this phase, characterized by the presence of a broad iron line at ~ 6.4 keV and Compton hump at ~ 30 keV. As the source brightens in the LHS, the radio luminosity increases, maintaining a flat radio spectrum. In this state, a compact jet has been resolved in a few cases in the radio band [see e.g. Stirling et al., 2001]. The radio spectrum is flat, consistent with self-absorbed synchrotron emission, and extends up to the near-infrared. The X-ray flux and radio flux show a strong positive non-linear correlation [Corbel et al., 2013]. The observational data are interpreted with the presence of a compact jet emitting in the radio through synchrotron and moving outwards with moderately relativistic speed [$\Gamma_J < 2$, see Fender et al., 2005]. Along this vertical branch, characteristic frequencies of strong noise components in the PDS increase [Belloni and Motta, 2016], often accompanied by type-C QPOs [Ingram and Motta, 2019]. Traditionally, wind detection has been linked to soft-state sources. However, in recent years, X-ray absorption lines have been

reported in certain hard-state observations [e.g., King et al., 2015, Wang et al., 2021b]. Additionally, P-cygni line profiles (produced by resonant scattering in an expanding outflow) have been detected in the visible band during the hard state [e.g., Muñoz-Darias et al., 2016, Jiménez-Ibarra et al., 2019], suggesting the presence of wind even in the LHS, preferentially observed at longer wavelengths (optical).

- **Intermediate states (B \rightarrow C):** As the source progressively increases its luminosity, it enters the horizontal branch of the HID, typically signifying a transitional stage from the hard to the soft state. This phase, collectively termed the *Intermediate States* (IMS), unfolds over a span of days to two weeks, marking a transition characterized by increased X-ray luminosity and a softer spectrum. The spectrum softens due to concurrent effects: the emergence of a substantial thermal disk component peaking around 1 to 2 keV and the steepening of the hard power-law component, shifting to a photon index of $\Gamma \sim 2.0 - 2.5$. However, the underlying physics driving this transition remains largely unknown [Remillard and McClintock, 2006]. A prevalent model [see Esin et al., 1997] proposes that for the transition to occur there must be an increase in the mass transfer rate, leading to the inward movement of the disk. When the disk is truncated far from the BH, fewer seed photons reach the hot inner flow, leading to a hard spectral component. As the disk moves inwards beneath the hot flow, the spectrum softens due to the significantly brighter disk component and a larger fraction of disk seed photons intercepting the corona, effectively cooling it via up-scattering. However, the observation of hysteresis in the evolution of a few transient sources [e.g. GX 339-4, Zdziarski et al., 2004] suggests that the mass accretion rate is not the only parameter at play in determining the spectral transitions [see e.g. Zdziarski and Gierliński, 2004]. The rapid spectral and timing property variations in this phase led to a subdivision into two sub-phases: the *Hard Intermediate State* (HIMS) and the *Soft Intermediate State* (SIMS).

- **Hard Intermediate State:** it is the first phase encountered, marked by a change of the timing and spectral properties with respect to the LHS [see e.g. Belloni et al., 2005]. The HIMS displays evident type-C Quasi-Periodic Oscillations (QPOs), with their frequency increasing as the source softens. The established correlation between radio-IR flux and X-ray flux breaks down during the HIMS, exhibiting non-monotonic radio emission variations [Fender et al., 2004]. Notably, a few sources entering the HIMS fail to transition further, returning to the LHS and eventually to quiescence [Brocksopp et al., 2004, Capitanio et al., 2009].

- **Soft Intermediate State:** In the SIMS, instead, type-C QPOs disappear, while type-B QPOs start appearing at different frequencies [Belloni and Motta, 2016]. This transition occurs over a timescale of a few seconds [Casella et al., 2004]. Instances of multiple back-and-forth transitions within days to weeks, and even down to minutes, have been observed [Casella et al., 2004, Belloni et al., 2005]. Around this transition, but not precisely coinciding with it, discrete relativistic jets are launched, observed as resolved moving radio spots or bright radio flares [Fender et al., 2005]. Although

proposed, a direct link between timing property variations and jet launch has been challenged, as jet ejection has been observed preceding the transition in certain cases [Fender et al., 2009].

- **Steep power-law state (S):** While the majority of sources exhibit no pronounced change in luminosity during the hard-to-soft and soft-to-hard transitions, pronounced variations have been identified, notably the emergence of the *steep power-law (SPL) state*. During this phase, rapid shifts in luminosity coincide with either the softening or hardening of the source spectrum, resulting in the introduction of a distinctive feature resembling a "dragon horn" into the traditional "q" pattern displayed in HID, as illustrated in Figure 1.11 [see Remillard and McClintock, 2006, for a more detailed discussion]. This behavior is not confined to isolated cases but has been observed across the brightest phases of numerous BHBs. Notably, during its first two years of operation, *IXPE* observed one such transition in a BHB, specifically 4U 1630-47 [Rodríguez Cavero et al., 2023]. Further exploration of this instance will be detailed in Chapter 4.
- **High/Soft state (C → D):** As the accretion disk progresses inwards toward the ISCO around the BH, a significant shift occurs, initiating the *High/Soft state (HSS)*. The presence of the inner disk leads to a substantial rise in disk flux, dominating the source spectra. Though the Comptonized emission persists, the remaining corona experiences intense Compton cooling due to the strong disk emission. This results in considerably softer Comptonized spectra, typically described by a power-law index with a photon index $\Gamma \geq 3$, extending beyond 500 keV [Done et al., 2007]. Unlike the hard tail observed in the LHS, the extended spectrum to 500 keV and beyond is believed to stem from non-thermal Comptonization, produced by Compton scattering on a non-thermal electron population, shaping the index primarily based on the electron distribution. To extend to 500 keV and beyond, the spectrum should be produced in a region with a rather small optical depth and high temperature. However, with a thermal distribution of electrons, these conditions would result in a bumpy spectrum, with individual Compton scattering orders separated, in contrast with the observed smooth power-law-like tail [see Done, 2010, for a more detailed discussion]. Temporal variability diminishes in this phase, occasionally revealing low-frequency QPOs, identifiable as either type-C or type-A. Radio jet emission is believed to be quenched in this phase [Fender et al., 2004]; until now no radio emission that can be attributed to the central source (and not from ejecta) has been detected down to upper limits of > 300 times that of LHS sources at the same X-ray flux [Russell et al., 2011a]. These are believed to be replaced by the presence of winds, in particular for sources observed with large inclination [Ponti et al., 2012], although X-ray absorption lines have been reported also in potentially low inclined sources [see e.g. Chakraborty et al., 2021].
- **From the HSS to quiescence (D → E → A):** The HSS, after the possible back transition to the previous intermediate states, is rather stable and can last for months [Belloni and Motta, 2016]. The luminosity tends to decrease, most likely because of a more or less steady decrease in mass accretion rate. At a

luminosity level well below that of the early HIMS (1 – 2 orders of magnitude less), a new transition takes place, eventually leading to a reversed sequence of states: starting from HSS, moving back to the SIMS and the HIMS, subsequently reaching the LHS, ultimately culminating in the termination of the outburst, and the source returning to its quiescent phase.

1.4.5 Observational Techniques

Having discussed the main observational properties of galactic BH, we now give a quick overview of the observational techniques used to distinguish a black hole from a neutron star (NS) and methods to estimate parameters like mass, distance, disk inclination, and BH spin.

Evidences for a black hole

Galactic BHs share several similarities with NS, especially when considering LMXBs. Because of this, discriminating between the two classes of objects can be a challenging task. As we mentioned in section 1.1, the collapsing star mass is the deciding factor in the formation of either a NS or a BH. As such, a measurement of the mass is the best indicator of the compact object nature: when the estimated mass exceeds $3M_{\odot}$, surpassing the maximum expected mass for a neutron star [Rhoades and Ruffini, 1974], the object is classified as a black hole. However, it is worth noting that a gap exists in the known BH and NS mass distribution between approximately $2M_{\odot}$ and $\sim 4 - 5M_{\odot}$, with few sources falling within this range [Gomez et al., 2015]. While the probability of this gap being a statistical anomaly is low [Farr et al., 2011], its existence suggests potential implications for core-collapse supernovae physics [Fryer et al., 2012].

When the mass of the compact object is not known, other distinguishing features help discern a BH. As outlined in section 1.4.1, the X-ray spectral profile associated with BHs is characterized by a soft, multi-color disk black body component and a hard power-law tail, in varying proportions. The accretion disk black body emission has a significantly lower characteristic temperature than the black body component originating from the NS surface [Done and Gierliński, 2003]; in fact, the black body characteristic of BHs is sometimes also referred to as *ultra-soft*. Hence, the presence of an ultra-soft + power-law spectrum is regarded as a spectral signature of a black hole [Remillard and McClintock, 2006]. In addition, galactic BHs exhibit rapid temporal variability in QPOs, that are linked to the spectral state and can be used in parallel with the spectral analysis to argue for the presence of a BH [Remillard and McClintock, 2006]. Moreover, BHs in hard state exhibit a strong correlation between X-ray and radio emission (see section 1.4). At a given X-ray luminosity, BHs have been noted to exhibit higher radio brightness compared to NS [see e.g. Coriat et al., 2011]. Therefore, the position of a source in an $L_{\text{Radio}}/L_{\text{X-ray}}$ diagram can serve as evidence to support the presence of a BH in a binary system. Lastly, the presence of a NS as the compact object is confirmed by observational features indicating the existence of a surface, such as Type-I bursts and/or pulsations [Tanaka and Lewin, 1995]

Distance

There are five methods commonly used to estimate the distance of a BH XRB source [for a more detailed discussion see [Jonker and Nelemans, 2004](#)]:

1. **Trigonometric parallax:** while it is the most precise and model-independent technique available, for numerous sources, this method is not practical. This is primarily because some sources are situated at considerable distances, necessitating sub-milliarcsecond astrometry to measure their parallaxes (only achievable through Very Long Baseline Interferometry). Additionally, some sources are too dim to be detected at radio wavelengths, or they are positioned in the Galactic plane where achieving high-precision astrometry is exceedingly challenging due to scatter broadening along the line of sight [see e.g. [Miller-Jones et al., 2009](#)].
2. **Counterpart star magnitude:** it is based on the comparison of the counterpart star derived absolute V-band magnitude with its apparent magnitude, taking into account a possible contribution from residual accretion. A first guess of the distance can be obtained by assuming that the absolute magnitude is that of a main sequence star of the observed spectral type, after determining the best-fit spectral type from the data. The more accurate method requires the determination of the radius, spectral type, and luminosity class directly from the data [[Jonker and Nelemans, 2004](#)].
3. **Jet proper motion studies:** limits on the distance are determined from the observed proper motion of receding and approaching blobs, assuming the jet ejections are intrinsically symmetric [see [Mirabel and Rodríguez, 1999](#), for a more detailed description of this method].
4. **Interstellar absorption studies:** in this case, distance estimation involves using the correlation between the observed equivalent widths of interstellar absorption lines and the color excess. This correlation is then used to convert the color excess to distance. Alternatively, high-resolution spectroscopic observations of interstellar absorption lines are employed to monitor the movement of individual gas clouds in velocity space. This velocity is then associated with distance by assuming it arises from Galactic rotation [[Jonker and Nelemans, 2004](#)].
5. **Dust scattering X-ray halos:** this method relies on observing a scattering halo around a point source, resulting from the interaction of X-ray radiation with dust grains in the interstellar medium. While theoretically applicable to a wide range of sources, this method is particularly effective for sources displaying rapid variations or bursts [see e.g. [Tiengo et al., 2010](#)], like transient BH XRBs. In this case, instead of a uniform halo, well-defined expanding rings of X-ray radiation can be observed. As the scattered radiation must travel a greater distance than the direct light, variations in the brightness of the central source manifest with a delay in the "echo" of the dust-scattering halo. By measuring this delay and the angular separation between the scattering halo and the source, the relative geometry of the scattering process can be determined. If the dust spatial distribution can be independently determined, it is possible to use this

measurement to constrain the source distance [e.g. Kalemci et al., 2018, Lamer et al., 2021].

BH Mass

During the quiescent phase of BHBs, detailed observations in the optical/infrared spectrum offer opportunities to study the binary companion, enabling the determination of crucial orbital parameters. These observations allow for the analysis of the donor star kinematics, which is crucial in the estimation of the BH mass. Once the companion is identified, determining the orbital period (P_{orb}) can be accomplished by detecting periodicity in either photometry (X-ray or optical/infrared) or radial velocity variations. Once P_{orb} is determined, radial velocity measurements of the secondary star can be utilized to calculate the mass function [see e.g. Tetarenko et al., 2016]:

$$f(M) = \frac{P_{orb}}{2\pi G} K_*^3 = \frac{M_{BH} \sin^3 i}{(M_{BH} + M_*)^2}. \quad (1.16)$$

Here $K_* = \nu_* \sin i$ is the semi-amplitude of the radial velocity curve. This mass function establishes a lower limit on the BH mass (M_{BH}). Further measurements of either $\nu_{BH} \sin i$ (the radial velocity of the compact object, often traced through accretion disk motion) or the counterpart star mass (determined through spectral typing, assuming it is a main-sequence star) enable the calculation of the mass ratio ($q = M_*/M_{BH}$).

BH spin and disk inclination

Measuring the spin of a Black Hole (BH) and determining the disk inclination are deeply interconnected. Presently, three distinct methods have evolved for estimating the BH spin parameter [see Reynolds, 2021, for a complete review]. Among these, two methods primarily rely on estimating the radius of the ISCO of the accretion disk (and thus employing the relation between the ISCO radius and the BH spin, see Equation 1.8), making them well-suited for observations of High Soft State sources. These methods are based on analyzing the BH-emitted spectra, focusing on either *reflection features* or the *thermal disk continuum*.

The study of the disk reflection component aims to measure the BH spin by assessing the gravitational redshift of spectral features emitted from regions close to the ISCO. This analysis focuses on the distortion of the observed X-ray reflection spectrum due to the Doppler effect from orbital motion and gravitational redshift within the black hole potential. As matter approaches the BH, emission lines develop distinct profiles, featuring sharp blueshifted peaks associated with relativistically beamed matter on the approaching side of the accretion disk and an extended redshifted wing coming from matter very close to the black hole. Figure 1.12 shows the predicted shape of Fe $K\alpha$ line, distorted by these effects. Importantly, the X-ray reflection spectrum is truncated by the ISCO; within the ISCO, the density of the accreting matter plummets as it accelerates radially inward, resulting in complete photoionization of ions in the plasma. Thus, the ISCO, and hence black hole spin, is imprinted on the X-ray reflection spectrum via the strength of the Doppler and gravitational broadening. However, it must be noted that the parameter space of the disk reflection model is quite large, as

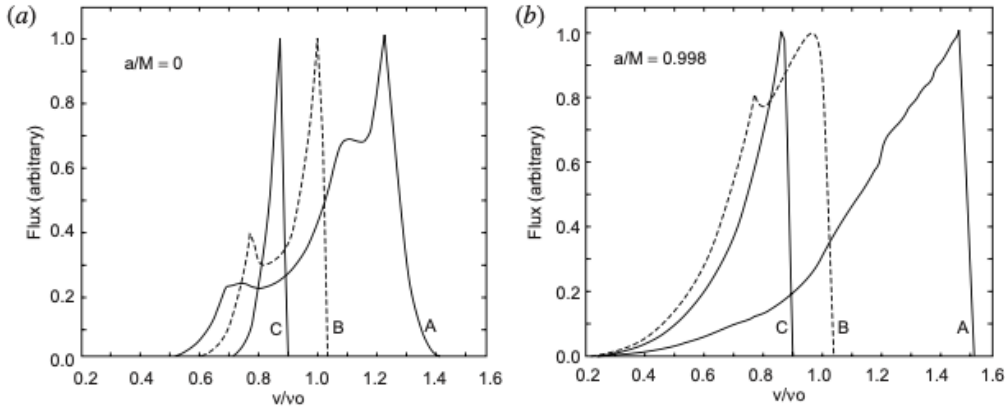


Figure 1.12: The predicted line shapes of the fluorescent 6.4 keV line for (a) Schwarzschild and (b) maximally rotating Kerr black holes. In both cases, the inclinations of the plane of the accretion disk to the plane of the sky are: A $\theta = 85^\circ$; B $\theta = 30^\circ$; C $\theta = 0^\circ$ [Longair, 2011].

these effects are also influenced by the disk inclination angle, the ionization state of the disk atmosphere, several elements' abundances (primarily Fe) and by the spectral shape of the incident radiation.

The thermal continuum fitting method relies on the BH spin influencing the ISCO location, and consequently affecting the inner disk temperature (see Figure 1.5). As mentioned in section 1.3, relativistic effects also have an impact on the disk thermal emission spectrum; Figure 1.13 shows fully relativistic models of thermal disk spectra for parameters relevant to an accreting stellar-mass black hole in an X-ray binary system [kerrbb, Li et al., 2005]. For a constant accretion rate, the spin dependence is strong, leading to changes by factors of $\sim 3 - 4$ in both the energy and normalization of the peak of the spectrum as one scans through the full range of spins. The applicability of this method is however limited by several factors; first, we need the system to be well described by the Novikov and Thorne [1973] model, with no (or weak) winds, no (or weak) corona. Second, similar to the study of the reflection features, this technique success depends on the independent estimate of several parameters, namely the accretion rate, the BH mass, the source distance, and the disk inclination.

These techniques are reliant on the inclination angle between the observer's line of sight and the disk symmetry axis. They can also help estimate this parameter, which can be independently calculated using other observations. A simple indication in this sense can be given by the observation of the source X-ray light curve folded at the system orbital period: the presence of eclipses or dips is indicative of the companion star passing between the BH and observer and thus considered an indication of a highly inclined disk [$i \leq 75^\circ$, see e.g. Wijnands et al., 2002]. Moreover, ellipsoidal variability in optical light curve studies offers information on disk inclination; this occurs as a result of the gravitational distortion of the counterpart star, causing the projected area and average temperature seen by the observer to vary differently with the orbital phase depending on the inclination [see Charles and Coe, 2006, for a detailed discussion of the entire process]. It must be noted however that accurate estimates are reliant on the correct identification of the radiation sources contributing to the optical light curve

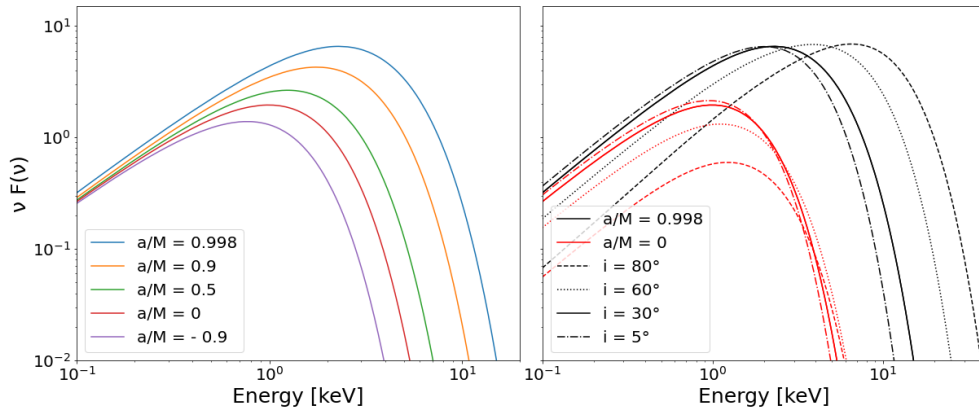


Figure 1.13: Model thermal spectra for an accretion disk around a $10 M_{\odot}$ BH, computed using the fully relativistic formalism as implemented in the `kerrbb` spectral model [Li et al., 2005] incorporated into the XSPEC spectral fitting package [Arnaud, 1996]. (*left*) Illustration of the spin dependence of thermal disk spectra. All other parameters are held fixed across these models, with inclination $i = 30^{\circ}$, $M_{BH} = 10 M_{\odot}$, $\dot{M} = 10^{18} \text{ g/s}^{-1}$, $f_{col} = 1.7$ and assuming a source distance of 10 kpc. (*right*) Illustration of the effects of inclination on disk spectra. Shown here are spectra with $i = 5^{\circ}$ (dotted-dashed), $i = 30^{\circ}$ (solid), $i = 60^{\circ}$ (dotted), $i = 80^{\circ}$ (dashed) for two spins, $a_s = 0$ (black) and $a_s = 0.998$ (red).

[Kreidberg et al., 2012]; in some cases, optical emission is likely dominated by the accretion disk [see e.g. Hakala et al., 2014], making it impossible to gain information on the system inclination from this observable.

Additionally, two more independent techniques have been proposed for studying these parameters. The first involves QPOs timing analysis (as discussed in section 1.4.2). Although not contingent on the disk inner extension or the source spectral state, its applicability is hindered by the rarity of high-frequency QPO observations. The second method, based on studying thermal emission polarization signatures, was originally proposed decades ago [Connors and Stark, 1977, Stark and Connors, 1977, Connors et al., 1980] but lacked necessary energy-dependent X-ray polarimetric data until the recent *IXPE* mission launch, reopening this investigative avenue (explored in detail in chapters 2 and 3).

Chapter 2

Polarization

2.1 Stokes parameters

Polarization in transverse waves is defined as the geometric orientation of oscillations. In the context of electromagnetic waves, it conventionally denotes the specific direction in which the electric field oscillates. An insightful exposition of this concept, introducing the notion of *Stokes parameters*, can be found in [Rybicki and Lightman \[1986\]](#), and is detailed here.

Let us consider a monochromatic wave traveling along the z -axis of an xyz orthonormal frame, represented by the wave vector $\vec{k} \parallel z$. This setup is depicted in [Figure 2.1](#), where the wave propagation direction is perpendicular to the page. The electric vector is defined as the real part of:

$$\vec{E} = \vec{E}_0 e^{i(\vec{k} \cdot \vec{r} - \omega t)} = (\vec{e}_x \cdot E_1 + \vec{e}_y \cdot E_2) e^{i(\vec{k} \cdot \vec{r} - \omega t)} \quad (2.1)$$

where \vec{e}_x and \vec{e}_y represent the base vectors along the x and y directions, respectively; \vec{r} stands for the position vector; ω denotes the frequency of the propagating wave, and t is the time at which the wave is observed. E_1 and E_2 are generally complex numbers, $E_1 = \mathcal{E}_1 e^{i\phi_1}$ and $E_2 = \mathcal{E}_2 e^{i\phi_2}$, which together give us amplitude and phase of the propagating wave. Taking the real part of the right-hand side of Equation (2.1), we find the physical components of the electric field along the axis x and y :

$$E_x = \mathcal{E}_1 \cos(\omega t - \phi_1) \quad E_y = \mathcal{E}_2 \cos(\omega t - \phi_2). \quad (2.2)$$

The equations describe the trajectory traced by the tip of the electric field vector in the xy plane, as illustrated in [Figure 2.1](#).

The trajectory takes an elliptical shape, leading to the classification of a monochromatic wave as generally *elliptically polarized*. To illustrate this, it is useful to express the electric field components in the frame $x'y'$, aligned along the semi-major axis of the ellipse. This frame is tilted at an angle χ concerning the laboratory rest frame xy , thus the electric field component can be expressed as:

$$E_{x'} = \mathcal{E}_0 \cos \beta \cos \omega t \quad E_{y'} = -\mathcal{E}_0 \sin \beta \sin \omega t, \quad (2.3)$$

where the angle β , as defined in [Fig. 2.1](#), spans from $-\pi/2$ to $\pi/2$. It describes the ellipse semi-axis lengths: $\mathcal{E}_0 |\cos \beta|$ and $\mathcal{E}_0 |\sin \beta|$, since $(E_{x'}/\mathcal{E}_0 |\cos \beta|)^2 + (E_{y'}/\mathcal{E}_0 |\sin \beta|)^2 =$

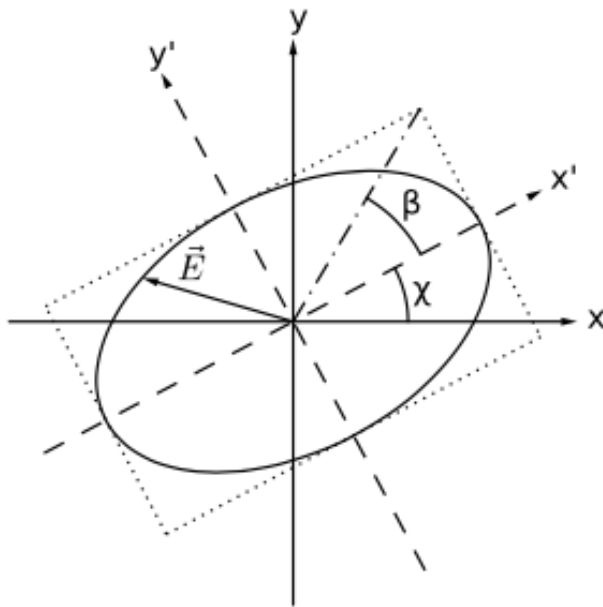


Figure 2.1: Polarization ellipse compared to the orientation of the laboratory rest frame xy .

1. When $0 \leq \beta \leq \frac{\pi}{2}$, the ellipse traces in a clockwise manner (*right-handed elliptical polarization*). Conversely, for $-\frac{\pi}{2} \leq \beta \leq 0$, the ellipse traces in a counter-clockwise manner (*left-handed elliptical polarization*), as viewed by an observer toward whom the wave is propagating. Two degenerate cases can occur:

- when $\beta \pm \pi/4$ the ellipse becomes a circle, and the wave is said to be *circularly polarized*;
- when $\beta = 0$ or $\pm\pi/2$ the ellipse collapses to a straight line, and the wave is said to be *linearly polarized*.

The electric field components in the laboratory frame xy and the ones in the ellipse major axis frame $x'y'$ are linked through a rotation by an angle χ , that can be expressed as:

$$\begin{pmatrix} E_x \\ E_y \end{pmatrix} = \begin{pmatrix} \cos \chi & -\sin \chi \\ \sin \chi & \cos \chi \end{pmatrix} \begin{pmatrix} E_{x'} \\ E_{y'} \end{pmatrix} \quad (2.4)$$

Writing the electric field components as in equations (2.2) and (2.3) we find that:

$$\begin{pmatrix} \mathcal{E}_1 \cos \phi_1 \cos \omega t + \mathcal{E}_1 \sin \phi_1 \sin \omega t \\ \mathcal{E}_2 \cos \phi_2 \cos \omega t + \mathcal{E}_2 \sin \phi_2 \sin \omega t \end{pmatrix} = \begin{pmatrix} \mathcal{E}_0 \cos \chi \cos \beta \cos \omega t + \mathcal{E}_0 \sin \chi \sin \beta \cos \omega t \\ \mathcal{E}_0 \sin \chi \cos \beta \cos \omega t - \mathcal{E}_0 \cos \chi \sin \beta \cos \omega t \end{pmatrix}. \quad (2.5)$$

Equation (2.5) must be satisfied for any time t , which means that we got a set of four

equations:

$$\mathcal{E}_1 \cos \phi_1 = \mathcal{E}_0 \cos \chi \cos \beta \quad (2.6)$$

$$\mathcal{E}_1 \sin \phi_1 = \mathcal{E}_0 \sin \chi \sin \beta \quad (2.7)$$

$$\mathcal{E}_2 \cos \phi_2 = \mathcal{E}_0 \sin \chi \cos \beta \quad (2.8)$$

$$\mathcal{E}_2 \sin \phi_2 = -\mathcal{E}_0 \cos \chi \sin \beta. \quad (2.9)$$

Given $\mathcal{E}_1, \mathcal{E}_2, \phi_1$ and ϕ_2 , these equations can be solved for \mathcal{E}_0, β and χ .

A helpful method to achieve this involves utilizing the *Stokes parameters* for monochromatic waves. Introduced by Sir George Gabriel Stokes in 1852 [Stokes \[1852\]](#), these parameters completely fix the parameters of the polarization ellipse, allowing to fully characterize the polarization state of the radiation in terms of intensities. The definition of the Stokes parameters can be obtained by manipulating equations (2.6)-(2.9). The first Stokes parameter, I , can be derived by squaring equations (2.6) - (2.9) and summing them:

$$I = \mathcal{E}_1^2 + \mathcal{E}_2^2 = \mathcal{E}_0^2. \quad (2.10)$$

The second Stokes parameter Q is defined by adding equations (2.6) and (2.8) squared and subtracting equations (2.7) and (2.9) squared:

$$Q = \mathcal{E}_1^2 - \mathcal{E}_2^2 = \mathcal{E}_0^2(\cos^2 \beta - \sin^2 \beta)(\cos^2 \chi - \sin^2 \chi) = \mathcal{E}_0^2 \cos 2\chi \cos 2\beta. \quad (2.11)$$

The third Stokes parameter U can be found by multiplying equations (2.6) and (2.8), adding the product of equations (2.7) and (2.9) and multiplying all by 2:

$$U = 2[\mathcal{E}_1 \mathcal{E}_2 \cos(\phi_1 - \phi_2)] = \mathcal{E}_0^2 \cos 2\beta \sin 2\chi. \quad (2.12)$$

Finally the fourth Stokes parameter V is defined by subtracting the product of equations (2.6) and (2.9) from that of equations (2.7) and (2.8), and multiplying the result by 2:

$$V = 2\mathcal{E}_1 \mathcal{E}_2 \sin(\phi_1 - \phi_2) = \mathcal{E}_0^2 \sin 2\beta. \quad (2.13)$$

The meaning of the four Stokes parameters is as follows: I is non-negative and is proportional to the total energy flux or intensity of the wave. Q and U describe the orientation of the ellipse and are associated with the polarization angle χ . V is the circularity parameter that measures the ratio of the principal axes of the ellipse. The wave has right- or left-handed polarization as V is positive or negative, respectively; $V = 0$ is the condition for *linear polarization*. On the other hand, $Q = U = 0$ is the condition for *circular polarization*. The Stokes parameters are related to the physical quantities of the electromagnetic wave by:

$$\mathcal{E}_0 = \sqrt{I} \quad (2.14)$$

$$\tan(2\beta) = \frac{V}{I} \quad (2.15)$$

$$\tan(2\chi) = \frac{U}{Q}. \quad (2.16)$$

It is clear that, since pure elliptical polarization is determined solely by three parameters (χ, β and \mathcal{E}_0), there must be a relation between the four Stokes parameters; for a monochromatic wave that relation is:

$$I = \sqrt{Q^2 + U^2 + V^2}. \quad (2.17)$$

The monochromatic waves just treated are said to be completely or 100% polarized since the electric vector displays a simple, non-random directional behavior in time. However, practical observations rarely involve single monochromatic components; instead, we encounter a blend of multiple components, each with its distinctive polarization. When dealing with non-monochromatic radiation, the characterization using the Stokes parameters (2.10)-(2.13) can be expanded by considering the time average of the wave physical properties. An intriguing scenario arises with the notion of a *quasi-monochromatic wave*, where over short intervals, roughly of the order $1/\omega$, the wave appears uniformly polarized, displaying a well-defined state of elliptical polarization. However, over much longer durations $\Delta t \gg 1/\omega$, during which $\mathcal{E}_1, \mathcal{E}_2, \phi_1$, and ϕ_2 undergo substantial variations, this state of polarization can undergo a complete transformation. In such instances, the definitions of the four Stokes parameters can be generalized as follows:

$$I = \langle E_1 E_1^* \rangle + \langle E_2 E_2^* \rangle = \langle \mathcal{E}_1^2 + \mathcal{E}_2^2 \rangle \quad (2.18)$$

$$Q = \langle E_1 E_1^* \rangle - \langle E_2 E_2^* \rangle = \langle \mathcal{E}_1^2 - \mathcal{E}_2^2 \rangle \quad (2.19)$$

$$U = \langle E_1 E_2^* \rangle + \langle E_2 E_1^* \rangle = \langle 2\mathcal{E}_1^2 \mathcal{E}_2^2 \cos(\phi_1 - \phi_2) \rangle \quad (2.20)$$

$$V = \frac{1}{i} (\langle E_1 E_2^* \rangle - \langle E_2 E_1^* \rangle) = \langle 2\mathcal{E}_1^2 \mathcal{E}_2^2 \sin(\phi_1 - \phi_2) \rangle, \quad (2.21)$$

where the brackets $\langle \rangle$ refer to the time averaging of the different combinations of $E_1(t)$ and $E_2(t)$:

$$\langle E_1 E_2^* \rangle = \frac{1}{T} \int_0^T E_1(t) E_2^*(t) dt. \quad (2.22)$$

Relation (2.17) does not hold for a quasi-monochromatic wave; in fact, using the Schwartz inequality it is possible to show that:

$$\langle E_1 E_1^* \rangle \langle E_2 E_2^* \rangle \geq \langle E_1 E_2^* \rangle \langle E_2 E_1^* \rangle, \quad (2.23)$$

where the equality sign holds only when the ratio of $E_1(t)$ to $E_2(t)$ is a complex constant, independent of time. This condition implies that the electric vector traces an ellipse with a fixed shape and orientation, and only undergoes a slow change in overall size with time. Such a wave is entirely equivalent to a pure elliptically polarized (i.e., monochromatic) wave due to their identical Stokes parameters. From the relation 2.23, and the definitions (2.18)-(2.21), we have:

$$I \geq \sqrt{Q^2 + U^2 + V^2}, \quad (2.24)$$

where the equality sign indicates a completely elliptically polarized wave.

Conversely, at the opposite end of the spectrum lies the completely *unpolarized* wave.

In this scenario, the phases between $E_1(t)$ and $E_2(t)$ maintain no fixed relationship, resulting in no preferred orientation in the xy plane. Consequently, we have $Q = U = V = 0$ and $I \geq 0$.

An essential property of the Stokes parameters is their additivity in the case of a superposition of independent waves. Here, *independent* indicates the absence of permanent phase relations between the waves, so that over the relevant time scales the relative phases can be considered as randomly distributed between 0 to 2π . In fact, for a superposition of N waves, each having its own $E_1^{(k)}(t)$ and $E_2^{(k)}(t)$ with $k = 1, 2, 3, \dots, N$, we have:

$$E_1 = \sum_k E_1^{(k)} \quad E_2 = \sum_k E_2^{(k)} \quad (2.25)$$

Since the waves phases are randomly distributed, only terms with $k = l$ survive the averaging, so:

$$\langle E_1 E_2^* \rangle = \sum_k \sum_l E_1^{(k)} E_2^{*(l)} = \sum_k E_1^{(k)} E_2^{*(k)} \quad (2.26)$$

From Equation 2.26 it is easy to derive the additivity between the Stokes parameters:

$$I = \sum_k I^{(k)} \quad (2.27)$$

$$Q = \sum_k Q^{(k)} \quad (2.28)$$

$$U = \sum_k U^{(k)} \quad (2.29)$$

$$V = \sum_k V^{(k)} \quad (2.30)$$

$$(2.31)$$

From the superposition principle derives that an arbitrary set of Stokes parameters can be decomposed as:

$$\begin{pmatrix} I \\ Q \\ U \\ V \end{pmatrix} = \begin{pmatrix} I - \sqrt{Q^2 + U^2 + V^2} \\ 0 \\ 0 \\ 0 \end{pmatrix} + \begin{pmatrix} \sqrt{Q^2 + U^2 + V^2} \\ Q \\ U \\ V \end{pmatrix}. \quad (2.32)$$

The first term on the right side represents the Stokes parameters characterizing a completely unpolarized wave with an intensity $I - \sqrt{Q^2 + U^2 + V^2}$, while the second term represents those of a completely (elliptically) polarized wave with an intensity $\sqrt{Q^2 + U^2 + V^2}$ as it satisfies the equality in Equation (2.24). Therefore, any arbitrary wave can be understood as an independent superposition of a completely polarized and a completely unpolarized wave. This decomposition allows to interpret the Stokes parameters for a quasi-monochromatic wave by considering the meanings previously assigned to both the completely polarized and the unpolarized parts. Hence, such a wave is defined as *partially polarized*. The degree of polarization is defined within

this framework as the ratio of the intensity of the polarized component to the total intensity:

$$\Pi = \frac{I_{pol}}{I_{total}} = \frac{\sqrt{Q^2 + U^2 + V^2}}{I}. \quad (2.33)$$

Due to *IXPE* inability to detect circular polarization, this thesis will exclusively focus on the study of linearly polarized waves, assuming $V = 0$. In this scenario, the definitions of the linear polarization degree (Π_L) and of the polarization angle (χ) are as follows:

$$\Pi_L = \frac{\sqrt{Q^2 + U^2}}{I} \quad \chi = \frac{1}{2} \arctan\left(\frac{U}{Q}\right). \quad (2.34)$$

2.2 Detecting Polarization

To measure the polarization of the incoming radiation it is necessary to use a polarimeter. The specific functioning of these instruments depends on the exploited physical mechanism; polarimeters exploiting photoelectric absorption, or Compton scattering, can detect the direction of the electron emitted (or accelerated) by the interaction with linearly polarized light. The instrument response depends on the preferential direction of the polarized radiation. For unpolarized radiation, where no specific angular preference exists, the polarimeter response remains uniform across all analyzed angular directions (see the left panel of Figure 2.2). Conversely, in the case of polarized radiation, the instrument generates a modulated response (see the right panel of Figure 2.2), described by [Fabiani and Muleri, 2014]:

$$N(\phi) = A \cos^2(\phi - \phi_0) + B \quad (2.35)$$

where A and B are constants, associated with the instrument response and with the radiation polarization degree. The instrument response to the incoming polarization vector is usually quantified through the introduction of the *modulation factor*, that is the semi-amplitude of the modulation curve produced by 100% polarized radiation normalized to its average value. This can be expressed as:

$$\mu = \frac{N_{100\%}^{max} - N_{100\%}^{min}}{N_{100\%}^{max} + N_{100\%}^{min}} \quad (2.36)$$

where $N_{100\%}^{max/min}$ is the maximum and minimum count rate (as defined in Equation 2.35) for completely polarized radiation. This parameter is related to the statistical robustness of the polarization detection [Weisskopf et al., 2010] and also allows for linking the modulated response to the Stokes parameters of the incoming radiation. The instrument response given by equation (2.35) can be rearranged, with some algebra, as:

$$N(\phi) = \frac{A}{2} (\cos(2\phi) \cos(2\phi_0) + \sin(2\phi) \sin(2\phi_0) + 1) + B \quad (2.37)$$

The Stokes parameters can be found by integrating equation 2.37 over the detection

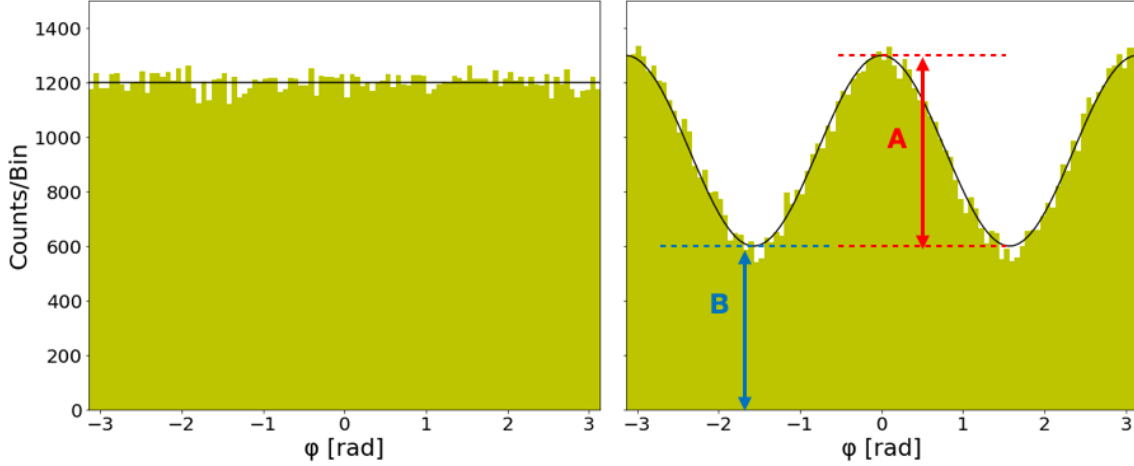


Figure 2.2: Illustration of the modulation curve derived from the measurement of the emission direction of the photoelectron in a Gas Pixel Detector (GPD) X-ray polarimeter. In the (*left*) panel the incoming radiation is assumed to be unpolarized, so the instrument response results flat. In the (*right*) panel is shown the modulation of a polarized signal; The amplitudes A and B are the same as in Eq. 2.35.

angles; considering the instrument response, we have:

$$I = \frac{1}{2\pi} \int_0^{2\pi} N(\phi) d\phi = \frac{A}{2} + B \quad (2.38)$$

$$Q = \frac{A}{2\mu} \cos 2\phi_0 \quad (2.39)$$

$$U = \frac{A}{2\mu} \sin 2\phi_0 \quad (2.40)$$

The detected polarization degree Π can be expressed as:

$$\Pi = \frac{\sqrt{Q^2 + U^2}}{I} = \frac{1}{\mu} \frac{\sqrt{\frac{A^2}{4} \cos^2 2\phi_0 + \frac{A^2}{4} \sin^2 2\phi_0}}{\frac{A}{2} + B} = \frac{A}{\mu(2B + A)} \quad (2.41)$$

so it only depends on the instrument response for polarized radiation (μ), on the amplitude of the modulation curve (A, with A = 0 representing unpolarized radiation), and on the detector response for unpolarized radiation (B). On the other hand, the polarization angle χ corresponds to the maximum of the modulation curve.

A fundamental quantity for polarization measurements is the *Minimum Detectable Polarization* (MDP). This quantity represents the degree of polarization that can be measured within a certain confidence level against the null hypothesis [see Weisskopf et al., 2010], i.e. assuming the source emission to be intrinsically unpolarized. It is not the sensibility of the instrument, but rather a threshold for the polarization detection: e.g. if the measurement is above the MDP₉₉ level, we can say that, at 99% confidence level, the detected polarization is real, and not due to stochastic noise. As such, it is important to stress that the MDP does not represent the uncertainty in a polarization

measurement. The formula for this quantity, as defined by Weisskopf et al. [2010], is:

$$MDP_{CL} = \sqrt{-s \ln(2 - CL)} \times \frac{\sqrt{N_S + N_B}}{\mu N_S} \quad (2.42)$$

where N_S is the source counts number, N_B is the total background counts, and CL is the confidence level. The confidence level used in polarimetry for assessing a polarimetric measurement is 99%; this level, lower than the 99.7% used as the standard level in spectroscopy, gives an indication of the 'photon hungry' nature of polarimetry since the unpolarized part of the source counts effectively act as an additional source of background. Assuming this standard c.l., Equation 2.42 gives:

$$MDP_{99} = \frac{4.29}{\mu R_S} \frac{\sqrt{R_S + R_B}}{T} \quad (2.43)$$

Here $R_S = N_S/T$ and $R_B = N_B/T$ are the detected source rate and the total background rate at the detector, respectively, while T is the observational time. Notably, MDP decreases with longer observation times, enabling the detection of lower polarization degrees, justifying the extended observation times used for *IXPE* observations, ranging from tens of kilo-seconds to mega-seconds.

2.2.1 Photoelectric absorption and Gas Pixel Detectors

After delving into the operational principles of a polarimeter, we can now shift our focus to the detector that made *IXPE* possible, which is known as the Gas Pixel Detector [GDP, Costa et al., 2001]. This instrument exploits the photoelectric effect, which is the dominant interaction process in the 2 – 8 keV energy band, especially for elements with low atomic number [Kaaret, 2014].

A photoelectric interaction involves a photon that is absorbed by an ion, resulting in the ejection of an electron from an inner shell, also called *photo-electron*. This process necessitates that the energy E of the absorbed photon exceeds the binding energy I required to liberate the electron, which emerges with a kinetic energy of $K_e = E - I$. Specifically, for the K-shell electron, the photoelectric cross section is described by [Heitler, 1954]:

$$\sigma_{ph}^K = 4\sqrt{2} \frac{8\pi r_0^2}{3} \alpha \left(\frac{E}{mc^2} \right)^{-7/2} \quad (2.44)$$

where α is the fine structure constant and $r_0 = e^2/(m_e c^2)$ is the classic electron radius, $r_0 = 2.82 \times 10^{-13}$ cm. This formula illustrates the maximum efficiency of the process occurring when $E = I$; as energy increases, the cross-section diminishes sharply ($\sigma_{ph}^K \propto E^{-7/2}$). The emission of the photo-electron leaves a vacancy in an inner shell of the atom, which is consequently filled by an electron from an outer shell. The energy release results in the production of an X-ray photon (fluorescence emission) or the emission of a further electron, in a process known as Auger effect. The direction of photo-electron emission tends to align with the electric field orientation of the absorbed photon, retaining information about the linear polarization of the incident radiation. For a linearly polarized photon, in the non-relativistic scenario, the angular distribution

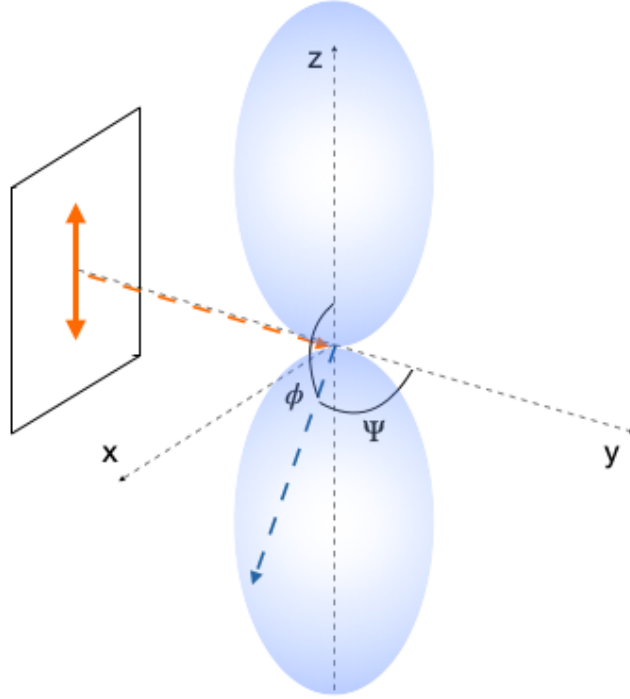


Figure 2.3: Illustration of the photoelectric absorption process. The incoming photon flight direction is shown in orange, as well as its polarization direction. The emitted photo-electron direction is shown in blue. The light-blue regions indicate the angular distribution of the photo-electron emission angles, as given by equation 2.45. The photo-electron is emitted preferentially along the photon electric field. The direction of emission is described by two angles: Φ is the azimuthal angle relative to the photon electric field vector, and Ψ is the emission angle relative to the photon momentum vector.

of the photo-electron is defined as [Heitler, 1954]:

$$\frac{\sigma_{ph}^K}{d\Omega} = r_0^2 \alpha^4 Z^5 \left(\frac{E}{mc^2} \right)^{-7/2} \frac{4\sqrt{2} \sin^2 \Psi \cos^2 \phi}{(1 + \beta \cos \Psi)^4} \quad (2.45)$$

Here ψ and Φ are the polar and azimuthal angles with respect to the incident photon flight direction (as shown in Figure 2.3); β is the photo-electron velocity in units of c . Linearly polarized incident photons cause the distribution of emitted photo-electrons per azimuthal angle to exhibit modulation as a $\cos(2\phi)$ function, as shown in Figure 2.2. The modulation amplitude (A in Figure 2.2) correlates directly with the polarization degree, with the distribution peak aligning with the direction of polarization.

The GPD (a cut-out view of which is shown in the left panel of Figure 2.4) exploits the angular dependence of the photoelectric absorption effect. In this device, a photon first traverses a beryllium window, enters an active gas volume, and upon absorption in the gas, triggers the emission of a photo-electron, which is more likely to be emitted in alignment with the photon electric field. As the photo-electron traverses the gas, it gradually loses energy, ionizing the gas and leaving behind a track. The active gas cell facilitating this photoelectric interaction consists of a 1 cm gap filled with pure

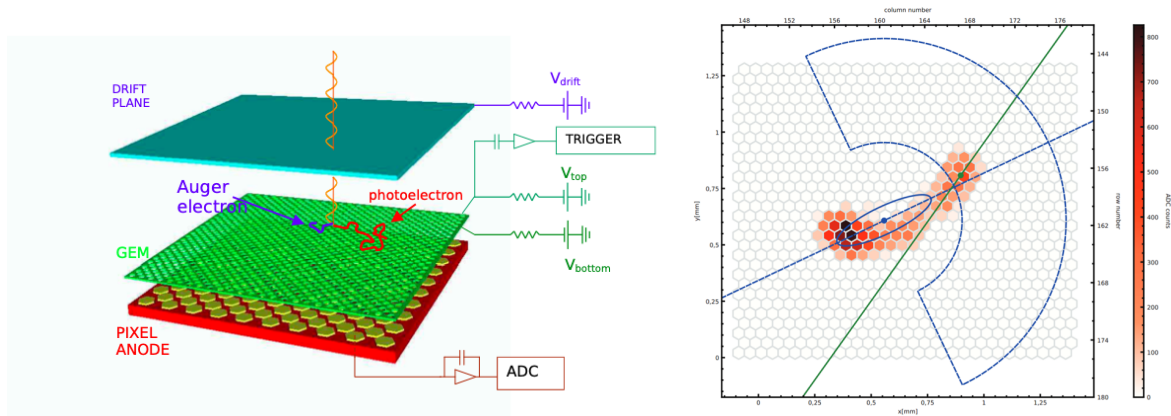


Figure 2.4: (*left*) Internal view of a Gas Pixel Detector. The volume of the gas cell is divided into two parts: the upper absorption gap, between the drift plane (which is also the entrance window) and the GEM top, and the lower transfer gap, between the GEM bottom and the readout ASIC [Kaaret, 2014]. (*right*) Real photo-electron track at 5.9 keV with the reconstructed direction of emission (green solid line) and absorption point (green dot). The blue dashed line is the first-step direction estimation based on the barycenter of the track (blue dot) from which the actual absorption point and emission direction are evaluated inside the blue half-circled area [Soffitta et al., 2021].

dimethyl-ether ((CH₃)₂O). An electric field, parallel to the optical axis, guides the primary ionization electrons generated by the photo-electron toward the Gas Electron Multiplier (GEM). This GEM is a dielectric foil with 9 μm copper metallization on both sides, featuring microscopic perforations (30 μm diameter, 50 μm pitch). The differential voltage applied to the GEM induces electron multiplication, enhancing the signal while preserving the track original shape. Subsequently, the charge generated is gathered by a pixellated anode plane, the upper layer of an ASIC (Application Specific Integrated Circuit) CMOS chip. Comprising 15 \times 15 mm² dimensions, this chip incorporates 105,600 hexagonal pixels with a 50 μm pitch. Each pixel interfaces with an underlying electronics chain equipped with signal pre-processing capabilities, facilitating the automatic localization of event coordinates. The polarization information is extracted statistically from the angular distribution of track emission directions of the photo-electrons. This information is reconstructed by imaging the track projections onto the readout plane, as shown in the right panel of Figure 2.4. The GPD maintains azimuthal symmetry in its response, enabling it to function as a non-rotating device suitable for placement at the focal point of X-ray telescope optics. Additionally, aside from its role as a polarimeter, the GPD exhibits commendable imaging capabilities, constrained primarily by the Point Spread Function (PSF) of the optics [Soffitta et al., 2013, Fabiani et al., 2014].

2.2.2 IXPE

We now describe the main characteristics of the *Imaging X-Ray Polarimeter Explorer (IXPE)* [Weisskopf et al., 2022]. Born as a collaboration between the NASA Marshall Space Flight Center (MSFC) and the Italian Space Agency (ASI), this project

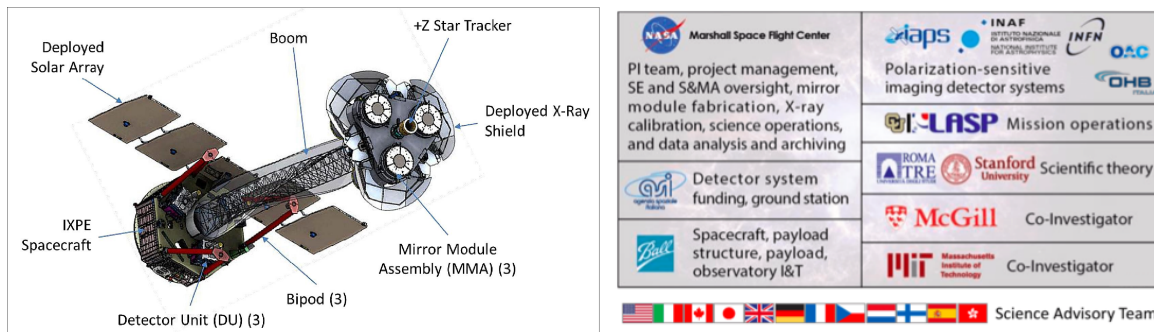


Figure 2.5: *Left*: The *IXPE* Observatory highlighting the key scientific payload elements. A second star tracker (not visible) is on the back of the spacecraft, pointing along the $-z$ axis. *Right*: Institutions, Universities, and organization partners of the *IXPE* mission.

was realized thanks to the involvement of several institutions, Universities, and organizations, as shown in the right panel of Figure 2.5. *IXPE* payload, shown in the left panel of Figure 2.5, consists of three identical X-ray telescopes each comprised of a Mirror Module Assembly (MMA) with a polarization-sensitive Detector Unit (DU) at its focus, each containing a GPD. The detectors are clocked at a 120° angle with respect to each other; this disposition, once the images from the three detectors are rotated and summed, allows for a reduction of spurious effects. A lightweight 4-meter long boom was deployed after launch to establish the appropriate focal length and to position each MMA above its respective detector. Fixed X-ray shields, in combination with collimators on each detector, limit stray radiation so that only X-ray photons that enter through an MMA can impinge on the detector entrance window. Two star trackers, one along the $+z$ axis as shown in Figure 2.5, and one point along the $-z$ axis but hidden by the spacecraft in the figure, provide pointing knowledge for the three-axis-stabilized spacecraft. The spacecraft supports the *IXPE* payload mounted on its top deck; command and data handling are controlled by an integrated avionics unit. This contains the flight software and handles the telemetry, data storage, and overall payload control. Communication is via S-band, with a 2 kbps command rate and a 2 Mbps downlink telemetry rate. A 6 GBytes on-board memory is assigned for data storage between downloads [Weisskopf et al., 2022].

The MMAs are comprised of 24 concentrically nested mirror shells, made of a nickel/cobalt alloy which provides optimum reflectivity over the *IXPE* energy band of 2–8 keV. The telescope field of view is limited by the size of the detector to $12.9' \times 12.9'$ (due to the full detector area of $15 \times 15 \text{ mm}^2$). The angular resolution is $\sim 25\text{--}30''$. The three MMAs effective area increases from $\sim 167\text{--}168 \text{ cm}^2$ at 2 keV to $\sim 195\text{--}200 \text{ cm}^2$ at 4.5 keV, while it decreases at high energies as illustrated in Figure 8 of Weisskopf et al. [2022]. The *IXPE* DUs contain a GPD (described in section 2.2.1), which images the photo-electron tracks produced by the absorbed X-ray photons. Each DU has an energy resolution of 0.59 keV at 2 keV, which roughly scales as $1/\sqrt{E}$ with energy. The timing resolution is $\approx 1\text{--}2 \mu\text{s}$. To enable in-flight calibration monitoring, each DU is equipped with a filter and calibration wheel assembly. These contain various radioactive sources that can be rotated in front of the GPD to provide for monitoring

gain, energy resolution, spurious modulation, and the modulation factor. Moreover, it contains an open position (for regular observations) and a gray filter, used to attenuate the flux of very bright sources. *IXPE* was launched on the 9 of December 2021, with a SpaceX Falcon9 rocket. It was placed in a 600 km circular, equatorial orbit to minimize the passage over the South Atlantic Magnetic Anomaly and maximize the number of passages per day over the Malindi Ground Station for communication with the Observatory.

The first results obtained with this telescope on stellar mass BHs in soft state will be presented in Part II, while the data reduction techniques employed in the *IXPE* data analysis are detailed in Appendix A.

2.3 Polarization in black hole binaries

Polarization is a powerful tool in astrophysics, offering unique insights into the physical processes occurring in celestial objects. It provides a wealth of information about magnetic fields, scattering mechanisms, and asymmetries in various astrophysical environments. In many wavelength ranges, such as the infrared and visible bands, radiation in the Universe tends to be dominated by emissions produced in stellar processes. This emission tends to exhibit a predominantly unpolarized nature due to the spherical structure of their emitting regions. Despite this, also in these observational bands, polarimetry has yielded fundamental results, e.g. the AGN unification model [Antonucci, 1993].

In the X-rays, the relevance of polarization has always been anticipated to be significantly higher. This expectation arises from the prevalence of acceleration phenomena governing the energy output of X-ray sources. Moreover, the presence of strong magnetic fields profoundly influences emissions in numerous white dwarf and neutron star sources within this range. Inverse Compton scattering in non-spherical geometries is widely believed to be the primary emission process from black hole accretion systems, both in Galactic binaries and in AGN. All these processes leave their distinct mark on the polarization properties of the observed radiation.

In the case of stellar mass BHs, two fundamental effects are influencing the polarization properties of the observed radiation: the scattering processes occurring within the disk atmosphere and in the corona, and the special and general relativity effects influencing the polarization state of photons propagating in a strong gravity regime; those will be described in the following sections.

2.3.1 Scattering

One of the fundamental interactions between photons and free electrons is known as scattering, with the simplest manifestation being *Thomson scattering*. This process, describable through classical electrodynamics, occurs when the energy of incoming photons in the electron comoving frame is considerably smaller than the rest mass-energy of the electron. However, as the energy of incoming photons approaches or surpasses $m_e c^2$ a quantum treatment, known as the *Klein–Nishina regime*, becomes necessary.

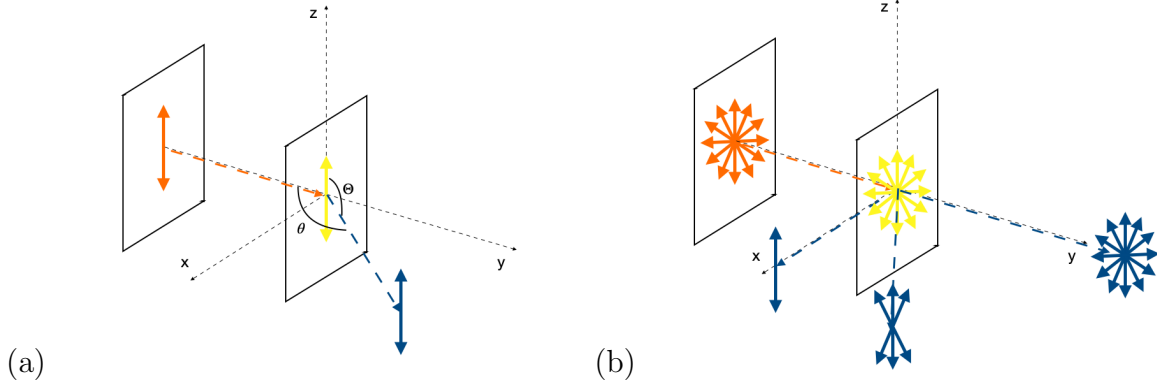


Figure 2.6: Simplified illustration of the scattering process. In both panels the incident radiation is propagating along the y axis. (a) The incident radiation is polarized along the z axis. (b) The incident radiation is unpolarized. The orange and blue solid lines indicate the polarization vectors of the incident and scattered radiation, respectively, while the yellow lines denote the electron oscillation vector

Thomson scattering

In the Thomson scattering regime, the interaction can be described with an electron at rest and an electromagnetic wave of frequency $\nu \ll m_e c^2/h$. The electron starts oscillating in response to the varying electric force eE (in the direction of the incoming wave polarization vector). The average square acceleration experienced during one oscillation period $T = 1/\nu$ can be expressed as:

$$\langle a^2 \rangle = \frac{1}{T} \int_0^T \frac{e^2 E_0^2}{m_e^2} \sin^2(2\pi\nu t) dt = \frac{e^2 E_0^2}{2m_e^2}. \quad (2.46)$$

The emitted power per unit solid angle is given by the Larmor formula: $dP/d\Omega = e^2 a^2 \sin^2 \Theta / (4\pi c^3)$, where Θ represents the angle between the acceleration vector of the electron and the propagation vector of the emitted radiation (see panel (a) of Figure 2.6). For the average acceleration given by Equation 2.46 Larmor formula simplifies to:

$$\frac{dP}{d\Omega} = \frac{e^4 E_0^2}{8\pi m_e^2 c^3} \sin^2 \Theta. \quad (2.47)$$

The resulting scattered radiation is linearly polarized in the plane defined by the incident polarization vector and the scattering direction. Consequently, if the incident radiation is fully polarized, the scattered radiation remains 100% polarized, irrespective of the scattering angle θ (i.e., the angle between the incident and scattered radiation propagation vectors). A simplified illustration of this process is shown in panel (a) of Figure 2.6. The flux of the incoming wave is $S_i = cE_0^2/(8\pi)$. The differential cross-section of the process then can be expressed as [Ghisellini, 2013]:

$$\left(\frac{d\sigma_T}{d\Omega} \right)_{pol} = \frac{dP/d\Omega}{S_i} = r_0^2 \sin^2 \Theta. \quad (2.48)$$

where r_0 is the classic electron radius. This expression denotes that the emitted power is maximal perpendicular to the electron oscillation ($\Theta = 90^\circ$) direction, and zero along

this direction ($\Theta = 0^\circ$). The scattered pattern of a completely polarized incoming wave is a torus, with the axis along the acceleration direction, as pictured in panels (a) and (b) of Figure 2.7.

The scattering of a completely unpolarized incoming wave can be derived by assuming that the incoming radiation is the sum of two orthogonal completely linearly polarized waves, and then summing the associated scattering patterns. Since we have the freedom to choose the orientations of the two polarization planes, it is convenient to choose one of these planes as the one defined by the incident and scattered directions, and the other one perpendicular to this plane. The scattering can be then regarded as the sum of two independent scattering processes, one with emission angle Θ , the other with $\pi/2$. If we note that the scattering angle is $\theta = \pi/2 - \Theta$, from Equation (2.48) we have:

$$\begin{aligned} \left(\frac{d\sigma_T}{d\Omega}\right)_{unpol} &= \frac{1}{2} \left[\left(\frac{d\sigma(\Theta)}{d\Omega}\right)_{pol} + \left(\frac{d\sigma(\pi/2)}{d\Omega}\right)_{pol} \right] = \\ &= \frac{1}{2} r_0^2 (1 + \sin^2 \Theta) = \frac{1}{2} r_0^2 (1 + \cos^2 \theta). \end{aligned} \quad (2.49)$$

In this case we see that the cross section depends only on the scattering angle θ . The scattered radiation pattern emerges as the amalgamation of two orthogonal "tori", each corresponding to a distinct polarization direction, as depicted in the bottom panel of Figure (2.7). When scattering completely linearly polarized radiation, only one 'torus' persists. However, when unpolarized radiation scatters, a degree of polarization arises due to the discrepancy between the two "tori" patterns. Both terms of the right hand side of Equation (2.49) refer to completely polarized scattered waves (but in two perpendicular planes). The difference between these two terms is then associated to the introduced polarization, which is then:

$$\Pi_T = \frac{1 - \cos^2 \theta}{1 + \cos^2 \theta}. \quad (2.50)$$

From this it is clear that the scattering process introduces some polarization, which is maximum (100%) when the angle between the incoming and the scattered photons is 90° (only one torus contributes), and zero for forward- and back-scattering events ($\theta = 0^\circ$ or 180°), where the two torii give the same contribution. A simplified illustration of this dependence is shown in panel (b) of Figure (2.6).

The total cross-section of the scattering process in the Thomson regime can be found integrating over the solid angle the differential cross-section given by Equation (2.49). This is usually referred to as the *Thomson cross-section*:

$$\sigma_T = \frac{2\pi r_0^2}{2} \int (1 + \cos^2 \theta) d\cos \theta = \frac{8\pi}{3} r_0^2 = 6.653 \times 10^{-25} \text{ cm}^2 \quad (2.51)$$

Compton scattering and Klein–Nishina cross-section

As the energy of the incoming photons increases and approaches the electron rest mass energy, the inclusion of quantum effects becomes necessary. Quantum influences manifest in two fundamental ways: firstly, through the kinematics governing the scattering process, and secondly, through the modification of the cross-sections.

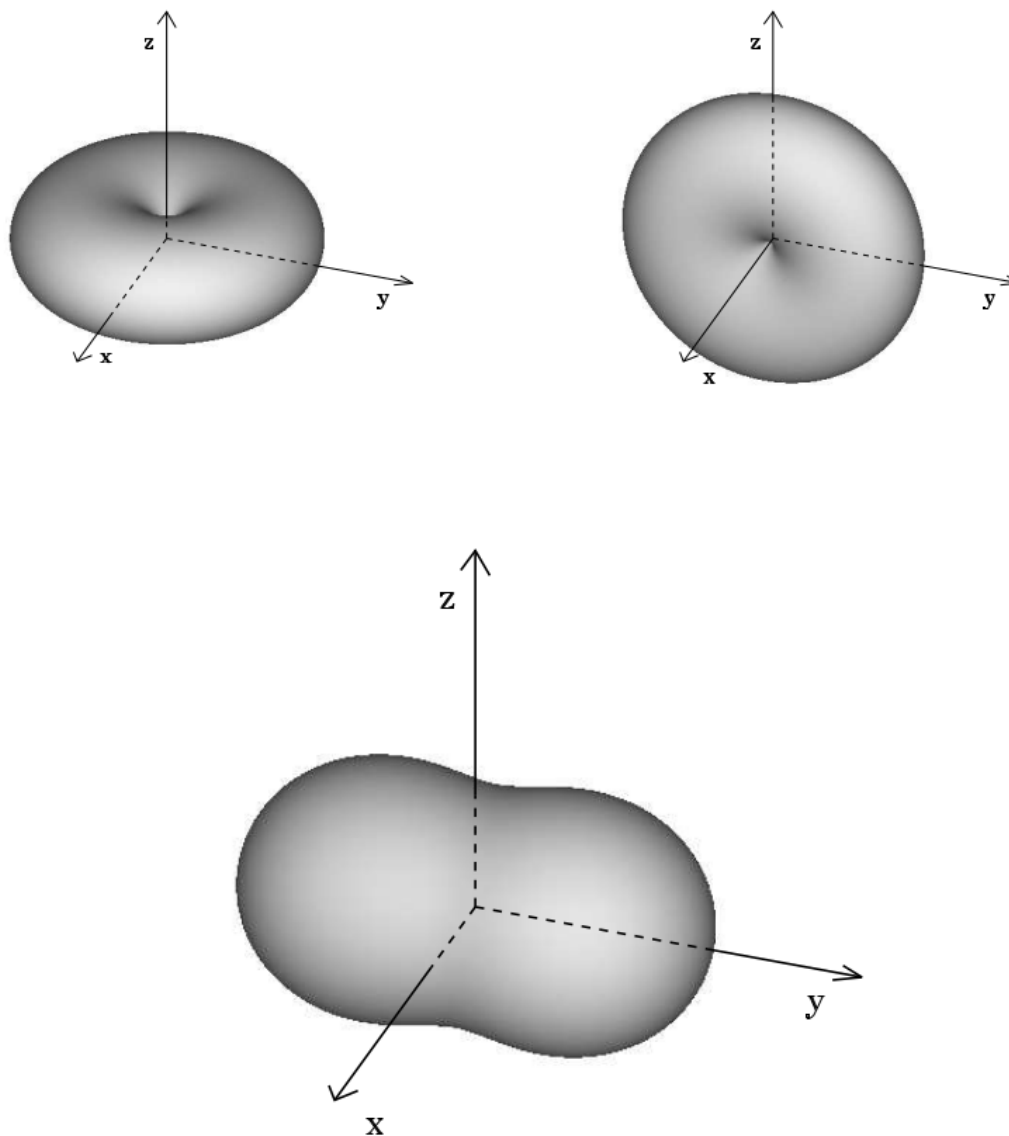


Figure 2.7: Angular distribution of the differential cross-section in the electron co-moving frame. The top panels illustrate the scattered radiation pattern for photons completely linearly polarized along the z axis (left) and along the x axis (right). The combined pattern of the two represents the scattering distribution for unpolarized radiation (bottom panel). Incoming photons are always assumed to propagate along the y axis [Ghisellini, 2013].

When considering the kinematics of this interaction, it is crucial to treat the scattering process as a relativistic collision. Let us delve into the interaction between an incident photon and a moving electron with velocity v in the laboratory frame of reference S . The 4-momenta of the photon before and after the interaction are denoted by $P_\nu = (h\nu/c, \hat{n}h\nu/c)$ and $P'_\nu = (h\nu'/c, \hat{n}'h\nu'/c)$, where \hat{n} and \hat{n}' represent the initial and final propagation directions of the photon, respectively. Concurrently, the corresponding 4-momenta of the electron are $P_e = (\gamma m_e c, \gamma m_e \vec{v})$ and $P'_e = (\gamma' m_e c, \gamma' m_e \vec{v}')$. Conservation of momentum and energy is expressed by:

$$P_\nu + P_e = P'_\nu + P'_e \quad (2.52)$$

Squaring both sides of this equation, and using that $P_e \cdot P_e = P'_e \cdot P'_e = m_e c^2$ and $P_\nu \cdot P_\nu = P'_\nu \cdot P'_\nu = 0$, we have:

$$(P_e + P_\nu)^2 = (P'_e + P'_\nu)^2 \rightarrow P_e \cdot P_\nu = P'_e \cdot P'_\nu \quad (2.53)$$

Multiplying equation (2.52) by P'_ν and using the equality (2.53) we have:

$$\begin{aligned} P_e \cdot P'_\nu + P_\nu \cdot P'_\nu &= P'_e \cdot P'_\nu + P'_\nu \cdot P'_\nu \rightarrow \\ P_e \cdot P'_\nu + P_\nu \cdot P'_\nu &= P_e \cdot P_\nu \end{aligned} \quad (2.54)$$

The scattering angle of radiation is given by $\hat{n} \cdot \hat{n}' = \cos \theta$, while we define as α and α' the angles between the incoming photon and the velocity vector of the electron before and after the collision, respectively, so that $\vec{v} \cdot \hat{n} = v \cos \alpha$ and $\vec{v}' \cdot \hat{n}' = v' \cos \alpha'$. Calculating the four-vector products, after some algebra, we have:

$$h\nu' = \frac{h\nu \left(1 - \frac{v}{c} \cos \alpha\right)}{1 - \frac{v}{c} \cos \alpha' + \frac{h\nu}{\gamma m_e c^2} (1 - \cos \theta)} \quad (2.55)$$

This relation shows that, in the Compton scattering regime, there is an exchange of energy in the interaction between the photon and the electron. In the limit of low-energy photons ($h\nu \ll m_e c^2$) this reduces to:

$$\frac{\Delta\nu}{\nu} = \frac{v}{c} \frac{(\cos \theta - \cos \theta')}{1 - \frac{v}{c} \cos \theta'} \quad (2.56)$$

At the first order the frequency changes behave as $\sim v/c$, and if the angles θ and θ' are randomly distributed a photon is just as likely to decrease as increase its energy. Thus there is no net increase in energy of the photons at the first order in v/c ; the latter comes out only at the second order v^2/c^2 [e.g. see Longair, 2011].

The fundamental relationships describing the polarization of radiation in the Compton regime have been studied extensively in many books and papers [see e.g. McMaster, 1961, Fernández et al., 1993, Poutanen and Vilhu, 1993, Poutanen, 1994, Matt et al., 1996]. Here we only report the most important relationships, to obtain a direct comparison with the scattered radiation polarization degree in the Thomson regime, described by equation (2.50). To do that, we will consider the free electron at rest, a scenario

known as *direct Compton scattering*. In this case $v = v' = 0$, $\gamma = 1$ and Equation (2.55) becomes:

$$h\nu' = \frac{h\nu}{1 + \frac{h\nu}{m_e c^2} (1 - \cos \theta)} \longrightarrow x' = \frac{x}{1 + x(1 - \cos \theta)} \quad (2.57)$$

where x and x' are the photon energies before and after the interaction in units of $m_e c^2$. From Equation (2.57) is clear that in the low energy regime ($x \ll 1$) the energy of the scattered photon is $x' = x$, recovering the Thomson scattering result. On the other hand, for $x \gg 1$ and $\cos \theta \neq 1$ we have $x' \rightarrow (1 - \cos \theta)^{-1}$, thus the scattered photon carries information only on the scattering angle, and not on its initial energy. The energy shift implied by Equation (2.57) is due to the recoil of the electron originally at rest, and becomes significant only when x becomes comparable with 1 (or more).

In this high-energy scenario, when quantum effects need to be taken into account to describe the electron-photon interaction, the differential cross-section of the scattering process is no longer described by the Thomson expressions (equations 2.48, 2.49 and 2.51). A generalization of those equations is given by the *Klein-Nishina* cross-section, which, if the incoming radiation is unpolarized, can be expressed in the following form [Matt et al., 1996]:

$$\left(\frac{d\sigma_{KN}}{d\Omega} \right)_{pol} = \frac{1}{2} r_0^2 \left(\frac{x'}{x} \right)^2 \left(\frac{x'}{x} + \frac{x}{x'} - 2 \sin^2 \theta \cos^2 \Psi \right). \quad (2.58)$$

where θ is the scattering angle and Ψ is defined as the angle between the polarization unit vector of the incident photon (\hat{p}) and the plane of scattering, also known as the *azimuthal scattering angle*. From Equation (2.61) it is possible to obtain the polarization degree of the scattered radiation, which can be expressed as:

$$\Pi_{KN}^{pol} = 2 \frac{1 - \sin^2 \theta \cos^2 \Psi}{\frac{x'}{x} + \frac{x}{x'} + 2 \sin^2 \theta \cos^2 \Psi}. \quad (2.59)$$

In the Thomson limit ($x = x'$) Π_{KN}^{pol} becomes equal to 1: a completely polarized incident beam gives completely polarized scattered beams. As the energy exchange becomes more relevant, the polarization degree of the scattered radiation tends to decrease; this is particularly true for the back-scattering process ($\theta = 180^\circ$), while in the forward-scattering process ($\theta = 0^\circ$) the resulting radiation remains polarized at 100%. If the scattering angle is 90° , a strong dependence on the azimuthal scattering angle Ψ is expected (see Figure 2.8). The polarization vector \hat{p}' for the scattered photons is linked to the incident radiation one by the following relationship:

$$\hat{p}' = \frac{1}{|\hat{p}'|} (\hat{p} \times \hat{d}) \times \hat{d}, \quad (2.60)$$

where \hat{d} is the direction of the scattered photon. The polarization vectors of the remaining $1 - \Pi_{KN}^{pol}$ fraction are instead randomly distributed in the plane normal to \hat{d} .

If the incoming radiation is unpolarized the differential cross-section can be obtained simply by averaging over the Ψ angle [Matt et al., 1996]:

$$\left(\frac{d\sigma_{KN}}{d\Omega}\right)_{unpol} = \frac{1}{2}r_0^2 \left(\frac{x'}{x}\right)^2 \left(\frac{x'}{x} + \frac{x}{x'} - \sin^2\theta\right). \quad (2.61)$$

The polarization degree of the scattered photon in this case assumes the following form:

$$\Pi_{KN}^{unpol} = \frac{1 - \cos^2\theta}{\frac{x'}{x} + \frac{x}{x'} - 1 + 2\cos^2\theta}. \quad (2.62)$$

Since the polarization vectors \hat{p} of the incoming photons are randomly distributed before the scattering, the azimuthal distribution of the scattered photons polarization vector will be isotropic, as in the Thomson case. As for Equation (2.50), also Equation (2.59) reduces itself to the result found in the Thomson regime (Equation 2.50) for $x = x'$. As the energy of the incoming photon increases, and the energy exchange becomes more important, the polarization degree of the scattered radiation tends to decrease, as shown in the bottom panel of Figure 2.8. Like in the case where the incoming radiation is polarized, as the energy increases the forward-scattering process tends to induce a larger polarization degree than the back-scattering. Because of this, the peak of the polarization degree distribution shifts from 90° towards lower inclination angles.

As for the Thomson cross-section, by integrating the Klein-Nishina differential cross-section over the solid angle it is possible to obtain the total cross-section of the interaction [see e.g. Rybicki and Lightman, 1986], defined by:

$$\sigma_{KN} = \frac{3}{4}\sigma_T \left\{ \frac{1+x}{x^3} \left[\frac{2x(1+x)}{1+2x} - \ln(1+2x) \right] + \frac{1}{2x} \ln(1+2x) - \frac{1+3x}{(1+2x)^2} \right\}, \quad (2.63)$$

For low energy photons, the cross-section converges towards the classical expression ($\sigma_{KN} \approx \sigma_T$). On the other hand, for the extreme relativistic regime we have:

$$\sigma_{KN} \approx \frac{3}{8}\sigma_T x^{-1} \left(\ln 2x + \frac{1}{2} \right) \quad (2.64)$$

The dependence of the Klein-Nishina cross-section on the incident photon energy is shown in Figure 2.9. As the photon energy increases, the cross-section diminishes from its classical value. Consequently, Compton scattering exhibits decreased efficiency for high-energy photons. Since the astrophysical objects this thesis focuses on, galactic black holes in soft state, tend to emit the bulk of their radiation below 100 keV, in most cases the Thomson scattering regime will be considered a suitable approximation for our analysis.

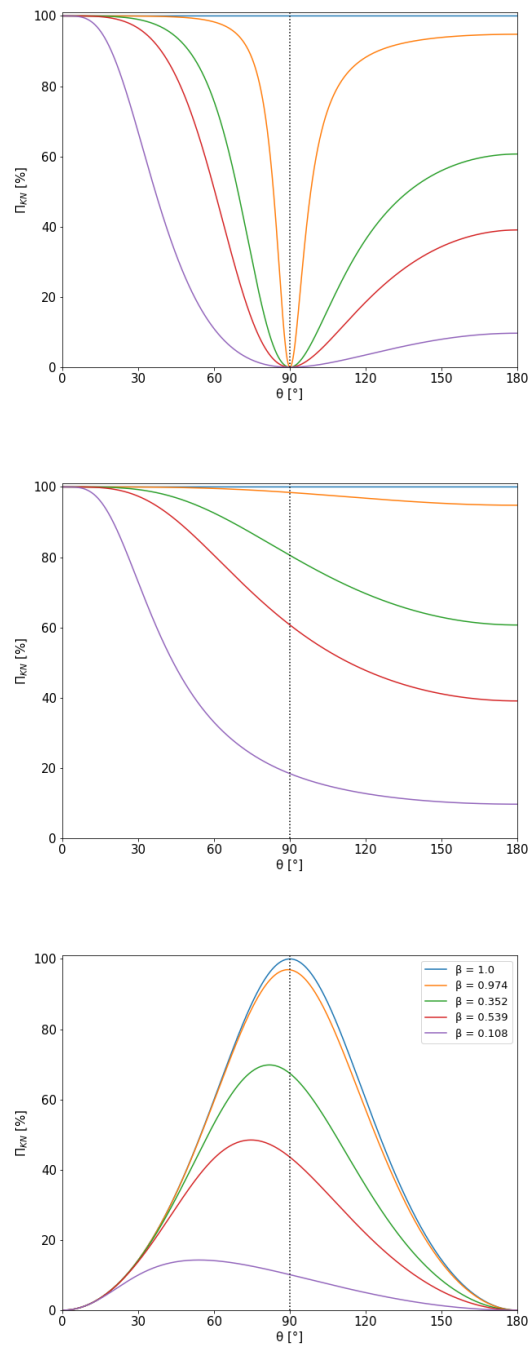


Figure 2.8: Polarization degree of the scattered radiation as a function of the scattering angle θ . The top and middle panels display the resulting polarization degree when the incident radiation is polarized either in the same direction (i.e. $\Psi = 0^\circ$, top) or perpendicularly (i.e. $\Psi = 90^\circ$, middle) to the scattered photon propagation direction, as for Equation (2.59). The bottom panel shows the results assuming the incident radiation to be unpolarized, described by Equation (2.62). The different colors indicate different values of the ratio between the initial and the final energy of the photon $\beta = x'/x$, with $\beta = 1$ indicating the Thomson scattering case.

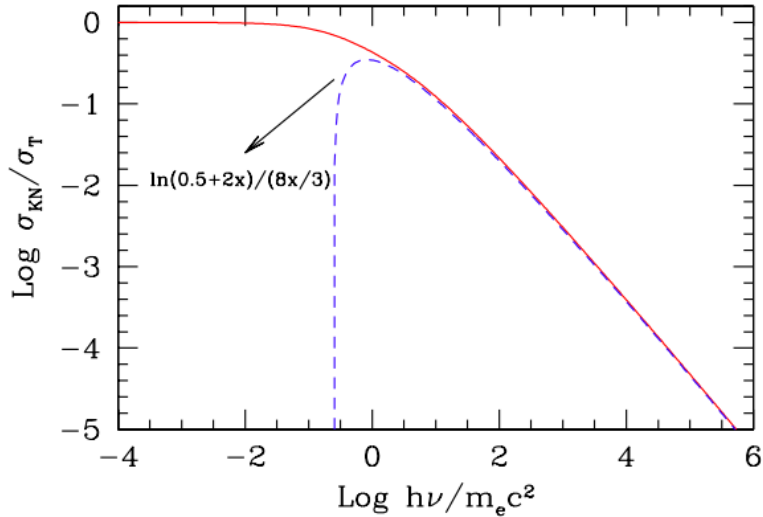


Figure 2.9: The total Klein–Nishina cross-section as a function of energy. The dashed line is the approximation at high energies as given in Equation (2.64) [Ghisellini, 2013].

2.3.2 Scattering in the disk and the corona

We now discuss how the scattering processes define the polarization properties of the different spectral components observed in stellar mass BHs spectra.

Disk thermal emission

In our previous discussion on accretion disks (Section 1.3), we have shown that the radiation emitted from these disks around stellar mass BHs appears as a multi-color black body due to temperature variations across the disk. The black body radiation emitted is, by definition, unpolarized. However, when accounting for the total disk emission, it is necessary to consider also the scattering processes that photons may undergo before leaving the disk atmosphere, that induce polarization. Due to the non-spherical distribution of matter in the disk, these result in a net polarization degree of the total disk emission.

To model this polarization, a commonly used approach in literature relies on computations by Chandrasekhar [1960] and Sobolev [1963], considering a scenario of pure electron scattering in a plane parallel atmosphere with infinite optical depth ($\tau \rightarrow \infty$). A Thomson scattering regime is usually assumed due to the disk relatively low temperatures (see section 1.3 and Figure 1.5). It is important to note that using this approximation means assuming that the disk atmosphere is completely ionized, and thus neglecting the contribution of all effects but scattering (e.g. photoelectric absorption) on the polarization properties of the emitted radiation. This topic will be expanded in Chapter 3.

The results of these computations are shown in Figure 2.10. The radiation emerging from the accretion disk atmosphere is expected to be polarized with a polarization degree that does not depend on the photon energy (as expected in the Thomson scattering regime), but only on the angle θ between the radiation direction and the disk

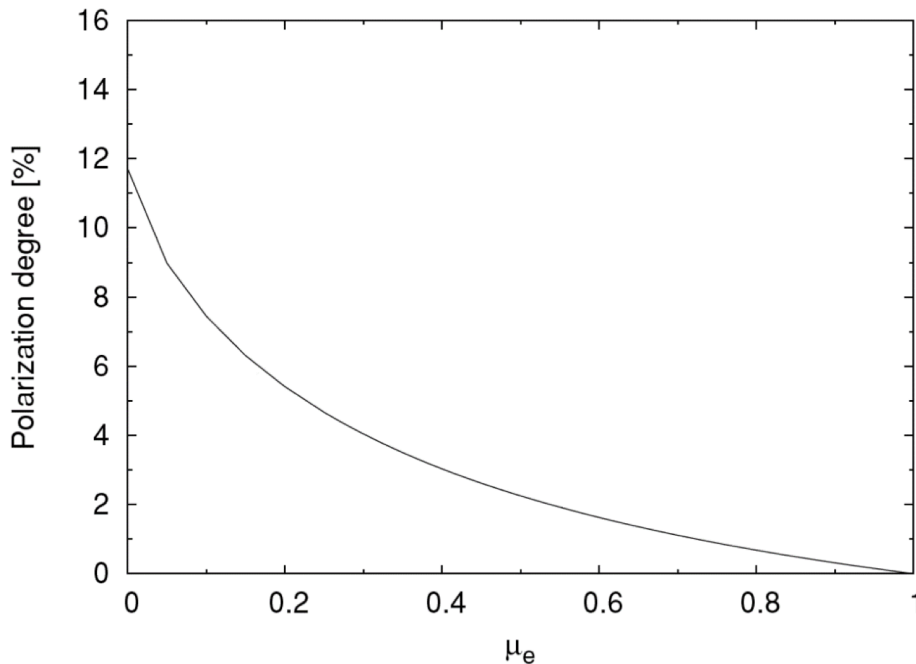


Figure 2.10: Polarization degree of the radiation emitted from a pure-scattering atmosphere as a function of the cosine of the emission angle $\mu_e = \cos\theta$ with respect to the normal to the atmosphere surface [data from Table XXIV in Chandrasekhar, 1960].

normal (i.e. between the observer line of sight and the disk symmetry axis), usually referred to as the *inclination angle*. When the disk is observed *face-on* ($\theta = 0^\circ$) the expected polarization degree is $\Pi = 0$, since we observe a symmetric structure. As the inclination angle increases, so does the asymmetry of the disk projected on the observer's sky, thus leading to an increase of the observed Π . This reaches a maximum value of 11.6% for an *edge-on* disk ($\theta = 90^\circ$). Regarding the direction of the polarization vector, because of the system symmetry, it is expected to be either perpendicular or parallel to the disk symmetry axis. Notably, in the hypothesis of no absorption in the atmosphere, polarization is indeed perpendicular to the axis if the optical depth is large ($\tau_e > 1$), while it is parallel to the axis for smaller values of τ_e [see e.g. Dovčiak et al., 2008, and references therein].

Corona emission

As we discussed in section 1.4.1, inverse Compton scattering in a corona is considered the dominant process responsible for the high energy emission observed in galactic BHs. While some information on the temperature and optical depth of the corona may be constrained from the spectral analysis of the hard component of the spectra, this analysis alone does not allow a clear determination of the structure of this region; because of this, many doubts on the corona origin and properties remain [Done et al., 2007]. The geometry of this region, however, has always been largely anticipated to leave a distinct mark on the polarimetric properties of the corona emission [Poutanen and Svensson, 1996, Schnittman and Krolik, 2010, Tamborra et al., 2018, Zhang et al., 2022]. Many possible geometries have been analyzed by several authors, both analyti-

cally and through numerical simulations. These usually predict the polarization vector of the emitted radiation to be either perpendicular or parallel to the disk symmetry axis (similarly to the disk emission), depending on the corona geometry.

As a general rule, geometries extended along the disk plane tend to emit radiation with a polarization degree parallel to the disk axis. An example of this is the *sandwich corona* (see panel (b) of Figure 1.8), a model predicted by numerical accretion disk simulations [see e.g. Kinch et al., 2021]; the polarization degree of this emission is expected to depend on several parameters, such as the disk luminosity, the BH spin, and the disk inclination angle, but it is usually expected to be lower than 10% in the *IXPE* observational band [see e.g. Schnittman and Krolik, 2010]. Moreover, this model usually predicts a 90° polarization angle swing at the energy from which the corona emission starts dominating over the underlying disk emission, corresponding with a minimum of the polarization degree, due to the two components mixing. A similar situation, but without the polarization angle rotation, can be obtained with a *wedge corona* (panel (d) of Figure 1.8), which can be originated by a composite accretion flow with an inner geometrically thick, optically thin laterally extended region of hot plasma replacing the inner region of a geometrically thin, optically thick accretion disk, possibly owing to evaporation of the inner disk [Krawczynski et al., 2022]. On the other hand, geometries in which the corona is a narrow plasma column centered on the BH spin axis tend to predict a polarization direction perpendicular to the symmetry axis. This is the case for the *lamp-post* model (panel (a) of Figure 1.8); in this case the polarization degree of the emission depends not only on the inclination angle but also on the specific corona shape, its height above the disk and its outflowing velocity [see e.g. Zhang et al., 2022]. It is also worth mentioning that the recent polarimetric observation of Cyg X-1 in the hard state seems to disfavor the latter configurations [Krawczynski et al., 2022].

Reflection component

The reflection component observed in BHB spectra is regarded as the result of the interaction of the radiation emitted from the corona (or from the disk itself, see section 2.3.3) with the disk atmosphere. As such, the properties of this emission are expected to be heavily influenced by the scattering processes; from the polarimetric point of view, this emission is expected to achieve very large values of polarization, possibly exceeding 20% [see e.g. Schnittman and Krolik, 2010, Taverna et al., 2020]. Because of the symmetry of the system, the polarization vector of this emission is usually found to be parallel to the disk axis. This component, however, is also characterized by prominent line emission, such as the fluorescent Fe K α line. Because of the chaotic nature of the line emission process, these photons are not expected to be polarized coherently, thus their contribution is expected to provoke a depolarization of the emission at specific energies [see e.g. Taverna et al., 2021]. Other than on the disk surface, also reflection from wind can be an important source of polarization. In this case, however, the polarization vector of the reflected radiation is expected to be perpendicular to the disk axis. Such configuration has been observed in the *IXPE* observation of Cyg X-3 [Veledina et al., 2023b]; this source exhibited a reflection-dominated spectrum with a particularly large polarization degree (up to 20%), while the energy-dependent analysis

revealed a dip in polarization degree in correspondence to the large Fe $K\alpha$ line observed in the spectrum. These results have been interpreted as due to the reflection on an optically thick wind structure.

2.3.3 Relativistic effects

Photons emitted from the accretion disk around a stellar-mass BH are affected by relativistic effects in several ways. They change their energy due to the gravitational and Doppler shifts since photons are emitted by matter rotating in a strong gravitational regime. Gravitational lensing further modifies the cross-section of the light tube as the photons propagate in the curved space-time; this effect is particularly strong for observers with high inclinations, especially for photons originating from behind the BH. The bending of light also impacts the emission angles of photons observed at infinity. Aberration caused by the motion of the disk matter plays its role as well. All these effects, the g-factor, lensing, and emission angle, influence the intensity of light that the observer at infinity measures. Furthermore, the polarization of the emitted radiation is significantly modified as photons travel through curved space-time, with their polarization vectors parallelly transported along the geodesics, resulting in a net rotation of the polarization angle. Moreover, the trajectories of some photons, because of gravitational lensing, force them to return to the disk surface, where they interact with the disk atmosphere before eventually reaching the observer at infinity. Termed as *returning radiation*, this component distinctly influences the polarization properties of the observed radiation compared to the *direct radiation* that reaches the observer without further interacting with the disk. Numerous researchers have computed the radiation emitted by matter in motion around a BH, employing various approximations and exploring different parameter spaces [e.g. Connors and Stark, 1977, Stark and Connors, 1977, Connors et al., 1980, Matt et al., 1993, Martocchia et al., 2000, Dovciak, 2004, Dovčiak et al., 2008, Schnittman and Krolik, 2009, 2010, Taverna et al., 2020]. This section aims to briefly outline the principal equations describing these effects, focusing specifically on their impact on the polarization properties of the emitted radiation.

Direct radiation

Assuming $GM_{BH} = c = 1$, the four-momentum $p_\mu = \frac{dx_\mu}{d\lambda'}$ of photons emitted from the disk traveling in Kerr space-time can be expressed, in the Boyer-Lindquist coordinates, as [see e.g. Misner et al., 1973]:

$$p^t = \frac{dt}{d\lambda'} = [a_s(l_s - a_s) + (r^2 + a_s^2)(r^2 + a_s^2 - a_s l_s)/\Delta]/r^2 \quad (2.65)$$

$$p^r = \frac{dr}{d\lambda'} = R_{sgn} \{(r^2 + a_s^2 - a_s l_s)^2 - \Delta[(l_s^2 - a_s^2) + q^2]\}^{1/2}/r^2 \quad (2.66)$$

$$p^\theta = -\frac{q}{r^2} \quad (2.67)$$

$$p^\varphi = \frac{d\varphi}{d\lambda'} = [l_s - a_s + a_s(r^2 + a_s^2 - a_s l_s)/\Delta]/r^2, \quad (2.68)$$

where $\Delta = r^2 - 2Mr + a^2$ and $\rho = r^2 + a^2 \cos^2 \theta$ are as defined in section 1.2.2. Here $l_s = \alpha(1 - \mu_0^2)^{1/2} = \alpha \sin \theta_0$ and $q^2 = \beta^2 + \mu_0^2(\alpha^2 - a_s^2)$ are Carter's constants of motion, with α and β being impact parameters measured perpendicular and parallel, respectively, to the spin axis of the black hole projected onto the observer's sky. The parameter α is defined to be positive when a photon travels in the direction of the four-vector $\frac{\partial}{\partial \varphi}$ at infinity, while β is positive if it travels in the direction of $-\frac{\partial}{\partial \theta}$ at infinity. The parameter θ_0 (and $\mu_0 = \cos \theta_0$) is the observer's inclination. Furthermore, the sign of the radial and θ components of the momentum are denoted by R_{sgn} and Θ_{sgn} . The affine parameter λ is defined in such a way that the conserved energy along the light geodesics is normalized to $-p^t = 1$.

As the photon propagates along the null geodesics, several effects concur into modifying its four-momentum p^μ [a detailed map of these effects can be found in Appendix D of [Dovciak, 2004](#)]:

- The joint influence of gravitational and Doppler shifts modifies its observed frequency, commonly quantified through the *g-factor*. This factor is expressed as the ratio of the energy of a photon received by an observer at infinity to its local energy upon emission from the accretion disk:

$$g = \frac{\nu_o}{\nu_e} = -\frac{1}{p_{e\ \mu} U^\mu}. \quad (2.69)$$

Here ν_o and ν_e denote the frequency of the observed and emitted photons, respectively, and U^μ is the four-velocity of the matter in the disk. As this parameter describes both gravitational and Doppler shifts, its value drastically decreases to zero near the horizon due to the strong gravitational effects. Further away from the black hole the Doppler shift prevails, thus the g-factor value will depend on the side of the disk considered: emissions from the approaching side yield a g-factor larger than 1, and vice versa. At larger disk radii where disk matter rotates slowly, both effects diminish, causing the g-factor to converge toward 1.

- The local emission angle of radiation reaching an observer (looking at the disk with a certain inclination angle) depends on the location of the emission point, as it is affected by gravitational lensing and special-relativistic aberration. The cosine of the emission angle can be expressed as:

$$\mu_e = \cos \theta_e = \frac{p_{e\ \alpha} n^\alpha}{p_{e\ \mu} U^\mu} \quad (2.70)$$

where n^α are the components of the disk normal. Close to the horizon, gravitational lensing governs photon trajectories, permitting only those emitted nearly parallel to the disk plane to reach the observer directly, while others are compelled to return to the disk surface. With increasing distance from the black hole, relativistic aberration predominantly shapes the emission angle, causing photons emitted from the approaching side of the disk to exhibit smaller emission angles than the disk inclination. As the distance from the black hole increases, the emission angle gradually converges toward the observer's inclination.

- Gravitational lensing can significantly amplify the emission from some parts of the disk, notably those located behind the black hole from the observer's perspective. This amplification, particularly pronounced for observers with significant inclination angles, can be quantified through the lensing factor, defined as the ratio of the cross-section dS_f of the light tube at infinity to the cross-section dS_\perp of the same light tube at the disk:

$$l = \frac{dS_f}{dS_\perp} \quad (2.71)$$

To estimate the total effect that gravitation has on the intensity of light coming from different parts of the disk, one has to take into account all three effects. These are usually combined into a single transfer function defined as [Dovčiak et al., 2008]:

$$G = g^2 \mu_e l \quad (2.72)$$

Furthermore, general relativity effects can combine to give a non-trivial net rotation to the integrated polarization vector [Stark and Connors, 1977, Connors and Stark, 1977, Connors et al., 1980]. Those effects can be described by defining the polarization vector f^μ as a normalized space-like 4-vector, perpendicular to the photon propagation direction (i.e. $k^\mu f_\mu = 0$ and $f^\mu f_\mu = 1$). This vector is parallelly transported along the photon null geodesic, i.e. $\nabla_k f^\mu = 0$, where ∇_k is the covariant derivative along the null geodesics. Since the polarization vector is, by definition, perpendicular to the radiation propagation direction, we can define the change of the polarization angle Ψ as the angle by which a vector parallelly transported along the light geodesic rotates with respect to the local frame at the disk and at infinity. At the disk we consider the local frame co-moving with it, with the x -axis in the direction $-\partial/\partial\theta$, in the plane defined by the normal of the disk n^μ and the momentum p_e^μ of the emitted photon, and is perpendicular to p_e^μ . The y -axis lies in the plane of the disk, perpendicular to the momentum p_e^μ and with direction $-\partial/\partial\varphi$. At infinity, we consider a static frame attached to the observer's sky with x -axis identified with the impact parameter β and y -axis identified with the impact parameter $-\alpha$. The change in the polarization angle Ψ is [see Dovčiak et al., 2008, and reference therein]:

$$\tan \Psi = \frac{Y}{X}, \quad (2.73)$$

where:

$$X = -(\alpha - a \sin \theta_0)k_1 - \beta k_2 \quad (2.74)$$

$$Y = (\alpha - a \sin \theta_0)k_2 - \beta k_1. \quad (2.75)$$

with the dimensionless BH spin a positive when the black hole rotates counter-clockwise, i.e. in the direction $-\partial/\partial\varphi$. The angle θ_0 is the observer's inclination, k_1 and k_2 are components of the complex Penrose-Walker constant of parallel transport along null geodesic $k_{pw} = k_2 - ik_1$ [Walker and Penrose, 1970]:

$$k_1 = arp_e^\theta f^t - r[ap_e^t - (r^2 + a^2)p_e^\varphi]f^\theta - r(r^2 + a^2)p_e^\theta f^\varphi \quad (2.76)$$

$$k_2 = -rp_e^r f^t + r[p_e^t - ap_e^\varphi]f^r + arp_e^r f^\varphi, \quad (2.77)$$

where r is the Boyer-Lindquist radial coordinate of the Kerr metric (see section 1.2.2) and the polarization vector is chosen to be in the direction of the x -axis in the above defined local frame on the disk.

The direct radiation properties are determined by studying the radiative transport of photons emitted from the disk and propagating in the curved space-time toward the observer at infinity. One possible way to do this, which is the one in use in the KYN code we implemented for the analysis described in chapter 3, is to integrate the local photon number f_{loc} over the disk surface. The observed photon flux per unit solid angle in the energy bin $\langle E, E + \Delta E \rangle$, $\Delta f_{obs} = dN/dt d\Omega_{obs}$, is [Dovčiak et al., 2008]:

$$\Delta f_{obs} = \int_{r_{in}}^{r_{out}} dr r \int_{\varphi}^{\varphi' + \Delta\varphi'} d\varphi \int_{(E)/g}^{(E+\Delta E)/g} G f_{loc} dE_{loc}. \quad (2.78)$$

Here r_{in} (r_{out}) is the inner (outer) radius of the disk, φ' and $\Delta\varphi'$ are the boundaries of the azimuthal integration domain (for integration over the entire disk surface $\varphi' = 0$ and $\Delta\varphi' = 2\pi$), and:

$$f_{loc} = \frac{dN_{loc}}{d\tau dS_{loc} d\Omega_{loc} dE_{loc}} \quad (2.79)$$

is the local photon flux emitted from the surface of the disk. From this, the observed radiation energy-dependent Stokes parameters can be found as:

$$i_{obs} = \int dS i_{loc}^{dir}(\theta, \phi) G \quad (2.80)$$

$$q_{obs} = \int dS [q_{loc}^{dir}(\theta, \phi) \cos 2\Psi - u_{loc}^{dir}(\theta, \phi) \sin 2\Psi] G \quad (2.81)$$

$$u_{obs} = \int dS [q_{loc}^{dir}(\theta, \phi) \sin 2\Psi + u_{loc}^{dir}(\theta, \phi) \cos 2\Psi] G \quad (2.82)$$

where i_{loc}^{dir} , q_{loc}^{dir} and u_{loc}^{dir} are the local, energy-dependent Stokes parameters of the direct radiation, θ and ϕ are the polar and azimuthal angle the photon emission direction makes with the disk normal and $dS = r dr d\varphi$ represents the surface integration element.

Returning radiation

The computation of the transfer function along the geodesics connecting the observer and emitter excludes the incorporation of the *returning radiation* component, i.e. photons emitted from one part of the disk and bent by gravitational lensing so that they are absorbed or reflected by another part of the disk, before eventually reaching the observer at infinity. To account for this aspect, a detailed tracing of the photon path, considering the transfer function along disk-to-disk geodesics, is essential [see e.g. Schnittman and Krolik, 2009]. Upon returning to the disk, incident photons interact with the disk atmosphere. While previous studies have explored the contribution of returning radiation, these investigations typically assume a pure scattering medium [Schnittman and Krolik, 2009, Taverna et al., 2020]. On the other hand, recent works tried to implement a more consistent treatment of this interaction [see e.g. Dauser et al., 2022], since the returning radiation component is regarded as a possible candidate for explaining the reflection features observed in some BHBs in soft state [Connors

et al., 2020, 2021]. However, these studies have not delved into the polarization aspects of this radiation component. To this day, a self-consistent treatment of the returning radiation spectral and polarization properties, including all the possible effects that reprocess the radiation in its interaction with the disk medium, is still lacking. The main theoretical work presented in this thesis aims to be a first step in this direction and will be described in chapter 3.

In the pure scattering case, the interaction between the returning photons and the disk atmosphere can be described using Chandrasekhar [1960] diffuse reflection formulae [see e.g. appendix A of Taverna et al., 2020]. This approach allows for the determination of the Stokes parameters of the reflected radiation. Subsequently, these parameters are propagated toward the observer at infinity using the same transfer functions described in Equations (2.80)-(2.82).

The disk polarization map, shown in Figure 2.11, provides a more detailed perspective on how relativistic effects shape the integrated polarization. At an observer inclination of $i = 75^\circ$, significant relativistic effects become evident. The intensified brightness on the left side of the disk results from special relativistic beaming of gas moving toward the observer. Meanwhile, general relativistic light bending produces a warped appearance on the far side of the disk, bending it upwards from the observer's viewpoint.

The polarization signature is superimposed on top of the intensity map; far from the BH, it aligns with classical outcomes described by Chandrasekhar [1960], indicating horizontal (or vertical) polarization of around $\Pi_L \approx 4\%$ for $i = 75^\circ$. Closer to the BH, relativistic beaming and gravitational lensing alter polarization behavior. Beaming causes photons emitted perpendicularly to the disk plane in the fluid frame to travel forward in the direction of the local orbital motion when seen by a distant observer. Consequently, this region exhibits a reduced effective emission angle, hence a lower degree of polarization (in the yellow high-intensity region on the left side of the BH). Simultaneously, gas moving away from the observer on the right side of the BH has an enhanced level of polarization because the observer sees photons emitted at a larger inclination in the fluid frame. Gravitational lensing causes the far side of the disk to appear warped up towards the observer, and thus have a smaller effective inclination and a smaller polarization degree. Moreover, gravitational lensing rotates the individual polarization vectors of the emission coming from the inner disk, causing a net depolarization where the light-bending effects are more relevant.

When the returning radiation is factored in, although there might be minimal changes in the overall observed spectrum, there is a significant shift in the polarization map, especially noticeable for observers at high inclination angles (see the right panel of Figure 2.11). Returning radiation photons initially emitted from the far side of the disk (top of the image) are reflected off the near (bottom) side with a relatively small scattering angle, maintaining a moderate horizontal polarization. On the other hand, photons emitted from the left side of the disk can be bent back to the right side (or vice versa), and then scatter at roughly 90° to reach the observer, thereby acquiring a large vertical polarization component. Although relatively small in total flux, this latter contribution can have a dominant influence on the total polarization due to its markedly large polarization degree.

The energy dependence of intensity, polarization degree, and angle, computed by

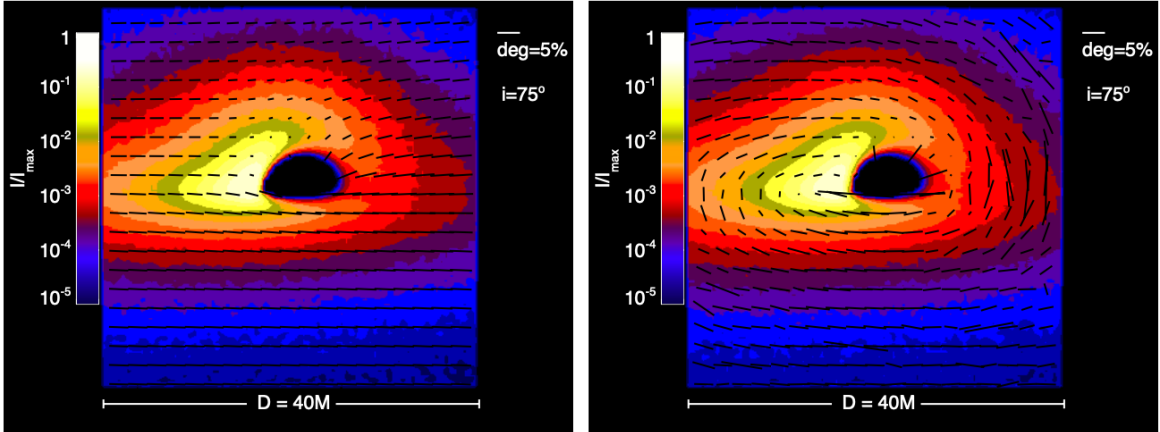


Figure 2.11: Two-dimensional maps of the normalized flux emitted by a thermal accretion disk. The observer is located at an inclination of 75° relative to the disk rotation axis, with the gas on the left side of the disk moving towards the observer. The black hole has spin $a/M = 0.9$, mass $M = 10M_\odot$, and is accreting at 10% of the Eddington limit with a Novikov-Thorne zero-stress emissivity profile, giving peak temperatures around 1 keV. The observed intensity is color-coded on a logarithmic scale and the energy-integrated polarization vectors are projected onto the image plane with lengths proportional to the degree of polarization. In the left panel is shown the contribution of direct radiation only, while in the right panel returning radiation is also included [Schnittman and Krolik, 2009].

Taverna et al. [2020] using the KYNBRR model (see chapter 3), is shown in *Figure 2.12*. As expected for large optical depths [see Dovčiak et al., 2008], direct radiation turns out to be polarized perpendicularly to the disk symmetry axis at lower energies, while the polarization angle associated with the direct radiation component χ_{obs}^{dir} slowly decreases at higher energies ($\gtrsim 2$ keV) under the effect of the polarization plane rotation. Similarly, on the low energy end the polarization degree is in agreement with the result predicted by Chandrasekhar [1960], $\Pi_{obs}^{dir} \approx 4\%$, and it tends to be independent of the radiation energy. For higher energies, the polarization degree experiences a decrease, due to the rotation of the polarization vector of the radiation emitted from the inner, hotter regions of the disk.

On the other hand, returning photons appear to be mostly polarized parallel to the disk axis ($\chi_{obs}^{ret} = 0^\circ$), although also in this case the polarization angle slightly declines above 10 keV due to general relativistic effects (even if by a smaller amount than in the direct radiation case). Moreover returning radiation has a much larger polarization degree than the direct component, with in general $8\% \leq \Pi_{obs}^{ret} \leq 20\%$. Looking at the total contribution (direct and returning radiation) we can observe a transition between the two regimes. In particular, the total polarization angle χ_{obs}^{tot} follows the curve of direct radiation alone as long as the fraction of returning photons becomes comparable to that of direct ones (see the spectra in the top rows), while it swings by 90° at higher frequencies. Likewise Π_{obs}^{tot} follows the behavior of direct radiation for lower energies, and it attains a minimum in correspondence with the polarization angle swing just described. The energy at which this transition occurs turns out to be smaller the larger the BH spin, since for rotating BH the ISCO lies nearer to the BH,

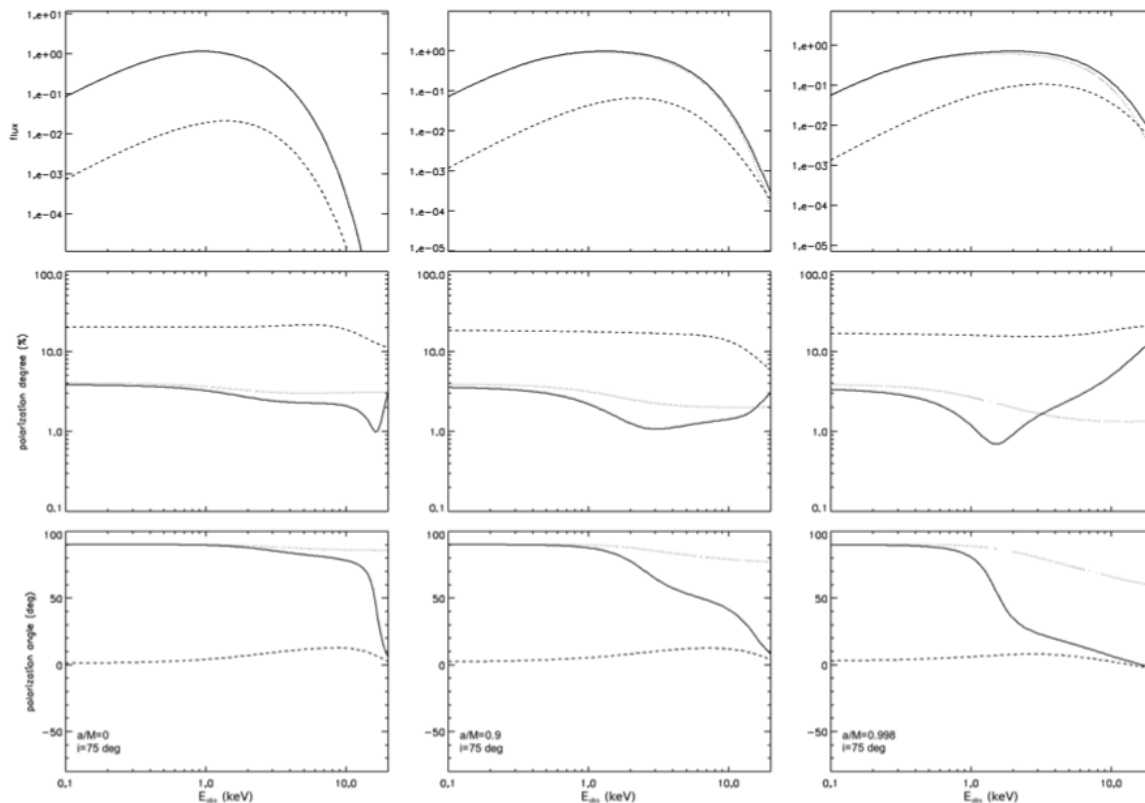


Figure 2.12: Spectrum (top row), polarization degree (middle row), and polarization angle (bottom row) plotted as functions of the photon energy at the observer for a BH of mass $M = 10 M_{\odot}$ and spin $a/M = 0$ (left-hand column), 0.9 (middle column), and 0.998 (right-hand column). The inclination angle between the observer’s line of sight and the disk symmetry axis is taken as 75° . In each plot, the contributions of direct and returning photons alone are marked by dotted and dashed lines, respectively, while the joint contribution (direct + returning radiation) is marked by solid lines [Taverna et al., 2020].

so general relativistic effects are more relevant (see section 1.2.2). As a consequence, for $a = 0$ returning photons start to dominate only at very high energies ($\gtrsim 10$ keV), once the spectrum of direct photons has sufficiently declined, while for $a = 0.9 M$ and $0.998 M$ the transition occurs already around $1 - 2$ keV, since more high-energy returning photons populate the spectral tail at those energies.

Chapter 3

Accretion disk emission polarization properties

The main goal of the theoretical part of this work is the exploration of the polarization properties of the radiation emitted from accretion disks. In the literature, the most widely adopted model for describing the polarization characteristics of this emission is based on the Chandrasekhar [1960] and Sobolev [1963] approximations, as introduced in section 2.3.2. This model inherently assumes complete ionization of the accretion disk medium, relying solely on Thomson scattering as the interaction between the matter and radiation in the disk atmosphere. This approximation offers a convenient simplification, facilitating a direct fitting of polarimetric data observed by *IXPE* (as detailed in the analyses presented in Part II of this thesis). Nevertheless, to achieve a full understanding of the accretion disk emission properties, it is necessary to consider all potential interactions between photons and the disk medium. This necessitates to incorporate additional processes such as Compton scattering and photoelectric absorption. This current work represents a dedicated effort towards a more comprehensive study of these interactions, aiming to provide a more detailed description of the various mechanisms affecting the polarization properties of accretion disk emission.

In our analysis, we studied the transmission of the accretion disk emission through an optically thick, partially ionized atmosphere located on top of the disk surface. The essentials of the method we employed have been outlined by Taverna et al. [2021]; in our work we built upon that model, both exploring a larger region of the parameter space and taking into account the effect of GR, introduced in section 2.3.3. First, we used a photoionization code to model the ionization profile of this layer; subsequently, we employed a Monte-Carlo code to study the polarized radiative transfer for photons emitted in the inner layer of the disk and propagating within this surface layer. This allows us to find the local spectral and polarization properties of this emission, as they would appear to an observer located on the disk surface. The final step of our computation is then the introduction of the relativistic effects in order to obtain the radiation properties as detected by an observer at infinity.

This final step requires particularly long computational time; this is true, in particular, for the returning radiation component, which is reflected by the disk surface before reaching the observer at infinity. A detailed study of this reflection process requires the use of our Monte-Carlo code in a different way: the surface layer is not illuminated by

radiation originating from the inner layers of the disk but instead by radiation arriving from above the disk itself. The incident radiation, however, possesses properties, both spectral and polarimetric, contingent upon its point of origin on the disk and the relativistic effects influencing its trajectory in the disk-to-disk path. The complexity introduced by these effects prevents the use of a simple black body shape as the seed emission for the Monte-Carlo code. To overcome this difficulty, we opted to employ the Monte-Carlo code as a sort of "Green's function", which allows us to derive the reflected radiation Stokes parameters based on the characteristics of the incident radiation. To achieve this, our simulations involved illuminating the surface layer using a monochromatic emission as the seed radiation. Executing these simulations across various incident energies enabled us to construct reflection tables that effectively describe the medium response to arbitrary incident radiations. The extensive computational time required for this task was a consequence of the large parameter space that needed exploration. For each radial bin of the disk, we conducted simulations involving multiple input energies and incident angles, where the latter represents the angle between the propagation direction of incident photons and the normal to the surface. Even in a conservative configuration with 10 incident angles, 10 seed monochromatic radiation energies, and 30 radial bins, the computational time could reach up to a few months. Given the considerable computational demands involved in building these reflection tables (currently in progress), a comprehensive description of the returning radiation component is deferred to a forthcoming publication [Marra et al., in prep]. In the present thesis, our focus remains on a detailed discussion of our modelization of the direct radiation component.

The codes employed in each step of our study are introduced in section 3.1. In section 3.2 a detailed study of the transmission of the disk emission through a partially ionized slab will be presented. Finally, in section 3.3 we will describe the expected spectral and polarization properties of the direct radiation component, also including GR effects.

3.1 Numerical implementation

3.1.1 CLOUDY and TITAN

In the initial phase of our analysis, we computed the ionization structure of the optically thick surface layer situated above the disk. To accomplish this task, we explored the capabilities of two distinct codes: CLOUDY [Ferland et al., 2017] and TITAN [Róžańska et al., 2002]. Both photoionization codes are designed to simulate relevant processes that occur in astrophysical clouds under several possible configurations. Besides the unique architecture and atomic database of each code, the primary distinction between the two lies in the treatment of collisional ionization processes, which CLOUDY incorporates while TITAN omits. CLOUDY, with its toggle capability for collisions, facilitates the exploration of different ionization equilibrium regimes, including pure Collisional Ionization Equilibrium (CIE), pure Photo Ionization Equilibrium (PIE), or a combination of both. On the other hand, TITAN is constrained to the PIE case but introduces unique features not found in CLOUDY, such as the potential for double illumination of the slab (power-law reflection from above and black-body transmission from below). This as-

pect, although not utilized in our current study, presents a possibility for more refined investigations into the ionization profile of the disk atmosphere in future research.

Initial results, obtained by toggling collisions on and off in CLOUDY during our study of the slab in PIE, suggest that collisions may not be crucial in this particular scenario, thus allowing a direct comparison of the results obtained with the two codes. The study performed in this scenario showed similar results in similar conditions. Nevertheless, a thorough comparison between TITAN and CLOUDY of the temperature and ionization profiles and spectra, depending on the slab density, irradiation properties and boundary conditions, still needs to be done. For the purposes of this thesis, we concentrate on presenting the results obtained employing CLOUDY. The computations involving TITAN are not included in this presentation, as they were independently conducted and privately shared by Jakub Podgorny.

In the simulations conducted using CLOUDY (version 22.01), we adopted a model where the slab has a constant hydrogen density. The temperature of the slab was specified based on the ionization regime under consideration, distinguishing between Collisional Ionization Equilibrium (CIE) and Photo Ionization Equilibrium (PIE):

- **CIE:** In this scenario, the ionization state of the disk medium is solely influenced by the collisions occurring within the plasma. To implement this setup, the CLOUDY code incorporates the `coronal` command, requiring only the equilibrium temperature of the plasma as a parameter.
- **PIE:** Here, the black body emission originating from the inner layers of the disk is introduced to modify the ionization profile of the plasma. Our physical configuration is to have a colder photosphere directly on top of hotter dissipative disk layers. In CLOUDY, this arrangement resembling a black body emitting source at the bottom of the slab is obtained by equating the integrated mean intensity at the illuminated face of the slab to the Stephan-Boltzmann law, as illustrated in the following code snippet:

```
blackbody T
intensity linear  $\sigma_{SB} T^4$ 
```

As such, the ionization parameter of the medium can be defined as:

$$\xi_{BB} = \frac{4\pi\sigma_{SB}T^4}{n_H} \quad (3.1)$$

where $\sigma_{SB} = (2\pi^5k_B^4)/(15h^3c^2) = 5.67 \times 10^{-5} \text{ erg cm}^{-2} \text{ s}^{-1} \text{ K}^{-4}$ is the Stephan-Boltzmann constant.

In both CIE and PIE cases, the temperature defined for the slab is subsequently assumed to be the black body temperature of the seed radiation used in the Monte-Carlo code. Describing the matter within the layer, we adopted the typical solar abundance [Asplund et al., 2005], focusing in particular on the elements with $Z = 1$ (hydrogen), 2 (helium), 6 (carbon), 7 (nitrogen), 8 (oxygen), 10 (neon), 14 (silicon), 16 (sulfur) and 26 (iron), neglecting the presence of dust.

Establishing an xyz reference frame, with the z -axis perpendicular to the slab, the code solves the ionization structure within the layer by dividing it into multiple slices

characterized by their height (z) relative to the base of the surface layer. In PIE simulations, this base corresponds to the illuminated face. The boundary condition for the computations is set when a specified value of hydrogen column density is reached (N_H^{max}), utilizing the `stop column density` command. Given the assumed constant density profile, this translates into adopting a maximum height (z^{max}) for the slab. While N_H^{max} serves as a third free parameter in our computations, its allowable values are inherently constrained by our code setup. The subsequent use of the Monte-Carlo code, `STOKES`, imposes limitations. Specifically, `STOKES` does not incorporate internal sources of free-free radiation within the slab. Consequently, our surface layer functions as a "passive" medium where radiation emitted from the inner layers of the disk undergoes reprocessing (scattering, absorption, and eventual re-emission as line emission) without being re-emitted as a thermal continuum. This constraint inherently restricts the allowed values of the slab column density, and by extension, the optical depth ($\tau_T^{max} \approx N_H^{max} * \sigma_T$). If N_H^{max} is too large, we deviate from a physically realistic situation by neglecting internal sources of thermal radiation within the slab, while if it is too low, we risk underestimating absorption effects. Despite these limitations, we find this approximation suitable for our study as it allows us to investigate the transmission of radiation in a partially ionized atmosphere while maintaining flexibility in exploring a broad region of the temperature and density parameter space.

In each simulation run, we generate output files containing the density of all the most important elements in our plasma in various ionization states, presented as a function of distance from the illuminated face (in CIE computations, these values are inherently constant). An overview file, providing information on the slab density and the temperature profile (constant in CIE) is generated as well. Additionally, auxiliary files are produced, containing information on the incident and transmitted continuum (specifically for PIE computations), and the optical depth for scattering and photoelectric absorption processes. While not strictly essential for the Monte-Carlo code functionality, these files serve as necessary diagnostic tools for ensuring the consistency of our simulations. Moreover, they play a crucial role in the comparative analysis with `TITAN` computations. A snippet of the code output is illustrated below:

```
save species densities \ions_JzzFeion.dat\ \Fe+26\
#this line is repeated for each of the atoms
#and ions of our interest

save element oxygen \oxygen.dat\
save element neon \neon.dat\
save element iron \iron.dat\
#Used to check the ionization profiles
#of the most important elements

save overview \overview.dat\
#Contains the Temperature and density profiles

save continuum units keV \continuum.dat\
#Contains the incident and transmitted continuum
```

```
save optical depths units keV \"tau.dat\"
#Contains the scattering and absorption optical depth
```

To generate the input file for **STOKES**, we use a **Python** code to convert the elements densities into fractional abundances:

$$F_{X\alpha}^i = \frac{n_{X\alpha}^i}{n_X^{TOT}} \quad (3.2)$$

where $n_{X\alpha}^i$ is the number density of the ionic species $X^\alpha(i)$, with α being the ionic charge and i the excitation level of the outermost electron. Here n_X^{TOT} denotes the total number density of the element X . These fractional abundances are computed for each of the slices in which **CLOUDY** subdivided the slab. Finally, the density, temperature, and fractional abundance profiles are averaged into a maximum of 50 layers, which compose the **STOKES** input. After several tests comparing slabs with 50 layers to configurations where 1 average layer was used to describe the entire slab, we found that the differences between the two cases are negligible. Therefore, for the sake of simplicity, we adopted the single-layer approximation for computational efficiency in the Monte-Carlo simulation for all results presented below.

3.1.2 STOKES

The subsequent step in our study involves the use of the Monte-Carlo code **STOKES** [originally developed by [Goosmann and Gaskell, 2007](#), see also [Marin et al. 2012](#), [Marin 2018](#)] to investigate the polarized radiative transfer for photons propagating within the surface layer. The input file required by **STOKES** includes information on the scattering region derived from **CLOUDY**, allowing the definition of the emission region from which photons are injected into the layer. The properties of the emitting region are specified using the **Emireg** command in the **STOKES** input file, following the syntax below:

```
Emireg G G_x G_y G_z x y z S S_1 S_p W T v_r v_phi v_theta I Q U V
```

Here, the switch G determines the geometry of the emitting region (e.g., $G = 1$ for a cylindrical region, $G = 4$ for a unidirectional photon source) centered around the coordinates (x, y, z) with dimensions G_x , G_y , and G_z . The switch S defines the input radiation spectrum, with $S = 0$ for a power-law emission, $S = 1$ for black body emission, and $S = 2$ for a Gaussian line. The subsequent parameter defines the power-law photon index α if $S = 0$, the black-body temperature T if $S = 1$, and if $S = 2$, two parameters are required to define the line energy and its width. S_p describes the percentage of the total photons emitted by the defined model. The switch W is used to choose the photon sampling method: if $W = 0$, the number of photons sampled in each spectral bin is distributed according to the defined spectral intensity function (power-law, black body, emission line), and each photon carries the same weight (unity). If $W = 1$, the same number of photons is distributed into each spectral bin, but each photon package is assigned a weight factor determined by the prescribed spectral intensity function. Consequently, the Stokes vector of the photons is re-normalized by the weight before being counted in the output. The final parameters define the presence of intrinsic time-lags (T), the bulk velocity of the emitting region (v_r, v_ϕ, v_θ) , and the Stokes parameters of the seed radiation (I, Q, U, V) .

For our simulations, we assumed the emitting source to be a point-like source located at the bottom of the atmospheric layer ($z = 0$). We imposed that all seed photons are emitted according to an unpolarized black body at the temperature defined in `CLOUDY`. Furthermore, no bulk motion is considered for the emission region. The corresponding `Emireg` line reads as follows:

```
Emireg 0 0 0 0 0 0 0 1 T 100 1 0 0 0 0 1 0 0 0
```

Photons are emitted following an isotropic angular distribution, meaning that the propagation directions along which photons are launched are sampled by the polar angles:

$$\theta_s = \arccos \sqrt{r_1} \quad (3.3)$$

$$\phi_s = 2\pi r_2 \quad (3.4)$$

with respect to the z -axis and the xz plane, respectively. Here r_1 and r_2 are random numbers ranging between 0 and 1.

Photons are then tracked along their trajectory, accounting for all possible interactions (such as Thomson and Compton scattering, free-free or photoelectric absorption, and line emission) they can undergo in the layer. In version 2.33, employed in the simulations presented in this thesis, Compton down-scattering is included but not Compton up-scattering. Although the latest version of the code (v 2.34) incorporates Compton up-scattering, this version is still being tested. It is crucial to note that the relevance of Compton up-scattering in the *IXPE* band should become significant at higher slab temperatures than those considered and expected from the [Novikov and Thorne \[1973\]](#) temperature profile (see Equation 1.14 and Figure 1.5). A more detailed examination of this aspect will be conducted in future studies.

All photons that are not absorbed within the layer are ultimately collected in various virtual detectors, each identified by the inclination θ_e and azimuth ϕ_e characterizing the corresponding viewing direction in the xyz frame. The total number of virtual detectors is determined by specifying the numbers of points N_θ and N_ϕ of the (θ, ϕ) angular mesh in the input. For each detector, the Stokes parameters of the collected photons along the corresponding viewing direction are summed together after rotating the different Stokes parameter reference frames around the detector line-of-sight to align with the detector frame.

The final output of each run comprises the Stokes parameters I , Q , U , and V of the emerging radiation as functions of the photon energy E and of the two viewing angles θ_e and ϕ_e . Due to the axial symmetry of the accretion disk, we are integrating over ϕ_e , thus imposing $N_\phi = 1$. The resolution N_E and the boundaries E_{min} and E_{max} of the photon energy band, as well as the number N_{phot} of seed photons to be launched in every single run, can be defined at the beginning of the `STOKES` input file, as illustrated in the following code snippet:

```
OutputFile Name 1
PhotonNum N_phot

IntermediateSave N_save
#Intermediate save points

SpecMinLim E_min
```

SpecMaxLim E_{max}

SpecScale 3

#Specifies the photons energies sampling:

#0 – linear in wavelength,

#1 – logarithmic in wavelength,

#2 – linear in energy,

#3 – logarithmic in energy

ThetaViewAng N_θ

PhiViewAng N_ϕ

PlaneSym no

#Selects whether to sum the contribution of photons

#emerging from above and below the slab

HalfSpace yes

#Used to restrict the output angles to the

#half-space above the slab

SpectRes N_E

All the STOKES simulations presented in the following sections have been performed launching $N_{phot} = 10^{10}$ photons per run, and collecting them along $N_\theta = 20$ angular directions. The energy range considered in each presented simulation corresponds to the one displayed in the respective figure.

3.1.3 KYN

The results obtained with STOKES describe the Stokes parameters of the radiation as it emerges from the disk atmosphere. Although these results can be analyzed to investigate the effect of absorption on the observed radiation (see Section 3.2), at this stage, they cannot yet be used to predict the observed polarization properties of the accretion disk emission. As outlined in Section 2.3.3, relativistic effects are expected to modify the spectral and polarization properties of photons propagating in a strong gravity regime. To account for these effects, we employed the relativistic ray-tracing package KYN, originally developed by Dovciak [2004]. Several independent codes originated from this suite and have been used to predict the emission properties of AGN and stellar mass BHs in various spectral states. In our investigation, we focused on two versions of KYN that exclusively study the accretion disk emission, without considering the possible presence of a comptonizing corona: KYNBB [Dovčiak et al., 2008] and its extension including returning radiation, KYNBBRR [Taverna et al., 2020].

KYNBB operates on an observer-to-emitter approach. The disk surface is sampled by a (r, φ) grid with $N_r \times N_\varphi$ points, where r is the radial distance from the central BH and φ the azimuth with respect to a reference direction in the plane perpendicular to the disk axis. Once the observer inclination θ_{obs} with respect to the disk normal is determined, the code traces back all possible null geodesics connecting the observer

to different points on the disk. For each emission point on the disk surface grid, all main quantities concerning radiative transport are then provided in terms of photon number. The original version of KYNBB assumes the disk emission to follow a multi-color black body distribution, with the disk temperature defined by the [Novikov and Thorne \[1973\]](#) profile, and to be polarized according to the [Chandrasekhar \[1960\]](#) profile. Subsequently, the code integrates the local Stokes parameters over the disk surface, taking into account the relevant GR effects using the formulae reported in Equations (2.78)-(2.82).

KYNBBRR was developed based on the KYNBB framework. This version of the code utilizes tables produced by the C++ code SELFIRR [based on the ray-tracing SIM5 package, [Bursa, 2017](#)]. SELFIRR computes all possible null geodesics connecting two different points on the disk surface, along which the returning photons travel. This code subdivides the disk surface into N_r incidence patches, each characterized by the radial distance r_i of their centers from the BH. For each value r_i , the tables contain the values of the incidence angles (θ_i, φ_i) , the radial distance r_e of the starting point, the emission angles (θ_e, φ_e) , the energy shift \bar{g} , the solid angle $\Delta\bar{\Omega}_i$ of the incidence patch, and the change in polarization angle Ψ . The radial grids that sample the disk surface in the two codes KYN and SELFIRR are the same, so that the contributions of direct and returning radiation can be summed together at each point of this surface grid without any additional numerical manipulation.

As in the case of direct radiation, the polarization degree (Π_e) and angle (χ_e) of returning photons at their emission point are given following the [Chandrasekhar \[1960\]](#) prescription. Returning photons are then reflected at the disk surface using the [Chandrasekhar \[1960\]](#) reflection formulae for single scattering to obtain the Stokes parameters of the reflected radiation. In particular, this reflection process is first computed for three distinct states of polarization, corresponding to unpolarized light ($\Pi_{refl} = 0$) and fully polarized radiation ($\Pi_{refl} = 1$) with $\chi_{refl} = 0^\circ$ and $\chi_{refl} = 45^\circ$, respectively. Then the Stokes vector for a generic state of polarization is reconstructed through the decomposition:

$$\begin{aligned} \bar{s}_{refl}(\Pi_{refl}, \chi_{refl}) = & \bar{s}_{refl}(0, -) + \Pi_e \{ [\bar{s}_{refl}(1, 0) - \bar{s}_{refl}(0, -)] \cos(2(\chi_e + \Psi)) \\ & + [\bar{s}_{refl}(1, \pi/4) - \bar{s}_{refl}(0, -)] \sin(2(\chi_e + \Psi)) \} \end{aligned} \quad (3.5)$$

All contributions from the different incidence directions at each incidence point are finally summed together, obtaining the contribution to the local Stokes parameters for returning photons. These are then summed with the direct radiation local Stokes parameters and integrated at the observer, following the same procedure described in Section 2.3.3.

The output of a typical KYN run consists of a table containing the values of the integrated Stokes parameters $s_{obs} = (I_{obs}, Q_{obs}, U_{obs}, V_{obs})$ as functions of the photon energy. This output can be used as a modeling tool to predict the polarization properties of the accretion disk emission for different values of the BH spin and the disk inclination. Moreover, KYNBB and KYNBBRR offer built-in emission models for use with XSPEC, enabling a direct spectro-polarimetric fit of the *IXPE* observations. KYNBBRR, in particular, has been employed to model all the galactic BH sources observed by *IXPE* in the soft state, as detailed in Part II of this thesis. As discussed earlier, my work on KYN has focused on improving the description of the interaction between the disk

medium and the emitted radiation. For this purpose, I worked on both KYNBB and KYNBBRR codes to implement the results of our CLOUDY+STOKES simulations in place of Chandrasekhar [1960] computations to describe the emerging and reflected photons spectral and polarization properties.

3.2 Transmission through a partially ionized slab

With the numerical framework established for our study, we can now delve into the results obtained by examining radiation transmission through a partially ionized slab situated on top of a black body emitting source. As outlined in Section 1.3, accretion disks are expected to exhibit a temperature profile that decreases radially. The specific temperature values depend on the BH spin and the accretion rate. To ensure the broad applicability of our analysis, we explored a diverse array of temperatures, encompassing various radial locations within the disk. Similarly, we investigated a wide range of densities. This approach aligns with the expected behavior of a physical atmosphere, which typically features a density profile decreasing with vertical height [e.g., Gaussian profile; Taverna et al., 2020, 2021, or a more general one, as in Davis et al. 2006]. Consequently, our analyses covered a broad spectrum of atmosphere densities ($T_{BB} \sim 0.1 - 1.5$ keV, $n_H \sim 10^{12} - 10^{21}$ cm $^{-3}$, $N_H \sim 10^{24} - 10^{25}$ cm $^{-2}$). Two main results are found by exploring this large parameter space (T_{BB} , n_H , N_H):

- The emerging radiation PA remained constant with energy and perpendicular to the slab normal. This agrees with expectations for passive atmospheres involving scattering [Dovčiak et al., 2008] and absorption [Taverna et al., 2021].
- The PD of emitted radiation showed significant dependence on the ionization structure of the slab medium. This dependence persisted regardless of the assumed ionization regime.

In scenarios characterized by low ionization, absorption effects wield a substantial influence on the spectral and polarization properties of emerging radiation. This is illustrated in Figures 3.1 for a slab in PIE, where the illuminating black body temperature is fixed at 0.3 keV, and the slab column density is set to 10^{24} cm $^{-2}$ (corresponding to an optical depth of $\tau_T \sim N_H \times \sigma_T \sim 0.67$ for Thomson scattering). Results are presented for three hydrogen density values: $n_H = 10^{19}$, 10^{20} , and 10^{21} cm $^{-3}$. In the top panel, the mean fractional abundances of iron, neon, and oxygen ions obtained from CLOUDY are depicted. Notably, even in this configuration, lighter elements tend to be fully ionized, whereas iron exhibits a notable presence of lower ionization states, with higher abundances for increased slab density. The first row of the bottom panel illustrates the optical depth for scattering and absorption processes derived by CLOUDY. In the considered energy range (0.1 to 50 keV), the scattering optical depth remains relatively constant and is equivalent to τ_T . Meanwhile, the photoelectric absorption optical depth, displaying a general decline with energy proportional to $\sim E^{-3}$, reveals distinct absorption edges, particularly within the *IXPE* observational band highlighted in yellow. As the slab density increases, the relevance of the absorption process intensifies. This trend is preserved in the emerging spectra, deviating from the input black body shape and exhibiting prominent absorption features.

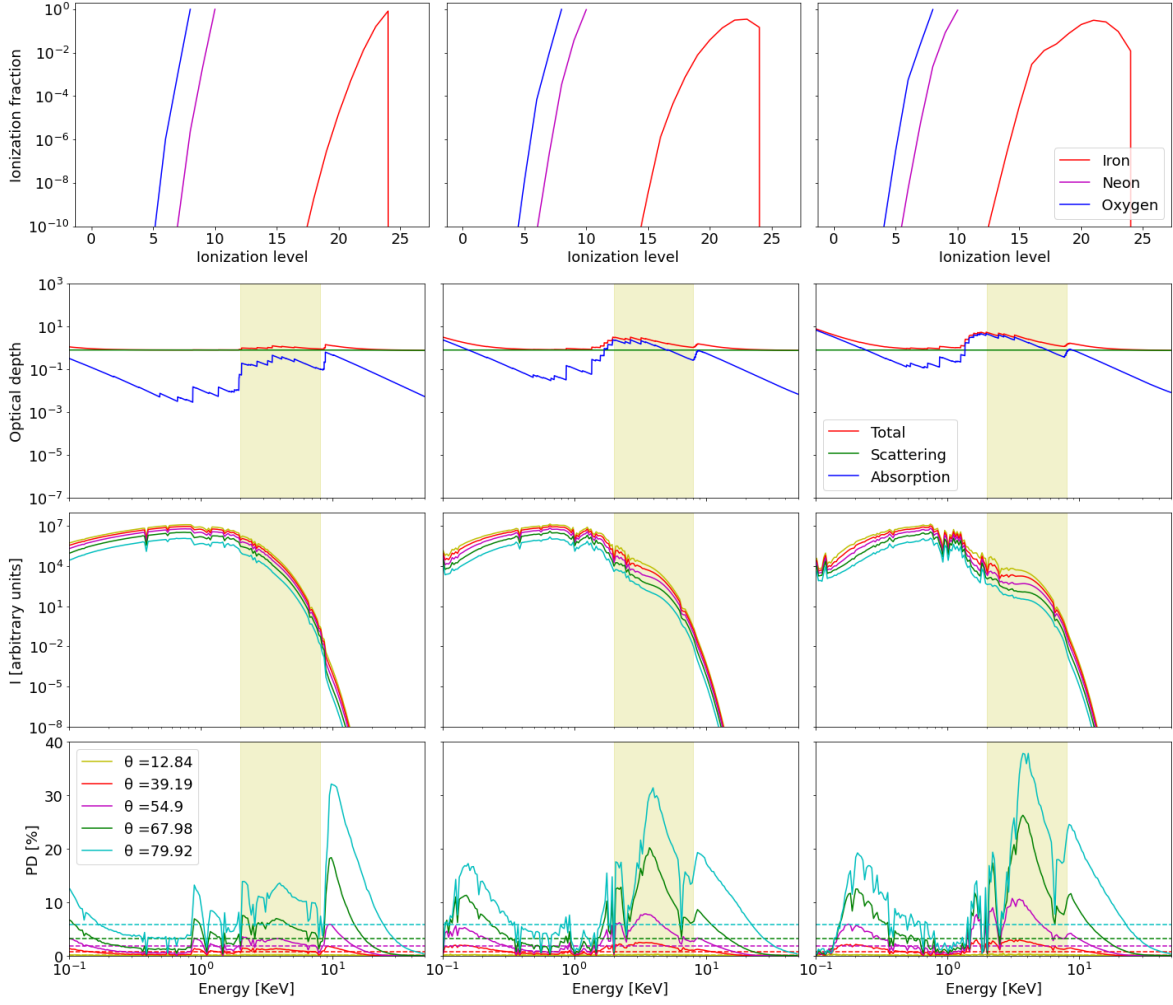


Figure 3.1: Comparison of three cases illustrating the transmission of single-temperature unpolarized black body radiation with $k_B T_{BB} = 0.3$ keV through a constant density slab ($N_H = 10^{24}$ cm $^{-2}$) using simulations conducted with the CLOUDY and STOKES codes in the PIE framework. Moving from left to right, the slab densities increases ($n_H = 10^{19}$, 10^{20} , and 10^{21} cm $^{-3}$), resulting in increased ionization for a consistent external illumination, as characterized by the ionization parameter $\xi \sim 4, 3, 2$, respectively, derived from Equation 3.1. *Top Panel:* Displays the fractional abundance of oxygen ions (blue), OI–OIX, neon ions (magenta), NeI–NeXI, and iron ions (red), FeI–FeXXVII within the slab. *Bottom Panel:* The top row presents the optical depth for scattering (green) and absorption (blue) processes, along with the total optical depth (red). The middle and bottom rows showcase the emerging spectra and PD for varying observer inclinations θ . Dashed horizontal lines in the bottom row represent PD values predicted using Chandrasekhar [1960] computations. The yellow shaded area emphasizes the IXPE observational band.

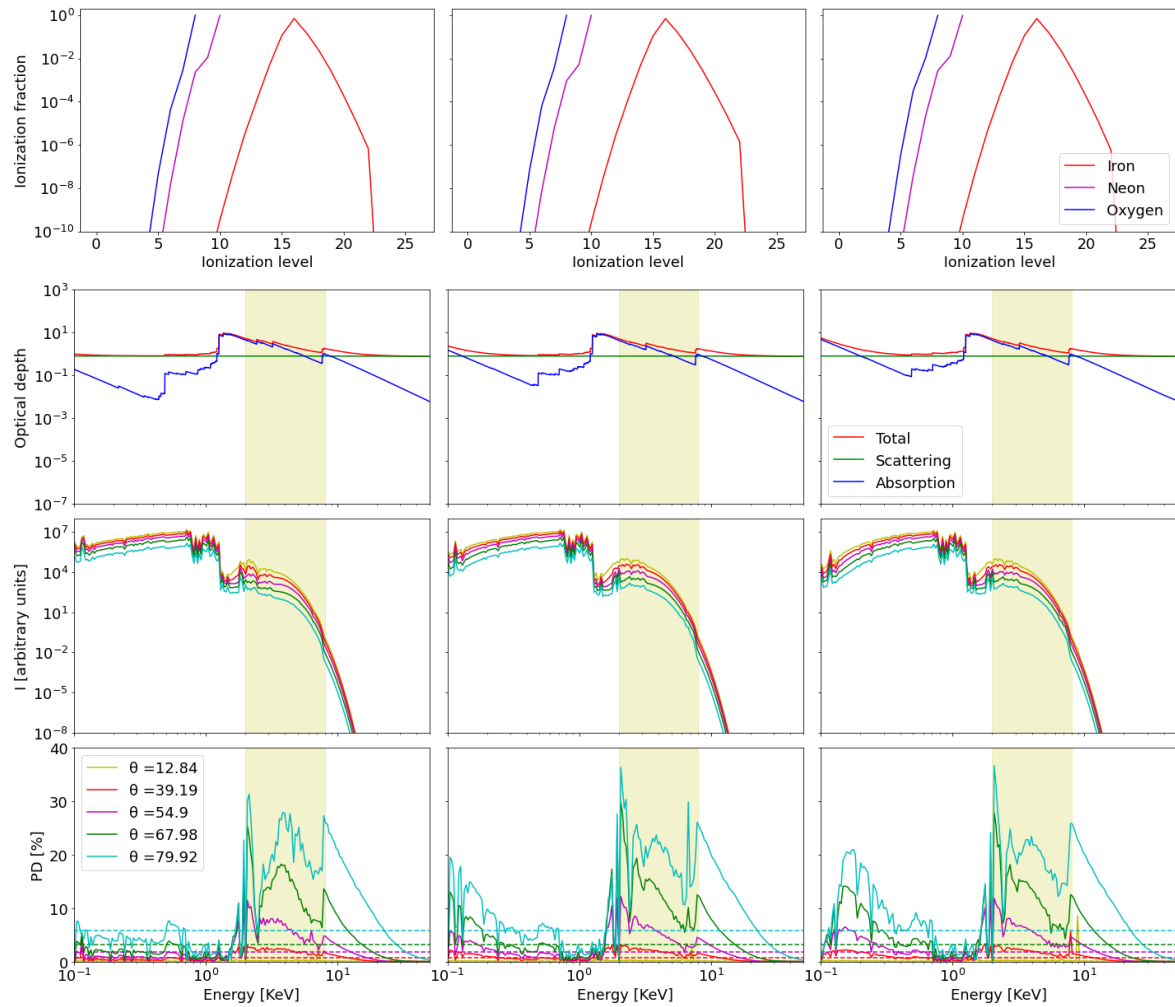


Figure 3.2: Same as Figure 3.1, but assuming the slab medium to be in CIE.

The resulting polarization degree of the emerging radiation consistently exhibits values significantly higher than those predicted by the approximations of Chandrasekhar [1960] and Sobolev [1963]. It is important to note that the Chandrasekhar [1960] predictions are based on the assumption of an infinite optical depth for the slab. Consequently, direct comparisons with our results, where a much lower optical depth ($\tau_T \sim 0.67$) was considered, must be approached with caution. Nevertheless, these predictions serve as a valuable starting point for understanding the processes amplifying the emerging radiation PD. As already described by Taverna et al. [2021], if the photoelectric opacity is higher at a particular energy band, it induces polarization through absorption. This effect can be explained by the fact that absorption predominantly impacts photons emitted from the bottom of the slab with large inclination angles. These photons must traverse a greater distance to exit the slab region. Consequently, at energy bands where absorption processes are most significant, the dominant contribution to the emerging radiation comes from photons injected into the slab with small inclination angles. These photons are more likely to undergo only one scattering event, leading to coherent polarization perpendicular to the slab normal. If the density is large enough, this effect becomes dominant between 2 and 5 keV, provoking a sharp PD increase in the middle of the *IXPE* energy band. However a drastic decrease is expected between 6 and 7 keV, due to the presence of strong emission lines in that range [in particular Fe XXV and Fe XXVI lines at 6.7 and 7 keV, see Figure 4 of Taverna et al., 2021]. Finally, the presence of the Fe absorption edge at 9.1 keV provokes a sharp increase in the PD profile at high energies, which is particularly evident as the layer density decreases.

Figure 3.2 shows the same results but assuming the slab medium in CIE. In this scenario, most of the iron in the slab medium is found at low ionization levels, and the ionization structure of the layer shows negligible variations when increasing the slab density. Consequently, the optical depth presents a similar energy dependence in the three density configurations presented, with the absorption processes being particularly relevant between ~ 1 and ~ 8 keV (as observed in the largest density case in PIE). The main variation due to the increasing density is observed at the low energy end of our simulations, with an increasing strength of the absorption contribution around 0.1 keV. The emerging radiation spectra show important absorption features, particularly at ~ 1 –2 keV, that correspond to a strong peak in the PD profile. The PD energy profile recalls the one observed in the largest density case in PIE (see right column of Figure 3.1), apart from the position of this peak that seems to shift from the middle of the *IXPE* band down to ~ 2 keV, due to the stronger contribution of photoelectric absorption at this energy.

The scenario is significantly altered when considering black body input radiation with a temperature of $T_{BB} = 1$ keV, as depicted in Figures 3.3 and 3.4. The CIE case (Figure 3.3), shows an increase of the iron ionization level for all the considered densities, reducing the impact of photoelectric absorption at all energies. The spectra still present some important absorption lines, but the overall black body shape is maintained. Because of this, the polarization degree of the emerging radiation is generally lower at all energies; the PD profile still presents peaks at ~ 2 keV and ~ 9 keV, in correspondence to the most relevant absorption edges, and shows a decreasing behavior in the *IXPE* energy band due to the Fe XXV and Fe XXVI lines depolarizing the spectra

at ~ 7 keV.

On the other hand, in the PIE case the slab medium is almost completely ionized, rendering the impact of photoelectric absorption negligible, except for very low energies in the case with the highest density. The PD profile exhibits a consistent behavior at low energies, aligning with the anticipated outcome for a pure Thomson scattering regime. At higher energies, however, the PD behavior has a clear bump. This is likely induced by Compton down-scattering at the exponential cut-off of the seed black body radiation. This mechanism effectively removes photons from the high-energy end of the spectra, akin to the absorption processes described previously. This interpretation gains further support from the observed dependence of the PD peak on the seed black body temperature, as illustrated in Figure 3.5. In this figure, four simulations were conducted by varying both temperature and density to maintain a fixed ionization parameter at $\log \xi \sim 5$. As the black body seed temperature transitions from 1.2 keV to 0.6 keV, the PD bump shifts towards lower energies, introducing an increasing trend in the PD profile within the *IXPE* energy band. It is crucial to note that our computations do not incorporate Compton up-scattering, which is likely to mitigate (though not eliminate) this effect [see e.g. Poutanen and Vilhu, 1993]. Since we assume the slab to be at the same temperature as the black body seed emission, we anticipate this effect to remain relevant even with Compton up-scattering. Nevertheless, a more detailed analysis of this effect will be conducted in the near future.

The increase in PD due to absorption and Compton scattering effects is observed to raise both with the inclination angle of the observer relative to the slab normal and the slab optical depth. While the dependence on the inclination angle is expected based on the Chandrasekhar [1960] and Sobolev [1963] approximations, the reliance on the slab optical depth, as depicted in Figure 3.6 for the high ionization regime, can be elucidated by considering that for larger optical depths, both absorption and Compton scattering effects become more significant. This phenomenon further diminishes the contribution of photons traveling diagonally inside the slab. As the optical depth increases, the Chandrasekhar [1960] profile is recovered in the region where Thomson scattering dominates, such as at the low-energy end in the highly ionized case illustrated in Figure 3.6. This result agrees with the analysis by Taverna et al. [2021], showing that in the pure scattering regime in the CLOUDY and STOKES setup, Chandrasekhar's limit is reached for $\tau \geq 3$.

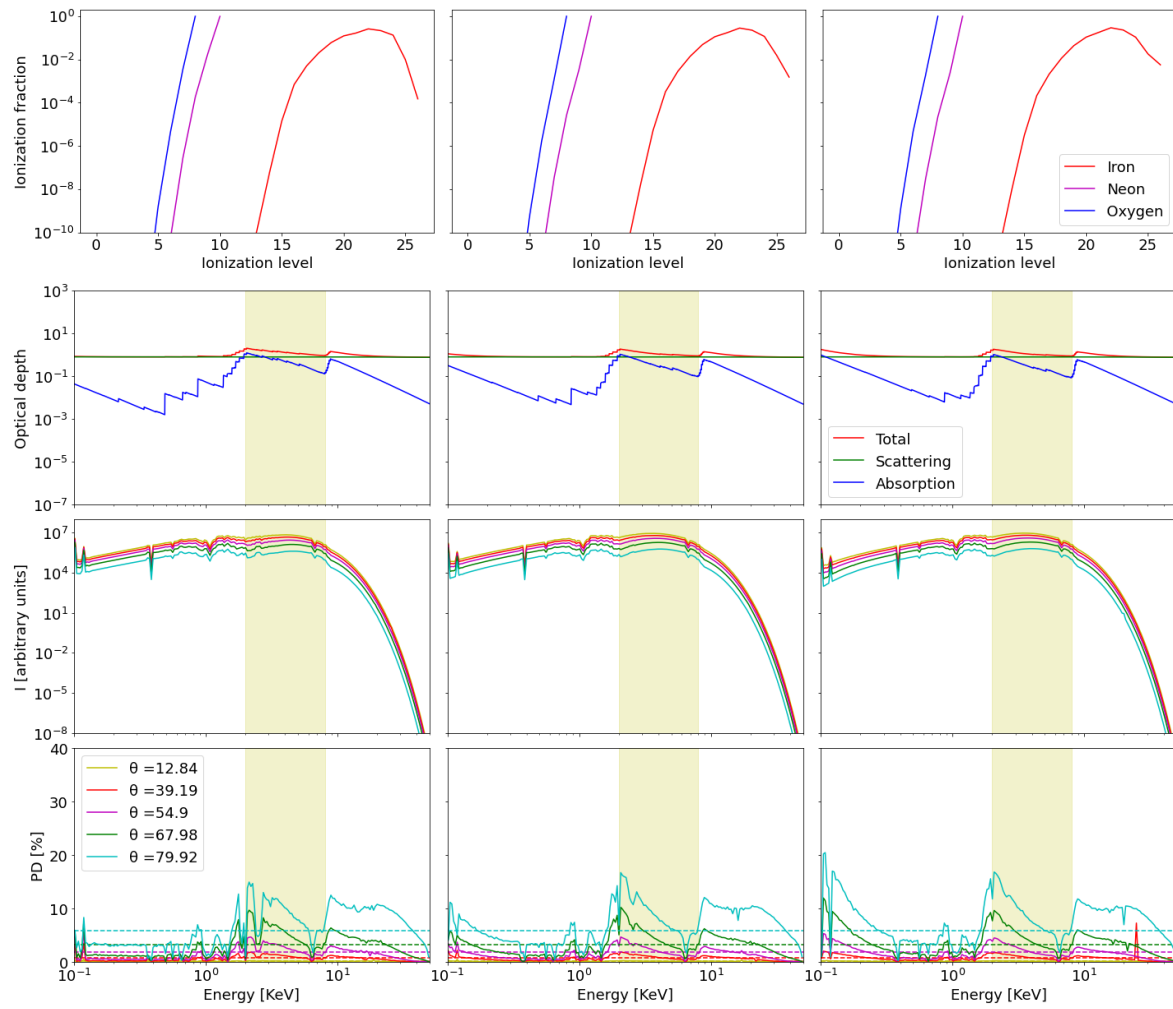


Figure 3.3: Same as Figure 3.2, but for a illuminating black body temperature of $k_B T_{BB} = 1$ keV.

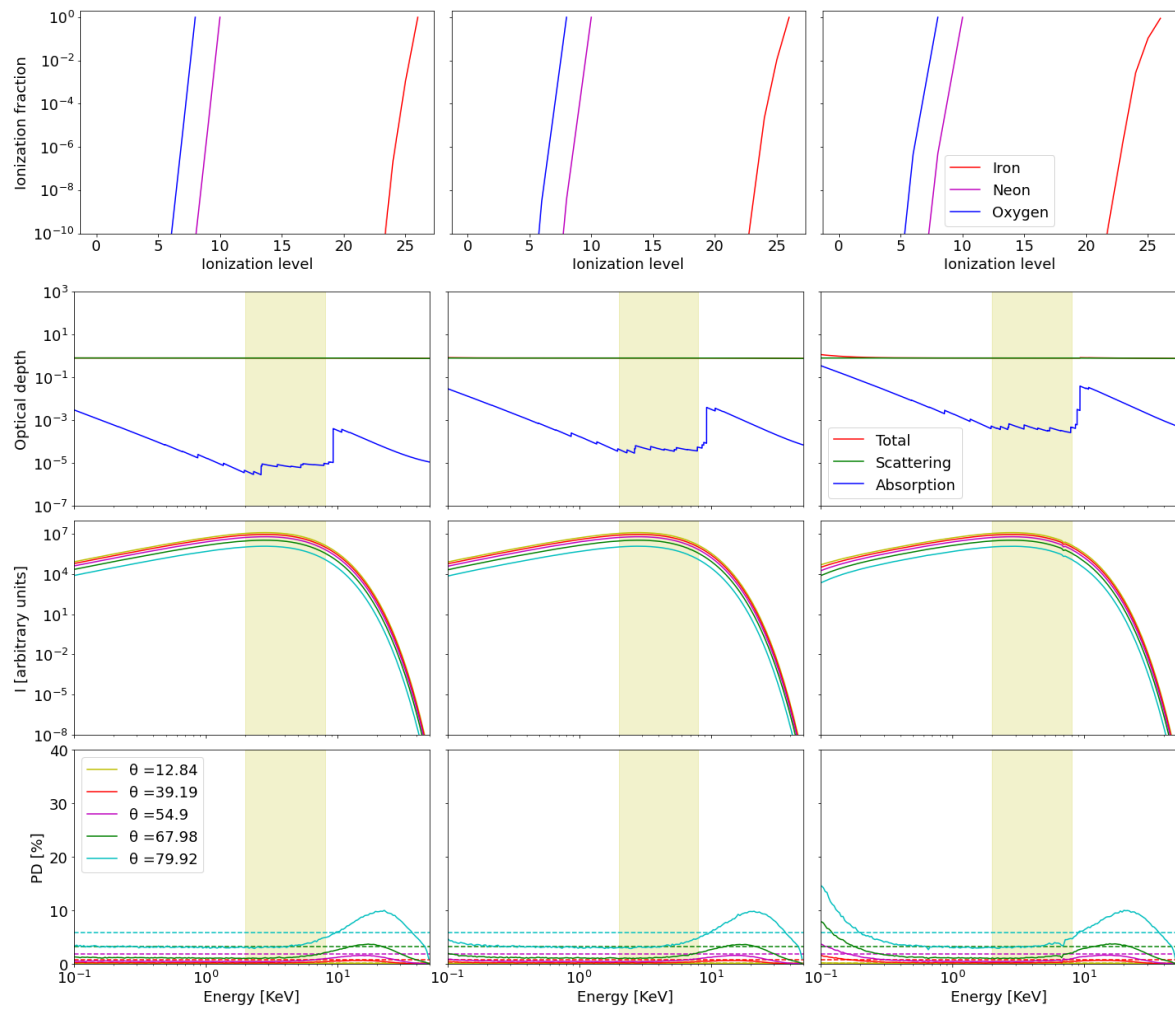


Figure 3.4: Same as Figure 3.3., but assuming the slab medium to be in PIE.

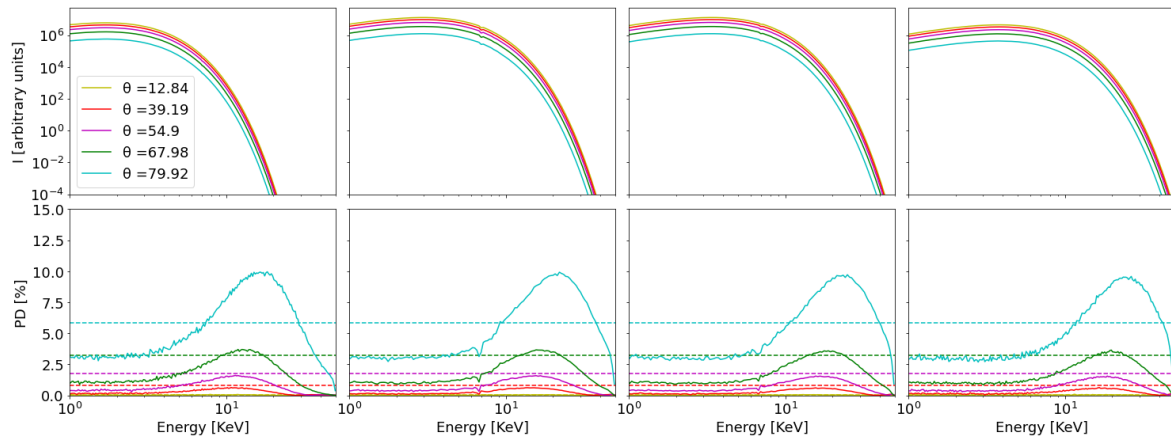


Figure 3.5: Spectra and polarization degree resulting from simulations conducted within the high ionization regime in PIE. Moving from left to right, the temperature of the black body radiation increases ($k_B T_{BB} = 0.6, 0.8, 1,$ and 1.2 keV, respectively), while the slab density is adjusted proportionately to maintain a constant ionization parameter, set at $\log \xi \sim 5$. Notably, the peak of the PD bump shifts towards higher energies with an increase in the temperature of the seed black body radiation.

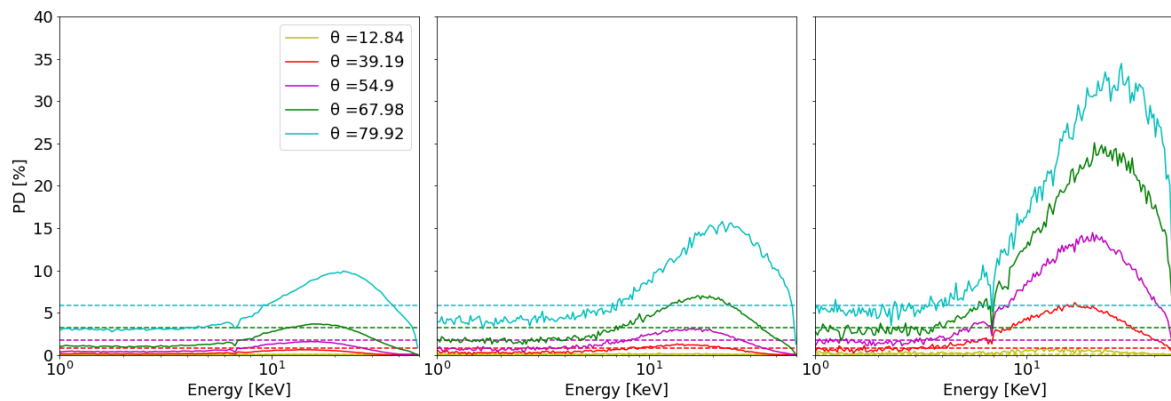


Figure 3.6: Simulation results illustrating the impact of increasing optical depth on the PD of the emerging radiation. The black body temperature and slab density are held constant at $T_{BB} = 1$ keV and $n_H = 10^{19}$ cm^{-3} , respectively. The figures depict three distinct values for the slab column density, arranged from left to right as $N_H = 10^{24}, 10^{24.17},$ and $10^{24.7}$ cm^{-2} , corresponding approximately to optical depths of 0.67, 1, and 3, respectively.

3.3 Direct emission from the whole disk

Accretion disk atmospheres can be modeled in various ways, depending on the specific accretion disk models, ionization regimes, and assumptions regarding density and temperature profiles. These profiles are, in turn, influenced by parameters governing the accretion process, such as the BH spin and accretion rate. Our present analysis serves as a follow-up study to the examination presented in [Taverna et al. \[2021\]](#), which primarily focused on the effects of photoelectric absorption on polarization, assuming a CIE for the disk atmosphere. Moreover, it described the spectro-polarimetric properties of radiation from the perspective of an observer located on the disk itself, without incorporating the crucial GR effects that modify radiation properties during its journey toward the observer. The work presented here aims to address these points by examining the effects of photoionization on the disk atmosphere ionization profile and incorporating GR effects, which involves the use of the ray-tracing package *KYN* to integrate the results reported from our *CLOUDY* and *STOKES* simulations. As discussed above, due to the long computational time required, our investigation is still in progress. Therefore, in this section, we present only the contribution of the direct radiation component, as defined in Section 2.3.3. The inclusion of returning radiation, particularly significant for rapidly rotating sources and crucial for comparing our results with *IXPE* observational data, will be thoroughly explored in a future publication.

In our previous investigation outlined in [Taverna et al. \[2021\]](#), we adopted a standard thin disk model [[Shakura and Sunyaev, 1973](#), [Novikov and Thorne, 1973](#)] wherein particles orbit the central BH at Keplerian velocity. The disk was assumed to extend up to the radius of the ISCO and subdivided into 30 radial bins logarithmically spaced between the ISCO and 30 gravitational radii. The axial symmetry of the disk implies that each radial bin corresponds to an annulus centered on the BH. Using our *CLOUDY* and *STOKES* setup, we analyzed the spectro-polarimetric properties of the radiation transmitted through the disk atmosphere for each of these radial bins. The temperature profile of the atmosphere was described by the [Novikov and Thorne \[1973\]](#) profile (see Equation 1.14). To model the hydrogen density $n_0(H)$ on the equatorial plane of the disk, we utilized the [Compère and Oliveri \[2017\]](#) density profile [see [Taverna et al., 2020](#), for further details]. To obtain the corresponding values of the density at the disk surface, we assume for the sake of simplicity a Gaussian prescription for the vertical structure, so that:

$$n(H, z_*) = n_0(H) \exp\left(-\frac{z_*^2(r)}{h^2}\right) \quad (3.6)$$

where h is the typical height of the disk at the radial distance r and z_* is the altitude above the disk equatorial plane at which the scattering optical depth calculated up to infinity is equal to 1. In our computations, we focused on a BH with a mass of $10M_\odot$ and considered two spin values: 0 and 0.998. The initial choice for the mass accretion rate ensured that the luminosity reached 10% of the Eddington limit (see Equation 1.9). The temperature and density profiles for these configurations are illustrated with solid lines in Figure 3.7. Additionally, we initially set the atmosphere optical depth to $N_H = 10^{24} \text{ cm}^{-3}$ in our simulations.

Subsequently, we utilized *STOKES* to compute the Stokes parameters of the emerging radiation from each radial bin. Figures 3.8 and 3.9 display the spectra and polarization

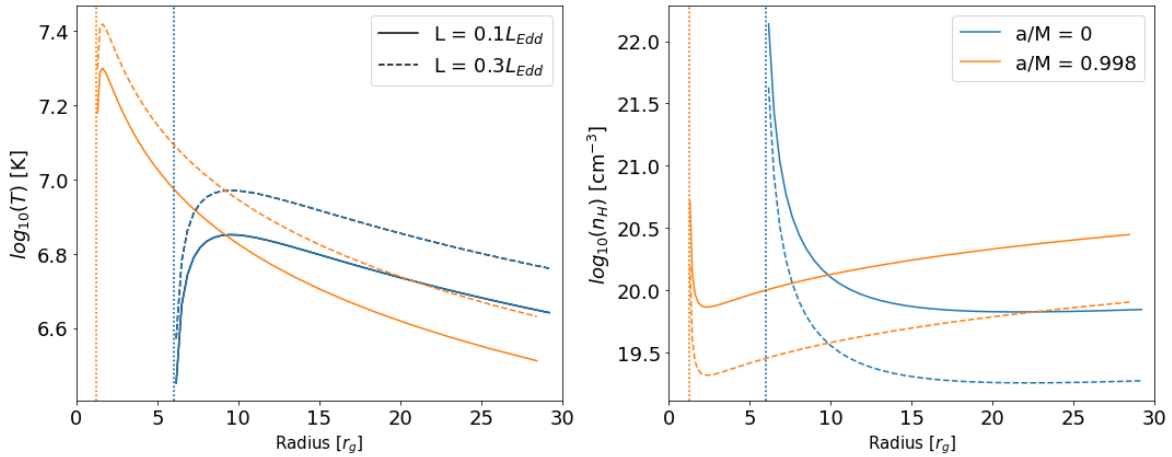


Figure 3.7: Radial profiles of surface temperature (left) and density (right) employed in CLOUDY computations, comparing scenarios for a non-rotating BH represented in blue and a maximally-rotating BH depicted in orange. Both BHs have a mass of $M = 10M_{\odot}$, while the hardening factor f_{col} was set to 1.8. Two possible values for the accretion rate have been considered: $\dot{M} = 0.1\dot{M}Edd$ (solid lines) and $\dot{M} = 0.3\dot{M}Edd$ (dashed lines). The vertical dotted lines highlight the ISCO location for the two BH spin values.

degree profile of the entire disk emission for both ionization regimes considered. To properly account for the varying number of photons emitted from each radial bin, we summed the fluxes of the Stokes parameters over the radial distance r . A weight was applied in this sum, considering the temperature of each bin and the area $A(r) = 2r\pi dr$ of each annular patch:

$$I_{loc}(E, \theta) = \sum_r I(r, E, \theta)A(r)T^4(r) \quad (3.7)$$

$$Q_{loc}(E, \theta) = \sum_r Q(r, E, \theta)A(r)T^4(r) \quad (3.8)$$

$$U_{loc}(E, \theta) = \sum_r U(r, E, \theta)A(r)T^4(r) \quad (3.9)$$

It is essential to note that the accurate method for considering emissions from various regions of the accretion disk involves integrating the Stokes parameters over the disk surface. However, since this integration step is correctly handled in KYN, and our current objective is to explore the processes influencing the spectro-polarimetric properties of the emerging radiation from the disk atmosphere, we opted to use Equations 3.7-3.9 here. The integration over the disk surface is addressed in the subsequent step.

Observing the top row of Figure 3.8, it is evident that the emerging photon flux is generally higher for a maximally rotating BH compared to the non-rotating case ($a = 0$). This difference can be easily explained by considering that, for $a = 0.998$, the disk extends much closer to the BH horizon, where temperatures are significantly higher than those in the non-rotating scenario. Specifically, temperatures peak at approximately 1.7 keV for $a = 0.998$, while reaching a maximum of around 0.6 keV for $a = 0$ (see the solid lines in Figure 3.7). Consequently, for the non-rotating BH, the seed black body peak can be expected to occur at ~ 1 keV; on the other hand,

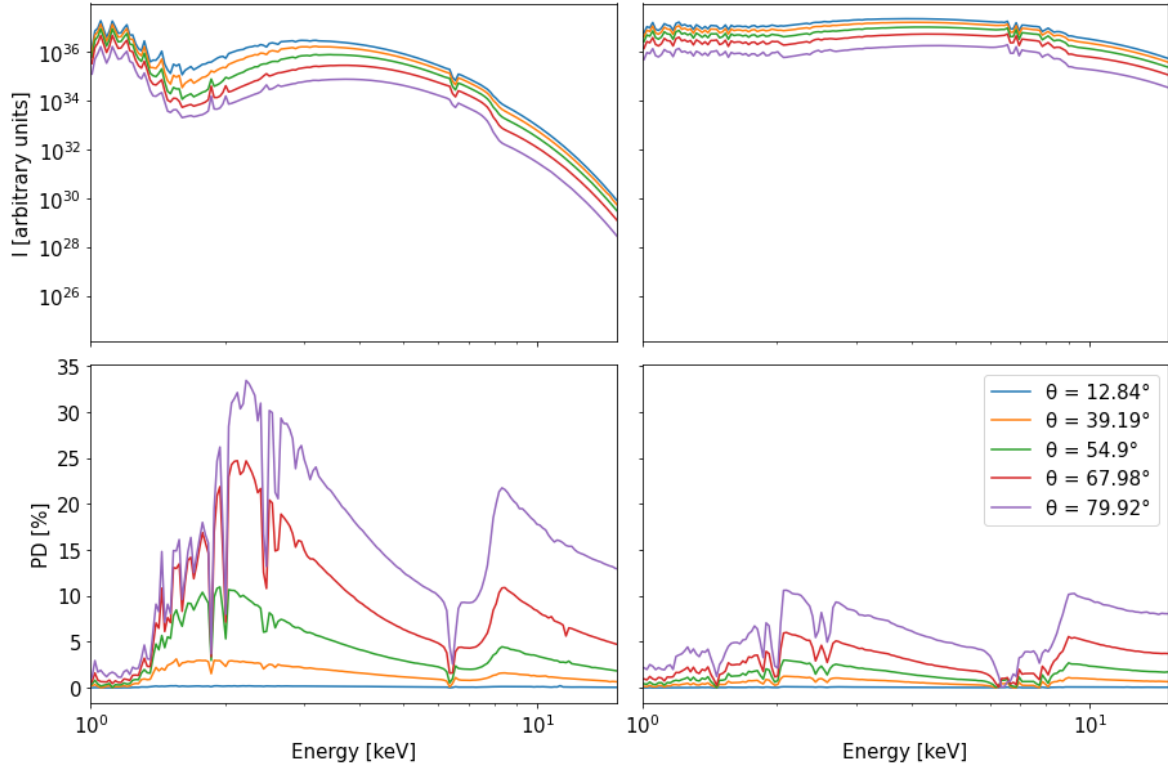


Figure 3.8: Plots of emerging spectra (top row) and polarization degree (bottom row) for the two BH spin values considered: $a = 0$ (left column) and $a = 0.998$ (right column), considering various inclination angles. The parameters are set as follows: black hole mass $M = 10M_\odot$, luminosity $L = 0.1L_{Edd}$, slab column density $N_H = 10^{24}$, and a hardening factor $f_{col} = 1.8$. The disk medium is assumed to be in CIE. Stokes parameters, appropriately weighted for the area and temperature of each radial patch, are aggregated over radial distance r (refer to Equations 3.7-3.9).

in the maximally rotating case, the maximum of the injected black body falls around 3 keV. Hence, in this case, the contribution of seed photons is much more significant across the selected 1–10 keV energy range. The impact of absorption is also evident, as highlighted by several spectral features superimposed on the continuum in both the $a = 0$ and $a = 0.998$ cases. These lines are primarily concentrated at lower energies (1–2 keV), with two prominent absorption features emerging at approximately 6.5 keV and 8 keV.

The corresponding polarization degree profiles exhibit characteristics consistent with the low ionization case discussed in section 3.2. Specifically, the radiation emerges with a constant polarization angle perpendicular to the disk symmetry axis. The polarization degree tends to be generally higher at energies dominated by photoelectric absorption. Consequently, in both cases, an increase in polarization degree is observed between 2 – 3 keV and at high energies around 10 keV, while a decrease occurs around 6 – 7 keV due to the spectral contribution of Fe XXV and Fe XXVI emission lines. For the non-rotating case ($a = 0$), the polarization degree is generally larger by a factor of approximately 2 – 3 compared to the maximally rotating BH case. This discrepancy arises from the stronger contribution of photoelectric absorption processes in the non-

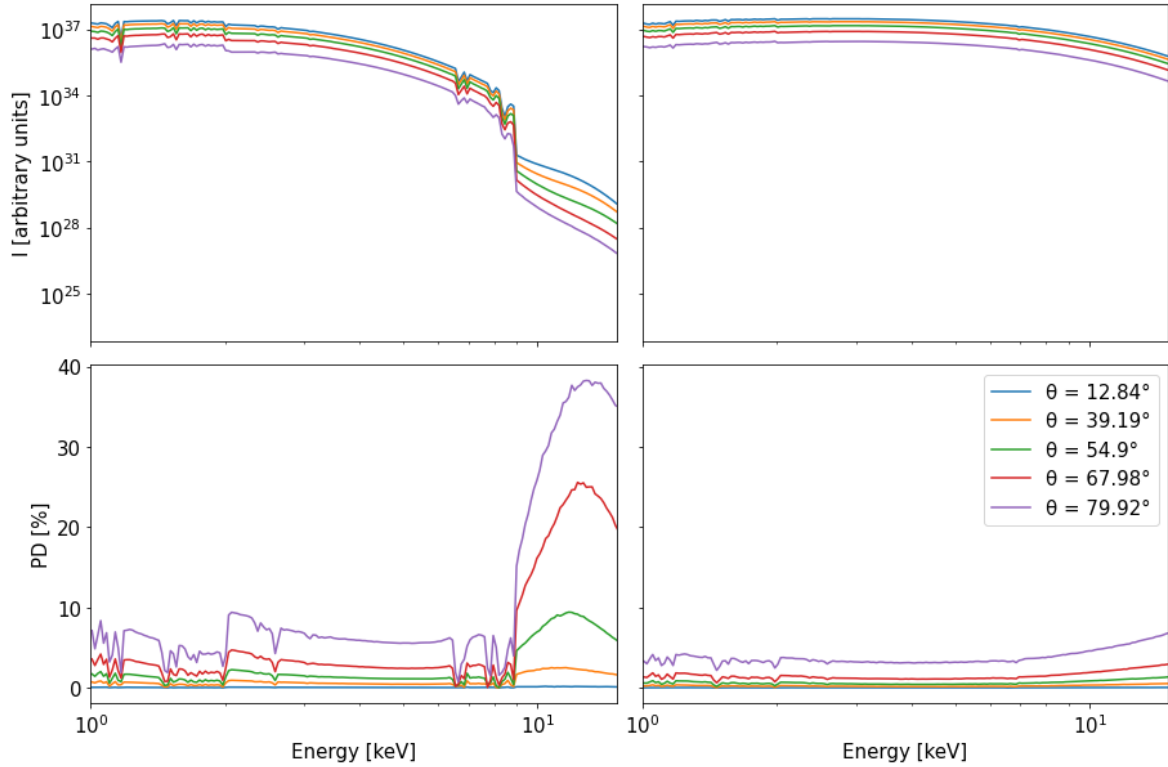


Figure 3.9: Same as Figure 3.8, but assuming the slab medium to be in PIE.

rotating case. An exception to this trend is observed at lower energies (around 1 keV) for $a = 0$, where the polarization degree is notably low (below 2%) for all inclinations. This can be attributed to the fact that primary photons in this scenario peak at energies such that photons emerging at 1–2 keV are predominantly seed photons, which are assumed to be unpolarized. In the maximally rotating case, despite the larger ionization of the disk medium due to higher temperature and lower density (refer to Figure 3.7), the disk medium remains far from the complete ionization regime discussed in section 3.2. The low optical depth considered for the slab, coupled with the generally high temperature of the radial bins composing the disk, prevents the observation of the high-energy polarization degree bump discussed earlier in the limited energy band we focused on.

Figure 3.9 displays the spectra and polarization degree obtained when assuming that the disk atmosphere is in PIE. As discussed in section 3.2, this configuration generally leads to a more ionized disk medium, thereby reducing the contribution from absorption processes. This is evident in the spectra for both spin values considered, which lack strong absorption features except for the notable Fe absorption edge observed at 9.1 keV for $a = 0$, consistent with the left column of Figure 3.1. Similar to the CIE case, the flux tends to be higher in the maximally rotating scenario compared to a non-rotating BH. The polarization degree profiles reflect this absence of pronounced absorption features in the spectra. Specifically, within the *IXPE* energy band, the predicted polarization degree values generally appear lower than those obtained in the CIE configuration, reaching approximately 10% and 4% for $a = 0$ and $a = 0.998$, respectively. Nevertheless, in the non-rotating case, a significant increase

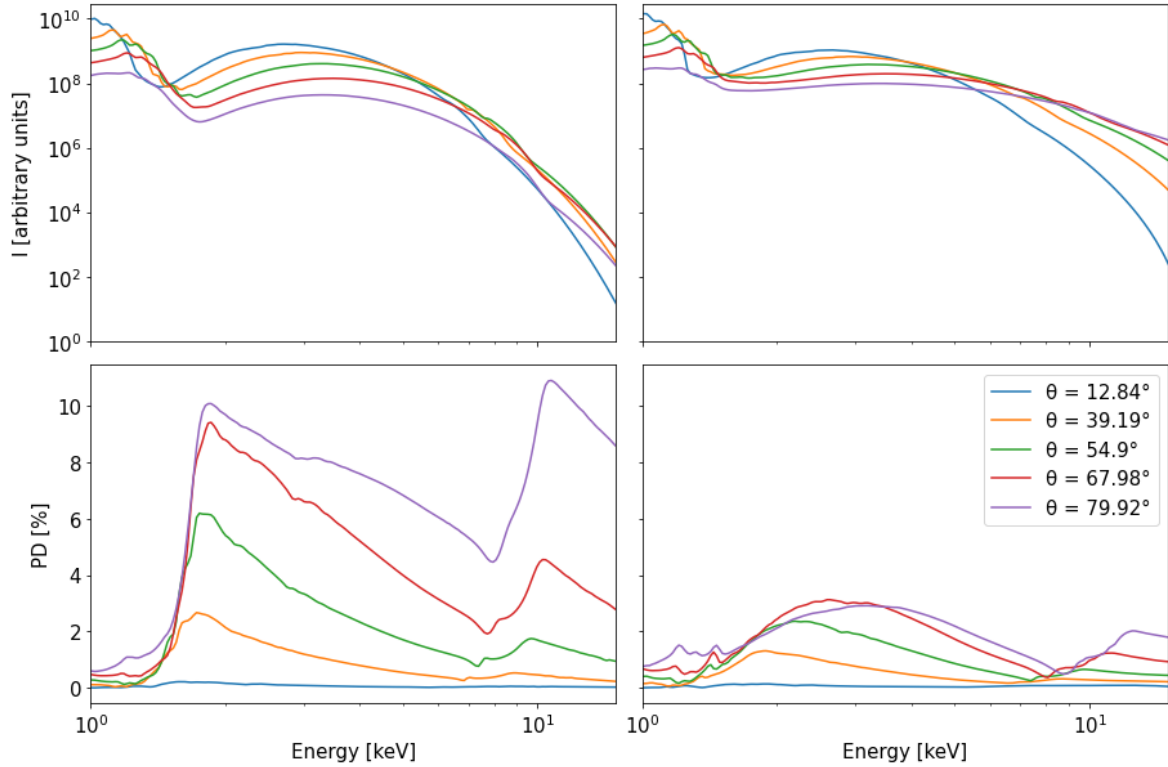


Figure 3.10: Spectra (top row) and polarization degree profile (bottom row) observed at infinity, computed in KYN. The Stokes parameters used for the emerging radiation are derived from our CLOUDY+STOKES simulations. Results for two distinct black hole spin values are presented: $a = 0$ in the left column and $a = 0.998$ in the right column. The black hole mass, accretion rate, hardening factor, and atmosphere optical depth remain consistent with those utilized in Figure 3.8.

in the polarization degree profile is observed at energies above the absorption edge in the spectra, reaching up to approximately 40% for highly inclined sources. While for $a = 0.998$ the disk medium results to be completely ionized, as indicated by the lack of spectral signatures due to absorption, because of the low optical depth of the slab the polarization degree only presents a small increase at high energies, likely the initial rise of the PD bump observed in Figure 3.4.

The subsequent step in our study involved using the Stokes parameters of the emerging radiation as input for KYN to investigate the properties of the emission at infinity. The results of these computations are depicted in Figures 3.10 and 3.11, which display the spectra and the PD profile for the same configurations explored in Figures 3.8 and 3.9, respectively. Upon comparing the two couples of figures, it becomes evident that both the spectra and the PD profile at the observer generally recall the profile at the disk. The gravitational and Doppler shifts tend to smooth most of the absorption features observed in the local spectra, except for the strong absorption feature at ~ 2 keV in the CIE configuration, and for the Fe absorption edge observed in the PIE case for a non-rotating BH. In low inclination scenarios, the spectra decrease at high energy, with this effect being more pronounced for a maximally rotating source due to stronger redshift effects in such configurations [see e.g., Figure 2 of Dovčiak et al.,

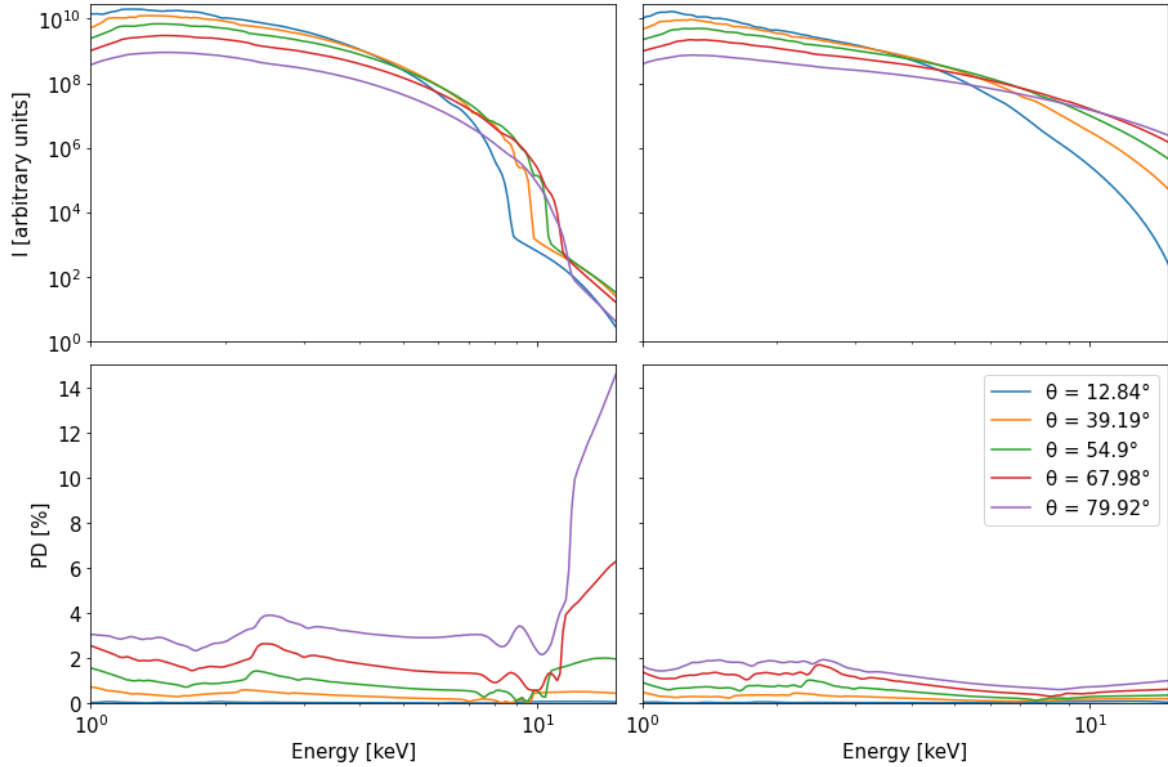


Figure 3.11: Same as Figure 3.10, but assuming the slab medium to be in PIE.

2008]. The polarization degree at the observer is generally found to be lower by a factor ~ 3 compared to the local one. This reduction is attributed to the depolarization of the observed radiation induced by the rotation of the polarization vector in a strong gravity regime (see section 2.3.3). This rotation is observable in the polarization angle profile illustrated in Figure 3.12. While the local polarization angle was constantly perpendicular to the disk axis ($PA = 0^\circ$), its value at the observer tends to decrease at high energies. This rotation is more pronounced in the maximally rotating case for low inclination scenarios and does not depend on the ionization regime of the disk atmosphere medium.

Despite the general decrease in observed polarization properties caused by the inclusion of GR effects, it is crucial to emphasize that, in the CIE configuration, the PD predicted by our model at infinity remains higher than the one obtained using the Chandrasekhar [1960] approximation [see e.g., Figure 4 of Dovčiak et al., 2008]. While in the PIE case the predicted PD tend to be lower, it is important to note that our results are obtained assuming a relatively low optical depth for the disk atmosphere ($\tau \approx 0.67$). As discussed in the previous section, considering a larger optical depth for the disk atmosphere has the potential to significantly enhance the polarization degree of the emerging radiation. Simultaneously, our findings are sensitive to the parameters governing the accretion mechanism and the disk structure, such as the hardening factor f_{col} and the accretion rate \dot{M} . To analyze the effect of varying these parameters on the observed polarization properties, we conducted additional simulations, considering either a larger accretion luminosity ($L = 0.3L_{Edd}$) or a greater hydrogen column density for the surface layer ($N_H = 5 \times 10^{24} \text{ cm}^{-2}$, corresponding to $\tau \approx 3.33$).

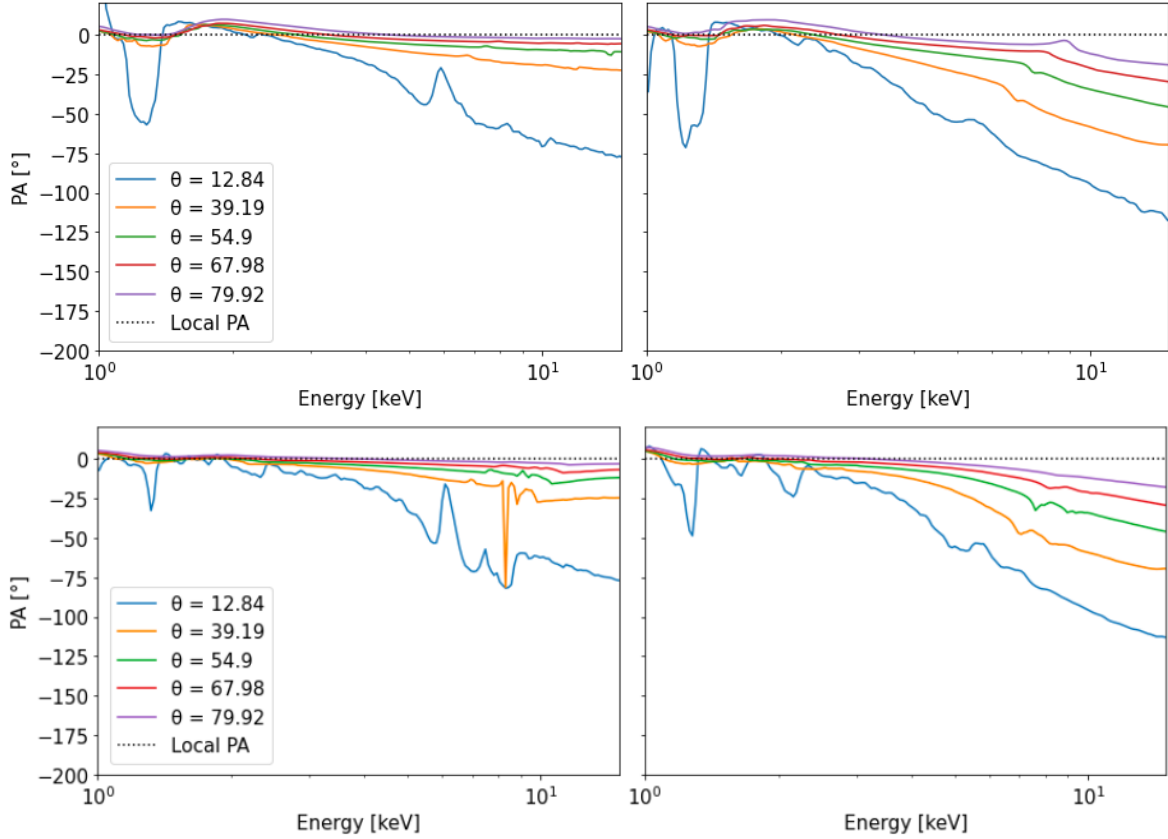


Figure 3.12: Polarization angle observed at infinity for a BH with spin $a = 0$ (left column) and $a = 0.998$ (right column), assuming the disk atmosphere in CIE (top row) or in PIE (bottom row).

When considering a larger accretion rate, the temperature and density profiles of the disk change as illustrated by the dashed lines in Figure 3.7. Specifically, the temperature experiences a general shift upwards by a factor of approximately ~ 1.3 , accompanied by a radial displacement of the maximum towards a slightly larger distance from the center. The density, on the other hand, decreases at all the considered radial distances by a factor of approximately ~ 3 . These modifications result in a more ionized disk medium, reducing the contribution of photoelectric absorption processes. The effects of these changes on the emerging and observed flux are respectively depicted in the top row of Figures 3.13 and 3.15, when assuming the disk surface layer in CIE, and in Figures 3.14 and 3.16 when including photoionization. In Figures 3.13 - 3.16 solid lines represent the behavior for the previously discussed case with $L = 0.1L_{Edd}$, and dotted lines represent that for $L = 0.3L_{Edd}$ (with a column density of $N_H = 10^{24} \text{ cm}^{-2}$). As expected, the emerging radiation photon flux achieves higher values when a higher accretion luminosity is considered due to the increased temperature across the disk surface. In the CIE configuration presented in Figure 3.13, for $a = 0$ (top-left panel), the low-energy peak associated with primary photons is noticeably broadened compared to the $L = 0.1L_{Edd}$ case. Additionally, the spectral features attributed to absorption are less pronounced due to the increased ionization fraction in the disk material. In the $a = 0.998$ case (top-right panel), spectra for $L = 0.3L_{Edd}$ appear to be harder than

for lower luminosities. In this case, no substantial differences can be observed in the absorption features, as noted before, since even at $L = 0.1L_{Edd}$ the temperature was sufficiently high to significantly reduce absorption effects. A similar result is obtained for a maximally rotating source in the PIE configuration (see Figure 3.14) as the disk medium already resulted completely ionized at $L = 0.1L_{Edd}$. On the other hand, for a non rotating BH the spectra do not present the strong Fe absorption edge observed in the initial configuration considered, as the larger luminosity of the disk is enough to completely ionize the Fe in the surface layer plasma.

Dash-dotted lines in Figures 3.13 - 3.16 illustrate the behavior of the emerging and observed flux for $N_H = 5 \times 10^{24} \text{ cm}^{-2}$. To isolate the effect of the variation in the atmosphere optical depth, we reverted to $L = 0.1L_{Edd}$ for this simulation. In contrast to the increase in accretion luminosity, in this case, the number of emerging photons is significantly lower across the entire energy range. The peaks of the spectral distributions fall at the same energy as in the original case, given the adoption of the same temperature profile. However, both in the Schwarzschild and in the maximally-rotating case, absorption features become dramatically more significant, with this effect being more pronounced for $a = 0$. Assuming that photons escape the layer at a z_{max} , considering to a larger optical depth implies that they are still involved in a conspicuous number of scatterings so that a lower number of emerging photons at that altitude z_{max} can be reasonably expected. Moreover, since an increase in the optical depth translates into a decrease in the photon mean free path inside the disk material, this also justifies the increase in absorption effects, despite the fact that temperature and density remain unchanged with respect to the initial case. In both scenarios, relativistic effects induce modifications to the spectra similar to those discussed in the initial case considered.

Much like the spectra, the PD of the emerging radiation is also affected by changes in luminosity and optical depth. The bottom row of Figure 3.13 depicts, for the CIE configuration, the PD profile for the same parameter values adopted for the flux in the top row. When increasing L to $0.3L_{Edd}$, the overall behavior is generally reduced by $\sim 1\text{--}2\%$ compared to the initial case. The reduction is more significant at lower energies due to the diminished impact of absorption edges around that energy. Substantial differences emerge when increasing values of N_H . For $a = 0$, the low energy peak of the PD profile tend to move towards larger energies, as the predicted PD value results to be particularly low below 2 keV. A possible explanation for this is that because of the dominant effect of absorption in this energy range the observed radiation is mainly composed by the unpolarized seed black body radiation. A steep rise occurs at high energy with increasing inclination angle, reaching $\sim 40\%$ at ≈ 10 keV due to the larger contribution of the Fe absorption edge. A similar high energy increase can be observed for $a = 0.998$, with the PD becoming as large as $\sim 20\%$ at 15 keV; this increasing PD trend is likely to be the low energy tail of the PD bump induced by Compton down scattering effects presented in Figures 3.4-3.6. A similar situation can be observed in the PIE case, illustrated in the bottom row of Figure 3.14. An increase in the disk accretion rate corresponds to a decrease of the PD, which is particularly important for a non-rotating source above 9 keV due to the disappearance of the Fe absorption edge. On the other hand, an increase of the layer optical depth leads to an increase of the emerging radiation PD. It is worth noting that, in the maximally rotating case, this increase provoke the low energy tail of the PD bump observed in

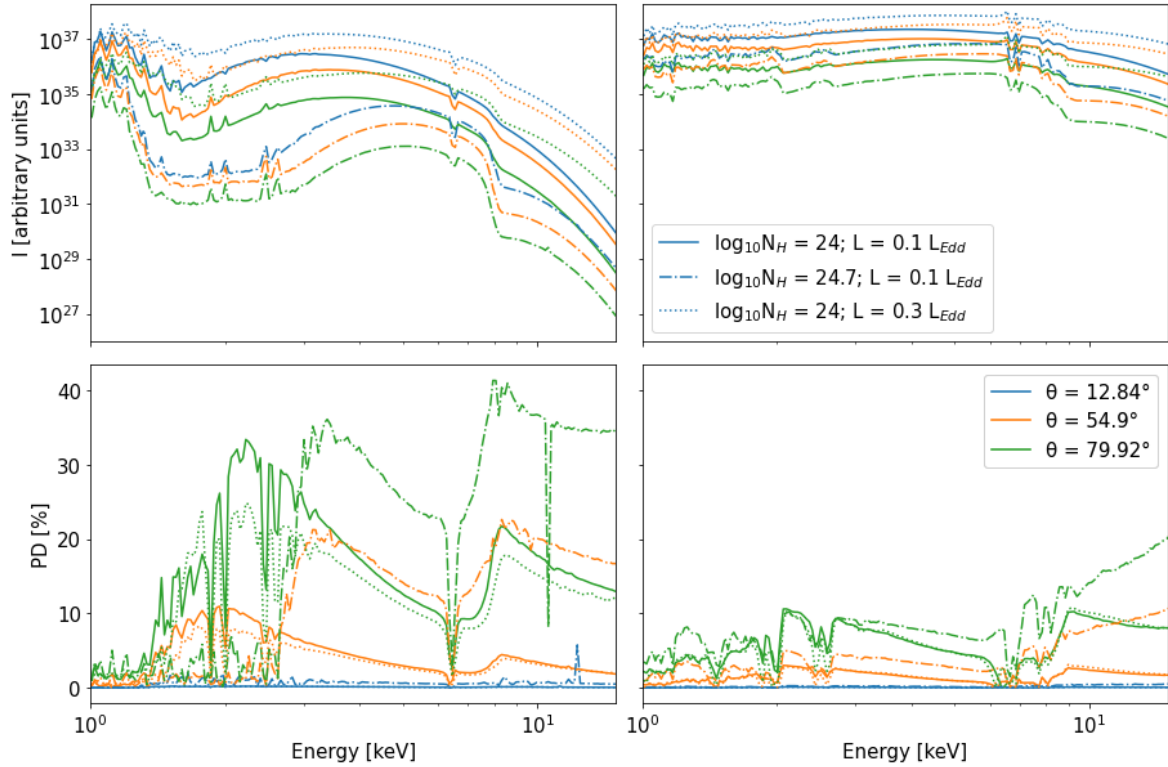


Figure 3.13: Spectra (top row) and PD profile (bottom row) of the radiation emitted from the disk surface are presented for two different black hole spins: $a = 0$ (left) and $a = 0.998$ (right). Each plot includes scenarios with varying parameters: $N_H = 10^{24} \text{ cm}^{-2}$ and $L = 0.1 L_{Edd}$ (solid lines), $N_H = 10^{24} \text{ cm}^{-2}$ and $L = 0.3 L_{Edd}$ (dotted lines), and $N_H = 5 \times 10^{24} \text{ cm}^{-2}$ and $L = 0.1 L_{Edd}$ (dash-dotted lines). Additionally, three inclination angles of the viewing direction are considered: $\theta = 12.8^\circ$ (blue), $\theta = 51.3^\circ$ (orange), and $\theta = 74.0^\circ$ (green). Other parameters are maintained at the same values as in Figure 3.10.

the highly ionized regime to move inside the *IXPE* observational band, effectively predicting an increasing behavior with energy of the PD. When accounting for GR effects, the PD profiles (illustrated in the bottom row of Figures 3.15 and 3.16) exhibit a general decrease across the entire energy band considered. In the scenario with a large optical depth, the PD behavior at high energies still shows an increase, with the largest value being approximately $\sim 30\%$ for $a = 0$ and $\sim 5\%$ for $a = 0.998$ at 15 keV in both the ionization regimes considered.

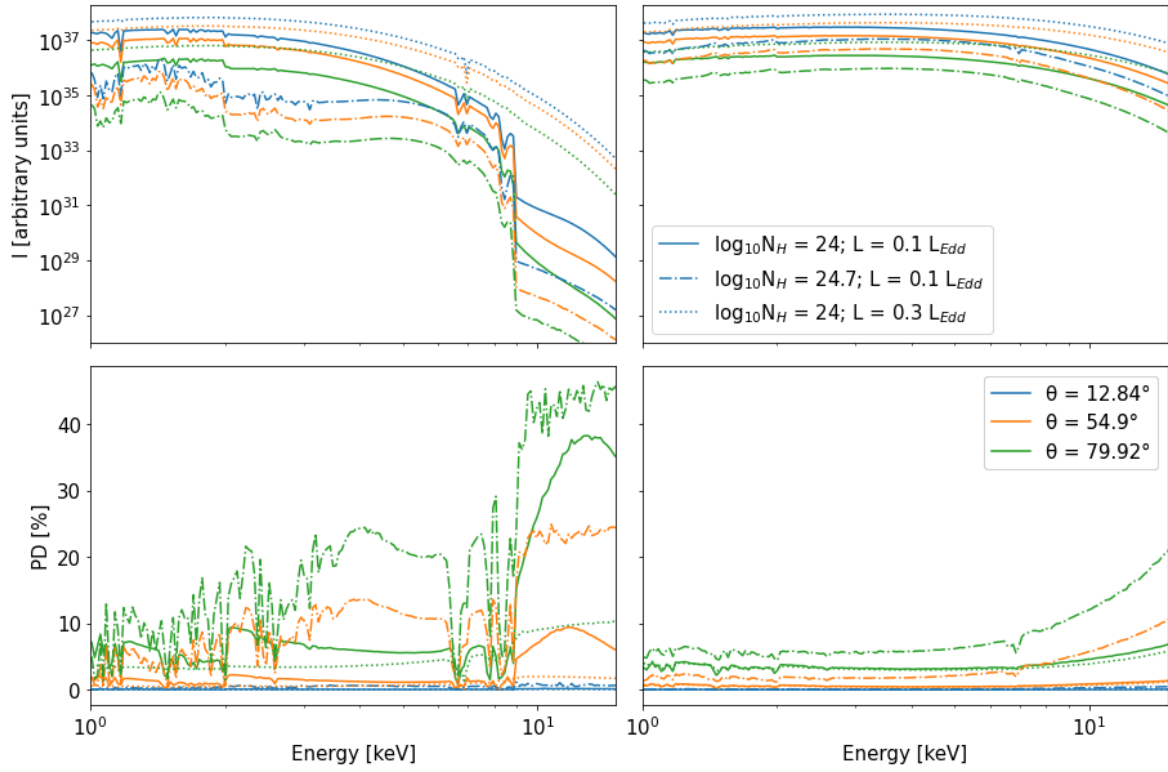


Figure 3.14: Same as Figure 3.13, but assuming the slab medium to be in PIE.

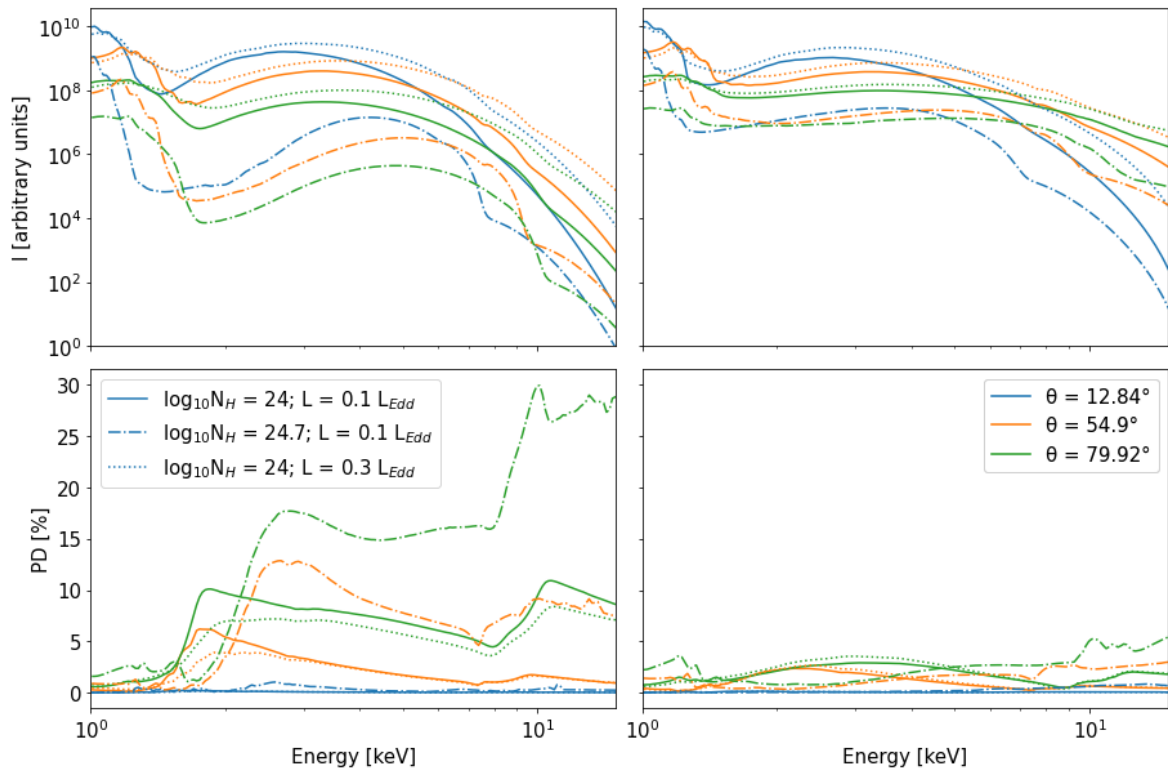


Figure 3.15: Spectra (top row) and polarization degree profile (bottom row) observed at infinity, computed in KYN for the same configurations illustrated in Figure 3.13

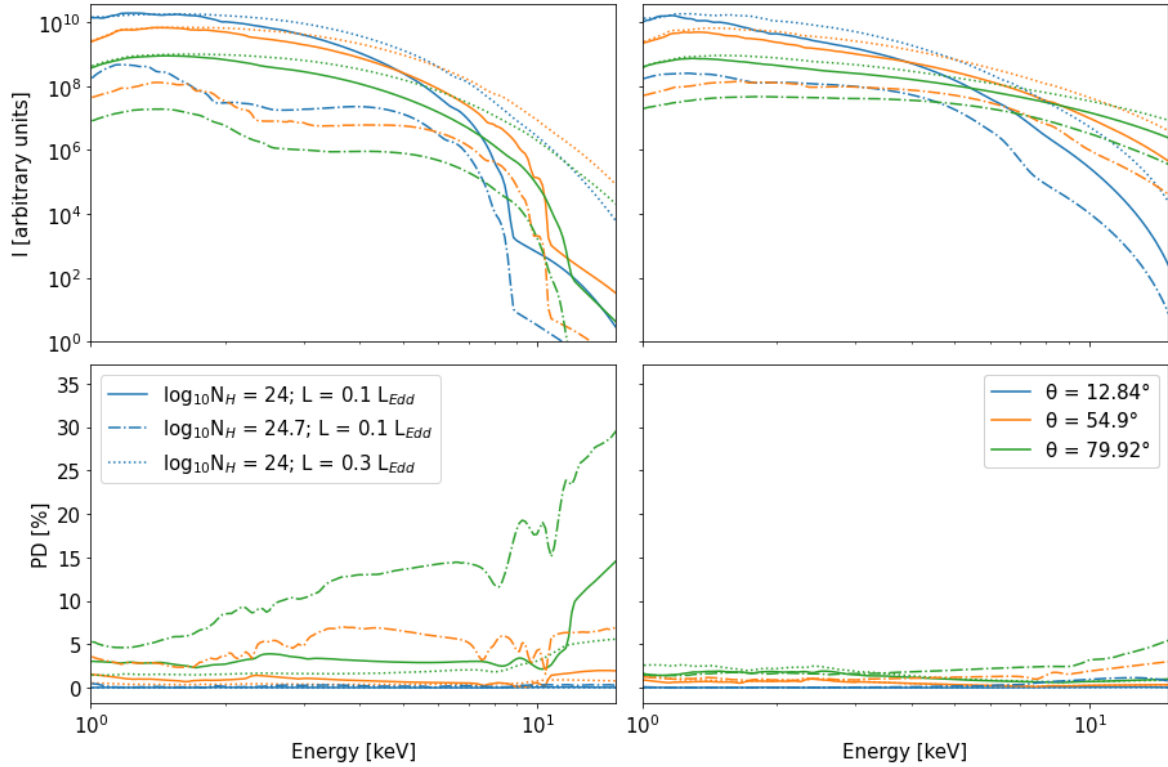


Figure 3.16: Spectra (top row) and polarization degree profile (bottom row) observed at infinity, computed in KYN for the same configurations illustrated in Figure 3.14.

3.4 Future projects

The simulations presented in this chapter highlight the importance of a detailed analysis of the interactions between the disk plasma and the emitted radiation in modeling the spectro-polarimetric properties of the soft state black holes observed by *IXPE*. Our code setup facilitates an extensive exploration of the parameter space, allowing for an investigation of accretion disk emission in various configurations of black hole spin, atmosphere optical depth, and accretion rate. Furthermore, this model can be readily extended to study other spectral contributions, such as the reflection of the corona emission onto the disk [Podgorný et al., 2023a], or the interaction of the accretion disk emission with a wind.

Due to its flexibility, the work presented here opens the door to several potential future projects. One immediate and significant extension is the inclusion of the returning radiation contribution, which, as already mentioned is planned for a forthcoming publication [Marra et al., in prep.]. The recent enhancements to the *STOKES* code, now incorporating Compton up-scattering, provide an opportunity for a more detailed investigation of the plasma-radiation interaction. Additionally, another clear avenue for extension involves a more detailed modeling of the disk atmosphere assuming the PIE regime. This becomes particularly relevant when considering the results of the first *IXPE* observations of stellar-mass black holes in the soft state, as presented in Part II of this thesis. Notably, three out of the four sources observed (such as 4U 1630-47, 4U 1957+115, and LMC X-3) exhibit a polarization degree that increases with energy

in the *IXPE* 2 – 8 keV band. While this behavior can be explained by taking into account the contribution of returning radiation (see, for instance, Figure 2.12), this explanation is viable only when considering rapidly rotating black holes, as in the case of 4U 1957+115, detailed in Chapter 5. For lower black hole spin values, a detailed modeling of the polarization degree increasing trend is still lacking. Therefore, the transmission of the emerging radiation through a highly ionized atmosphere could provide a plausible solution to explain the observed data. The initial analysis in this direction has already been conducted using the results obtained with the TITAN and STOKES setup to model the unprecedented polarimetric data observed in 4U 1630-47, as detailed in Chapter 4.

Part II

Observations

First IXPE observations of stellar mass black holes in soft state

The second part of this thesis is focused on the work I have done during the second half of my Ph.D., on the analysis of the first polarimetric data obtained by *IXPE* on stellar mass BH in soft state (except 4U 1630-47, which has also been observed during a transition toward the SPL state). All the studies presented here have been published or accepted for publication. The targets' names and date of *IXPE* observation, their spectral state, and the average polarization degree and angle detected by *IXPE* in the 2-8 keV band are detailed in table 3.1. My contribution has focused mainly on the data reduction, the spectral and polarimetric analysis of the data, and the modelization of the polarimetric result. In particular:

- for the first observation of 4U 1630-47, presented in [Ratheesh et al. \[2024\]](#), I have worked on the modelization of the polarimetric data, employing the simulations described in Chapter 3 to produce modified versions of KYNBBRR which were used in the spectro-polarimetric analysis of the observed data. In the second observation of this source, I have performed the spectral and spectro-polarimetric fit of the NICER, *NuSTAR* and *IXPE* data, finding an estimate of the polarization properties of the power-law component. This second observation is detailed in [Rodriguez Cavero et al. \[2023\]](#), and both 4U 1630-47 observations are presented in Chapter 4.
- I have coordinated the working group on the analysis of the 4U 1957+115 observation, presented in [Marra et al. \[2024\]](#) and detailed in Chapter 5. Moreover, I have performed the data reduction, the spectral, and the spectro-polarimetric

Source	Date	Spectral state	PD	PA
4U1630-47	23/08 - 2/09 2022	HSS	$8.3 \pm 0.2\%$	$17.8^\circ \pm 0.6^\circ$
	10/03 - 14/03 2023	SPL state	$6.8 \pm 0.2\%$	$21.3^\circ \pm 0.9^\circ$
4U1957+11	12/05 - 24/05 2023	HSS	$1.9 \pm 0.6\%$	$42.2^\circ \pm 7.9^\circ$
LMC X-1	19/10 - 28/10 2022	HSS	$< 2.2\%$	-
LMC X-3	7/07 - 8 /07 and 12/07 - 21/07 2023	HSS	$3.2 \pm 0.6\%$	$42.0^\circ \pm 6.0^\circ$

Table 3.1: Stellar mass black hole sources observed by *IXPE* and presented in this thesis.

analysis of the NICER, *NuSTAR* and *IXPE* data.

- for the observation of LMC X-1 [Podgorný et al., 2023b], presented in Chapter 6, I have worked on the spectral analysis of the NICER, *NuSTAR* and *IXPE* data, and performed the spectro-polarimetric fit of *IXPE* data estimating an upper limit on the thermal component polarization degree.
- I have worked on the spectro-polarimetric analysis of *IXPE* data for the observation of LMC X-3, presented in Chapter 7 and further detailed in Svoboda et al. [2024b].

Chapters 4-7 cover the description of the data, the spectral and spectro-polarimetric analysis performed on each of the sources listed in Table 3.1. A detailed description of the data reduction techniques employed is presented in Appendix A. We followed similar steps in the analysis of each source: we initially checked for the timing properties of the observations at our disposal, analyzing the light curves of all instruments involved in the analysis. Subsequently, we performed a spectral fit of NICER [Arzoumanian et al., 2014], *NuSTAR* [Harrison et al., 2013] data. This step has the fundamental goal of estimating the flux contribution of each spectral component in the *IXPE* band and checking for possible variations of the source spectral state. Since the main purpose of these analyses is to present an interpretation of the first polarimetric observations of these sources, we have not investigated the inconsistencies between NICER and *NuSTAR* data found during the observations, likely of instrumental origin. These have been modeled either by adding to the model additional EDGE components, using an empirical convolution model (MBPO), restricting the energy range of our analysis to reduce the overlap between the two instruments, or adjusting the response file gains using the `gain fit` command in `xspec`. A more detailed analysis of these features is deferred to future studies.

Then, we included *IXPE* I , Q and U spectra in the analysis, and performed a spectro-polarimetric fit of our data. We first employed an empirical model (either POLCONST or POLLIN) to study the energy dependency of each spectral component polarization properties. This approach allowed us to disentangle the contribution of each spectral component to the observed polarization, a crucial step in understanding the polarization properties of the disk emission. Finally, we performed a more detailed analysis of the thermal emission polarization properties employing the physical model KYNBBRR, which we already introduced in chapter 3.

Chapter 4

4U 1630-47

4.1 Introduction

Discovered by the Uhuru satellite in 1969 [Giacconi et al., 1962, Friedhorsky, 1986], 4U 1630-47 stands as a transient low-mass X-ray binary system, with recurrent outbursts observed approximately every 2 to 3 years [Kuulkers et al., 1998, Capitanio et al., 2015]. Notably, the 1984 outburst provided insights into its X-ray spectral and timing properties, strongly suggesting the presence of a black hole as the compact object [Parmar et al., 1986]. However, peculiar outburst behavior [Chatterjee et al., 2022] has hinted at a more complex system than initially presumed. The accurate characterization of this binary system remains challenging due to significant line-of-sight (LOS) extinction [Reid et al., 1980, Parmar et al., 1986], resulting in poorly constrained parameters such as the black hole mass, the system distance, and its inclination angle. Estimates based on the dust scattering halo around the source suggest a distance ranging from 4.7 to 11.5 kpc [Kalemci et al., 2018]. Observations of X-ray dips and the absence of eclipses indicate a relatively high inclination angle of approximately $\sim 60^\circ - 75^\circ$ [Tomsick et al., 1998, Kuulkers et al., 1998]. Furthermore, the source spectrum has revealed intriguing features, including evidence of an outflowing wind during soft accretion states, evidenced by strong, blueshifted absorption lines corresponding to Fe XXV and Fe XXVI transitions [Díaz Trigo et al., 2014b, King et al., 2014, Miller et al., 2015, Pahari et al., 2018, Gatuzz et al., 2019]. Dominated by a thermal component during outbursts [Parmar et al., 1986], this system presents an ideal opportunity for investigating disk properties. Several attempts at reflection spectral modeling consistently indicate a high spin, with measurements suggesting $a_s = 0.985_{-0.014}^{+0.005}$ [King et al., 2014], $a_s = 0.92 \pm 0.04$ [Pahari et al., 2018], and $a_s \gtrsim 0.9$ [Connors et al., 2021].

4.2 Datasets

The 4U 1630-47 system was observed twice by *IXPE*, initially in August 2022 and subsequently in March 2023. In July 2022, continuous monitoring using the Gas Slit Camera (GSC) aboard the Monitor of All-sky X-ray Image (MAXI, [Matsuoka et al., 2009]) indicated a rise in the count rate, signaling an outburst from the source [Jiang et al., 2022]. Capitalizing on this outburst, *IXPE* conducted a target of opportunity

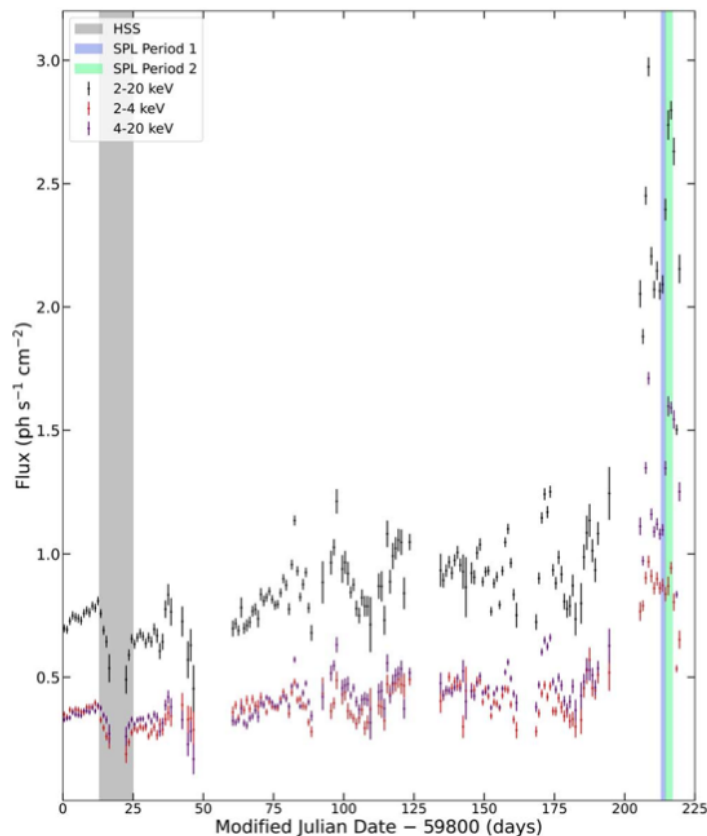


Figure 4.1: MAXI X-ray light curves of 4U 1630-47, between 2022 August 9 and 2023 March 22. The flux in the 2 – 20, 2 – 4 and 4 – 20 keV energy bands are reported in black, orange, and purple, respectively. The gray-shaded region corresponds to the first *IXPE* observation, when the source was in the HSS, while the regions shaded in blue (Period 1) and green (Period 2) correspond to the second observation when the source was in the SPL state.

(ToO) observation, starting on August 23, 2022, and ending on September 2, 2022, for a total exposure of approximately 460 ks. Concurrently, NICER [Arzoumanian et al., 2014] conducted 11 observations spanning from August 22 to September 1, 2022, totaling approximately 27 ks, while *NuSTAR* [Harrison et al., 2013] observed the source three times: on August 25 and 29, 2022, and September 1, 2022, with elapsed times of 38.3 ks, 31.6 ks, and 32.5 ks across the three snapshots.

The second targeted observation by *IXPE* occurred between March 10 and 14, 2023, spanning approximately 150 ks. This observation followed a notable increase in flux reported by MAXI daily monitoring of the source, as depicted in Figure 4.1. Within this figure, the gray highlighted region corresponds to the initial observation, during which the MAXI flux hovered around $0.62 \text{ ph s}^{-1} \text{ cm}^{-2}$. Subsequently, denoted by the blue and green highlighted sections, the second observation registered higher flux levels, approximately $2.24 \text{ ph s}^{-1} \text{ cm}^{-2}$ and $2.77 \text{ ph s}^{-1} \text{ cm}^{-2}$, respectively. Notably, during these later intervals, the 4 – 20 keV flux (depicted in purple in Figure 4.1) exhibited a more pronounced increase compared to the 2 – 4 keV flux (illustrated in orange), indicating an increase in spectral hardness over this period. Similar to the

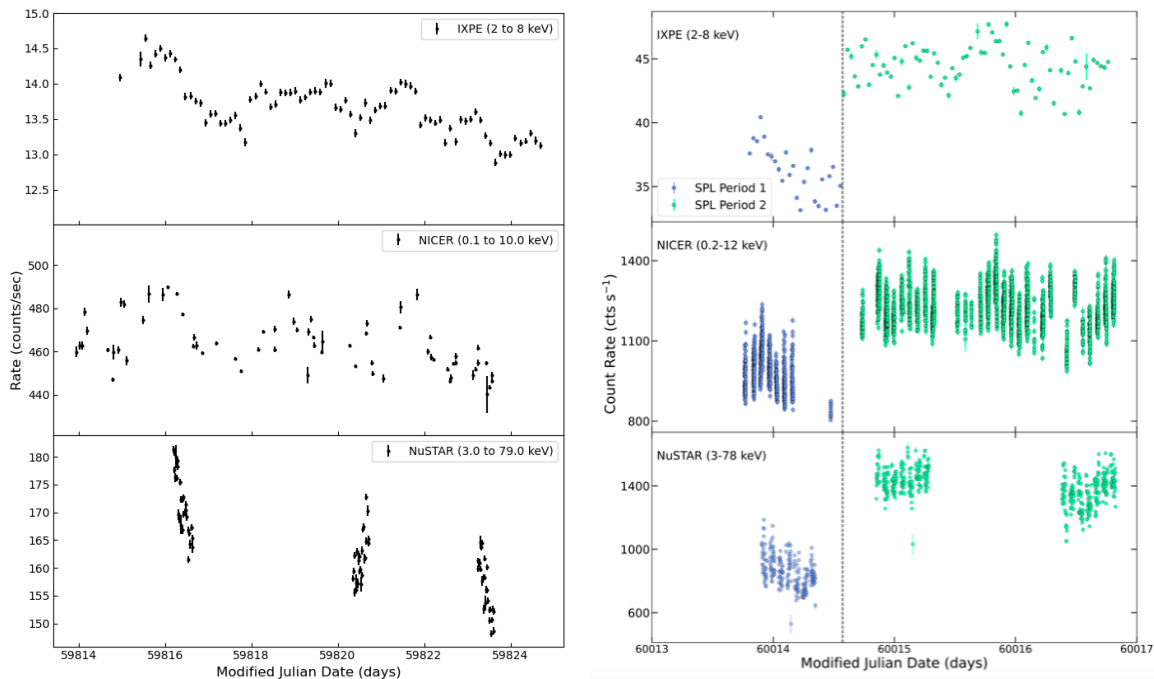


Figure 4.2: *IXPE*, *NICER*, and *NuSTAR* light-curves during the HSS (left) and SPL state observations (right). The selected energy ranges for *IXPE*, *NICER*, and *NuSTAR* data are 2–8 keV, 0.1–10 keV, and 3–79 keV, respectively, during the HSS observation. During the SPL state observation, the respective energy ranges are 2–8 keV, 0.2–12 keV, and 3–78 keV. In both observations, the *IXPE* light curves give the combined count rates of all three Detector Units (DUs).

first observation, a joint observational campaign involving *NICER* and *NuSTAR* was conducted concurrently with *IXPE* observation of the source. *NICER* observed the source from March 10 to March 13, accumulating approximately 32.81 ks across six observations. Meanwhile, *NuSTAR* captured the source three times, for a net exposure of approximately 28.35 ks. For an elaborate overview of the data reduction process employed in both observations, please refer to Appendix A.

Figure 4.2 illustrates the *IXPE*, *NICER*, and *NuSTAR* observations conducted during both *IXPE* campaigns. Throughout the first observation, the detected flux demonstrated relative stability, exhibiting variations of approximately 10% below 10 keV and 15 – 20% above 10 keV. During the second observation, instead, a sudden increase in the source flux occurred around the time denoted by the vertical dashed line in figure 4.2. The *IXPE*, *NICER*, and *NuSTAR* count rates increased by approximately 23%, 25%, and 63%, respectively. The continuous coverage by *IXPE* revealed that this increase occurred abruptly, within about 2.6 ks.

A comprehensive understanding of the source state during the two observations can be obtained from the hardness–intensity diagram (HID) derived from 4U 1630-47 *NICER* data, as depicted in Figure 4.3. This includes data from the first (shown in black) and second (shown in blue and green) observations conducted simultaneously with the *IXPE* measurements, along with archival data (shown in grey). The source position in the diagram during the first observation aligns with archival data from

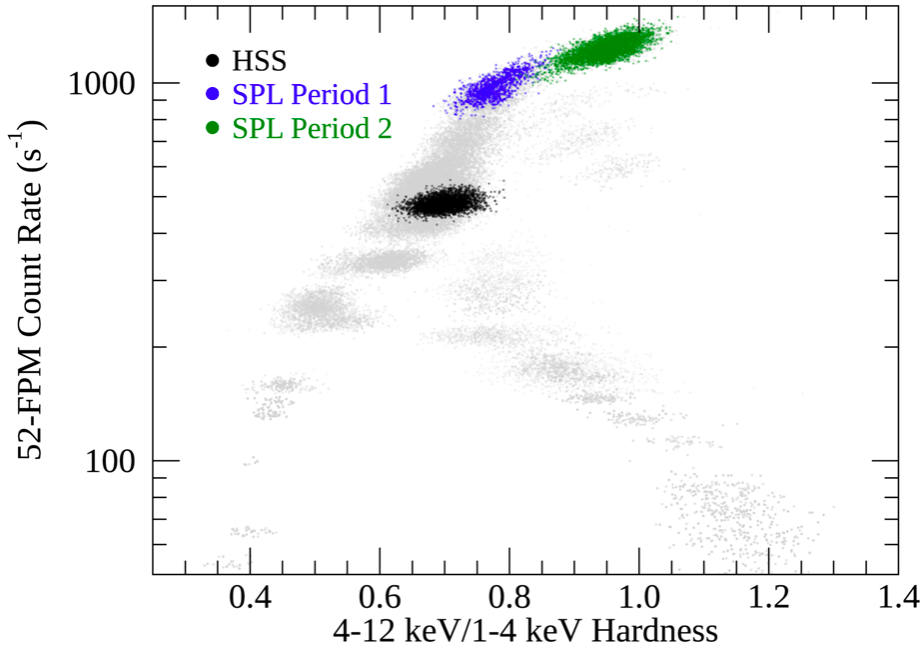


Figure 4.3: Hardness-intensity diagram from NICER data of the HSS (black) and SPL state Period 1 (blue) and Period 2 (green), in 8 s intervals. Data from all previous NICER observations of 4U 1630–47 are shown in gray. Rates have been normalized as if all 52 of NICER FPMs were pointing at the source.

observations in the soft state. Hence, we will refer to this data as the HSS observation in the subsequent analysis. Between the first and second *IXPE* pointings, the NICER energy flux exhibited a substantial increase, accompanied by an increase in the contribution from the hard component. This trend became particularly prominent after the abrupt transition observed during the second observation (refer to Figure 4.2). Therefore, we designate the data from the second observation as the SPL state observation; given the distinct transition observed during this pointing, we segmented our *IXPE*, NICER, and *NuSTAR* data into two periods: Period 1 (depicted in blue) and Period 2 (depicted in green), demarcating the data before and after 13:42:53 UTC on March 11, 2023. Conversely, during the HSS observation, as the *IXPE* lightcurve has not exhibited pronounced time variability, for the sake of simplicity, our analysis was conducted on the time-averaged *IXPE* dataset.

Typically, astrophysical black hole candidates exhibit a counter-clockwise motion through a hardness-intensity diagram during outbursts (as discussed in section 1.4.1). However, in Figure 4.2, the evolution of 4U 1630-47 shows a clockwise trajectory near the apex of the HID, consistent with previous observations of the source in the SPL state using *Suzaku* [Hori et al., 2014]. Notably, the source variability along the HID [see Figure 11 by Tomsick et al., 2005] complicates the interpretation, making it uncertain whether the source transitions from the HSS to the LHS through a high-intensity SPL regime or if this observation captures an unusual trajectory. Furthermore, Figure 4.2 does not present a distinct bright hard state, aligning with the findings of Capitanio et al. [2015]. This absence might signify a deviation from the standard HID Q-track shape proposed in Fender et al. [2004]. Alternatively, as suggested by Tomsick et al.

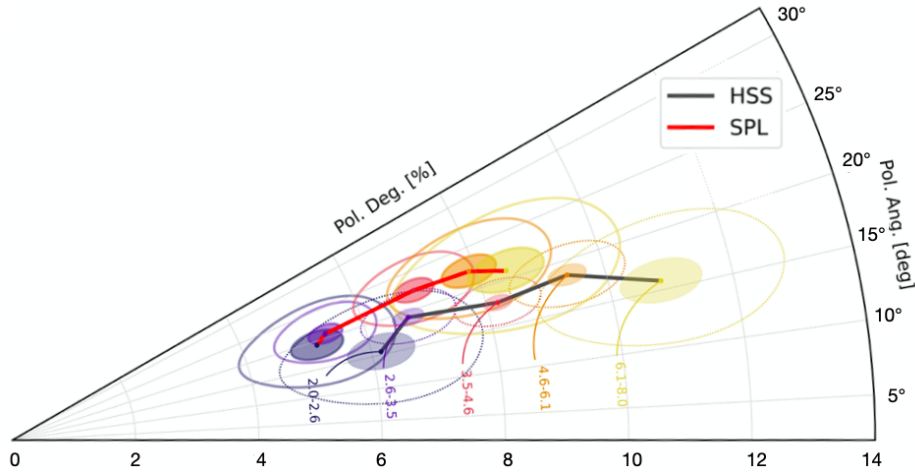


Figure 4.4: Measured PD and PA of 4U 1630-47 in 5 logarithmic energy bins: 2.0–2.6, 2.6–3.5, 3.5–4.6, 4.6–6.1, and 6.1–8.0 keV. The black line and transparent contours show the polarization in the HSS. The red solid line and solid contours show the polarization in the SPL state. The shaded and unshaded ellipses show their 68.3% and 99.7% confidence regions, respectively. Errors on PD and PA computed by IXPEOBSSIM are derived from the Q and U Gaussian errors according to the formalism developed by Kislak et al. [2015].

[2014], a low large-scale magnetic field in the disk could potentially delay the transition to the LHS.

Polarization measurement

In the first *IXPE* observation of 4U 1630–47, a robust detection of linear polarization emerged, with a statistical confidence exceeding approximately 50σ . Within the 2–8 keV range, the polarization degree (PD) measured $8.32 \pm 0.17\%$, and the position angle (PA), taken east of North, registered at $17.8^\circ \pm 0.6^\circ$ (with uncertainties reported at the 68% confidence level). Notably, the PD exhibited a rise from approximately 6% at 2 keV to 10% at 8 keV, while the polarization direction remained consistent across this energy range within the statistical precision of the measurements (see Figure 4.4). However, it is important to note that the radio jet associated with this source has never been spatially resolved, hindering direct comparison between the polarization angle and the source orientation in the sky plane.

Conversely, during the SPL state observation, *IXPE* measured a PD of $6.8 \pm 0.2\%$ at a PA of $21.3^\circ \pm 0.9^\circ$ (east of North) within the 2–8 keV band, exhibiting a statistical confidence level exceeding 30σ . This SPL state observation recorded a PD approximately 1.5% lower than the HSS PD of $8.32\% \pm 0.17\%$. Figure 4.4 shows the polarization signatures averaged over time during both states across five logarithmic energy bands. Despite the transition to a different state, the PA remains consistent within $< 3\sigma$ during both the HSS and SPL observations. Moreover, the PD maintains an increasing trend with energy, ranging from approximately 5% at 2 keV to 8% at 8 keV. The summary of measured PD and PA in different spectral states is given in Table 4.1.

Spectral state	Polarization degree	Polarization angle	Thermal contribution		Power-law contribution	
	[%]	[deg]	Fit 1	Fit 2	Fit 1	Fit 2
HSS	8.32 ± 0.17	17.8 ± 0.6	0.97		0.03	
SPL Period 1	7.55 ± 0.44	21.7 ± 1.7	0.54	0.83	0.46	0.17
SPL Period 2	6.52 ± 0.24	21.3 ± 1.1	0.08	0.60	0.92	0.40
SPL Total	6.75 ± 0.21	21.3 ± 0.9	–		–	

Table 4.1: Polarization properties during the two *IXPE* observations of 4U 1630-47. The estimated fractions of the thermal and power-law flux contributing to the 2–8 keV energy band, calculated in the spectral analysis described in section 4.3, are also given.

4.3 Spectral analysis

HSS observation

For the HSS observation, we conducted a spectral fit using quasi-simultaneous *NICER* and *NuSTAR* energy spectra. Specifically, we selected data sets from *NICER* corresponding to the periods covered by *NuSTAR* observations. These three observations are denoted as Obs 1, Obs 2, and Obs 3. We performed a spectral analysis of the data using the `xspec` package [v12.13.0c, Arnaud, 1996] and employed the following model:

$$\text{TBABS} * \text{CLOUDY} * (\text{KERRBB} + \text{NTHCOMP}) \quad (4.1)$$

Our spectral model incorporates a thermal accretion-disk emission accounting for relativistic effects (`KERRBB`, Li et al. [2005]), a Comptonized emission component (`NTHCOMP`, Zdziarski et al. [1996], Życki et al. [1999]), an ionized absorber modeled with `CLOUDY` (`CLOUDY`, Ferland et al. [2017]), and cold absorber (`TBABS`, Wilms et al. [2000]), to account for Galactic as well as local absorption. The `CLOUDY` absorption table consistently reproduces absorption lines through a slab with a constant density of 10^{12} cm^{-3} and a turbulence velocity of 500 km s^{-1} , illuminated by the unabsorbed intrinsic best-fit Spectral Energy Distribution (SED) described below. This component was implemented to model the Fe XXV and Fe XXVI absorption lines detected in *NICER* spectra, indicative of the presence of a wind; the model parameters that were left free in the fitting procedure are the slab ionization parameter ξ , its optical depth N_{Heq} and its redshift z . For the `NTHCOMP` model, we assumed seed photons from the multicolored disk black-body emission (`inp_type` parameter = 1) and fixed the temperature to $kT_{\text{bb}} = 1.47$, derived from initial fitting using `DISKBB`.

Additionally, we introduced an empirical `EDGE` model to address instrumental features observed around $\approx 2 - 3 \text{ keV}$ in the *NICER* spectra and approximately at $\approx 10 \text{ keV}$ in the *NuSTAR* spectra. The gold M edge in the *NICER* spectra is a well-known instrumental characteristic. We fixed the edge energy to $E = 2.4 \text{ keV}$, consistent with the value reported by Wang et al. [2021a] in the analysis of MAXI J1820+070 *NICER* spectra. Regarding the origin of the $\approx 10 \text{ keV}$ edge in the *NuSTAR* spectra, it is less well understood but has been observed in other sources (for instance, in the analysis of LMC X-1, see chapter 6 and Podgorný et al. [2023b]). Despite attempts to incorporate a reflection component, a secondary Comptonization component, or an additional ionized absorption into the model, none of these components enhanced the overall fit or improved the residuals in this specific segment of the *NuSTAR* spectrum. Consequently, we opted to model this feature using the empirical `EDGE` model. To

Inclination	Spin	Mass	Accretion rate	Fit goodness
i (deg)	a_s	$M_{\text{bh}} (M_{\odot})$	$M_{\text{dd}} (10^{18} \text{ g s}^{-1})$	χ^2 (2935 dof)
70	0.7	$9.98^{+0.06}_{-0.08}$	3.9 – 4.3	4693
	0.998	$29.8^{+0.02}_{-0.02}$	0.99 – 1.09	3585
85	0.7	$16.1^{+0.01}_{-0.01}$	8.3 – 8.9	3711
	0.998	$59.8^{+0.04}_{-0.02}$	1.02 – 1.12	3563

Table 4.2: Spectral fit results from the HSS observation assuming various fixed values of black hole spin and inclination angles. The analysis employs the KERRBB model, as described in Equation 4.1.

account for potential absolute calibration discrepancies between NICER and *NuSTAR* instruments, allowing for slight differences in the spectral slope and normalization between the instruments, we utilized the MBPO model, following the approach detailed in Krawczynski et al. [2022]. The best-fit parameters for these cross-calibration and instrumental features are shown in Table 4.4.

Due to the inherent degeneracy among the black hole mass, spin, inclination, and distance parameters in the KERRBB model (see sections 1.4.1 and 1.4.5), we constrained the source distance to $D_{\text{bh}} = 11.5$ kpc [Kalemci et al., 2018]. It is important to note that a smaller D_{bh} , such as 4.7 kpc [the lower limit derived by Kalemci et al., 2018] cannot be excluded. However, adopting this smaller distance would lead to a substantially reduced black hole mass and accretion rate. For instance, considering a spin $a_s = 0.97$ and inclination $i = 75^\circ$, the best-fit black hole mass would approximate $M_{\text{bh}} \approx 26M_{\odot}$ and $M_{\text{bh}} \approx 12M_{\odot}$, and the effective accretion rate would correspond to $M_{\text{dd}} \approx 1.8 \times 10^{18} \text{ g s}^{-1}$ and $M_{\text{dd}} \approx 0.3 \times 10^{18} \text{ g s}^{-1}$ for $D_{\text{bh}} = 11.5$ kpc and $D_{\text{bh}} = 4.7$ kpc, respectively. Furthermore, it is worth noting that the best-fit value of the black hole mass is notably influenced by the spin and inclination parameters. Table 4.2 presents the mass and accretion rate results obtained using KERRBB for a fixed distance $D_{\text{bh}} = 11.5$ kpc, considering different combinations of spin and inclination values. The goodness of the fit demonstrates a preference for configurations with extreme values of BH mass, spin, and disk inclination. In fact, the best-fit, resulting in a $\chi^2/\text{dof} = 3563/2937$, is found for BH spin $a_s \gtrsim 0.99$, inclinations $i \approx 85, \text{deg}$, and black hole masses $M_{\text{bh}} \gtrsim 50M_{\odot}$ (see the last line of Table 4.2). It is worth noting that the estimated mass from this analysis significantly surpasses previous estimates by Seifina et al. [2014] (approximately $10M_{\odot}$).

To address the extreme results obtained from the model described in equation 4.1, we made adjustments by replacing KERRBB with the SLIMBH model [Sądowski, 2011]. This alternative model accommodates the vertical structure of the disk via the TLUSTY code [Hubeny and Hubeny, 1998]. It proves particularly important for higher accretion rates and luminosities $L > 0.3, L_{\text{Edd}}$, scenarios where the conventional thin standard accretion disk model falters, necessitating a large hardening factor to achieve a suitable fit to the spectra [Straub et al., 2011]. Consequently, the revised best-fit model employed in our analysis can be expressed as follows:

$$\text{TBABS} * \text{CLOUDY} * (\text{SLIMBH} + \text{NTHCOMP}) \quad (4.2)$$

The goodness of fit for this model yields a $\chi^2/\text{dof} = 3494/2933$, for the best-fit parameters detailed in Table 4.3. The source spectra, folded around the best-fit model,

Comp.	Parameter (unit)	Description	Obs 1	Obs 2	Obs 3
TBabs	N_{H} (10^{22} cm $^{-2}$)	H column density	$7.92^{+0.07}_{-0.02}$	$7.94^{+0.02}_{-0.02}$	$7.85^{+0.02}_{-0.02}$
CLOUDY	$\log \xi$	ionisation	$5.13^{+0.06}_{-0.04}$	$5.01^{+0.09}_{-0.03}$	$4.95^{+0.07}_{-0.04}$
	$\log N_{\text{Heq}}$	H column density	$24.03^{+0.02}_{-0.02}$	$24.03^{+0.03}_{-0.01}$	$24.04^{+0.03}_{-0.02}$
	z	Redshift	$-0.0002^{+0.0001}_{-0.0002}$	$-0.003^{+0.001}_{-0.001}$	$-0.003^{+0.001}_{-0.001}$
SLIMBH	M_{bh} (M_{\odot})	Black hole mass		$18.0^{+0.7}_{-1.2}$	
	a_s	Black hole spin		$0.71^{+0.03}_{-0.14}$	
	L_{Edd}	Luminosity	$0.53^{+0.03}_{-0.03}$	$0.51^{+0.02}_{-0.02}$	$0.49^{+0.02}_{-0.02}$
	i (deg)	Inclination		$85^{+0}_{-1.4}$	
	α	Viscosity		0.1^{\dagger}	
	D_{bh} (kpc)	Distance		11.5^{\dagger}	
	hd	Hardening factor		-1^{\dagger}	
	l_{flag}	Limb-darkening		0^{\dagger}	
	v_{flag}	Self-irradiation		0^{\dagger}	
	norm	normalisation		1^{\dagger}	
	NTHCOMP	Γ	Photon index	$2.6^{+0.2}_{-0.2}$	$3.6^{+0.2}_{-0.2}$
kT_e (keV)		Electron temp.		500^{\dagger}	
kT_{bb} (keV)		Seed photon temp.		1.47^{\dagger}	
norm (10^{-2})		normalisation	$2.6^{+1.1}_{-0.7}$	$6.3^{+1.8}_{-1.7}$	13^{+3}_{-3}
χ^2 / dof			3494/2933		

Table 4.3: Spectral fit parameters to simultaneous NICER and *NuSTAR* observations with the model detailed in equation 4.2. Uncertainties are reported at the 90% c.l.. Parameters indicated with \dagger are kept frozen in the spectral analysis. Note that the maximum allowed inclination value by the SLIMBH model is 85° .

is shown in Figure 4.5. The reduced chi-squared value $\chi_{\text{red}}^2 = \chi^2/\text{dof} \lesssim 1.2$ provides a good fit, given the fact that we have not applied any systematics to the data that would account for uncertainties in instrument calibration between NICER and *NuSTAR* as well as possible spectral variability within the individual exposures since the data acquired by the two missions were not strictly simultaneous (we have restricted the NICER data to be within the *NuSTAR* observations, but we did not do the opposite since the statistics of such restricted *NuSTAR* data would be too low). While variable absorption lines contribute to the chi-square in the joint spectral fits of NICER and *NuSTAR*, we opted not to extensively explore this aspect being outside the main scope of our study. It is essential to note that these lines do not significantly affect the critical continuum parameters in our analysis. The revised fit necessitates a black hole mass of $\sim 18M_{\odot}$ and a black hole spin of $a_s \sim 0.7$, aligning more closely with expectations [Seifina et al., 2014]. Notably, the luminosity measures $L \approx 0.5 L_{\text{Edd}}$, indicating the suitability of the slim disk approximation over the geometrically thin disk model in this context.

Our spectral analysis is consistent with the source being in HSS, as the soft X-ray spectrum results to be dominated by the thermal accretion disk emission. *NuSTAR* data revealed a slight variation in the comptonisation component, as the photon index varies in the range $\Gamma \approx 2.8$ – 4.8 . In the 2–8 keV energy range, the comptonisation component contributes 2–3% and is almost negligible in the soft X-ray band analysis.

Component	Parameter	Description	NICER	<i>NuSTAR</i>	
				FPMA	FPMB
MBPO	$\Delta\Gamma$	Power-Law index	0^\dagger	-0.101 ± 0.008	
	N_{mbpo}	Normalization	1^\dagger	1.16 ± 0.02	
EDGE	E [keV]	Threshold energy	2.4^\dagger	-	
	τ	Optical depth	0.074 ± 0.005	-	
EDGE	E [keV]	Threshold energy	-	9.7 ± 0.1	
	τ	Optical depth	-	0.056 ± 0.006	

Table 4.4: Modeling cross-calibration and instrumental features in the final spectral fit presented in Table 4.3. Uncertainties are stated at the 90% c.l.. Parameters indicated with † are kept frozen in the spectral analysis.

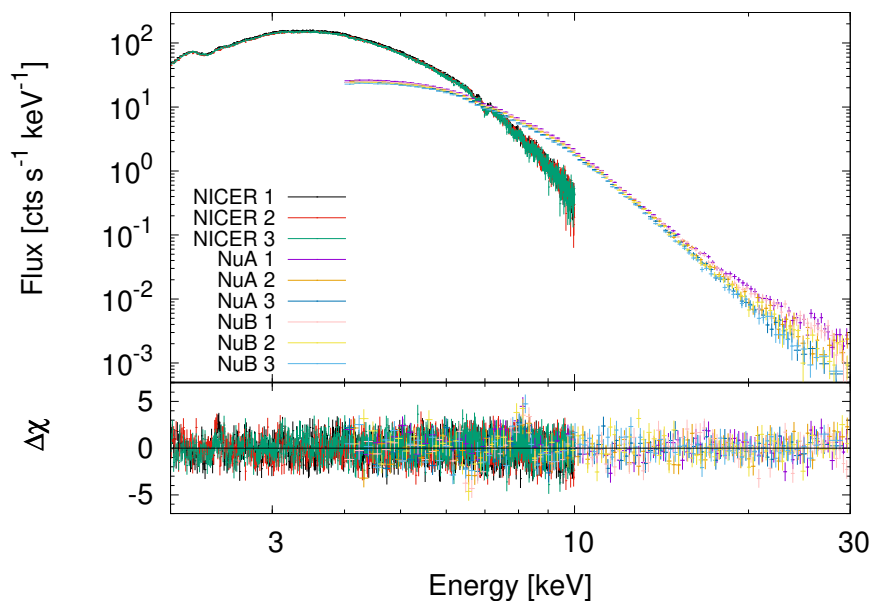


Figure 4.5: Spectral fit of simultaneous HSS data from NICER and *NuSTAR* using the model described in equation 4.2. The upper panel shows the spectra, while the data residuals from the model ($\Delta\chi$ values) are shown in the bottom panel.

SPL state observation

Between the first and the second observation, the source transitioned into a more luminous and harder SPL state, showing an increase in 2 – 50 keV flux and a sizeable change in the spectral shape at energies above 5 keV. To study the variation of the thermal and Comptonized component contributions to the observed spectra, we performed a joint fit on the NICER and *NuSTAR* spectra. Since our aim here is only to give an estimate of the polarization degree and angle of the two spectral components, we performed our analysis on the two instruments time-averaged spectra, subdivided into two groups each, corresponding to Periods 1 and 2 of the SPL state *IXPE* observation (see Figure 4.2). Moreover, to further simplify our approach, we restricted our study to the 2 – 10 keV energy range for NICER data and to the 8 – 70 keV range for *NuSTAR* ones in order to reduce cross-calibration uncertainties between the two instruments. The choice to analyze *NuSTAR* data starting from 8 keV, in particular, is due to the large inconsistencies between the NICER and *NuSTAR* data below this energy, although some cross-calibration residuals can still be observed in the 8 – 9 keV range. We used the *NuSTAR* spectra up to 70 keV since above that the background was comparable to the data. For consistency with the HSS observation, our analysis in `xspec` employed the same model described by Equation 4.1. To maintain consistency, we fixed the source distance in the `KERRBB` model at $D = 11.5$ kpc. moreover, for the sake of simplicity, we maintained the system inclination at a fixed value of $i = 75^\circ$, allowing only the black hole spin, mass, and accretion rate to vary during the fitting procedure.

This analysis confirmed the variation of the source spectral properties. In the HSS observation, several absorption lines, indicative of the presence of an outflowing wind, have been detected in NICER spectra and modeled employing a `cloudy` absorption table. The SPL state observation, instead, shows no prominent absorption lines; while attempting to employ the `cloudy` component with the same ionization parameter as observed in the HSS phase, we found that it led to an upper limit of $N_{\text{H}} \leq 10^{22} \text{ cm}^{-2}$ for the wind column density along the line of sight. Notably, allowing the ionization parameter to freely vary often resulted in fitting to unrealistically high values. Consequently, we omitted this component from the fitting procedure. The disappearance of these prominent blueshifted Fe XXV and Fe XXVI lines has several potential explanations. One possibility lies in the over-ionization of the wind [Díaz Trigo et al., 2014a], causing these lines to disappear. Another hypothesis revolves around intrinsic alterations in the physical properties of the wind itself [Hori et al., 2014] during the SPL state, contributing to the absence of these features in the spectra.

We employed the `NTHCOMP` component considering two different scenarios for the input radiation: a disk black body or a single black body seed. In Fit 1, we assumed multicolor disk blackbody seed radiation (`inp_type` parameter = 1) and fixed its temperature based on the values obtained initially using `DISKBB` ($kT_{\text{bb}} = 1.46_{-0.01}^{+0.02}$; $1.54_{-0.02}^{+0.01}$ keV in Period 1 and 2, respectively). Fit 2 utilized a single blackbody as the input radiation (`inp_type` parameter = 0) and allowed the temperature to vary during the fitting process. The choice of the `NTHCOMP` input radiation influences the flux contributions of both components, as summarized in Table 4.1, consequently impacting the respective polarization properties. This is due to the different low energy contributions of `NTHCOMP` when using a multi-color black body in place of a single black body,

Component	Parameter (unit)	Description	Value Fit 1		Value Fit 2	
			SPL Period 1	SPL Period 2	SPL Period 1	SPL Period 2
TBABS	N_{H} (10^{22} cm $^{-2}$)	Hydrogen column density	$7.84^{+0.02}_{-0.04}$	$7.71^{+0.02}_{-0.02}$	$7.63^{+0.03}_{-0.03}$	$7.78^{+0.02}_{-0.02}$
KERRBB	a_s	Black hole spin	$0.71^{+0.25}_{-0.15}$	-	$0.72^{+0.18}_{-0.21}$	-
	i (deg)	Inclination	75.00^{\dagger}	-	-	-
	M_{bh} (M_{\odot})	Black hole mass	$10.51^{+3.51}_{-2.54}$	-	$9.37^{+2.95}_{-2.14}$	-
	M_{dd} (10^{18} g s $^{-1}$)	Effective mass accretion rate	$6.22^{+0.98}_{-0.33}$	$1.22^{+0.25}_{-0.21}$	$4.91^{+0.61}_{-0.48}$	$6.91^{+0.57}_{-0.61e}$
	D (kpc)	Distance	11.5^{\dagger}	-	-	-
	hd	Hardening factor	1.7^{\dagger}	-	-	-
	r_{flag}	Self-irradiation	Yes	-	-	-
	l_{flag}	Limb-darkening	No	-	-	-
	norm	Normalization	1.0^{\dagger}	-	-	-
NTHCOMP	inp_type	Seed photon shape	Disk blackbody		Blackbody	
	Γ	Photon index	$2.64^{+0.02}_{-0.01}$	$2.94^{+0.01}_{-0.01}$	$2.61^{+0.02}_{-0.02}$	$2.93^{+0.01}_{-0.01}$
	kT_e (keV)	Electron temperature	500.00^{\dagger}	-	-	-
	kT_{bb} (keV)	Seed photon temperature	$1.46^{+0.02}_{-0.01}$	$1.54^{+0.01}_{-0.02}$	$0.91^{+0.24}_{-0.18}$	$1.88^{+0.38}_{-0.36}$
	norm	Normalization	$1.09^{+0.02}_{-0.02}$	$3.68^{+0.01}_{-0.01}$	$0.41^{+0.05}_{-0.05}$	$0.13^{+0.02}_{-0.02}$
EDGE 1	edgeE (keV)	Threshold energy	$2.43^{+0.01}_{-0.01}$	-	-	-
	MaxTau (10^{-2})	Absorption Depth at threshold energy	$6.14^{+0.40}_{-0.41}$	-	-	-
EDGE 2	edgeE (keV)	Threshold energy	$9.49^{+0.05}_{-0.05}$	-	-	-
	MaxTau (10^{-2})	Absorption Depth at threshold energy	$1.88^{+0.21}_{-0.22}$	-	-	-
MBPO	N_{NICER}	Normalization	1.035 ± 0.002	-	-	-
	N_{FPMB}	Normalization	0.994 ± 0.001	-	-	-
	Γ_{NICER}	Power-law index	0.0664 ± 0.0033	-	-	-
	Γ_{FPMB}	Power-law index	0.0095 ± 0.002	-	-	-
$\chi^2/\text{d.o.f}$			2502.68/2399			

Table 4.5: Best-fitting parameters for joint NICER and *NuSTAR* spectral fitting for SPL Period 1 and SPL Period 2. We assume a zero-torque inner boundary condition. Uncertainties are stated at the 90% confidence level.

which influences the KERRBB accretion rate in the fitting procedure and consequently the thermal radiation contribution to the total flux. Figure 4.6 displays the unfolded spectra and data residuals for both fits, with the best-fit parameters outlined in Table 4.5. Notably, while both fits exhibit similar residual trends, in Period 2 (green), the contribution of KERRBB to the total flux in Fit 2 is notably larger than in Fit 1, highlighted by the dashed lines.

Similar to the analysis of the HSS observation, we applied an empirical absorption EDGE model at energies 2.42 keV and 9.51 keV to address instrumental features reported in the NICER and *NuSTAR* spectra, respectively. Additionally, we employed the cross-calibration model MBPO to mitigate cross-calibration uncertainties between NICER and *NuSTAR*. For the *NuSTAR* focal plane module A (FPMA) we fixed the normalization to 1 for all fitting groups, corresponding to the recommended value in Madsen et al. [2022] and kept the slope fixed to zero.

4.4 Polarimetric analysis and theoretical modeling

Next, we integrated the *IXPE* spectra into our fitting process. In the HSS observation, we conducted this analysis using the entire time-averaged *IXPE* dataset, a selection based on the relative stability of the light curve (see to the left panel of Figure 4.2). For the SPL state observation, we partitioned the *IXPE* data into two distinct periods, aligning with the segments discussed in the earlier spectral analysis section.

Our initial focus in this phase centered on an empirical investigation of the polarization properties across both observations. To achieve this, we kept the spectral parameters at the values derived from the spectral analysis, as outlined in Tables 4.2

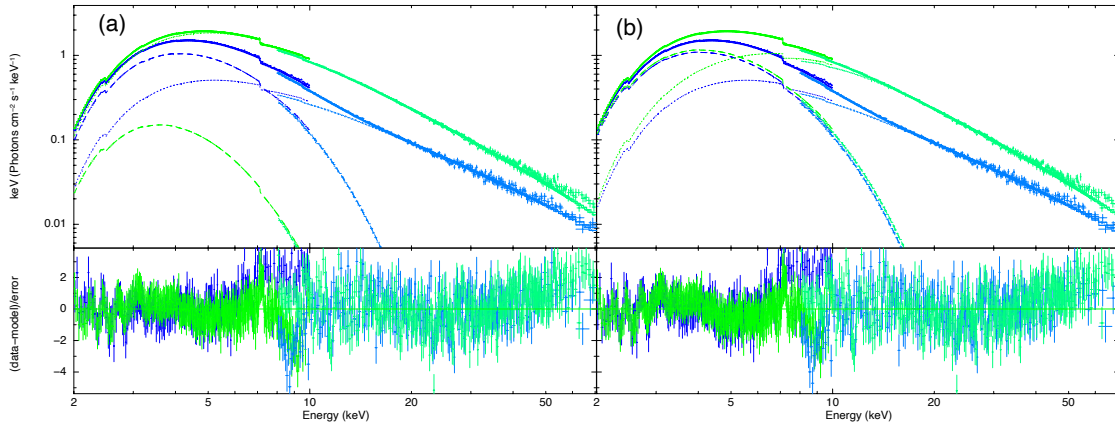


Figure 4.6: Fits of 4U 1630-47 NICER and NuSTAR X-ray spectra for SPL Period 1 (blue) and Period 2 (green): (a) Disk blackbody assumed as seed radiation for the power-law component (Fit 1). (b) Single-temperature black body assumed as seed radiation for the power-law component (Fit 2). Unfolded spectra around the best-fitting model in F_E representation, the total model (solid) and the KERRBB (dashed) and NTHCOMP (dotted) contributions for each data set are shown in the top panels while the data-model residuals in σ are shown in the bottom panels.

and 4.5. We employed a POLLIN component to model the dependence of polarization observables on photon energy E . This convolution model allows for a linear description of both the polarization degree (PD) and position angle (PA), represented as $PD = p_0 + \alpha(E/1, \text{keV})$ and $PA = \phi + \beta(E/1, \text{keV})$. The model has four free parameters: PD and PA slopes (α and β) and the extrapolated PD and PA values at 1 keV (p_0 and ϕ_0). The linear fits of PD and PA are shown in Figure 4.7. We found that, despite the evident spectral differences, the HSS and SPL state observations have a similar linear dependence of the PD on the photon energy. For the HSS, we found $p_0 = 3.47\% \pm 0.54\%$, $\alpha = 1.12\% \pm 0.13\%$ with the null hypothesis probability of 3.55×10^{-16} for a constant function. For the SPL state Period 1 observation, these parameters change to $p_0 = 2.7\% \pm 1.3\%$, $\alpha = 1.08\% \pm 0.32\%$ with the null hypothesis probability of 1.42×10^{-2} for a constant function. For the SPL state Period 2 observation, these parameters are $p_0 = 2.44\% \pm 0.70\%$, $\alpha = 0.88\% \pm 0.16\%$ with the null hypothesis probability of 4.56×10^{-7} for a constant function. Both the HSS and SPL Period 1 and Period 2 observations show relatively energy-independent PA in the *IXPE* band, with the fitted value of PA being $18.0^\circ \pm 0.5^\circ$, $21.4^\circ \pm 1.8^\circ$ and $21.5^\circ \pm 0.9^\circ$ with the null hypothesis probability of 0.607, 0.854 and 0.877, respectively.

4.4.1 Thermal component

We can now focus on modeling the polarization properties of each spectral component. In the HSS observation, in particular, we found that the power-law contribution in the *IXPE* band is almost negligible. Consequently, the substantial polarization degree observed is anticipated to arise primarily from the thermal disk contribution.

Predictions from the standard thin disk model suggest that the observed $\sim 8\%$

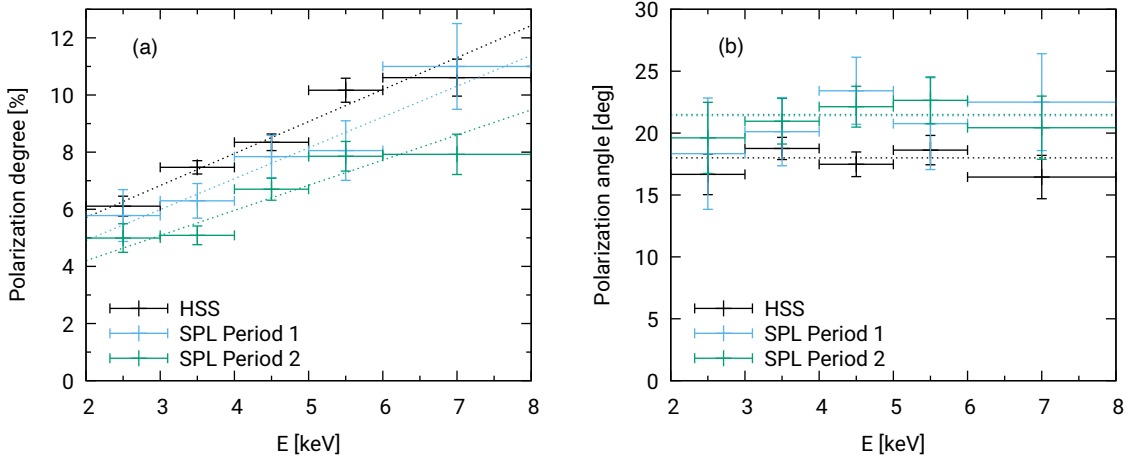


Figure 4.7: (a) PD and (b) PA as a function of energy in the *IXPE* 2 – 8 keV energy range. Comparison of the 4U 1630-47 polarization properties in the HSS (black) and the SPL Period 1 (blue) and Period 2 (green). Linear fits for PD and constant fit for PA are shown in dotted lines.

polarization degree in the HSS state could be achieved, but only under the assumption of a system viewed at a notably high inclination angle. In the classical, pure electron-scattering model [Chandrasekhar, 1960, Sobolev, 1963], the polarization degree observed could be attained for binary inclinations $\gtrsim 85^\circ$, as depicted in Figure 4.8. Such high inclinations would render the X-ray source obscured by the outer segments of the accretion disk, an aspect further supported by an observed opening angle of $\sim 12^\circ$ in the outer disk regions de Jong et al. [1996]. Furthermore, for sources at inclination $> 80^\circ$ complete eclipses are expected, but no such occurrences have been detected in this source. A lower inclination scenario becomes plausible by considering partial ionization within the disk medium, incorporating absorption phenomena within the disk atmosphere. As discussed in Chapter 3, absorption processes can produce an increase in the emerging radiation polarization degree. In this way, the lower limit on the inclination of the system, required by the high polarization degree, becomes compatible with the maximum inclination expected for the X-ray binaries $i_{\max} \sim 78^\circ$ [de Jong et al., 1996].

While scattering within a fully ionized atmosphere results in an achromatic polarization degree, absorption processes introduce an energy dependency [Taverna et al., 2021]. In our earlier discussion in Section 3.2, we delved into the computations within a highly ionized regime, revealing that radiative transfer in a slab structure can yield an increasing polarization degree corresponding to the energy of the emerging radiation. This phenomenon likely arises due to Compton down-scattering occurring in correspondence to the steep decrease of the incident black body spectrum. It is however important to note that despite the capability of these computations results in a rising polarization degree across the *IXPE* energy band, they predict a plateau in polarization degree between 0.2 and 2 keV for $\tau \lesssim 10$, consistent with pure-scattering outcomes because of the lack of significant absorption processes in this band due to the ionization of light elements. Consequently, the observed 6% polarization degree at 2 keV robustly constrains the inclination of the emitting patches to be equal or exceed

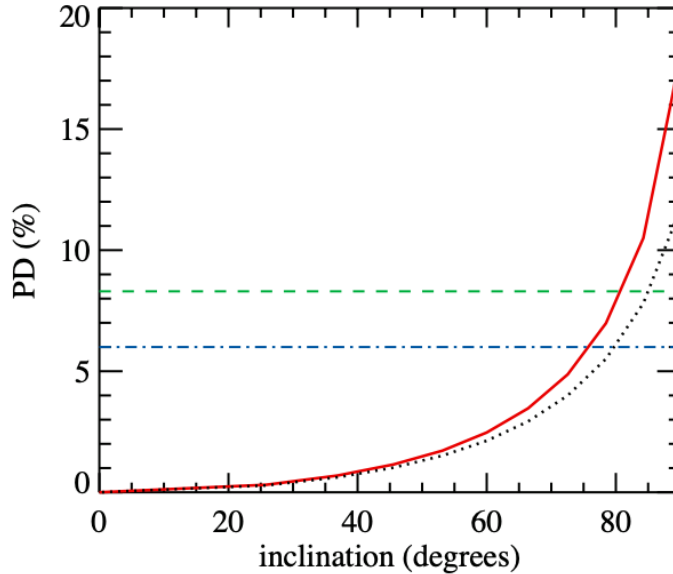


Figure 4.8: Comparison of polarization degrees across various inclinations: the pure electron-scattering atmosphere (black dotted line) versus the scenario with partial ionization of matter (including absorption effects) and distributed sources (red solid line). Additionally, the green dashed line represents the average polarization within the *IXPE* band, while the blue dot-dashed line denotes the polarization at approximately 2 keV.

80° (see Figure 4.8).

Model to data comparison

We now compare our model predictions with the observed spectro-polarimetric data, exploring potential solutions to increase the observed PD of the thermal component. Given the relatively low ($\sim 3\%$) flux contribution attributed to the power-law component in the spectral analysis of the HSS observation, we opt to exclude the `NTHCOMP` component from the analysis (see Equation 4.2), and assume that the only contribution to the polarimetric data is given by the thermal disk emission. Consequently, for the sake of simplicity, we do not incorporate the *NuSTAR* data, concentrating exclusively on *NICER* spectra and the Q and U spectra derived from *IXPE*.

For this analysis, we use the Novikov-Thorne geometrically thin disk model `KYNBBRR` [Dovčiak et al., 2008, Taverna et al., 2021, Mikušincová et al., 2023] instead of `KERRBB` and `SLIMBH`. As described in chapter 3, `KYNBBRR` is similar to `KERRBB`, but allows us to study also the polarization properties of this component in different scenarios. The other model components are the same as already described in the spectral analysis section; thus the model implemented for the fitting procedure is as follows:

$$\text{TBABS} \times \text{CLOUDY}(\text{KYNBBRR}). \quad (4.3)$$

Given that certain system properties such as inclination, distance, BH mass, and spin are indirectly estimated rather than directly measured, we examine the polarization properties of our models across a spectrum of high inclination values and BH spin possibilities. Subsequently, we fit the other parameters influencing the spectral shape

Incl.	Spin	Mass	Accretion rate	Normalization	Fit goodness
i (deg)	a_s	$M_{\text{bh}} (M_{\odot})$	$\dot{M}/\dot{M}_{\text{Edd}}$	norm	χ^2 (792 dof)
70	0	3^{\dagger}	0.451 ± 0.003	2.13 ± 0.02 ^(a)	730
	0.998	23.59 ± 0.10	0.1221 ± 0.0003	0.75614^{\dagger}	638
75	0	3^{\dagger}	0.424 ± 0.003	3.02 ± 0.03 ^(b)	719
	0.5	3.59 ± 0.02	0.1992 ± 0.0005	4.93827^{\dagger}	732
	0.7	3.80 ± 0.02	0.1759 ± 0.0005	4.93827^{\dagger}	719
	0.9	15.57 ± 0.07	0.2402 ± 0.0006	0.75614^{\dagger}	670
	0.998	29.5 ± 0.1	0.1005 ± 0.0002	0.75614^{\dagger}	632
85	0	3^{\dagger}	0.6336 ± 0.0005	4.93827^{\dagger}	728
	0.998	48.7 ± 0.2	0.0724 ± 0.0002	0.75614^{\dagger}	629

Table 4.6: The comparison of spectral fit results for different fixed values of system inclination and black hole spin with the model described by equation 4.3. If not noted otherwise, a source distance of 11.5 kpc is assumed, which corresponds to a KYNBBRR normalization of 0.76. In case the fitted BH mass hits the lower limit of $3M_{\odot}$, we assumed a distance of 4.5 kpc corresponding to a KYNBBRR normalization of 0.49. If, after this modification, the fitted BH mass once again hits the lower limit of $3M_{\odot}$, we fix it to this value and fit the normalization. This happened in two cases, with the fitted values of the normalization corresponding to a distance of 6.85 kpc^(a) and 5.75 kpc^(b).

based on observed spectra. Only then we fit the polarization properties using the observed energy dependence of the polarization degree and angle. This process aids in evaluating the model capacity to explain these observations and potentially offers insights into constraints concerning spin and/or inclination. In the current spectral analysis, a 1% systematic error is applied to the *NICER* data. The outcomes of the best spectral fits are summarized in Table 4.6.

In the next step, we freeze all the parameters influencing the spectral shape and solely focus on fitting the observed polarization degree and angle from *IXPE* data. In this endeavor, we introduce different variations of the KYNBBRR model:

- **Model (A):** the original model, which assumes Chandrasekhar approximation of pure scattering atmosphere for direct radiation and Chandrasekhar’s diffuse reflection formulae for the returning radiation contribution. In the fit, we assumed an albedo of 0.5 and left the orientation of the system on the observer’s sky as the only free parameter.
- **Model (B):** A possible way to increase the local polarization degree is to assume a larger emission angle in the local reference frame co-moving with the accretion disk. Due to the relativistic aberration effect, this could happen in case of an outflowing atmosphere having relativistic speeds in the vertical direction, i.e. perpendicular to the disk. In this second flavor, we assume a decreasing radial profile of the vertical outflow velocity, i.e. $\beta(r) = \beta_0 r^{-q}$ with β being the speed in units of speed of light in the vacuum. This model then has two new parameters, β_0 and q , that influence the predicted polarization properties.

Incl.	Spin	model (A)	model (B)	model (C)	model (D)
i (deg)	a_s	$\chi^2(\text{PD}/\text{PA}/\text{tot})$	$\chi^2(\text{PD}/\text{PA}/\text{tot})$	$\chi^2(\text{PD}/\text{PA}/\text{tot})$	$\chi^2(\text{PD}/\text{PA}/\text{tot})$
70	0	1573/8.9/1581	33/8.0/40	626/7.7/634	11.5/7.9/19.4
	0.998	2236/280/2517	84/80/164	1551/66/1617	12.2/57/69
75	0	1132/7.8/1140	35/7.8/43	387/7.7/395	11.8/7.8/19.6
	0.5	1529/13/1542	37/8.8/45	506/8.3/514	12.2/8.3/20.5
	0.7	1722/21/1743	37/10/47	606/9.8/616	12.5/9.3/21.8
	0.9	2077/53/2130	41/15/56	828/15/843	12.7/12.9/25.7
	0.998	2162/258/2420	65/56/121	1309/48/1357	12.1/41/53
85	0	658/7.8/666	55/7.7/63	42/7.9/50	13.3/7.9/21.2
	0.998	2098/187/2285	30/21/51	765/21/786	12.9/18.6/31.54

Table 4.7: Comparison of the goodness of PD and PA fits using different flavors of the KYNBBRR model. Note that both the PD and PA were binned in 11 energy bins; the dof for each model are equal to 21, 19, 20 and 17, respectively. The fits with $\chi_{\text{tot}}^2 < 22$ are denoted in bold and the best-fit parameter values of these cases are shown in Table 4.8.

Incl.	Spin	orientation	speed norm	speed index	speed
i (deg)	a_s	χ_o	β_0	q	$\beta(T_{\text{max}})$
70	0	-70.7 ± 0.5	0.65 ± 0.14	0.54 ± 0.19	0.50
75	0	-71.2 ± 0.5	0.56 ± 0.18	0.72 ± 0.29	0.40
	0.5	-70.1 ± 0.5	0.65 ± 0.18	0.73 ± 0.26	0.47
	0.7	-68.9 ± 0.5	0.71 ± 0.17	0.70 ± 0.23	0.53
85	0	-72.5 ± 0.5	0.6 [†]	2.1 ± 0.2	0.22

Table 4.8: The best-fit parameters of the KYNBBRR model (D), which assumes that the disk emission is reprocessed within an outflowing ionized layer. Since the optical thickness of the layer and its outflow speed were degenerate, we eventually kept the optical thickness frozen to $\tau = 7$. We characterize the outflow speed by its value at the radius where the disk temperature peaks, $\beta(T_{\text{max}})$, shown in the last column.

- **Model (C):** In this third flavor the model incorporates outcomes from radiative transfer computations within a partially ionized atmosphere, as detailed in section 3.2. Specifically, it assumes an ionized passive slab with finite optical depth and constant density. The local emission properties are computed using the TITAN and STOKES codes. Here, the local polarization degree relies on the disk temperature (following the Novikov-Thorne temperature profile), emission angle (calculated via ray-tracing in the curved space-time for a specific observer inclination), and the optical thickness of this layer.
- **Model (D):** This final variant combines the effects illustrated in Models (B) and (C). It assumes a partially ionized atmosphere with an outflow velocity perpendicular to the disk plane, blending the characteristics described in the former models.

The χ^2 fit results with these four models are reported in Table 4.7, while a com-

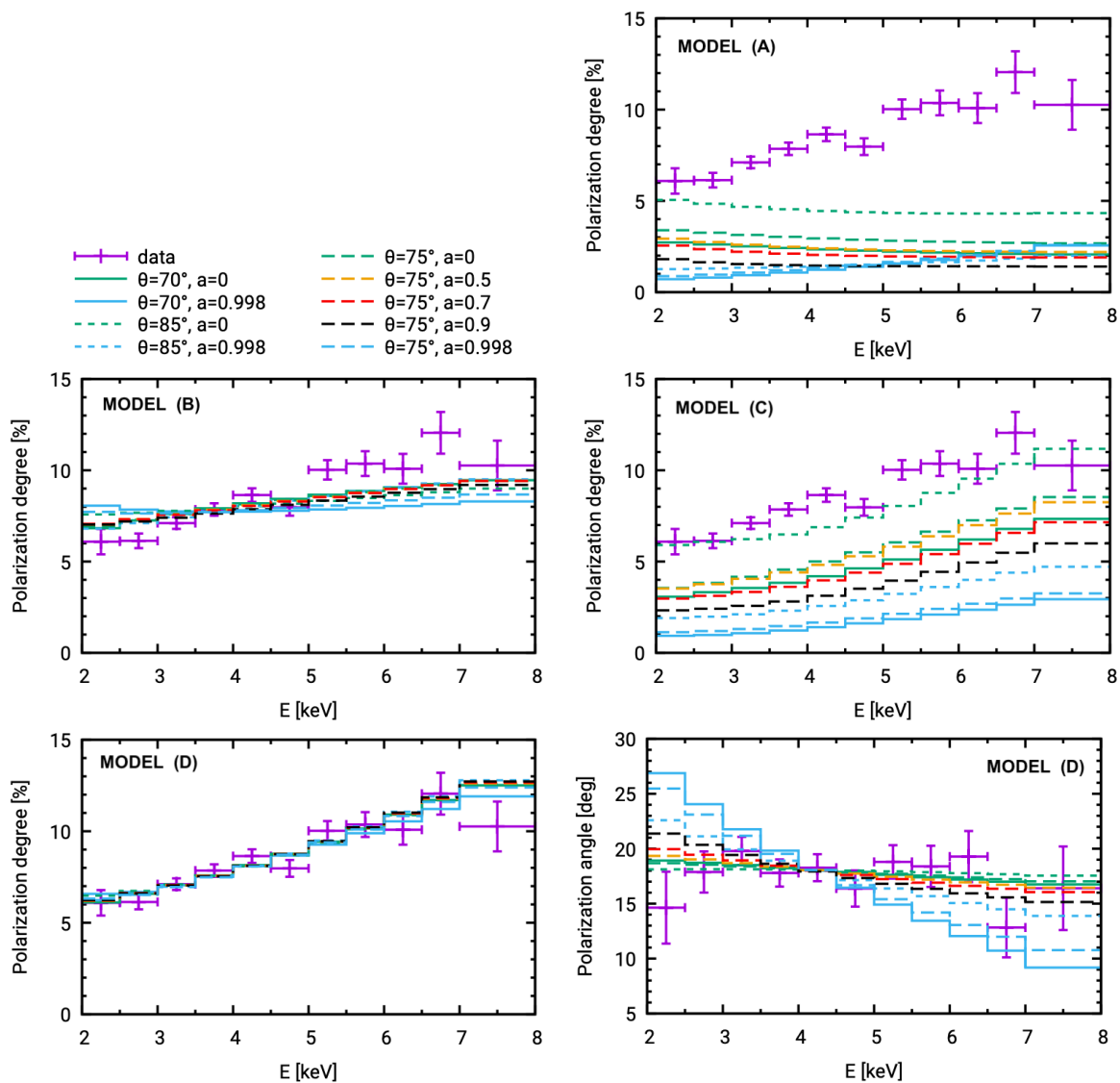


Figure 4.9: Comparison of the observed 4U 1630-47 polarization properties (purple points with 68% confidence level error bars) with the prediction of the different flavors of the KYNBBRR model, as detailed in the text. Different lines indicate different values for the BH spin and the disk inclination. The best-fit model (Model (D)) polarization degree and angle are shown in the bottom two panels; the model assumes a large optical thickness of the disk atmosphere (~ 7), and a significant outflow velocity ($v \sim 0.5c$)

parison of the observed polarization properties of the source in HSS with the models prediction is shown in Figure 4.9. Only for Model (D) we can find an acceptable fit, for the parameters presented in Table 4.8. We found that the predicted polarization degree of Model (A) is generally too low, even considering extreme spin and inclination configurations. In Model (B) we reach the high PD values observed, but the model fails to fit the PD increase with energy. On the other hand, Model (C) explains the observed PD increase with energy, but the magnitude of the polarization degree is too low. Finally, Model (D) can fit the polarimetric data quite well, for the best-fit parameters shown in Table 4.8; it is important to note that to achieve the observed polarization degree the scattering layer has to be outflowing with approximately half of the speed of light, and a significant optical depth is found for the scattering layer (~ 7). Moreover, the PA energy dependence predicted with the different flavors of KYNBBRR is very similar since the local polarization angle is always assumed to be parallel to the disk. The predicted PA is thus dependent mainly on the relativistic effects, and the comparison with the data generally disfavor the largest possible values of the BH spin (see bottom right panel of Figure 4.9).

Up to now, we have investigated possibilities of how to increase the polarization degree of the direct component emitted from the accretion disk. Another way to increase the total PD of the thermal component would be by increasing the contribution of returning radiation, which would naturally explain the observed PD increase with energy (see section 2.3.3 and chapter 5). However, the observed PD appears too high to be solely explained by returning radiation within the standard thin disk framework. For a rough estimate of how much self-irradiation would be needed to describe the data, we conducted an exploratory nonphysical fitting exercise, allowing the *albedo* (i.e. the ratio of reflected radiation to incident radiation) to exceed unity. Assuming an inclination of 75° and integrating the radiative transfer calculations within the disk atmosphere discussed earlier, the fitted albedo values were 4.5, 11.4, 17.1, 22.2, and 36.2 for spin values of 0.998, 0.9, 0.7, 0.5, and 0, respectively. This investigation reaffirms that within the standard disk scenario, explaining the observed polarimetric data without introducing substantial outflow velocities remains challenging.

4.4.2 Comptonized component

The HSS observation revealed remarkable polarization properties attributed to the accretion disk emission. On the other hand, the SPL state observation of 4U 1630-47 provided the opportunity to delve into the polarization characteristics of the comptonized component. Comparing the polarization properties between these two spectral states highlighted striking similarities, apart from a consistent $\sim 2\%$ decrease in the polarization degree across the entire *IXPE* energy range.

Given these similarities, and considering the substantial flux contribution from the power-law component in the SPL state observation, we hypothesized that its polarization signature would resemble that described in the preceding section for the thermal emission. To explore this hypothesis, we performed a polarimetric fit of the data starting from the spectral analysis described in section 4.3. Here, we incorporated all *IXPE* spectra into the analysis, maintaining spectral parameters fixed to the values as detailed in Table 4.5. The only exceptions were the MBPO model parameters, allowed to

Detector	Parameter (unit)	Description	Value Fit 1		Value Fit 2	
			SPL Period 1	SPL Period 2	SPL Period 1	SPL Period 2
1	N	Normalization	0.736 ± 0.005	0.720 ± 0.004	0.844 ± 0.012	0.834 ± 0.008
	E_{br} (keV)	Energy breaking point	4.4 ± 0.4	5.5 ± 0.3	4.2 ± 0.4	5.5 ± 0.2
	Γ_1	Power-law index	0.12 ± 0.03	0.013 ± 0.011	0.13 ± 0.04	0.03 ± 0.02
	Γ_2	Power-law index	-0.27 ± 0.11	0.59 ± 0.15	-0.23 ± 0.09	-0.59 ± 0.14
2	N	Normalization	0.704 ± 0.005	0.718 ± 0.003	0.81 ± 0.01	0.83 ± 0.01
	E_{br} (keV)	Energy breaking point	4.8 ± 0.5	4.6 ± 0.2	4.7 ± 0.4	4.7 ± 0.2
	Γ_1	Power-law index	0.07 ± 0.03	0.08 ± 0.02	0.08 ± 0.03	0.09 ± 0.02
	Γ_2	Power-law index	-0.4 ± 0.2	-0.42 ± 0.06	-0.35 ± 0.16	-0.43 ± 0.07
3	N	Normalization	0.679 ± 0.005	0.684 ± 0.003	0.778 ± 0.008	0.791 ± 0.008
	E_{br} (keV)	Energy breaking point	5.5 ± 0.3	5.0 ± 0.3	5.6 ± 0.4	5.1 ± 0.2
	Γ_1	Power-law index	0.10 ± 0.02	0.08 ± 0.02	0.10 ± 0.03	0.09 ± 0.02
	Γ_2	Power-law index	-0.77 ± 0.31	0.46 ± 0.10	-0.73 ± 0.31	-0.48 ± 0.09
$\chi^2/\text{d.o.f.}$			3693.9/3293		3693.3/3293	

Table 4.9: Best-fitting MBPO cross-calibration parameters for IXPE spectra corresponding to SPL Periods 1 and 2 for both disk blackbody (Fit 1) and blackbody (Fit 2) seed photons. Uncertainties are stated at the 90% confidence level.

vary independently for each of the three *IXPE* detector units. The best-fit parameters for both periods and utilizing both models are tabulated in Table 4.9.

Starting from model 4.1, we convolved the thermal and power-law spectral components with two POLLIN models. This allowed us to attribute polarization to each component separately assuming that the PD depends linearly on the photon energy E : $\text{PD} = p_0 + \alpha(E/1 \text{ keV})$. We assumed that the polarization of this thermal component remains constant between the HSS and SPL states requiring that $p_{0\text{Thermal}} = 3.47\%$ and $\alpha_{\text{Thermal}} = 1.12\%$ as per the HSS fit shown in Figure 4.7. Due to the relatively constant PA during the HSS, SPL Period 1, and SPL Period 2 observations (Figure 4.7), we further assumed that the thermal and non-thermal components have the same PA and allowed it to vary between SPL periods. Additionally, the PA appears to be energy-independent so our fits take the PA to be constant with energy: $\text{PA} = \psi$. The estimated flux contribution of the power-law component depends on the chosen model parameters, impacting the inferred polarization properties of this component, as illustrated in Table 4.1.

Figure 4.10 presents a summary of our linear fits depicting the non-thermal component PD from Fits 1 and 2, alongside the assumed thermal component PD for reference. For Fit 1, we assumed a multi-color black body as the Comptonized component input radiation (Figure 4.6a). For the PD of the power-law component, we found that $\alpha_{\text{Fit1}} = 1.05\% \pm 0.45\%$ and we set an upper limit on $p_{0\text{Fit1}}$ of 2.7%. The computed PAs for Period 1 and Period 2 are $\psi_{\text{Fit1-P1}} = 21^\circ.0 \pm 3^\circ.4$ and $\psi_{\text{Fit1-P2}} = 21^\circ.7 \pm 2^\circ.2$. For Fit 2 (Figure 4.6b), we assume a simple black body as a seed for the power-law radiation. In this case, the thermal emission is the main source of flux in the 2 – 8 keV energy range for both Periods 1 and 2. The PD of the power-law component can be fitted with $\alpha_{\text{Fit2}} = 0.96\% \pm 0.26\%$ and we were only able to set an upper limit on $p_{0\text{Fit2}}$ of 1.3%. The corresponding PAs for Period 1 and Period 2 are $\psi_{\text{Fit2-P1}} = 21^\circ.0 \pm 3^\circ.5$ and $\psi_{\text{Fit2-P2}} = 21^\circ.7 \pm 2^\circ.1$. We also calculated the 2 – 8 keV average PD of the power-law component from the *IXPE* I , Q , and U fluxes. For Fit 1, we get $7.0\% \pm 3.2\%$ and $6.8\% \pm 2.6\%$ in Periods 1 and 2, respectively. For Fit 2, we get $6.8\% \pm 3.9\%$ and $7.0\% \pm 2.2\%$ in Periods 1 and 2, respectively.

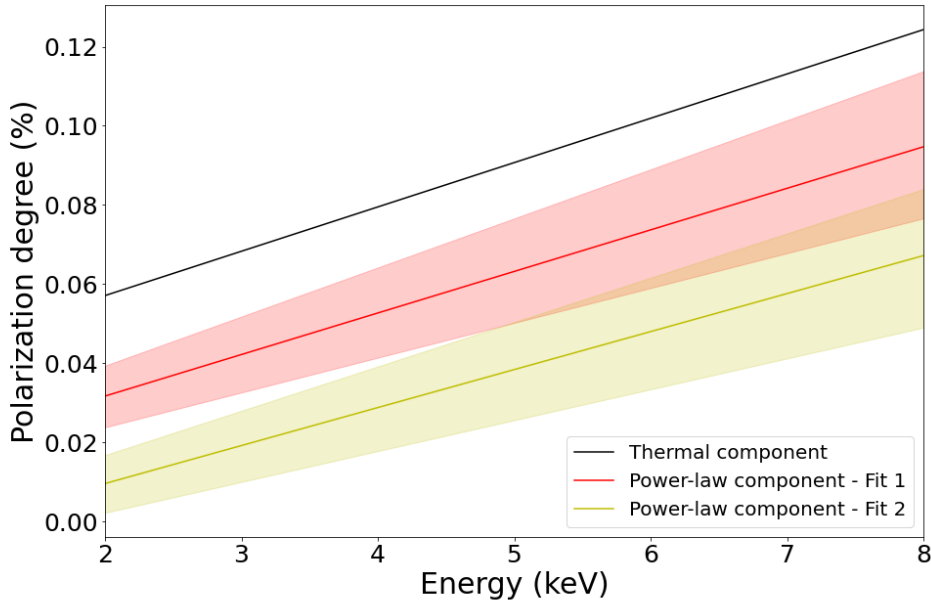


Figure 4.10: Best linear fits with respect to the energy of thermal component (black), power-law component for Fit 1 (red), and power-law component for Fit 2 (yellow). The shaded regions show the 1σ confidence intervals.

4.5 Discussion

The two *IXPE* observations of 4U 1630-47 found the source emission to have a particularly large polarization degree; the interpretation of these results is still far from being completely convincing, and our study suggests that they can be explained in the framework of the standard thin disk model only with significant modifications.

Our spectral analysis revealed that during the first observation, the source was found in a clear soft state, with the spectrum being dominated by the thermal disk emission despite a small contribution ($\sim 3\%$ in the 2 – 8 keV band) of a power-law component. Moreover, prominent absorption lines were detected in *NICER* spectra, and attributed to the presence of an outflowing wind. We found that the source spectra favor configurations with large spin and inclination; furthermore, we obtained better-fit results by implementing a thin disk model (SLIMBH) in place of a standard thin disk model (KERRBB). We thus assumed the disk emission to be responsible for the high and energy-dependent PD of 4U 1630-47, increasing from 6% at 2 keV to 10% at 8 keV. Detailed modeling of this emission revealed that the standard thin disk model cannot explain this large PD, barring extreme configuration with highly inclined disks, which would be in contrast with the source timing properties. Considering scattering from free and bound electrons in a partially-ionized plasma increases the predicted PD in the disk rest-frame from the pure electron scattering case, and also in principle enables an increase of PD with energy (see Chapter 3). However, also these proved to not be enough when accounting for relativistic effects, which generally provoke a net depolarization of the observed radiation (see section 2.3.3).

When considering relativistic vertical motion within an outflowing disk atmosphere, our model showed considerable changes in relativistic corrections. Predictions indicated higher PD owing to the photons reaching observers being emitted at larger inclination angles, a result of relativistic beaming effects. Modeling the partially ionized slab model with this extra effect allowed us to describe the observed PD and PA. Our findings suggested a scenario with a low black hole spin ($a_s \lesssim 0.5$) coupled with a highly-ionized atmosphere exhibiting a substantial optical depth ($\tau \sim 7$), outflowing perpendicular to the accretion disk at a velocity of $v \sim 0.5c$. The imprinted absorption lines in the spectrum, displaying a blue shift velocity of $v \sim 0.003 c$, likely originate from an equatorial wind positioned farther from the disk compared to the rapidly outflowing atmosphere. This material might represent an initial rapid and dense outflow at the disk surface, gradually dispersing and decelerating at larger distances—a characteristic reminiscent of Magneto-Hydrodynamic (MHD) winds [Blandford and Payne, 1982, Contopoulos, 1994, Fukumura et al., 2010] previously proposed to explicate the blue-shifted absorption lines in this source [Fukumura et al., 2021].

Additionally, we explored modeling the polarization signature of the thermal component by considering geometrically thicker disks like the slim disk [Abramowicz et al., 1988] or the puffy disk [Wielgus et al., 2022]. Although these models predict larger and energy-increasing PDs, even after meticulous fine-tuning of parameters (BH spin, observer inclination, disk thickness), they fell short of fully replicating the observed PD.

The second *IXPE* observation of 4U 1630-47 provided unexpected results as well. The source was found in a SPL state and was observed during a transitional phase characterized by a flux increase and the hardening of the spectra. Despite their very different energy spectra, we found that the HSS and SPL exhibit surprisingly similar polarization properties, with the SPL state PD increasing from 5% to 8% between 2 to 8 keV. The change in PA between the two observations, $\sim 3^\circ$, is not statistically significant ($< 3\sigma$).

The unexpectedly large PD observed also in this second observation, where wind signatures were not detected, ruled out the hypothesis that the large PD in the HSS was due to the radiation interaction with the wind. This assumption was further rebutted by other studies demonstrating that reflection off a highly ionized wind via Thomson scatterings leads to relatively constant PD [Ratheesh et al., 2021, Veledina et al., 2023b], contrary to what was observed. Additionally, for reflected flux to contribute significantly to the total spectrum, the wind solid angle on the X-ray source must be larger. If the reflection occurred off a distant wind rather than the inner part of the accretion disk, it should generate emission lines; however, such signatures were absent in the NICER and *NuSTAR* energy spectra.

While the HSS spectrum was dominated by the thermal component, the componentization component increased by a large factor between the HSS, SPL Period 1, and Period 2, although its exact flux contribution is model-dependent. Since the polarization angle stays almost the same with vastly different flux contributions of the power-law component, this component has to be polarized in a similar direction as the thermal component. Our polarimetric analysis reveals that the power-law component has an energy-integrated PD of 6.8 – 7.0% in both cases analyzed, i.e. using either multicolor disk black body or single temperature black body as seed photons for

Comptonization. Since both cases suggest substantially different contributions of this component to the total flux, we consider this estimate to be quite independent of the model assumptions. Note that the dominating thermal component in HSS had a PD of 8.3%, thus the Comptonized component is slightly less polarized than the thermal one by approximately $1.3 - -1.5\%$.

This similarity of the PD and directions is puzzling if the emission comes from spatially distinct regions and is produced by different physical emission mechanisms. The direct thermal emission generally aligns its polarization parallel to the accretion disk, except near the innermost stable circular orbit (ISCO), where gravitational effects rotate the polarization angle by around 10° [Connors and Stark, 1977]. In contrast, returning radiation photons exhibit polarization perpendicular to the direct thermal radiation [Schnittman and Krolik, 2009]. Commonly invoked to explain the power-law component, Comptonization yields polarization perpendicular to the spatial extent of the Comptonizing plasma [Poutanen and Svensson, 1996, Schnittman and Krolik, 2010, Krawczynski and Beheshtipour, 2022]. The alignment of polarization directions between the thermal and power-law emissions could imply an extended Comptonizing plasma perpendicular to the accretion disk, a departure from previous inferences for the hard state of Cyg X-1 [Krawczynski et al., 2022]. However, it is worth noting that for a slab corona geometry, polarization is parallel to the disk at photon energies where the first Compton scattering dominates the flux [Poutanen et al., 2023].

The *IXPE* findings hint at a fascinating parallel between the soft state and the SPL state, suggesting similar disk geometries and emission processes underlying both observations. In the HSS, the observed high PD emerges from an outflowing, partially-ionized accretion disk atmosphere due to Thomson scattering. During transitions between soft and hard states, spectral fittings often indicate Comptonization from low-temperature thermal or hybrid electrons, typically around ~ 10 keV [Gierliński et al., 1999, Zdziarski et al., 2001, Życki et al., 2001]. If electron heating and acceleration mechanisms, like shocks or magnetic re-connection, do not operate efficiently, the electrons within the outflow attain Compton temperatures of a few keV. However, a sudden increase in electron heating and acceleration might shift the effect of scattering on photon energies. Initially, the scatterings tend to be predominantly elastic, maintaining roughly constant photon energies. Yet, a transition to inverse Compton scatterings could occur, causing photon energy gains in the plasma frame. Increased electron temperatures generally lead to reduced PD, as observed in simulations (e.g., Figure 2.8 or Figure 2 of Poutanen [1994]). Nonetheless, for these relatively low electron temperatures, the impact is relatively modest, and the resulting polarization signatures remain similar, albeit not identical, to those under Thomson scattering conditions. The fluctuations in PD observed during the HSS and SPL states might originate from alterations in the scattered fraction and/or the velocities within the outflows.

Chapter 5

4U 1957+115

5.1 Introduction

Low-mass X-ray binaries (LMXBs) typically display strong variability in their X-ray emission. A notable exception to this behavior is represented by 4U 1957+115. Discovered in 1973 by the *Uhuru* satellite, during its scan of the Aquila region [Giacconi et al., 1974], the source is exceptional for being one of a few historically persistently active BH candidates. This short list also includes LMC X-1, LMC X-3, Cyg X-1, and Cyg X-3, which are, unlike 4U 1957+115, classified as high-mass X-ray binary systems [Orosz et al., 2009, 2014, Miller-Jones et al., 2021, see also Chapters 6 and 7]. In line with the first two of those sources, 4U 1957+115 always exhibits a soft X-ray spectral state [e.g., Yaqoob et al., 1993, Ricci et al., 1995, Nowak and Wilms, 1999, Nowak et al., 2008, 2012, Maitra et al., 2014, Sharma et al., 2021, Barillier et al., 2023]. Furthermore, the source has never shown any observable radio jet [Russell et al., 2011b], which aligns with the source’s persistent soft state behavior. Remarkably, the absence of any radio hot spot detection has led to the establishment of the most rigorous upper limits on the radio-to-X-ray flux ratio for a BH in soft state [Maccarone et al., 2020].

Unfortunately, limited information is available regarding the system’s mass, distance, and inclination; this is due to its persistent nature, which hampers optical measurements of binary parameters which are best done during quiescence. Optical emission is likely dominated by the accretion disk [Hakala et al., 2014], but optical observations by Thorstensen [1987] revealed a nearly sinusoidal orbital variation with a period of 9.329 ± 0.011 hr and $\pm 20\%$ orbital modulation. Several lines of argument have attributed this phenomenon to the irradiation of the companion star’s surface [Margon et al., 1978] by the accretion disk of the compact object [Bayless et al., 2011, Mason et al., 2012, Gomez et al., 2015]. This suggests that, from the perspective of the primary, the secondary star occupies a substantial solid angle, which implies a relatively small separation and thus a relatively low total mass for the binary system. This is consistent with the primary being either a neutron star [Bayless et al., 2011] or a low mass BH [$M < 6.2 M_{\odot}$, Gomez et al., 2015]; both possibilities are also allowed by the $\approx 0.25 - -0.3$ mass ratio derived by Longa-Peña [2015] through Bowen fluorescence line studies. Although no study of the nature of the compact object has been conclusive, the lack of Type I bursts, pulsations, ‘surface emission’ components or signatures of a boundary layer emission in the X-ray spectra of the source disfavour the neutron star

hypothesis [Maccarone et al., 2020].

According to interstellar medium absorption modelling along the line of sight, the source is believed to be located outside the Galactic plane, at a minimum distance of approximately 5 kpc [Nowak et al., 2008, Yao et al., 2008]. In a recent study by Barillier et al. [2023], which analysed the parallax and proper motion data from the Gaia EDR3 catalogue [Gaia Collaboration et al., 2021], and assuming that 4U 1957+115 is located in the Galactic halo, the distance probability distribution was found to peak at 6 kpc. However, the study revealed a substantial cumulative probability (17%) in the range of 15 to 30 kpc. From this, and from *NuSTAR* data analysis, they derive a mass probability distribution for the source, 50% of which corresponds to $M < 7.2M_{\odot}$. Notably, a significant portion of the mass probability distribution (22%) is found to lie within the ‘mass gap’ of $2 - 5 M_{\odot}$, which is known to contain only a limited number of sources [Özel et al., 2010, Farr et al., 2011, Gomez et al., 2015].

The absence of eclipses and any orbital modulations in the X-ray light curve [Wijnands et al., 2002] allowed for the estimate of an upper limit between 65° and $\approx 75^{\circ}$ for the source inclination, which is consistent with the model of optical variability [Hakala et al., 1999]. Furthermore, this inclination range is also in agreement with the absence of a highly ionised wind [Ponti et al., 2012, Parra et al., 2023]. On the other hand, X-ray spectral fitting analyses tend to predict large values for the system’s inclination, such as $\sim 78^{\circ}$ [Maitra et al., 2014]. Conversely, several optical modulation studies favour systems with lower inclinations [e.g. $\sim 13^{\circ}$, Gomez et al., 2015].

As a soft-state source, 4U 1957+115 X-ray spectrum is dominated by the accretion disk emission, with a minor contribution from a Comptonization component and weak reflection features [Sharma et al., 2021]. A correlation has been observed between the brightness of the source and the contribution of the Comptonized component; by analysing *NuSTAR* observations, Barillier et al. [2023] described the increasing behavior of the hard tail with rising flux with two different tracks, with one having significantly stronger tails than the other [e.g. see Figs. 8–10 in Barillier et al., 2023]. Their proposed explanation for this correlation is a reduction of the disk hardening factor associated with the increase in the amplitude of the power-law tail; this scenario suggests that electron scattering in a hot corona becomes more important as it diminishes in the upper layers of the optically thick accretion disk. Through the analysis of the reflection component and continuum fitting of the disk component, several estimates of the BH spin in 4U 1957+115 have been obtained. These estimates consistently describe the source as rapidly rotating, with spin values as high as $a_s > 0.9$ [Nowak et al., 2012], $a_s > 0.98$ [Maitra et al., 2014], $a_s \sim 0.85$ [Sharma et al., 2021] and $a_s = 0.95$ [Draghis et al., 2023].

5.2 Datasets

4U 1957+115 was observed by *IXPE* on 2023 May 12–24 for a net exposure time of ~ 571 ks. Concurrently, NICER [Arzoumanian et al., 2014] observed the source for the entire duration of the *IXPE* campaign, in continuous observations typically lasting ~ 10 min, for a total exposure time of 58 ks spread among 12 ObsIDs. *NuSTAR* [Harrison et al., 2013] observed the source with its two co-aligned X-ray telescopes in three separate observations. The net exposure times for these observations were 18.7

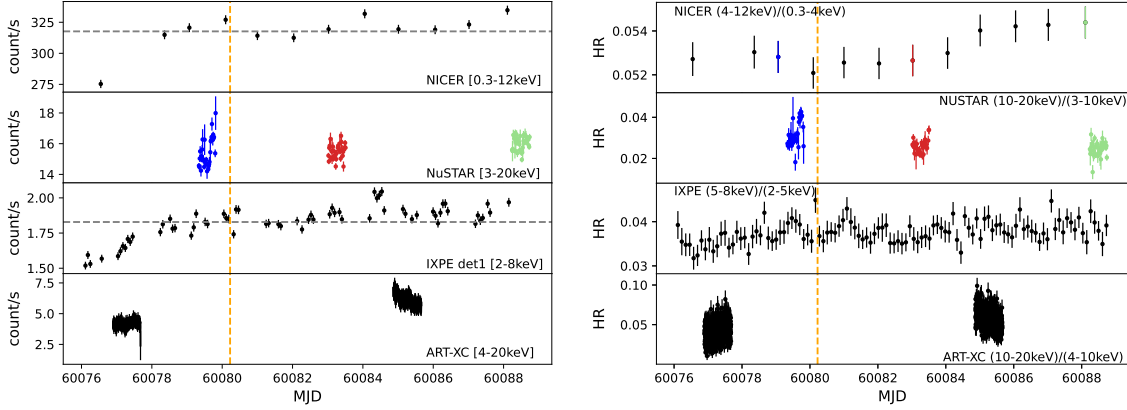


Figure 5.1: Light curves of 4U 1957+115 as seen by NICER in 0.3–12 keV, *NuSTAR* in 3–20 keV, *IXPE* in 2–8 keV and ART-XC in the 4–12 keV energy band. *NuSTAR* data colored in blue, red and green refer to the three epochs described in the spectral analysis and used in the spectra shown in Fig. 5.3. The vertical orange line shows the subdivision of the *IXPE* observation described in section 5.2.1, and the dashed horizontal lines in the NICER and *IXPE* light curves indicate the mean values of the count rate.

ks, 20.2 ks and 19.7 ks, respectively. The Mikhail Pavlinsky ART-XC [Pavlinsky et al., 2021] telescope observed 4U 1957+115 twice on May 13 and May 21, for 68 and 67 ks, respectively. The data reduction process for all the data in our analysis is detailed in Appendix A.

To analyze the flux variability of the source during the *IXPE* campaign we studied the light curves from the simultaneous observations at our disposal, using the following energy ranges: *IXPE* (2–8 keV), NICER (0.3–12 keV), *NuSTAR* (3–20 keV) and *SRG/ART-XC* (4–30 keV). *IXPE* and NICER cover the soft X-ray band and *NuSTAR* and ART-XC the hard X-ray band over a period of 14 days. The binning size of each instrument is 1 ks for *NuSTAR*, 623 s for NICER, 100 s for ART-XC, and 6 ks for *IXPE*. We see from the left panel of Figure 5.1 that the flux significantly increases in the soft X-ray band on the first three days of monitoring with NICER and *IXPE*, and then fluctuates around an average value on the last 10 days. In the hard X-ray band, the count rate for *NuSTAR* appears generally constant within the error bars, while a count rate increase is observed between the two ART-XC observations.

In order to analyse the change of state of the source, we calculate the hardness ratio defined as the ratio between the hard energy band over the soft energy band. We define the respective hard/soft energy bands for each instrument: *IXPE* 5–8 keV/2–5 keV, NICER 4–12 keV/0.3–4 keV, *NuSTAR* 10–20 keV/3–10 keV and ART-XC 10–20 keV/4–10 keV. The right panel of Figure 5.1 shows the evolution of the hardness ratio calculated from the *IXPE*, NICER, *NuSTAR* and ART-XC data. The *IXPE* hardness ratio fluctuates between 0.030 and 0.045 over the whole period of observation. For NICER, the hardness ratio varies between 0.052 and 0.054. By calculating the null hypothesis probability fitted with a constant, we have a p-value of 0.0024 for NICER and $4.7003 \cdot 10^{-5}$ for *IXPE*. Therefore, NICER hardness ratio remains constant within the error bars but is more variable for *IXPE*. Regarding *NuSTAR*, the hardness ratio

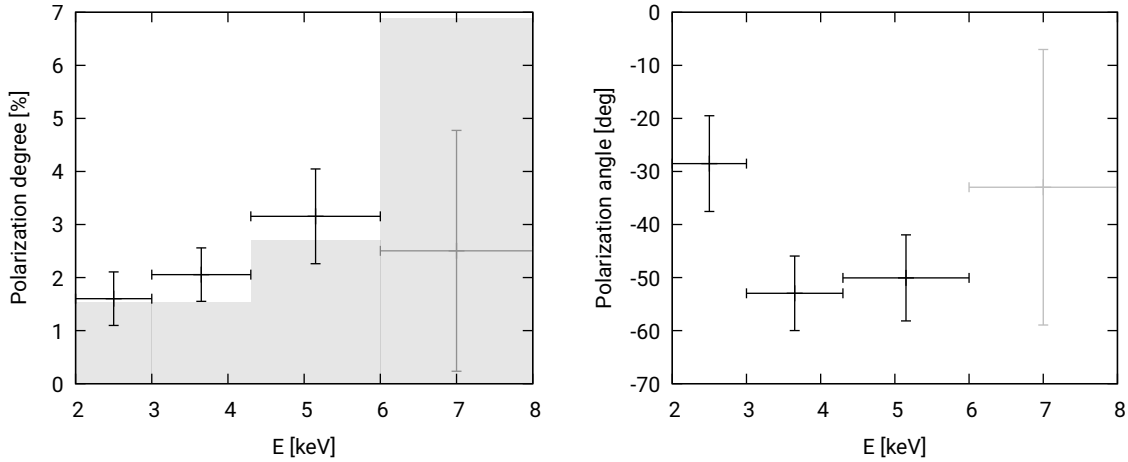


Figure 5.2: Measured PD (*left*) and PA (*right*) of 4U 1957+115. The shaded grey area in the PD-plot is an estimate of the MDP_{99} , showing significant polarization measurement from 2 keV up to 6 keV.

decreases from 0.045 to 0.02 in 10 days, indicating a slight transition of the source toward a softer state. The ART-XC hardness ratio slowly increases at the start of the observations and decreases at the end, which is in agreement with the results from *NuSTAR*.

5.2.1 Polarization measurement

The *IXPE* observation of 4U 1957+115 revealed an average PD in the 2–8 keV band of $1.9\% \pm 0.4\%$ at a PA of $-42^\circ.2 \pm 5^\circ.2$, with a statistical significance of 5.2σ . The measurement exceeds the minimum detectable polarization threshold, MDP_{99} , which is 1.14% in our observation. Figure 5.2 displays the time-averaged polarization properties in four energy bands: 2–3, 3–4.3, 4.3–6, 6–8 keV; the first three bins show a slight increase in PD with energy, while the fourth bin shows data below the MDP_{99} for that energy range, resulting in an upper limit. Meanwhile, the PA exhibits a change between the 2–3 keV and the 3–4.3 keV energy bands, after which it remains relatively constant within statistical uncertainties.

Since the timing analysis of the source revealed a slight variation of the hard component during the first part of the *IXPE* observation (see Figure 5.1), we tried to subdivide the *IXPE* data to investigate possible time variability of the polarization. We found that in the initial part of the observation, marked in Figure 5.1 and roughly corresponding to the increase in flux detected in *IXPE* and *NICER* light curves, we were unable to significantly detect polarization, as the polarization strength was below the MDP_{99} of 2.06% in that time interval. Subsequently, throughout the remaining observing period, the polarization properties remained steady, with a PD slightly exceeding that calculated for the entire duration of the *IXPE* observation (refer to Table 5.1). Because the polarization properties identified in these distinct periods aligned, within statistical uncertainties, with the findings from the total observation, for the sake of simplicity we decided to conduct our polarimetric analysis using the entire *IXPE* observation data set. This choice is also motivated by the relatively little variation of the soft

Time interval	PD (%)	PA (deg)
Total	1.9 ± 0.4	-42.2 ± 5.2
First period	< 2.2	Unconstrained
Second period	2.39 ± 0.45	-40.6 ± 5.8

Table 5.1: PD and PA found in the entire *IXPE* observation and when subdividing it into two periods, as marked in Figure 5.1.

component observed in the timing analysis, leading us to assume that the polarimetric properties of the disk emission do not change significantly during the observation.

5.3 Spectral analysis

For the spectral analysis of our source, we focused on *NuSTAR* and NICER simultaneous observations, as indicated in Figure 5.1, performing a joint fit of the spectra of the two satellites. As the *NuSTAR* high energy flux decreases during the three observations, we adopted different energy ranges according to the energy at which the background starts dominating: 3–30 keV in Period 1, 3–25 keV in Period 2 and 3–20 keV in Period 3. For the NICER data, we fitted the spectra in the 0.7–8 keV energy range for all periods. We used the XSPEC package [v12.13.0c; Arnaud, 1996] and employed the following model in the analysis:

$$\text{TBABS}^*(\text{KERRBB}+\text{EXPABS}^*\text{POWERLAW}). \quad (5.1)$$

In addition, a cross-calibration constant was included to account for discrepancies between the *NuSTAR* FPMA, FPMB and NICER spectra. This constant was kept fixed at 1 for the *NuSTAR* FPMA, while the best-fitting values for *NuSTAR* FPMB and NICER are 0.981 ± 0.003 and 0.940 ± 0.003 , respectively. The spectral model includes a TBABS [Wilms et al., 2000] component to account for interstellar absorption. A KERRBB component is used to describe the accretion disk emission, properly accounting for relativistic effects [Li et al., 2005]. A POWERLAW component was included as a phenomenological representation of the Comptonized emission originating from the corona, which was convolved with an EXPABS component to include a low-energy roll-off. The roll-off energy was obtained in a preliminary analysis using DISKBB in place of KERRBB and equating it to the inner disk temperature. This initial modelling with DISKBB revealed a large disk emission peak temperature (1.39 ± 0.01 , 1.41 ± 0.01 and 1.44 ± 0.02 keV in Periods 1,2 and 3, respectively), which are typical for this source [Sharma et al., 2021, Barillier et al., 2023].

As described in section 1.4.5, disk continuum fitting often encounters substantial degeneracy among various spectral parameters. These parameters encompass the BH mass, distance, accretion rate, hardening factor, system inclination and BH spin. This challenge is notably pronounced in the case of this source, primarily because of the limited availability of robust constraints regarding mass and distance [Barillier et al., 2023]. Several analyses disfavour configurations with low spin and/or inclination values

Component	Parameter (unit)	Description	Values		
			Period 1	Period 2	Period 3
TBABS	$N_{\text{H}}(10^{22} \text{ cm}^{-2})$	Hydrogen column density	0.17 ± 0.01	0.18 ± 0.01	0.19 ± 0.01
KERRBB	η	Inner-torque modification	0^\dagger	-	-
	a_s	BH spin	0.992 ± 0.001	-	-
	i (deg)	Inclination	75^\dagger	-	-
	M_{BH} (M_\odot)	BH mass	4.6^\dagger	-	-
	\dot{M} (10^{16} g s^{-1})	Mass accretion rate	3.47 ± 0.01	3.59 ± 0.01	3.72 ± 0.02
	D (kpc)	Distance	7.8^\dagger	-	-
	hd	hardening factor	1.7^\dagger	-	-
	r_{flag}	Self-irradiation	1^\dagger	-	-
	s_{flag}	Limb-darkening	0^\dagger	-	-
	norm	Normalization	1^\dagger	-	-
	EXPABS	E_C (keV)	e-folding energy	1.39 ± 0.01	1.41 ± 0.01
POWERLAW	Γ	Photon index	1.93 ± 0.09	-	-
	norm (10^{-3})	Normalization	10.05 ± 1.52	4.74 ± 0.71	2.79 ± 0.45
χ^2/dof			975.4/951		

Table 5.2: Best-fitting parameters obtained in the spectral analysis of NICER and *NuSTAR* data during the three periods of observation. EXPABS e-folding energy has been obtained from an initial modelling using DISKBB. Uncertainties are stated at the 90% c.l.. Parameters indicated with \dagger are kept frozen in the spectral analysis.

Component	Parameter	NICER	<i>NuSTAR</i>		<i>IXPE</i>		
			FPMA	FPMB	DU1	DU2	DU3
CONSTANT		0.981 ± 0.003	1^\dagger	0.940 ± 0.003	0.82 ± 0.01	0.78 ± 0.01	0.72 ± 0.01
GAIN	slope	1.03 ± 0.01	-	-	0.99 ± 0.01	0.98 ± 0.01	0.99 ± 0.01
	offset [10^{-2} keV]	-7.38 ± 0.18	-	-	-1.52 ± 0.18	2.23 ± 0.24	1.46 ± 0.16

Table 5.3: Modeling cross-calibration and instrumental features in the spectral and spectro-polarimetric fits presented in Table 5.2 and 5.4

due to the broad spectral peak in the disk emission typically observed in this source [Maitra et al., 2014, Sharma et al., 2021]. In our analysis, we initially left the system inclination free to vary in the fitting procedure; the best fit was obtained for the maximum value allowed by the model ($i = 85^\circ$). However, the lack of any X-ray evidence for binary orbital modulation [Wijnands et al., 2002] suggests that the source inclination cannot exceed $\approx 75^\circ$; thus we decided to freeze the inclination of the system to $i = 75^\circ$, following the approach used in the X-ray analysis performed by Nowak et al. [2008, 2012]. We kept the BH spin, its mass and the distance free to vary in the fitting procedure, together with the accretion rate, while we assumed a value of 1.7 for the hardening factor. Due to the strong degeneracy between mass and distance, however, this procedure yielded very large uncertainties on both parameters. Since the main purpose of this work is to analyse the polarimetric data of our source, for the sake of simplicity we decided to fix the mass and distance to the best fiducial values obtained by Barillier et al. [2023] combining Gaia parallax measurements with the *NuSTAR* spectral analysis: $M_{\text{BH}} = 4.6 M_\odot$ and $D = 7.8$ kpc. Additionally, due to the decline in high-energy flux during the second and third *NuSTAR* observations (see Fig. 6.2), the POWERLAW photon index Γ became difficult to constrain in these periods. Hence, we linked it across all three observations, while permitting the POWERLAW normalization

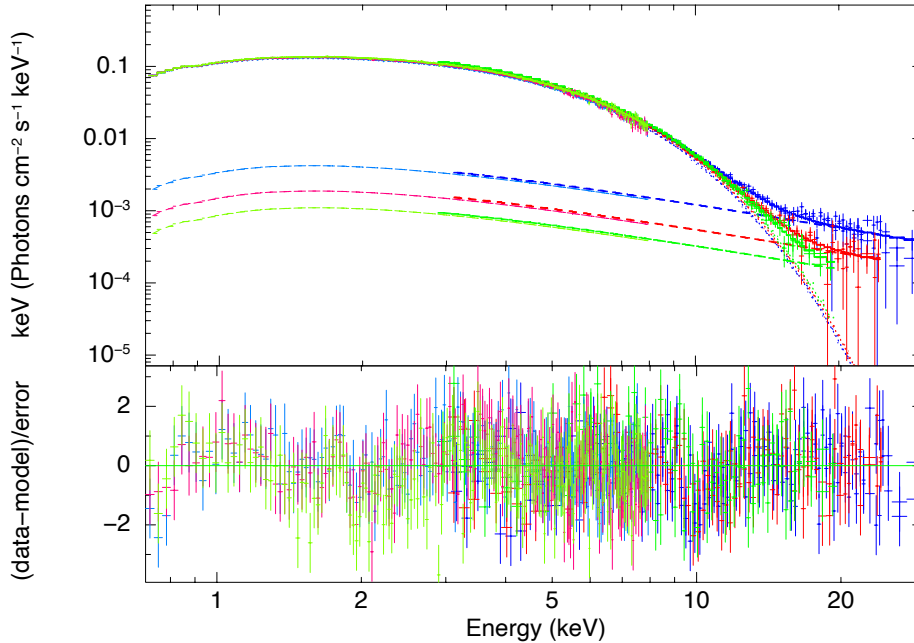


Figure 5.3: NICER and *NuSTAR* spectra of 4U 1957+115. *Top panel*: unfolded spectra (i.e. the flux $F(E)$) for the best-fitting model described by Model 5.1 during Periods 1, 2 and 3 are shown with blue, red and green colors, respectively. The total model for each period, the contributions of the KERRBB and the POWERLAW models are shown with the solid, dotted and dashed lines, respectively. *Bottom panel*: Model – data residuals in units of σ .

to vary independently for each period.

However, the fit is statistically unacceptable with $\chi^2/\text{dof}=2136/953$, primarily due to substantial residuals in NICER spectra below 3 keV. These residuals are usually attributed to calibration issues, as similar occurrences have been noted in past observations of this source [Barillier et al., 2023] and other accreting BHs (see chapters 4 and 6). Given that Model 5.1 effectively describes *NuSTAR* data ($\chi^2/\text{dof}=470/438$), we decided to address the large residuals by adjusting the response file gains in NICER spectra (using the `gain fit` command in XSPEC). Moreover, we assigned 1% systematic uncertainties for the NICER data sets, within the mission recommendations,¹ resulting in a revised $\chi^2/\text{dof}=975.4/951$. The optimal spectral parameter values are detailed in Table 5.2, and the unfolded spectra along with the data-model residuals are shown in Fig. 5.3². The cross-calibration constant and the GAIN parameters are shown in Table 5.3.

Our spectral analysis allowed us to decompose the spectra in a dominating soft component, representing the accretion disk emission, and a weak hard tail, describing

¹NICER calibration recommendations can be found at <https://heasarc.gsfc.nasa.gov/docs/nicer/analysisisthreads/cal-recommend/>

²Due to the strong degeneracy between the hardening factor and the BH spin parameter we further investigated if the high spin scenario depicted by the spectral fit remained consistent assuming different values for the hd parameter. When setting $hd = 2$ our analysis yielded a BH spin of $0.953^{+0.032}_{-0.004}$, with a χ^2/dof of 979.5/951. On the other hand, when considering $hd = 1.5$, we obtained a lower limit for the BH spin of 0.997, with a χ^2/dof of 973.9/951.

the photons scattered in the corona. While the disk accretion rate exhibits only a slight variation between the three *NuSTAR* observations, the POWERLAW normalization shows a decrease between the first and the second periods, as suggested by the hardness ratio shown in Figure 5.1. This is further reflected by the 2–8 keV flux contribution of the hard component, which goes from 2.3% in Period 1 to 1.0 and 0.7% in Periods 2 and 3, respectively. Significantly, this analysis did not reveal any discernible reflection features. However, it is noteworthy that previous studies of this source have demonstrated that incorporating relativistic reflection models often enhances the overall fit quality [Draghis et al., 2023]. Nonetheless, delving into this detailed investigation lies beyond the intended scope of this work and is deferred to a future publication.

5.4 Polarimetric analysis

We now incorporate the polarimetric information provided by *IXPE* into our spectral fit. In this section, we take the first exploratory step of fitting a spectro-polarimetric model to the *IXPE* *Q* and *U* spectra. For this purpose, we first incorporated *IXPE* *I* spectra into the fitting procedure using Model 5.1. Given that the *IXPE* observation extends over a longer time frame compared to the *NuSTAR* and NICER observations utilized in the spectral fitting detailed in section 5.3, we made the decision to maintain all spectral parameters fixed at the values reported in Table 5.2. The only exceptions to this were the disk accretion rate and the normalization of the POWERLAW component, which we allowed to vary, together with *IXPE* data cross-calibration constants. The values obtained for the mass accretion rate and for the POWERLAW component normalization are shown in Table 5.4; both are consistent with the values obtained in the spectral analysis described in section 5.3. The best-fitting values of the calibration constant are 0.82 ± 0.01 , 0.78 ± 0.01 and 0.72 ± 0.01 for *IXPE* DU1, DU2 and DU3, respectively. As was already noticed in other accreting BHs [Krawczynski et al., 2022, Podgorný et al., 2023b, Rodriguez Cavero et al., 2023], a simple constant is not enough to account for cross-calibration uncertainties between *IXPE*, NICER and *NuSTAR*; for this reason, we performed a fit on the response file gains of *IXPE* spectra, presented in Table 5.3. The fit resulted in a $\chi^2/\text{dof}=436/442$.

As a following step, we incorporated the *IXPE* *Q* and *U* spectra in our analysis, adopting our best-fit spectral model and applying the same gains and the same cross calibration factors as for the *I* spectra. We assigned a constant PD and PA to the model using a `polconst` component, and performed a fit in the same four energy bands defined in Figure 5.2, leaving only the PD and PA of the `polconst` model as free parameters. Figure 5.4 shows the contours, calculated using 50 steps for each parameter, in the polar plot of PD and PA. The PD shows a slight increase with energy as in Figure 5.2, while the PA is found to have a constant behavior, within statistical uncertainties. To determine the statistical significance of the observed increase in PD, we conducted a comparison by fitting the *Q* and *U* spectra across the entire *IXPE* energy range. We considered scenarios where PD and PA were either held constant or allowed to vary. When both PD and PA were held constant across energy, the resulting χ^2/dof was 82.7/64. Allowing PD to vary while keeping PA constant improved the fit ($\chi^2/\text{dof}=74.6/63$), while permitting changes in both PD and PA did not significantly enhance the fit, yielding $\chi^2/\text{dof}=72.7/62$. Using an F-test to compare these models, we

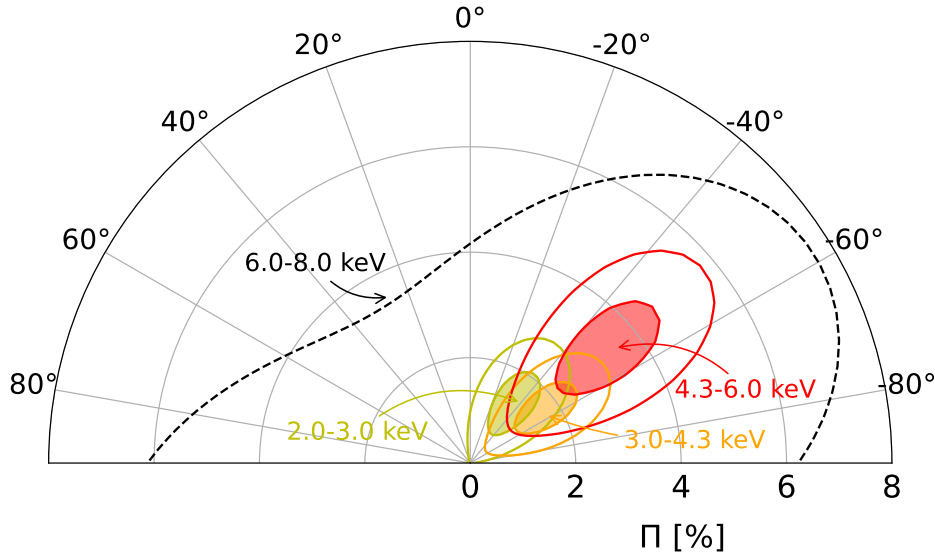


Figure 5.4: Polar plot of the PD and PA, assuming the spectral best-fit model, in 4 energy bins: 2.0–3.0, 3.0–4.3, 4.3–6.0 and 6.0–8.0 keV. The shaded and unshaded regions show the 68% and 99.9% confidence areas, respectively, in the first three energy bins. The dashed line indicates the 99.9% confidence level upper limit in the fourth energy bin.

found that the model allowing varying PD while maintaining a constant PA is preferred over the model with constant PD and PA, at a confidence level of 99%.

We then proceeded to incorporate in the fit a physical model that self-consistently describes the spectro-polarimetric properties of the thermal emission. For this purpose, we replaced `KERRBB` with the model `KYNBBRR` (introduced in Chapter 3). To implement this model in the analysis we first used it to fit the *IXPE I* spectra, leaving only the accretion rate and the normalization as free parameters. The best-fitting values for these parameters are shown in Table 5.4. The fit resulted in $\chi^2/\text{dof}=488/445$, assuming no contribution from the returning radiation (`albedo`= 0); the resulting spectral fit was insensitive to variation of the `albedo` parameter. This absence of a spectral signature attributed to the returning radiation component deviates from recent findings in soft state BH outbursts. In these contexts, returning radiation has been proposed as a plausible source for observed relativistic reflection features, as seen in studies like [Connors et al., 2020, 2021]. These investigations, alongside theoretical predictions by Dauser et al. [2022], characterized the returning radiation component using the `RELXILLNS` model, an evolution of the `RELXILL` suite of relativistic reflection models that assumes a single-temperature black-body as the incident radiation source. The discrepancy in results likely arises from the crucial difference in the way reflection is treated in the two models: while `KYNBBRR` describes the reflection process using Chandrasekhar [1960] diffuse reflection formulae, assuming a completely ionized disk atmosphere [see also Taverna et al., 2020], it lacks the capacity to replicate any reflection features in the spectra, as `RELXILLNS` does. Since we have not found any apparent reflection features present in the spectra, we consider the use of this pure scattering approximation in our spectro-polarimetric analysis justified. This choice is reinforced by Taverna et al.

Component	Parameter (unit)	Values
kerrbb	Mass accretion rate (10^{16} g s^{-1})	3.54 ± 0.03
polconst	norm (10^{-3})	5.67 ± 1.38
	χ^2/dof	436/442
kynbrr	Mass accretion rate ($10^{-2} M_{\text{Edd}}$)	$1.64^{+0.02}_{-0.05}$
	norm	1.92 ± 0.03
	χ^2/dof	488/445
kynbrr	χ_0 ($^\circ$)	$-67.5^{+22.9}_{-12.5}$
	albedo	Unconstrained
polconst	PD	Unconstrained
	PA	Unconstrained
	χ^2/dof	73.4/62

Table 5.4: Best- fitting parameters obtained in the *IXPE* spectral fit using model 5.1 and in the spectro-polarimetric analysis of *IXPE* data using the `kynbrr` model, both detailed in Sect. 5.4.

[2021]’s results, indicating that due to higher temperatures and lower plasma densities, the matter within the inner regions of rapidly rotating BHs accretion disks is anticipated to be almost entirely ionized.

As the parameters obtained were consistent with the values obtained with Model 5.1, we extracted from the code the theoretical prediction for the thermal emission PD and PA, presented in Figure 5.5. As the self-irradiation contribution becomes more significant, the PD shows an increase with energy due to the large PD expected for this component. Simultaneously, the PA exhibits a 90° rotation with energy, as the returning photons are expected to be polarized perpendicularly to the ones that directly reach the observer after leaving the disk atmosphere. If the albedo parameter is large enough, this rotation occurs below 2 keV, leading to a relatively constant behavior of the PA with energy in the *IXPE* energy interval [Taverna et al., 2020]. Subsequently, we froze all the spectral parameters of the model and focused on the fit of *IXPE* Q and U spectra. We employed a POLCONST model to describe the hard component polarization properties and left its parameters free to vary in the fit together with the KYNBRR albedo and orientation (χ_0) parameter, which indicates the accretion disk axis position angle. We obtained a $\chi^2/\text{dof}=73.4/62$, for the best-fit values detailed in Table 5.4. However, the soft component ALBEDO and the hard component PD and PA remained unconstrained during the fitting procedure. This can be understood by looking at the contour plots presented in Figure 5.6, which shows the 68%, 90% and 99% confidence level contours for the allowed values of the hard component PD and the albedo parameter. The contours indicate a degeneracy between the two parameters, suggesting two different ways to explain the increasing trend of the PD with energy: either a very large PD of the hard component or a strong contribution from returning radiation.

As we discussed in chapter 4, the *IXPE* observation of 4U 1630-47 in the step power-law state measured a PD of the coronal emission of about 7% [Rodríguez Cavero et al., 2023]. Considering the similarities between these two sources, both being ac-

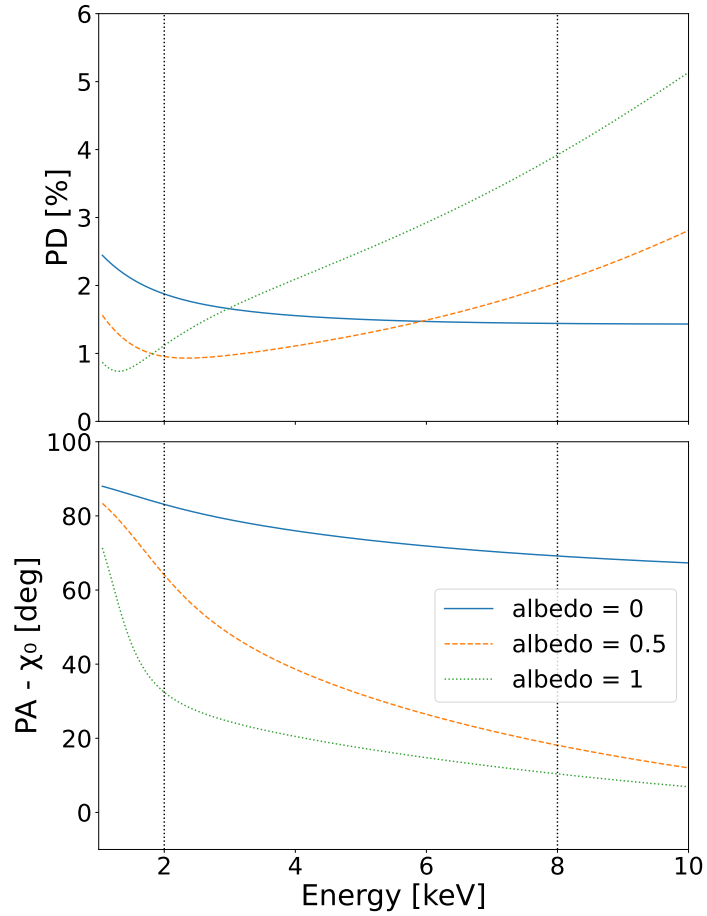


Figure 5.5: PD (*top*) and PA (*bottom*) predicted by the KYNBBRR model for the disk emission, assuming all system parameters fixed at their respective best-fitting values (see Table 5.2). The different colors indicate different contributions of the returning radiation component, regulated by the `albedo` parameter. The vertical dashed lines highlight the 2–8 keV energy range. Here, the PA is defined with respect to the disk axis position angle χ_0 .

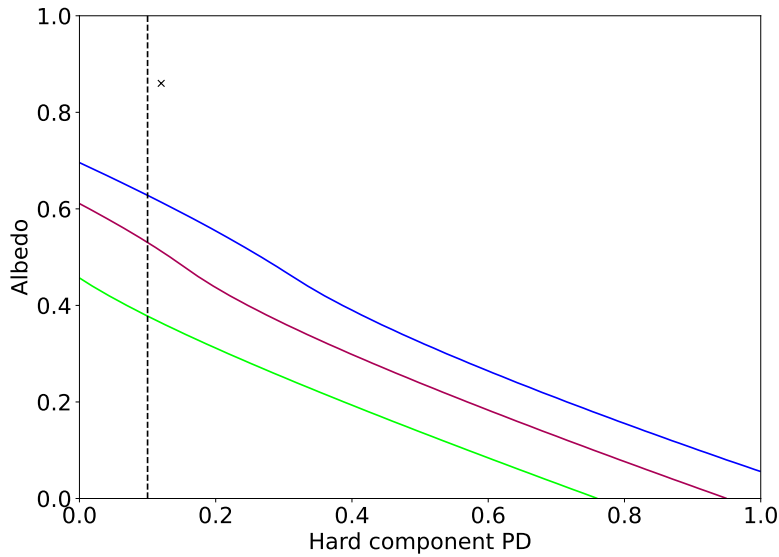


Figure 5.6: Contour plot of the corona emission PD and the `kynbbrr` albedo parameter, which regulates the returning radiation contribution. Blue, red, and green lines indicate 68%, 90% and 99% confidence levels for two parameters of interest, respectively, while the black cross indicates the best-fitting parameters. The dotted vertical line represents the assumed upper limit on the corona emission PD, as described in the text.

creting BH systems likely observed at large inclination angles, we imposed an upper limit of 10% on the PD of the hard component of 4U 1957+115. With this assumption, the only viable explanation for the polarimetric data is the inclusion of returning radiation. Hence, our polarimetric fit shows that the standard thin disk model can effectively describe the polarimetric data of this source, but it is necessary to consider the contribution from self-irradiation (assuming a 10% PD for the corona emission, we find a lower limit of 0.73 for the `albedo` parameter).

As detailed in Sect. 5.2, the initial part of our *IXPE* observation did not yield a detectable polarization signal, as outlined in Table 5.1. Notably, our first *NuSTAR* observation, which displays the largest hard component contribution to the spectra, occurred near the end of this period. Considering the reduced hard component contribution during the rest of the observation, the observed low PD might be explained by depolarization of radiation from the accretion disk by the corona emission. A similar situation was observed in LMC X-1 (see Chapter 6), where the low PD detected by *IXPE* was attributed to the combination of two spectral components, disk and corona emission, polarized perpendicularly to each other [Podgorný et al., 2023b]. To investigate this scenario, we attempted to independently fit the polarimetric data in the first period. We made the assumption that the polarization characteristics of the thermal emission remained constant throughout the observation and represented them using the best-fitting `KYNBBRR` model, derived from our analysis of the entire *IXPE* observation. Employing a `POLCONST` component to characterize the polarization properties of the hard component, we estimate an upper limit to the PD of 17% during the initial

phase of the *IXPE* observation when assuming the corona emission to be polarized in the direction of the disk axis. This upper limit increased to 38% in the perpendicular configuration.

The polarimetric fit described above indicates that the standard Novikov-Thorne thin disk model [Novikov and Thorne, 1973], assuming the large spin and inclination values found in the spectral analysis, successfully explains the polarimetric data. As a further analysis, we tried to test whether the standard thin disk model can effectively describe the polarimetric data for different values for the BH spin and the disk inclination, in order to put some constraints on the value of these parameters.

For this purpose, we repeated the procedure described above, but this time we explored different values for the BH spin and the system inclination. The spectral fit favoured configurations with large spin and inclination values, so when we reduced these parameters' values, we had to relax some of the initial assumptions on the model to achieve an acceptable fit. Specifically, we allowed the source distance and disk hardening factor to vary freely, as they tend to increase significantly when considering lower spin and inclination values, albeit above the limits suggested by Gaia parallax measurements [Maccarone et al., 2020, Barillier et al., 2023] and disk atmosphere modelling [Shimura and Takahara, 1995].

Figure 5.7 displays the soft component PD and PA predicted by the KYNBBRR fit for different spin and inclination values. As the BH spin decreases, the ISCO location moves further away from the central BH. Consequently, the fraction of photons forced to return to the disk surface diminishes. When the BH spin becomes sufficiently low ($a_s \lesssim 0.96$), the contribution of returning radiation is no longer sufficient to explain the increase in PD with energy, and its primary effect is to depolarize the direct emission. On the other hand, when the disk inclination angle decreases, the observed PD decreases across the entire *IXPE* band, while the PA exhibits larger rotations with energy.

We conducted a polarimetric fit on the *IXPE* *Q* and *U* spectra while assuming different values for the BH spin and the disk inclination. Our analysis identified that the configuration with spin $a_s = 0.998$ and disk inclination $i = 75^\circ$ provided the most accurate description of the data, resulting in a χ^2/dof of 72.5/62. On the other hand, the best polarimetric fit assuming spin $a_s = 0.5$ resulted in the notably larger $\chi^2/\text{dof} = 79.2/62$; furthermore, this configuration demands an exceptionally high PD for the corona component, with a lower limit of 51%. When assuming the fiducial value of 10%, the χ^2/dof increases to 84.9/63. This considerably worse fit results from the absence of a significant increase in energy of the PD within the *IXPE* energy band, as illustrated in the leftmost column of Figure 5.7. Figures 5.8 and 5.9 present the chi-squared values and contour plots between the PD of the corona emission and the KYNBBRR albedo parameter for four different combinations of these parameters. As the BH spin or the disk inclination angle decreases, a larger corona PD is required to account for the PD increase with energy. Notably, for cases where $a_s < 0.96$ or when assuming a disk inclination lower than 50° , the corona PD exceeds the fiducial upper limit of 10%. Consequently, assuming a standard thin disk model, these configurations are disfavoured.

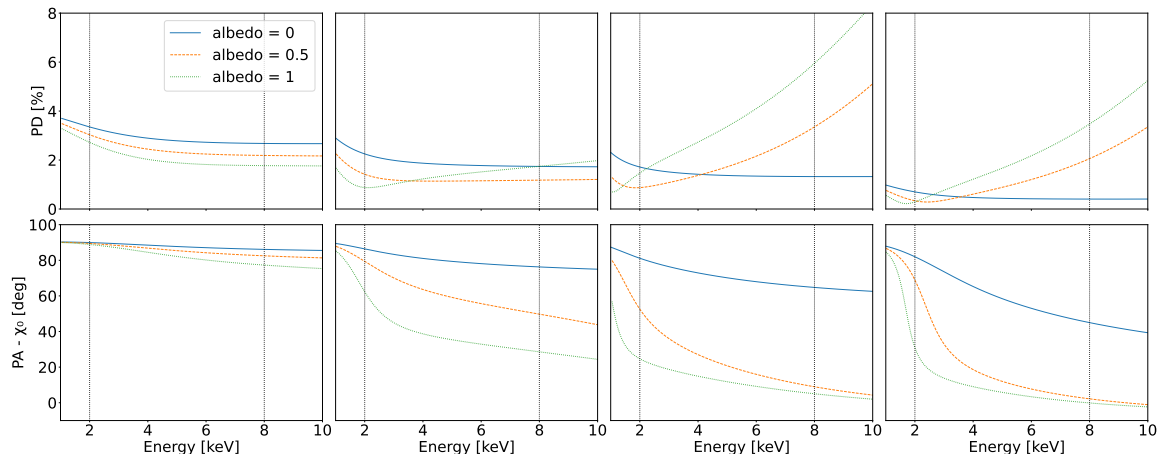


Figure 5.7: PD (*top row*) and PA (*bottom row*) predicted by the KYNBBRR model for the disk emission assuming different values for the BH spin and for the system inclination: from left to right $a_s = 0.5$ and $i = 75^\circ$, $a_s = 0.96$ and $i = 75^\circ$, $a_s = 0.998$ and $i = 75^\circ$, $a_s = 0.998$ and $i = 50^\circ$. The different colors indicate different contributions of the returning radiation component, regulated by the `albedo` parameter. The vertical dashed lines highlight the 2–8 keV energy range. Here, the PA is defined with respect to the disk axis position angle χ_0 .

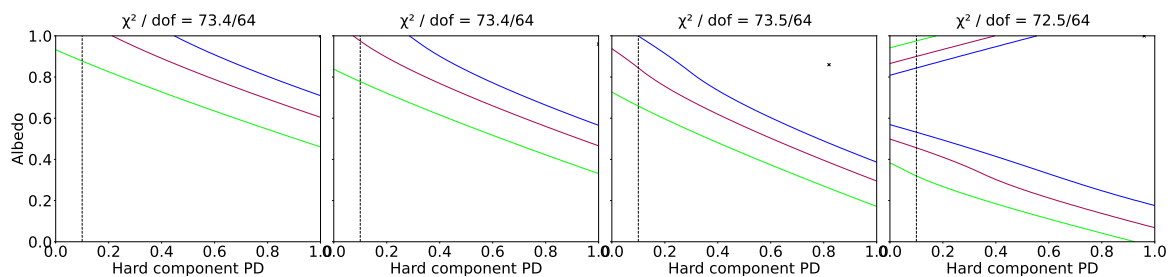


Figure 5.8: Contour plot of the corona emission PD and the KYNBBRR `albedo` parameter, assuming four different spin values: from left to right $a_s = 0.95, 0.96, 0.97$ and 0.998 . The system inclination is assumed to be 75° in all cases. Blue, red and green lines indicate 68%, 90% and 99% confidence levels for two parameters of interest, respectively, while the black cross indicates the best-fitting parameters. The dotted vertical line represents the assumed upper limit on the corona emission PD.

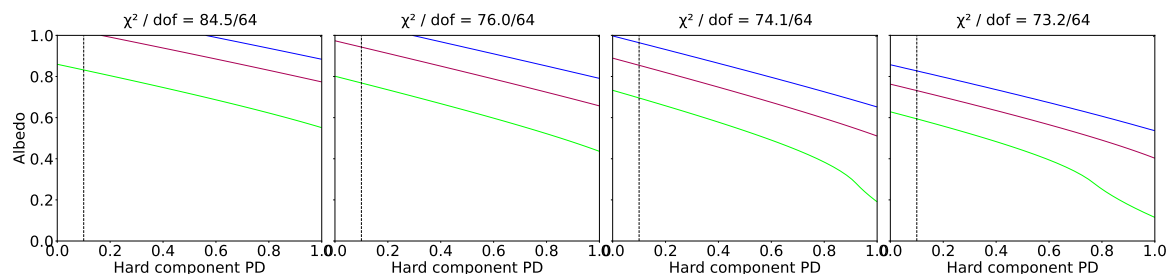


Figure 5.9: Same as Fig. 5.8, but assuming a fixed spin value of 0.998 and considering different values for the accretion disk inclination: from left to right $i = 45^\circ, 50^\circ, 55^\circ$ and 60° .

5.5 Discussion

We discussed the first X-ray spectro-polarimetric observational campaign on the LMXB accreting BH system 4U 1957+115, with coverage by the *IXPE*, *NICER*, *NuSTAR* and *SRG* missions. Our spectral analysis indicated that the source was in a soft state, characterized by a predominant thermal disk emission, with only a minor contribution from a Comptonized component and no clear reflection features. We observed a diminishing trend in the contribution of the hard X-ray tail during the observation period, with the initial *NuSTAR* data exhibiting the strongest power-law tail. Notably, this trend was not discernable from the *IXPE* and *NICER* data, highlighting that the Comptonization component becomes relevant only above ~ 10 keV, contributing only marginally in the *IXPE* energy range (2.3%, 1% and 0.7% during the three *NuSTAR* observations). Our spectral fitting, utilising a relativistic accretion disk emission model, strongly favoured configurations characterised by large inclination angles and high spin values. By fixing the inclination, mass and distance parameters to fiducial values, we estimated the BH spin to be 0.992 ± 0.003 , which aligns with the literature values, considering the uncertainties [but see Sharma et al., 2021]. The polarimetric observation of 4U 1957+115 revealed a time-averaged 2–8 keV PD of $1.9\% \pm 0.4\%$ with a polarization angle of $-41^\circ, 8 \pm 5^\circ, 7$. The polarization angle remains constant across different energy bins, while the PD shows a slight increase with energy, raising from $\approx 1.6\%$ between 2 and 3 keV to $\approx 3.1\%$ in the 4.3–6.0 keV energy band. The observed polarimetric data are consistent with theoretical predictions for thermal emission originating from an optically thick and geometrically thin disk with a Novikov-Thorne profile, assuming Chandrasekhar [1960] and Sobolev [1963] prescription for polarization due to electron scattering in semi-infinite atmospheres. This agreement is achieved by accounting for the substantial contribution of self-irradiation. It is important to note that the inclusion of absorption effects could alternatively explain the increase of the PD with energy, mimicking the contribution of returning radiation (see chapters 3 and 4). The impact of absorption, however, is estimated to be negligible in the disk atmosphere of rapidly rotating BHs, because matter in the inner regions of the accretion disk is expected to be almost completely ionized, due to the larger temperatures and lower densities of the plasma [Taverna et al., 2021]. Additionally, we can exclude the contribution of highly ionized gas along the line of sight due to the lack of spectral features. Therefore, we regard the pure scattering atmosphere as a reasonable approximation to model our data. Our spectro-polarimetric analysis indicates that configurations with low BH spin values or low inclination angles are disfavoured within the standard Novikov-Thorne thin disk model, in agreement with the spectral analysis. In fact, such configurations struggle to explain the observed increase of PD with energy without requiring unphysically high PD values for the power-law component.

Chapter 6

LMC X-1

6.1 Introduction

LMC X-1 is the first discovered extragalactic black-hole (BH) X-ray binary system [Mark et al., 1969]. Being located in the Large Magellanic Cloud, the source has a well-determined distance of 50 ± 1 kpc [Pietrzyński et al., 2013]. LMC X-1 is persistent and bright; hence, it has been studied extensively since its discovery. While many X-ray binary systems change their spectral state over time, LMC X-1 has always been observed in the soft state with $L_X \sim 2 \times 10^{38}$ erg s⁻¹ [Nowak et al., 2001, Wilms et al., 2001]. Typically more than 80 percent of the X-ray flux can be attributed to the thermal/disk component [see e.g. Nowak et al., 2001, Steiner et al., 2012, Bhuvana et al., 2021, Jana et al., 2021, Bhuvana et al., 2022]. The remainder of the X-ray flux can be decomposed into coronal power-law emission [Sunyaev and Titarchuk, 1980], a broad Fe-line from the relativistic disk [Fabian et al., 1989], and a narrow Fe-line that most likely originates from scattering off highly ionized wind from the stellar companion [Steiner et al., 2012].

Optical and near-infrared observations reveal an O7/O9 giant donor with a mass of $M_2 = 31.8 \pm 3.5 M_\odot$ [Orosz et al., 2009]. The same dynamical study confirms a BH accretor with a mass of $M_{\text{BH}} = 10.9 \pm 1.4 M_\odot$ and an orbital inclination $i = 36.4^\circ \pm 1.9^\circ$. The measured orbital period of LMC X-1 is 3.90917 ± 0.00005 days [Orosz et al., 2009], based on high-resolution optical spectroscopy. Over an orbit, the X-ray flux exhibits achromatic sinusoidal amplitude modulations of 7% associated with the inferior/superior conjunctions and Thomson scattering and absorption by the stellar wind [Nowak et al., 2001, Orosz et al., 2009, Hanke et al., 2010]. Strong red noise variability is observed on timescales shorter than the orbital period [Schmidtke et al., 1999, Nowak et al., 2001, Bhuvana et al., 2022]. Also, low-frequency QPOs were observed on several occasions [e.g. Alam et al., 2014], which do not fit well within the standard low-frequency QPO ABC classification [Belloni and Motta, 2016].

Measurement of the BH spin in LMC X-1 is of great interest. The system is a high-mass X-ray binary, and estimation of the BH spin is useful for stellar evolution and cosmological studies [see e.g. Qin et al., 2019, Mehta et al., 2021]. The donor star is 5 Myr past the zero-age main sequence and believed to be filling 90 per cent of its Roche lobe. This, and the inferred dynamical parameters of the system, suggest that LMC X-1 is likely a precursor of an unstable mass transfer phase and a common-envelope merger

[Podsiadlowski et al., 2003, Orosz et al., 2009, Belczynski et al., 2021]. Such systems are of potential interest for gravitational-wave studies, especially regarding the spin of the BH [Belczynski et al., 2021, Fishbach and Kalogera, 2022, Shao and Li, 2022]. Many spectroscopic studies have estimated the spin of the BH in LMC X-1, using the continuum and relativistic line fitting techniques in Kerr space-time, assuming the spin is aligned with the system axis of symmetry [see Tripathi et al., 2020, for LMC X-1 studies beyond the Kerr metric]. They infer remarkably high spin values: $0.85 \lesssim a \lesssim 0.95$ [continuum method; Gou et al., 2009, Mudambi et al., 2020, Jana et al., 2021, Bhuvana et al., 2021] and $0.93 \lesssim a \lesssim 0.97$ [Fe-line method; Steiner et al., 2012, Bhuvana et al., 2022]. Along with the high spin, high accretion rates of $0.07 \lesssim \dot{M}/\dot{M}_{\text{Edd}} \lesssim 0.24$ and luminosities $0.1 \lesssim L_X/L_{\text{Edd}} \lesssim 0.16$ are estimated [the quantities are defined in Bhuvana et al., 2022]. The power-law index tends to be steep $2 \lesssim \Gamma \lesssim 4$ [Nowak et al., 2001, Gou et al., 2009, Jana et al., 2021, Bhuvana et al., 2022]. A counter-argument to the high spin of LMC X-1 through X-ray spectroscopy was given by Koyama et al. [2015] that introduced a double Compton component model to fit the data, which allows a larger disk inner radius, leading to a lower spin estimate.

A ~ 15 pc parabolic structure in the form of a surrounding nebula (wind or jet powered) was detected in both optical and radio observations [Pakull and Angebault, 1986, Cooke et al., 2008, Hyde et al., 2017]. The nebula is aligned with an inner ~ 3.3 pc ionization cone of 50° projected full opening angle seen in He II and O III lines, which is believed to be directly related to the BH accreting structure [Cooke et al., 2007, Cooke et al., 2008]. The jet of LMC X-1 has not been detected yet [Fender, 2006, Hughes et al., 2007, Hyde et al., 2017] and is likely to be switched off since the binary is persistently in the thermal state [Cooke et al., 2007].

6.2 Datasets

IXPE observed LMC X-1 between 2022 Oct 19 and 2022 Oct 28, for a total exposure time of ~ 562 ks for each of its three telescopes. Simultaneous X-ray observations were performed with the NICER [Arzoumanian et al., 2014], *NuSTAR* [Harrison et al., 2013] and ART-XC [Pavlin et al., 2021] instruments to better characterize the source spectrum. In particular, NICER observed LMC X-1 along the entire *IXPE* observational campaign, for a total of 13.5 ks useful time among 10 ObsIDs from 2022 October 19–28. The *NuSTAR* spacecraft acquired a total of 19 ksec of data on 2022 October 24. The Mikhail Pavlinsky ART-XC telescope observed LMC X-1 on 2022 Oct 27 with a total exposure of 84.4 ks. A detailed description of the data reduction techniques employed is presented in Appendix A.

Daily monitoring by the Gas Slit Camera (GSC) onboard of MAXI [Matsuoka et al., 2009] confirmed that during our observations, there were no outbursts or long-term flux variations. To analyze the flux variability of LMC X-1 during the *IXPE* observation we produced light curves from the simultaneous observations by NICER, *NuSTAR* and ART-XC (see Fig. 6.1). We used the following energy ranges for the light curves: 0.3–12 keV, 3–20 keV, and 4–12 keV, respectively for NICER, *NuSTAR* and ART-XC. Despite ART-XC registering useful signals up to 35 keV, we used a shorter energy band for the timing analysis due to the sharp decrease of the mirror systems effective area above the nickel edge at ≈ 12 keV. The corresponding time bins were 920 s for NICER,

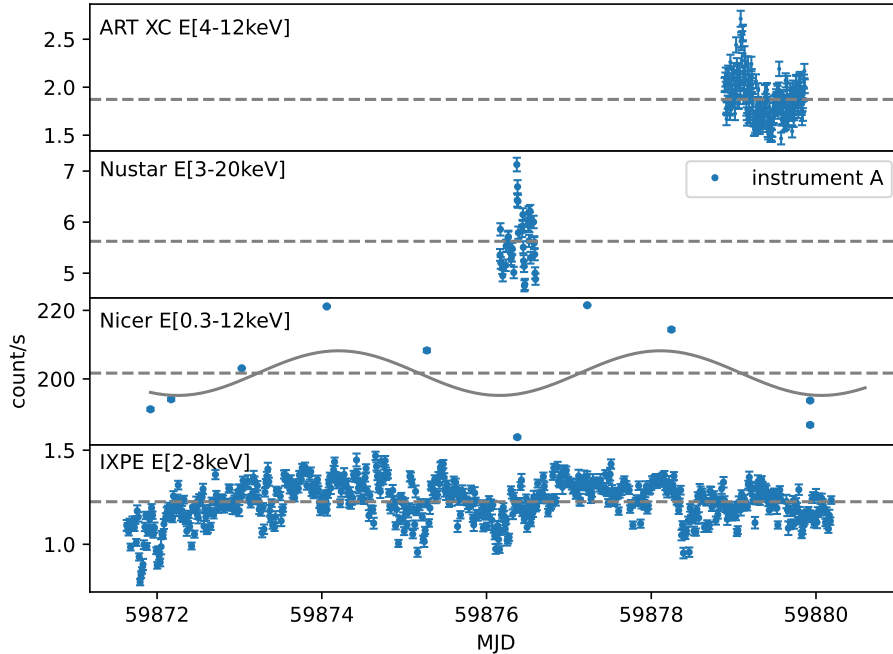


Figure 6.1: X-ray light curves of LMC X-1. *Top panel*: ART-XC light curve for the energy range 4–12 keV. *Second panel*: *NuSTAR* light curve for the energy range 3–20 keV from the instrument A of *NuSTAR*. *Third panel*: NICER light curve for the energy range 0.3–12 keV with a sinusoidal curve showing the expected orbital modulations of the X-ray flux based on previous *RXTE* monitoring of the source. *Bottom panel*: *IXPE* light curve for the energy range 2–8 keV. The dashed horizontal lines are the average count rate for each light curve.

400 s for *NuSTAR* and ART-XC, and 1000 s for *IXPE*.

The *IXPE* and NICER observations cover 10 days, while *NuSTAR* and ART-XC complement these observations with snapshots in the hard X-ray band. Our *IXPE* and NICER observations thus include about two and half orbits of the BH and companion star. Orosz et al. [2009] measured orbital modulations of the X-ray flux to be consistent with the periodicity measured from optical data. The X-ray orbital modulation was revealed via a set of *RXTE*/ASM [Levine et al., 1996] data from over 12 years of monitoring, and it was attributed to the electron scattering and absorption in the stellar wind from the companion star [Orosz et al., 2009, Levine et al., 2011]. To estimate the X-ray flux orbital modulations in the current observations, we took the orbital ephemeris from the ‘adopted’ model in Table 3 of Orosz et al. [2009]; in particular, we assumed the orbital period of 3.90917 days and the time of the superior conjunction of 53390.8436 MJD (Modified Julian Date). We took the parameters of the best-fitting sinusoidal curve from their table 1 for the 1.5–12 keV energy band, where they reported parameters averaged over the 12 years observation with *RXTE*, and we rescaled to the NICER count rate. The NICER count rate versus orbital phase is then $f(\phi) = a_0 - a_1 \cos(2\pi\phi)$ where, once rescaled, the parameters are $a_0 = 201.69$ and $a_1 = a_{1,RXTE} \times \frac{a_0}{a_{0,RXTE}} = 6.51$ and ϕ is the phase. The curve is shown along with the NICER data in the third panel of Fig. 6.1.

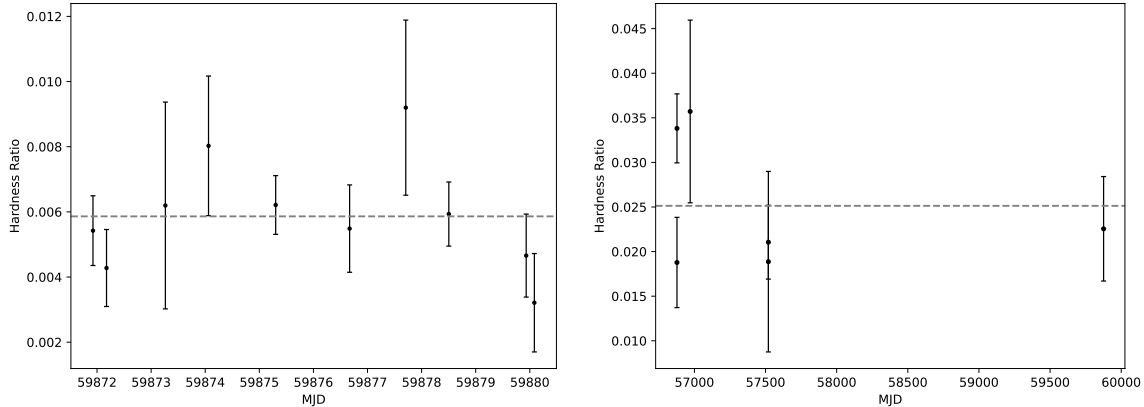


Figure 6.2: Time variation of X-ray hardness ratios. The dashed lines are the average values of the hardness ratios. *Left panel*: Ratio of the NICER count rates in the hard band (3–12 keV) over the total flux (0.3–12 keV). *Right panel*: Ratio of the *NuSTAR* count rates in the hard band (8–20 keV) over the total flux (3–20 keV).

Comparison of the curve and the data indicates that the expected orbital modulations can explain the X-ray variations in the NICER light curve. The amplitude of the NICER data modulation is higher than the amplitude from the *RXTE*-ASM analysis. This is most likely due to the different energy bands of the instruments, the NICER camera being more sensitive in the low energies where most counts are detected and affected by the circumstellar absorption, and thus the amplitude of the modulation might be larger. Any stochastic variations, which can also contribute to the single observation, are smeared out in the averaging over 12 years of monitoring with *RXTE*. Similar modulations are apparent in the *IXPE* light curve. The X-ray flux minima correspond to superior conjunctions of the BH that are associated with enhanced absorption and reduced scattered emission due to the wind from the companion.

In the light curves acquired in the hard X-ray band (*ART-XC* and *NuSTAR*), stochastic noise dominates over the orbital modulations. Similar to previous research [see [Koyama et al., 2015](#)], we observe an increase in stochastic red noise variability with energy. The power spectrum in the hard band can be described with a power law with index ≈ -1 and normalization consistent with the previous measurements [see e.g. [Bhuvana et al., 2021](#)]. No obvious QPOs were observed in the power spectrum. It should be noted, that low-frequency QPOs were previously observed in this system during short episodes of spectral hardening within the soft state [[Ebisawa et al., 1989](#), [Alam et al., 2014](#)].

Using the NICER and *NuSTAR* spectral data, we calculated the hardness ratio defined as the ratio between the flux in the hard band and the total flux. We defined the soft vs. hard bands to be 0.3–3 keV vs. 3–12 keV for NICER, and 3–8 keV vs. 8–20 keV for *NuSTAR*. In Fig. 6.2, we show the evolution of the hardness ratio for the NICER and *NuSTAR* data. The NICER hardness ratio is consistent with being constant with an average hardness of 0.0059. The low hardness indicates that the source is in the soft state when the accretion-disk thermal emission dominates in the X-ray spectrum. The average *NuSTAR* hardness ratio is 0.025 for the simultaneous observation with *IXPE*.

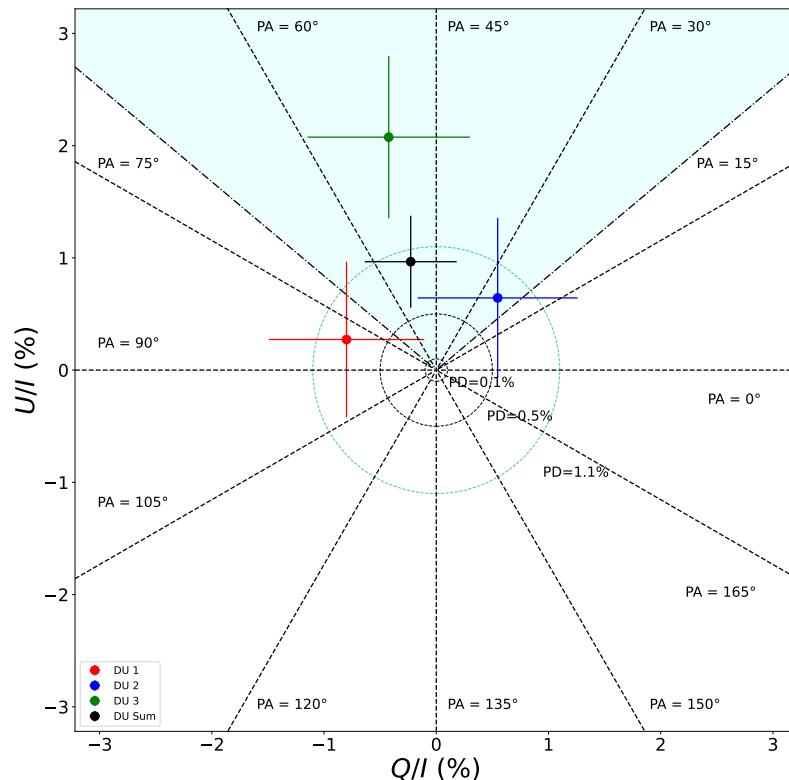


Figure 6.3: Normalized Q/I and U/I Stokes parameters and corresponding polarization degree and angle for DU1 (red), DU2 (green), DU3 (blue), and the sum of the three units (black). The (light green) circle represents the MDP value at the 99% confidence level and the cyan-shaded area the direction and projected full opening angle of the ionization cone. The data are obtained using a single energy bin in the 2–8 keV energy band. We report the uncertainties at 1σ level (i.e. at the 68.3% c.l.).

6.2.1 Polarization measurement

Considering the sum of the three DUs, *IXPE* measured a polarization degree of $1.0 \pm 0.4\%$, with a polarization angle of $51.6^\circ \pm 11.8^\circ$ in the north-east direction. The detected PD lies below the MDP_{99} for the observation of 1.1% (as defined in equation 2.43); as such, we cannot exclude the possibility that the detected polarization signal is due to stochastic fluctuations. Because of this, the measurement corresponds to a 3σ upper limit on polarization degree of 2.2%, while the polarization angle must be considered as unconstrained.

However, the normalized Stokes parameters (Q/I and U/I) for a single energy bin 2-8 keV, shown in Figure 6.3, hints at the polarization angle being roughly aligned with the ionization cone structure detected in He II and O III line ratio maps at 225° north-east (with a projected full opening angle 50°) [Cooke et al., 2007, Cooke et al., 2008].

Although no significant average polarization is observed, a time-dependent signal may still be present in the *IXPE* observation. To check for this possibility, we adopted the dedicated `ixpeobssim` function to calculate the normalized Stokes parameters Q/I

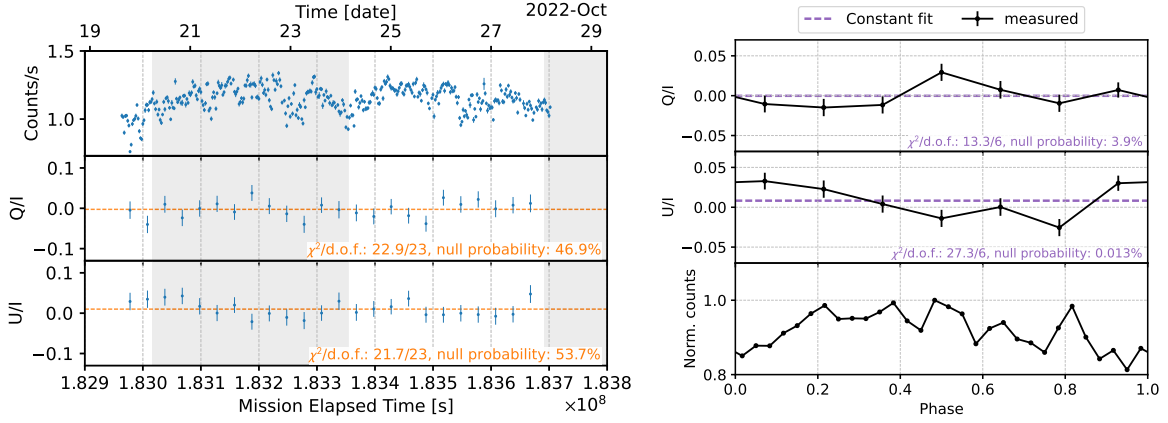


Figure 6.4: (left): Counting rate (top) and normalized Stokes Q and U parameters (middle and bottom, respectively) measured by *IXPE* as a function of time in the 2 – 8 keV energy band. The time bin is 2 ks for the counting rate and 30 ks for Q and U . The gray-shaded and white regions identify subsequent orbits of LMC X-1. (right): Variation of the normalized Stokes parameters Q (top) and U (middle), and of the normalized *IXPE* flux (bottom, normalized to its maximum observed value) as a function of the orbital phase of LMC X-1, selecting only the events in the 2 – 4 keV energy range. In both panels the horizontal, dashed lines are the best fit with a constant line: the obtained χ^2 , the number of degrees of freedom, and the corresponding null probability are indicated.

and U/I in time bins of 30 ks (see left panel of Figure 6.4). These can be considered independent normal variables [Kislat et al., 2015] and we fit their values as a function of time with a constant line. The fit null probability, which gives the probability that the observed variations around the model are due to chance alone, is $\approx 50\%$ for both Q/I and U/I . We repeated a similar procedure to investigate the possible dependence of polarization on the orbital phase. We first derived the phase of each event from its arrival time using the orbital ephemeris. Then, we folded the events into 7 phase bins. We found that the variation of the normalized Stokes parameters in the entire *IXPE* energy band are compatible with statistical fluctuations, with a null hypothesis probability of 1.1%. However, selecting only the events in the 2–4 keV energy range, the null probability is reduced to 0.0057%, as shown in the right panel of Figure 6.4. This further supports the fact that the emission from LMC X-1 may indeed be polarized at a few percent, but its polarization angle, degree, or both, could depend on the orbital phase. When summing over time scales comparable to the orbital period, an orbital-phase-dependent polarization would be averaged to a low value that would be undetected in the phase-average analysis. However, *IXPE* observed only two complete orbits of LMC X-1 (see Figure 6.4); therefore further observations would be needed to detect orbital-phase-dependent polarization with high statistical confidence.

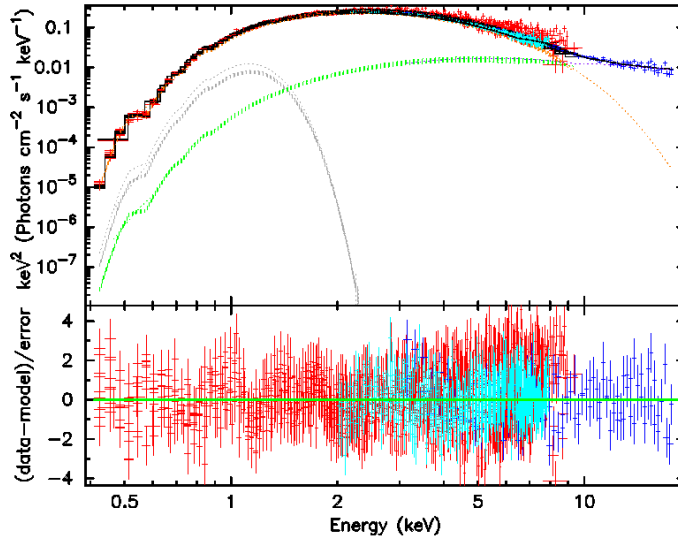


Figure 6.5: X-ray spectra of LMC X-1. *Top panel*: NICER (red), *NuSTAR* (blue), and *IXPE* (cyan) spectra unfolded around the best-fitting model described by Model 6.1 in $EF(E)$ space. The total model for each data set is shown in black with individual GAUSSIAN, KERRBB, and NTHCOMP contributions in light gray, orange, and green, respectively. *Bottom panel*: Model-data deviations (residuals) in σ .

6.3 Spectral analysis

To investigate the various contributions to the source emission we performed a joint spectral analysis of the NICER, *NuSTAR*, and *IXPE* data. Due to the flux and the hardness ratio stability during the observation (see Figure 6.1 and 6.2), we employed the three instruments time-averaged spectra for the spectral fitting procedure. We used the *NuSTAR* spectra up to 20 keV as the background signal becomes comparable to that of the source at higher energies. The ART-XC data were not used for this analysis, because of the significant noise found in the observations. We used the XSPEC package and employed the following Model:

$$\text{GABS} \times \text{TBFEO} (\text{GAUSSIAN} + \text{KERRBB} + \text{NTHCOMP}). \quad (6.1)$$

We used KERRBB [Li et al., 2005] to model general relativistic accretion disk emission from a multi-temperature blackbody and NTHCOMP [Zdziarski et al., 1996, Życki et al., 1999] for the thermally Comptonized continuum. For the KERRBB model, we kept the BH mass and distance fixed at the values reported for the source ($M_{\text{BH}} = 10.9 M_{\odot}$, $d = 50$ kpc) and assumed the disk axis to be aligned with the binary system orbital inclination ($i = 36.4^{\circ}$), i.e. the disk is not warped. We fixed the dimensionless spin parameter of the BH to the best-fitting value of 0.92 found with the continuum fitting method by Gou et al. [2009]. We also kept the spectral hardening factor fixed at 1.7 and assumed no torque at the inner disk edge.

We assumed a simple black body as the seed radiation for the NTHCOMP component and allowed its temperature to vary in the range 0.4 – 1.0 keV. The lower limit was obtained from prior modeling where kT_{bb} was tied to the kT_{in} of the multi-blackbody model DISKBB to calculate the temperature of the inner edge of the accretion disk and

Component	Parameter (unit)	Description	Value
TBFE0	N_{H} (10^{22} cm $^{-2}$)	Hydrogen column density	$0.938^{+0.001}_{-0.001}$
	O	Oxygen abundance	$0.882^{+0.004}_{-0.004}$
	Fe	Iron abundance	$0.78^{+0.01}_{-0.01}$
	z	Redshift	0.0 [†]
KERRBB	η	Inner-edge torque	0.0 [†]
	a_s	Black-hole spin	0.92 [†]
	i (deg)	Inclination	36.4 [†]
	M_{bh} (M_{\odot})	Black-hole mass	10.9 [†]
	M_{dd} (10^{18} g s $^{-1}$)	Mass accretion rate	$1.756^{+0.002}_{-0.002}$
	D_{bh} (kpc)	Distance	50 [†]
	hd	Hardening factor	1.7 [†]
	r_{flag}	Self-irradiation	1 [†]
	l_{flag}	Limb-darkening	0 [†]
	norm	Normalization	1.0 [†]
NTHCOMP	Γ	Photon index	$2.60^{+0.02}_{-0.02}$
	kT_e (keV)	Electron temperature	100.00 [†]
	kT_{bb} (keV)	Seed photon temperature	$0.888^{+0.005}_{-0.005}$
	norm (10^{-3})	Normalization	$2.23^{+0.03}_{-0.03}$

Table 6.1: Best-fitting parameters (with uncertainties at 90% c.l.) of the joint NICER, *NuSTAR*, and *IXPE* spectral modeling with the combined model described by Model 6.1. χ^2/dof for the fit is $\chi^2/\text{dof} = 3497.83/2571$. Parameters indicated with [†] are kept frozen in the spectral analysis. The cross-calibration and instrumental features are shown in Table 6.2.

the Compton up-scattering of seed photons at this temperature. The upper limit is set to the maximum kT_{in} fitted to archival data reported in Gou et al. [2009]. The blackbody seed photon temperature was 0.888 ± 0.005 keV, consistent with values reported in Gierliński et al. [2001] and Kubota et al. [2005]. We find a photon index of 2.60 ± 0.02 , well within previously reported ranges employing the NTHCOMP and POWERLAW models [Jana et al., 2021].

A GAUSSIAN component was added at 0.88 keV with a line width of 0.25 keV to account for an emission feature that resembles the first-order scattering of anisotropic photons onto isotropic electrons [see e.g. Figure 8 by Zhang et al., 2019]. The observation 3 of NICER presented a more pronounced GAUSSIAN component that required different line energy and normalization parameter values with the line width consistent to other NICER observations within the 90% confidence interval. Furthermore, a GABS component was used to model a broad Gaussian-like absorption artifact at 9.66 keV detected with *NuSTAR* that may be due to Comptonization in the upper layers of the disk not being modeled properly, an inhomogeneous corona, a broad instrumental absorption feature, or an unmodelled weak reflection component. The line energies for both of the identified emission and absorption-like features, E_1 in GAUSSIAN and GABS respectively, are left frozen while their line widths and normalization/depth are allowed to vary freely.

TBFE0 [Wilms et al., 2000] was used to account for the X-ray absorption by hy-

Component	Parameter	NICER	NuSTAR		DU1	IXPE	
			FPMA	FPMB		DU2	DU3
GAUSSIAN	E_{line} [keV]	0.88 [†]	-	-	-	-	-
	σ [keV]	0.25 ^{+0.01} _{-0.01}	-	-	-	-	-
	norm [10^{-2} photons $\text{cm}^{-2} \text{s}^{-1}$]	1.74 ^{+0.06} _{-0.06}	-	-	-	-	-
GABS	E_{line} [keV]	-	-	9.66 [†]	-	-	-
	σ [keV]	-	-	0.9 ^{+0.2} _{-0.2}	-	-	-
	Strength [keV]	-	-	0.22 ^{+0.06} _{-0.06}	-	-	-
MBPO	Γ_1	$-0.153 \pm 0.008^{(1)}$	0 [†]	0 [†]	-0.296 ± 0.009	-0.254 ± 0.009	-0.247 ± 0.009
	Γ_2	-	-	-	1.1 ± 0.03	1.3 ± 0.07	1.6 ± 0.04
	E_{br}	-	-	-	6.38 ± 0.03	6.77 ± 0.04	6.49 ± 0.03
	N_{mbpo}	$0.879 \pm 0.005^{(1)}$	0.869 [†]	0.867 ± 0.005	0.693 ± 0.005	0.684 ± 0.005	0.660 ± 0.005

Table 6.2: Modeling cross-calibration and instrumental features in the spectral and spectro-polarimetric fits presented in Table 6.1. GAUSSIAN parameter values for the NICER observation 3 are $E_1 = 0.85$ keV and $\text{norm} = 0.034 \pm 0.001$ photons $\text{cm}^{-2} \text{s}^{-1}$. NICER MBPO power-law index was fixed between the 10 observations, while the normalization was allowed to vary. The respective normalization values in the observations 2–10 are: 0.896 ± 0.005 , 0.840 ± 0.004 , 1.022 ± 0.007 , 0.958 ± 0.005 , 0.967 ± 0.005 , 1.000 ± 0.005 , 0.944 ± 0.004 , 0.864 ± 0.005 , 0.879 ± 0.005 .

drogen, oxygen, and iron. The fitted equivalent hydrogen column which accounts for absorption in our Galaxy, in the Large Magellanic Cloud and in the binary system was $(0.938 \pm 0.001) \times 10^{22} \text{cm}^{-2}$. We note that while this value is smaller than the $(1.0 - 1.3) \times 10^{22} \text{cm}^{-2}$ reported in Hanke et al. [2010], these higher values worsen the fit. Although the metallicity should vary along the line of sight, we use a single absorber for simplicity. The iron and oxygen abundances relative to Solar are allowed to vary freely.

We find the best-fitting model has $\chi^2/\text{dof} = 3497.83/2571$. We estimate a BH accretion rate of $\dot{M} = (1.756 \pm 0.002) \times 10^{18} \text{g s}^{-1}$, consistent with values reported for the source in Zdziarski et al. [2023]. The flux in the 2–8 keV energy range is dominated by the accretion disk emission with KERRBB contributing 94%, while the coronal emission (NTHCOMP) contributes 6%. Figure 6.5 shows the unfolded spectra and the best-fitting parameters as reported in Table 6.1. The obtained χ^2/dof for the best-fitting model is greater than 1, despite the addition of a 0.5% systematic uncertainty to all instruments used in the data analysis apart from NICER, where we accounted for 1.5% systematic uncertainty, according to the mission’s recommendation¹. This may be due to several reasons: cross-calibration uncertainties between the different instruments, short-term source variability, different exposure intervals of the various satellites, and complexity of the X-ray spectra of Galactic BHs which may be not fully captured by the model. However, as a detailed spectral analysis is beyond the scope of the paper and a visual inspection of the residuals seems to indicate that the global fit is not obviously incorrect, we used the best-fitting model to derive the polarization properties of the various spectral components.

¹NICER calibration recommendations can be found at <https://heasarc.gsfc.nasa.gov/docs/nicer/analysisisthreads/cal-recommend/>

Component	Parameter (unit)	Description	Value
POLCONST (1)	Π (%)	Polarization degree	≤ 1.6
	Ψ (deg)	Polarization angle	Unconstrained
POLCONST (2)	Π (%)	Polarization degree	≤ 35.3
	Ψ (deg)	Polarization angle	Unconstrained

Table 6.3: Best-fit parameters of the *IXPE* polarimetric analysis. The components POLCONST (1) and (2) are used in Model 6.2 to describe the polarization properties of the disk and the corona emission, respectively.

6.4 Polarimetric analysis

For the polarimetric fit of our data, we removed the NICER and *NuSTAR* spectra and included the *IXPE* Q and U spectra. Since our aim here was to explore the polarimetric properties of the source with the simplest possible model, we removed both GAUSSIAN and GABS component from Model 6.1 and we convolved the thermal and the Comptonized components with the polarization model POLCONST; this is characterized by two parameters, the polarization degree Π and angle Ψ , both constant with energy. Thus we employed Model 6.2 in the fitting procedure defined as follows:

$$\text{TBFE0} * (\text{POLCONST} * \text{KERRBB} + \text{POLCONST} * \text{NTHCOMP}). \quad (6.2)$$

We maintained the spectral parameters frozen at the values shown in Table 6.1, while allowing both components' polarization degree and angle to vary freely during the fitting procedure. As a result, we obtained a best-fit $\chi^2/\text{dof} = 842.5/894$, with the polarization parameters values listed in Table 6.3.

Because we obtained only an upper limit on the polarization degree, we were not able to constrain the polarization properties of both spectral components at the same time. Thus we decided to further analyze the polarimetric data by tying the two components' polarization angles. In particular the polarization degree and angle associated with the accretion disk thermal emission were left free to vary, while we linked the polarization angle of the coronal emission to that of the thermal emission. As we discussed in section 2.3.2, the polarization vector of the thermal emission is expected to be either parallel or perpendicular to the disk symmetry axis. However, the Chandrasekhar-Sobolev result and many simulation studies suggest that the thermal emission is locally likely to be polarized perpendicular to the disk symmetry axis, especially when considering optically-thick disk atmospheres with large optical depth [Dovčiak et al., 2008, Taverna et al., 2020], or when accounting for absorption processes alongside scattering ones [Taverna et al., 2021, see also Chapter 3]. The coronal emission polarization vector can be either parallel or perpendicular to the disk axis, however, the observation of Cyg X-1 [Krawczynski et al., 2022] as well as theoretical predictions for a flat corona sandwiching the disk [see e.g. Poutanen and Svensson, 1996, Schnittman and Krolik, 2010, Krawczynski and Beheshtipour, 2022] suggest that this component is polarized in the same direction as the disk axis. Hence, in this polarimetric fit we forced the polarization vectors of the two components to be perpendicular to each other. In this configuration, the total polarization degree of the model is given

by the difference between the two components' contribution, effectively allowing for two unphysically large polarization degree values at the same time. To avoid this, we restricted our analysis to three reasonable values for the coronal emission polarization degree: 0%, 4% [the best-fitting value for coronal emission polarization degree found for Cyg X-1 in [Krawczynski et al., 2022](#)], and 10%. The resulting contour plots for the polarization degree and angle of the thermal emission are shown in Fig. 6.6. The ionization cone orientation of $\sim 50^\circ$ suggests that the projected accretion disk plane is perpendicular to the projected jet-remnant direction [see e.g. [Krawczynski et al., 2022](#)], i.e. approximately $-45^\circ \pm 25^\circ$ in our plots, which is marked by the yellow-shaded region in Fig. 6.6, taking into account the observed projected full opening angle of the ionization cone. Thus the thermal component is expected to be polarized in this direction.

When assuming the coronal emission to be unpolarized, we found an upper limit of 2.5% on the thermal emission polarization degree, while forcing the polarization angle to be directed as the projected accretion plane this value reduces to 1%, which is marked by the orange dot in top panel of Fig. 6.6. When taking into account the coronal emission polarization, the contour plots show two minima, representing two allowed configurations. In one case the thermal component is polarized in the same direction as the projected accretion plane with a low polarization degree, while in the other it is polarized perpendicularly to it, but with a larger polarization degree. In both cases, the polarization degree upper limits tend to increase, becoming as high as 2.4% and 2.2% when the Comptonized component polarization degree is fixed at 4% and 10%, respectively; and 0.9% and 0.9%, if we further assume the suggested system orientation, which is marked by the orange dots in middle and bottom panels of Fig. 6.6. These polarization degree values are all well within the Chandrasekhar estimates for the polarization of thermal radiation. The polarization angle value is unconstrained at the 99% c.l. in all cases (see Fig. 6.6).

We also attempted a joint spectro-polarimetric fit in XSPEC, using a physical model of thermal emission KYNBBRR [[Taverna et al., 2020](#), [Mikušincová et al., 2023](#)], while keeping the phenomenological constant polarization prescription to the power-law component. Although this approach in theory allows to put constraints on the polarization of the Comptonization component, the BH spin and the accretion disk inclination, we could not obtain any reasonable restrictions on these parameters, given our spectral and polarimetric data.

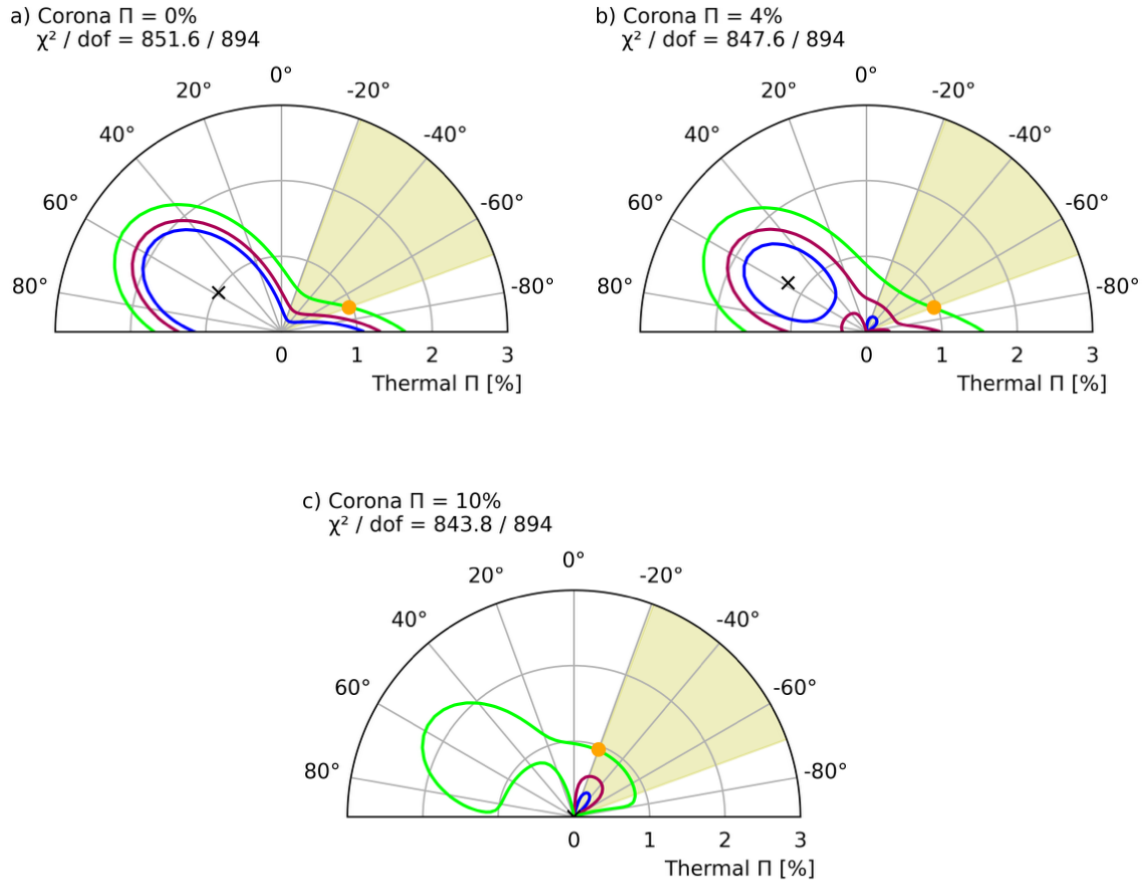


Figure 6.6: Contour plots of the polarization degree Π and angle Ψ associated to the accretion disk thermal emission. Blue, red, and green lines indicate 68%, 90%, and 99% c.l. for two parameters of interest, respectively. The black cross indicates the best-fit parameters for the χ^2/dof value shown in the label. The coronal emission is assumed to be polarized perpendicularly to the thermal component, and its polarization degree is fixed at 0% (*top*), 4% (*middle*), and 10% (*bottom*). The yellow-shaded region indicates the projected accretion disk plane, perpendicular to the projected ionization cone. The orange dots represent the 3σ upper limit of thermal emission polarization degree, assuming that this component is polarized in the same direction as the projected accretion disk plane, i.e. perpendicularly to the observed projected ionization cone direction. The accretion disk is assumed to be aligned with the orbital inclination $i = 36^\circ$.

Component	Parameter (unit)	Description	Value
TBFE0	N_{H} (10^{22} cm^{-2})	Hydrogen column density	$0.624_{-0.165}^{+0.003}$
	O	Oxygen abundance	$0.82_{-0.44}^{+0.01}$
	Fe	Iron abundance	< 0.41
	z	Redshift	0.0^{\dagger}
COMPPS	τ	Optical depth	1.26 ± 0.09
	kT_{e} (keV)	Electron temperature	10 ± 1
	kT_{bb} (keV)	Inner disk temperature	0.81 ± 0.01
	cosIncl	Cosine of the inclination angle	0.81^{\dagger}
	cov_fac	Covering fraction	1^{\dagger}
	R	Reflection fraction	0^{\dagger}
	norm	Normalization	94 ± 4
GABS	E_1 (keV)	Line energy	9.64^{\dagger}
	σ (keV)	Line width	1.17^{\dagger}
	Strength (keV)	Line depth	1.15^{\dagger}

Table 6.4: Parameters of the best fit (with uncertainties at 90 per cent confidence level) of the joint NICER and *NuSTAR* spectra using the COMPPS model. G_{min} parameter of the COMPPS was set to -1 to obtain a fully thermal distribution of electrons, and all other parameters not mentioned in the table are set at default values. χ^2/dof for the fit is 1231/1125.

6.4.1 Slab-Corona modeling

As an additional modelization of the low polarization degree observed by *IXPE*, we performed simulations of a slab coronal geometry with a cold disk and a hot Comptonization medium above it using the radiative transfer code COMPPS [Veledina and Poutanen, 2022]. This code splits the radiation field produced by Compton scattering in different orders and computes their intensities, source functions and polarization [Poutanen et al., 2023], following the procedures described in Poutanen and Svensson [1996]. For consistency with the spectral data, we performed additional spectral fit with this model, using the same spectra as in the spectral analysis described in section 6.3. As COMPPS describes both the comptonized component and the underlying disk emission, we replaced it to the KERRBB and NTHCOMP of Model 6.1. Moreover, to prevent potential confusion arising from the soft excess feature discussed in Section 6.3, data below 1 keV for NICER were excluded from the analysis, as well as the GAUSSIAN component. Thus, the spectral model employed in XSPEC is:

$$\text{GABS} \times \text{TBFE0} (\text{COMPPS}). \quad (6.3)$$

In the COMPPS model, the covering fraction was fixed to unity while the reflection fraction was set to zero, as no reflection features were seen in the spectra. We used a constant to account for instrumental uncertainties, TBFE0 for the neutral absorption and an additional gaussian absorption between 9 to 10 keV GABS to account for an absorption feature discussed in detail in the spectral analysis in Section 6.3. The

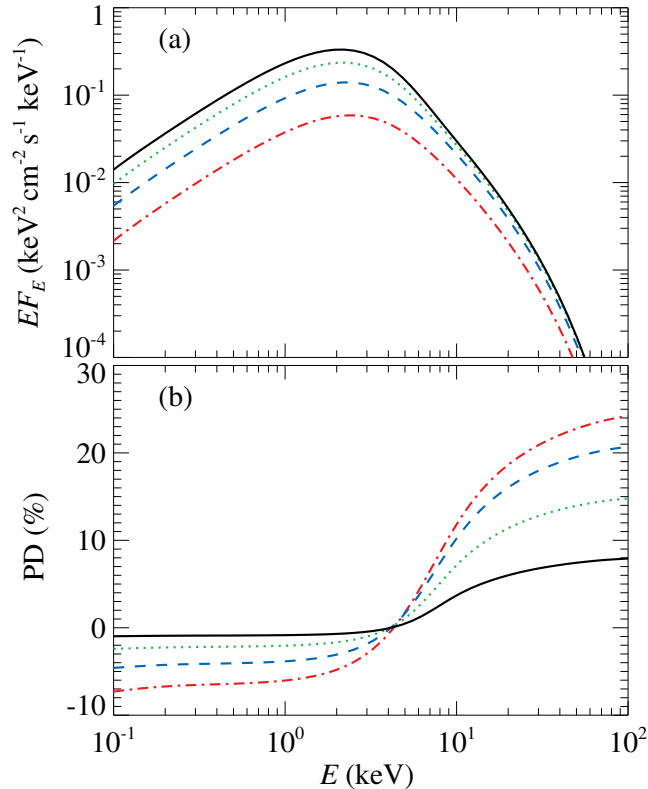


Figure 6.7: Spectral energy distribution (a) and polarization degree (b) obtained for the slab corona model. Lines correspond to different inclinations: $i = 30^\circ$ (black solid), 45° (green dotted), 60° (blue dashed) and 75° (red dot-dashed).

constant for NICER spectrum was frozen at 1.0, while the fit resulted in 0.91 and 0.89 for *NuSTAR*-FPMA and *NuSTAR*-FPMB, respectively. We obtained the best fit for an inner disk temperature of 0.81 ± 0.01 keV, for an electron temperature of 10 ± 1 keV and for an optical depth of 1.26 ± 0.09 . The χ^2/dof for the fit is 1231/1125. The parameters of the fit are outlined in Table 6.4. The χ^2/dof appears better than for the spectral fit described in Section 6.3 due to the intentional reduction of the NICER energy range, which excludes some intricate spectral features in the soft X-rays (see Fig. 6.5), and due to the better capture by the COMPPS model of the joint spectrum.

Using the spectral parameters detailed in Table 6.4, we modeled the polarization properties of the system, assuming the disk photons to be polarized according to the Chandrasekhar-Sobolev profile [Chandrasekhar, 1960, Sobolev, 1963]. The resulting spectra and polarization degree for different inclinations ($i = 30^\circ, 45^\circ, 60^\circ$ and 75°) are shown in Figure 6.7. Positive(/negative) PD values correspond to polarization parallel(/orthogonal) to the disk axis. The change of polarization sign at ~ 5 keV is a known feature of the slab corona geometry [see e.g. Poutanen and Svensson, 1996], as the sign of each Compton scattering order is controlled by the angular distribution of the incoming (seed) photons. We find that, for the considered parameters, the switch between negative and positive polarization degree occurs in the middle of *IXPE* range. This might be the reason for the low net polarization degree averaged over the entire 2–8 keV band, and can plausibly serve as a mechanism for switching between the positive

and negative polarization degrees seen in Fig. 6.4: variations of the parameters lead to variations of the characteristic energy of zero polarization. In this case, the variations likely have a stochastic, rather than periodic (e.g. at orbital period) origin.

6.5 Discussion

The first X-ray polarimetric observation of LMC X-1 by *IXPE* found a low polarization degree for the source, slightly below the MDP_{99} value of 1.1%. As such, we consider the result as an upper limit, and the polarization direction cannot be constrained. The normalized Q and U Stokes parameters of the three DUs, however, hints toward an alignment of the source polarization with the ionization cone observed in He II and O III line ratios, suggesting the need of new polarimetric observation to confirm this hypothesis. This is supported also by the weak evidence for time variability of the polarization, that could also be attributed to a stochastic origin in a slab corona scenario sandwiching a thermally radiating accretion disk. Our spectral analysis found the source in the high/soft state with a dominant thermal component in the X-ray band, a power-law Comptonization component that begins to prevail around ~ 10 keV, and a negligible reflection contribution. The polarimetric data are consistent with theoretical predictions for pure thermal emission from a geometrically thin and optically thick disk with a Novikov-Thorne profile, assuming Chandrasekhar's prescription for polarization due to scattering in semi-infinite atmospheres. Spectro-polarimetric fitting leads to upper limit (at 99% confidence level) on the polarization degree of the thermal radiation to be 1.0%, 0.9% or 0.9% when the polarization of power-law component is fixed to 0%, 4% or 10%, respectively, if the two components are polarized perpendicular to each other and if we assume a preferred system orientation given by the optical data from literature. The observation did not allow statistically significant constraints on the BH spin nor the disk inclination.

Chapter 7

LMC X-3

7.1 Introduction

The subject of this Chapter is the study of the first X-ray polarization measurement of LMC X-3, as detailed by Svoboda et al. [2024b]. LMC X-3 is an X-ray binary located in the Large Magellanic Cloud (LMC) at the most recently estimated distance $D = 49.59 \pm 0.09$ (statistical) ± 0.54 (systematic) kpc [Pietrzyński et al., 2019]. The mass of the black hole, companion star, and the inclination of the system are constrained from optical photometric and spectroscopic observations: $M_{\text{BH}} = 6.98 \pm 0.56 M_{\odot}$, $M_{\text{star}} = 3.63 \pm 0.57 M_{\odot}$, and $i = 69^{\circ}, 2$ [Orosz et al., 2014]. In the X-rays, LMC X-3 was first detected by *Uhuru* satellite [Leong et al., 1971] and has subsequently been observed by all major X-ray satellites, owing to its persistent nature. These studies revealed the source to reside primarily in the soft state [Treves et al., 1988, Ebisawa et al., 1993, Nowak et al., 2001], with only rare hard-state occurrences [Wilms et al., 2001, Wu et al., 2001] and occasional entry into an anomalous low state characterized by a drop in X-ray flux by a few orders of magnitude [Smale and Boyd, 2012, Torpin et al., 2017].

Given the known distance and almost persistent stay in the high/soft state, LMC X-3 has been identified as one of the most promising targets for black-hole spin measurements using the X-ray continuum fitting method. Steiner et al. [2010] analyzed a large set of RXTE observations and found a constant inner disk radius until reaching a critical luminosity, found to be around $0.3 L_{\text{Edd}}$. For higher luminosities, the measured value for the innermost disk radius increased, indicating a change in the structure of the accretion disk or the disk atmosphere. To account for this behavior, slim-disk models were developed [Straub et al., 2011]. The slim disk is a solution with the aspect ratio $H/R \lesssim 1$ (where H is the scale height of the disk and R is the radius from the center). However, the apparent increase of the innermost disk radius at high luminosity remained unsolved.

As discussed in section 1.1, the BH spin is closely related to the innermost disk radius, assuming the accretion disk extends down to ISCO. The first spin estimates of LMC X-3 were affected by uncertainty due to the unknown mass of the black hole. More accurate spin measurements were possible only following precise determination of the black hole mass from optical spectroscopy [Orosz et al., 2014]. The spin was measured through the X-ray continuum fitting method as $a_s \approx 0.2$ [Steiner et al., 2014]. The low value of the black-hole spin has been subsequently confirmed in more recent

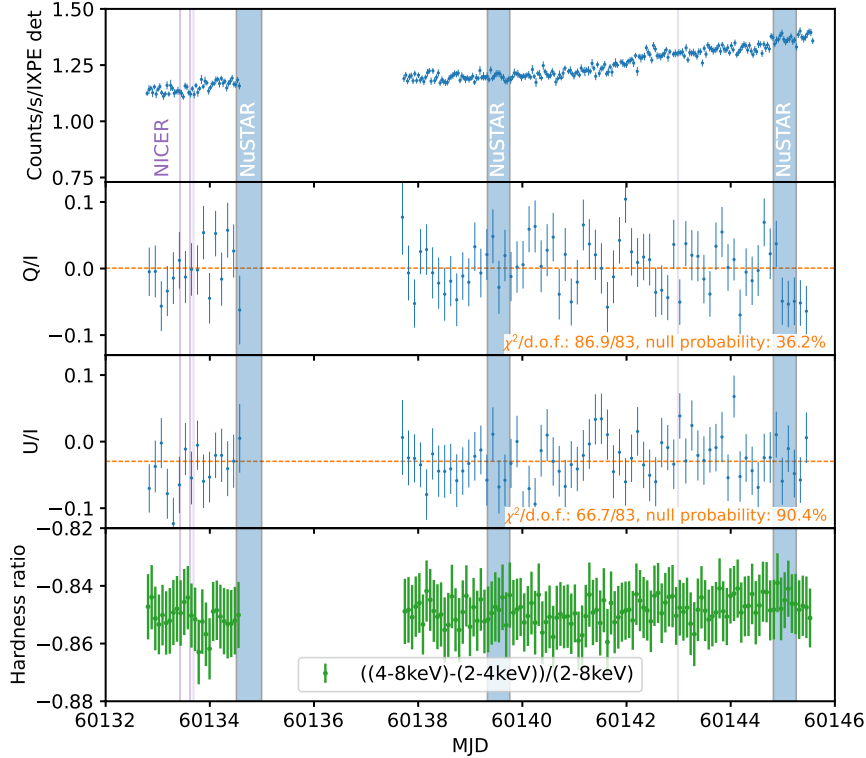


Figure 7.1: *IXPE* light curve: variation of the counts (*top* panel), normalized Stokes parameters Q/I (*second* panel) and U/I (*third* panel), and spectral hardness (*bottom* panel), as a function of time (in Modified Julian Date). The dates of the accompanying observations by NICER and *NuSTAR* are indicated as shaded regions.

analyses [Bhuvana et al., 2022, Yilmaz et al., 2023]. Yilmaz et al. [2023] reported a measured value for black-hole spin as $a_s \approx 0.1$. In their analysis, they relaxed the condition of a constant innermost radius at ISCO and showed a scatter of the inner disk radius measurements in different observations during the outbursts (see their Figure 7 and 9).

7.2 Datasets

LMC X-3 was observed in July 2023 by multiple X-ray instruments. *IXPE* observed the source on 2023 July 7–8 and 12–21 with a total exposure time 562 ks. NICER Arzoumanian et al. [2014] carried out two observations of LMC X-3 during the *IXPE* campaign, on 2023 July 8 and 17, for a useful exposure time of ≈ 2.2 ks and ≈ 160 s, respectively. These two observations were initially extracted separately per continuous GTI segment. After checking their mutual consistency, we merged them together for the spectral analysis. Three accompanying observations by the *NuSTAR* satellite [Harrison et al., 2013] were performed at the beginning, in the middle and at the end of the *IXPE* observation with the total net exposure time of ≈ 85 ks. We found that the background dominates over source above 20 keV. Therefore, we limit the *NuSTAR* data of LMC X-3 at high energy to be below 20 keV in all spectral analysis. Moreover,

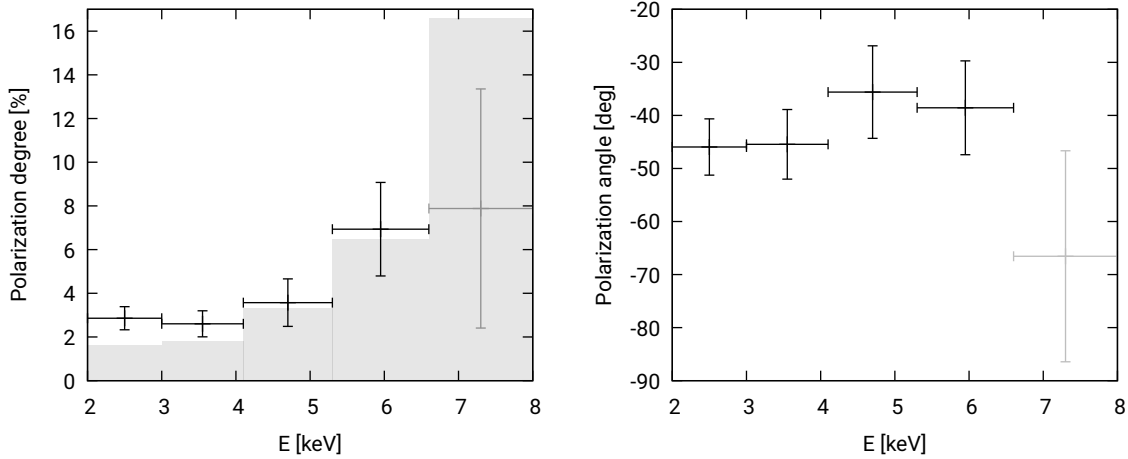


Figure 7.2: Measured PD (*left*) and PA (*right*) shown with 1σ error bars. The shaded area in the PD-plot is an estimate of the MDP_{99} , showing the significant polarization measurements from 2 keV up to ≈ 6.5 keV.

simultaneous to NUSTAR, the Neil Gehrels SWIFT Observatory [Gehrels et al., 2004] observed LMC X-3 with exposure times of 1.3 ks (09 July 2023), 1.8 ks (14 July 2023), and 1.9 ks (20 July 2023). Data reduction and processing are described in more detail in Appendix A.

7.2.1 Polarization measurement

The IXPE light curve is shown in Figure 7.1. LMC X-3 shows a steady continuous increase of the flux during the exposure. The count rate (averaged over all 3 GPDs) increased from about 1.2 cts s^{-1} at the beginning of the observation to 1.5 cts s^{-1} at the end of the observation. The Q/I and U/I light curves are shown in the middle panels of Figure 7.1. The variations observed are consistent with statistical fluctuations only, with a successful joint fit of a constant to both Q/I and U/I light curves achieving $\chi^2/\text{dof}=153.7/166$. There is also no evidence for any significant changes in the spectral hardness, defined as the difference between counts in the hard (4–8 keV) and soft (2–4 keV) energy bands divided by the total number of counts in the 2–8 keV band, as shown in the bottom panel of Figure 7.1.

The average 2–8 keV PD for all three detectors is $\text{PD} = 3.2\% \pm 0.4\%$, and the $\text{PA} = -45^\circ \pm 4^\circ$. The measurements are above the MDP_{99} , which in our observation is 1.23% in 2–8 keV. The energy dependence of PD and PA is shown in Figure 7.2, with the data binned in 5 energy bins. Measurement of the polarization above the MDP_{99} is achieved in the entire band except for the highest-energy bin (6.5–8 keV) where the MDP_{99} is higher than the actual measurement. In the 2–5 keV energy band, the PD is around 3%. An increasing trend of polarization with energy is apparent from the plot, but the measurement uncertainty gets significantly larger (see more in section 7.5). The polarization angle is consistent with being a constant with only possible small deviations at higher-energy bins.

7.3 Spectral analysis

Our study of the spectral properties of the source started with a preliminary analysis of the time variability of NICER, *NuSTAR* and *Swift* spectra. For this purpose, we used a simple absorbed multi-colored disk black body emission [Mitsuda et al., 1984] and power-law component for the Comptonization; we included TBABS model to account for absorption in the line-of-sight in our Galaxy [Wilms et al., 2000] and fixed the value of the hydrogen column density $N_{\text{H}} = 4.5 \times 10^{20} \text{ cm}^{-2}$ from a full sky HI survey [HI4PI Collaboration et al., 2016]. We further add a cross-normalization factor to account for changes between different instruments. The model in XSPEC notation is `CONST*TBABS*(DISKBB + POWERLAW)`. The disk temperature as well as the power-law photon index values were linked between different instruments and also between different exposures. Only the normalization factors of both components (disk black body and power law) were allowed to vary to determine if there is any spectral variability and of which component.

We found that the disk blackbody emission dominates the spectrum with the Comptonization component being significant only for *NuSTAR* observations. For the inner disk temperature, we obtained the value $kT \approx 1.1 \text{ keV}$. We get the power-law photon index of $\Gamma \approx 2.4$. The *NuSTAR* observations reveal a clear variability of the Comptonization component above $\approx 15 \text{ keV}$. The simple DISKBB + POWERLAW model allows us to estimate the fraction of the Comptonized emission, which is less than 1% in 2–8 keV, with the strongest Comptonization component being measured in the last observation. From this quick analysis, it is evident that the Comptonization contributes very little to the *IXPE* 2–8 keV energy band, and thus we can assume that the measured polarization is related to the main component, which is the thermal emission of the accretion disk.

From comparing the three *Swift* spectra, we see that there is no significant variability in the soft X-ray band, confirming the results suggested from the *IXPE* hardness ratio shown in Figure 7.1. However, a small but apparent difference is around 1.5 keV between the first and the other two observations. Any further investigation of this discrepancy is beyond the scope of this analysis. Therefore, we limited the *Swift* spectra to be in the 2–8 keV energy range for the subsequent spectral analysis with the merged spectra. Similar discrepancies below 2 keV are likewise seen between SWIFT and NICER measurements. These residuals lead to a fit that is not formally acceptable, with a chi-square value of $\chi^2 = 1255$ for 411 degrees of freedom ($\chi_{\text{red}}^2 \approx 3$).

To improve these results, considering the negligible variability of the source spectra, we merged the *Swift* and *NuSTAR* over the three observations. We further performed a spectral analysis of 7 data sets (1 NICER, 2 *NuSTAR* detectors FPMA and FPMB, 1 *Swift* and 3 detectors of *IXPE*) with a cross-calibration constant fixed to 1 for NICER and allowed to vary between 0.8 and 1.2 for the other detectors. To model the already described cross-calibration uncertainties with the *IXPE* spectra, we applied the gain model to fit the offset slope and intercept for *IXPE*. Figure 7.3 shows the time-averaged spectra of different detectors in the top panel.

We first employed a relativistic accretion disk model KERRBB [Li et al., 2005] convolved with a non-relativistic Comptonization model SIMPL [Steiner et al., 2009, Sun-

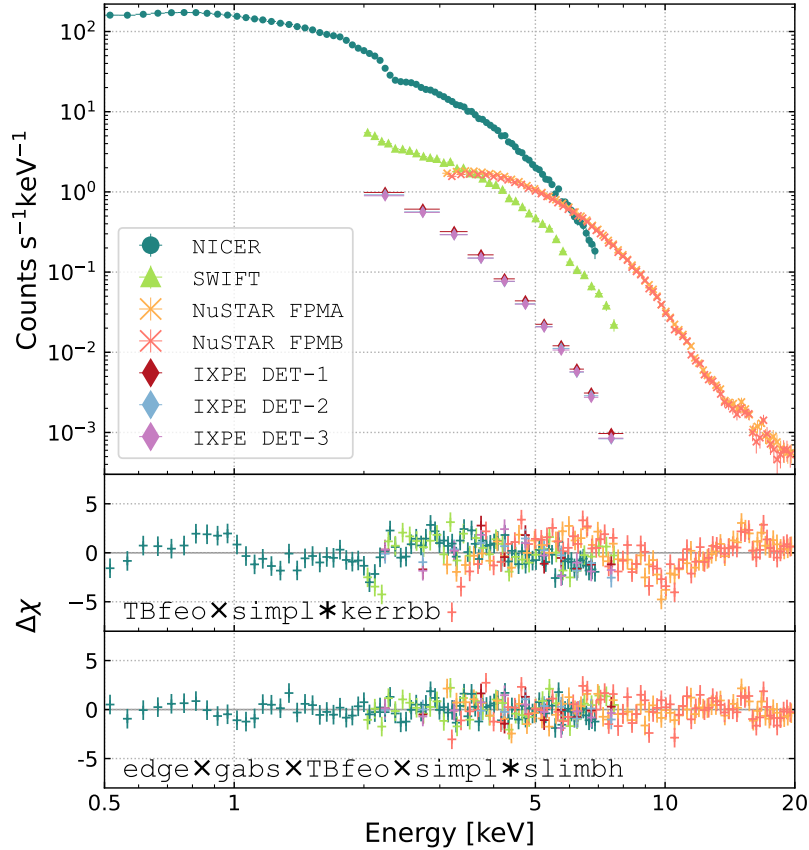


Figure 7.3: *Top*: Time-averaged NICER, *NuSTAR*, *Swift*, and *IXPE* data. *Middle*: The residuals of the data from the model using `tbfeo × simpl * Kerrbb`. *Bottom*: The residuals of the data from the final best-fit model.

yaev and Titarchuk, 1980], allowing for both up- and down-scattering:

$$\text{TBFE0}*\text{SIMPL}*\text{KERRBB} \quad (7.1)$$

For absorption, we employed the TBFE0 model allowing for different oxygen and iron abundances. Because the LMC is a low-metallicity environment, we let the abundances to be in the interval 0.25–1. The fit converged to $N_{\text{H}} \approx 0.03 \times 10^{22} \text{ cm}^{-2}$ with the oxygen and iron abundances being pegged at their low-value limits at 0.25. We note that since the column density is lower than the column density expected in the line-of-sight in our Galaxy, the low oxygen and iron abundances may be an artifact of calibration uncertainties in the 0.5–1 keV band for NICER and/or due to variations of the absorption column within our Galaxy. No evidence for local absorption is consistent with LMC X-3 location at a large distance from the center of the LMC, away from any gaseous nebulae.

With model 7.1, we obtained the dimensionless black hole spin $a_s = 0.20 \pm 0.02$, accretion rate $\dot{M} \approx (4.5 - 5.6) \times 10^{18} \text{ g s}^{-1}$, and the photon index pegged at $\Gamma = 2.0$, which was the lowest allowed value. We allowed the hardening factor of the KERRBB model to vary and we obtained $h_d \approx 1.7$ for *NuSTAR* and $h_d \approx 1.9$ for NICER. The fit was formally not acceptable with $\chi^2/\nu = 676/274 \approx 2.5$, mainly due to discrepan-

Component	Parameter (units)	Description	Value			
			NICER	<i>NuSTAR</i>	<i>Swift</i>	<i>IXPE</i>
TBfeo	N_{H} (10^{22} cm^{-2})	H column density		0.046 ± 0.003		
	O	abundance		0.3 ± 0.2		
	Fe	abundance		0.8 ± 0.4		
SLIMBH	M_{bh} (M_{\odot})	Black hole mass		6.98^{\dagger}		
	a/M	Black hole spin		0.19 ± 0.02		
	L_{Edd}	Luminosity	0.40 ± 0.01	0.43 ± 0.01	0.41 ± 0.02	$0.50^{+0.02}_{-0.04}$
	i (deg)	Inclination		69.2^{\dagger}		
	α	Viscosity		0.1^{\dagger}		
	D_{bh} (kpc)	Distance		49.59^{\dagger}		
	hd	Color hardening		-1 (i.e. using TLUSTY)		
	l_{flag}	Limb-darkening		0^{\dagger}		
	v_{flag}	Self-irradiation		0^{\dagger}		
	norm	normalization		1^{\dagger}		
	SIMPL	Γ	Photon index		2.7 ± 0.3	
FracSctr		scattered fraction		$0.012^{+0.001}_{-0.002}$		
χ^2 / dof				$277/265 \approx 1.04$		

Table 7.1: Spectral fit parameters with the final preferred spectral model, as described in equation 7.3. Uncertainties are reported at the 90% confidence level. Parameters indicated with \dagger are kept frozen in the spectral analysis.

cies between NICER and *NuSTAR* data, whose residuals had opposite slopes in the overlapping energy band (see the second panel of Figure 7.3 at 3–8 keV energy band).

The lowest measured accretion rate $4.5 \times 10^{18} \text{ gs}^{-1}$ corresponds to the luminosity $L = \eta \dot{M} c^2 \approx 0.3 L_{\text{Edd}}$ (where $\eta \approx 0.065$ is the accretion efficiency for $a_s = 0.2$). At such a luminosity, LMC X-3 might deviate from the standard thin disk model, and a slim disk scenario was proposed to take place at the high-luminosity regime [Straub et al., 2011]. Therefore, we replaced the KERRBB model with the SLIMBH model [Sądowski, 2011, Straub et al., 2011]:

$$\text{TBFEO*SIMPL*SLIMBH} \quad (7.2)$$

We obtained a significantly better fit with $\chi^2/\nu = 414/277 \approx 1.5$, thanks to the improved consistency of the data residuals between NICER and *NuSTAR*. The only residuals were now narrow features around 2 keV and 2.4 keV for NICER and 10 keV for *NuSTAR*, which are visible in the second panel of Figure 7.3. Similar residuals in the NICER data were already reported for the other presented sources (see chapters 4, 6, 5) and attributed to calibration uncertainties. The 10 keV dip in the *NuSTAR* data is not apparent in a simple DISKBB+POWERLAW fit and is thus most likely a model-dependent feature present in residuals of both, SIMPL*KERRBB and SIMPL*SLIMBH, models. A similar feature was also reported in the analysis of LMC X-1 (see chapter 6) with the KERRBB + NTHCOMP model, suggesting its relation to an interplay between a high-energy tail of the relativistic thermal disk emission model and Comptonization. For our final model, we account for the 2 and 10 keV features with narrow Gaussian absorption lines and the 2.4 keV feature with a ‘smeared-edge’ component. The goodness of the final fit is $\chi^2/\nu = 277/265 \approx 1.04$. The residuals from the best-fit model are shown in the third panel of Figure 7.3. The values of the best-fit model are summarized in Table 7.1.

Component	Parameter	NICER	NuSTAR		Swift	IXPE		
			FPMA	FPMB		GPD 1	GPD 2	GPD 3
CONSTANT		1 [†]	1.18 ± 0.03	1.16 ± 0.03	1.23 ± 0.07	0.88 ± 0.02	0.86 ± 0.02	0.81 ± 0.02
GABS	E (keV)	2.07 ± 0.04		9.9 ± 0.1	2.14 ± 0.04		-	
	σ (keV)	0.08 ^{+0.02,pegged} _{-0.06}		0.1 (pegged)	0.03 ± 0.03		-	
EDGE	E (keV)	2.35 ± 0.05		-	-		-	
	τ (keV)	0.02 ± 0.02		-	-		-	
GAIN	slope	-		-	-	0.95 ^{+0.02} _{-0.01}	0.96 ± 0.01	0.95 ^{+0.02} _{-0.01}
	offset (keV)	-		-	-	0.08 ^{+0.02} _{-0.04}	0.05 ^{+0.03} _{-0.04}	0.07 ^{+0.03} _{-0.04}

Table 7.2: Modeling cross-calibration and instrumental features in the final spectral fit.

The spin value is consistent with the measurements using the KERRBB model, $a_s \approx 0.20 \pm 0.02$. The spectral hardening in the SLIMBH model is not a free parameter but is instead calculated using the vertical structure computed using the TLUSTY code [Hubeny and Lanz, 1995]. The estimated luminosity is in the range $L = 0.40 - 0.45 L_{\text{Edd}}$ depending on which detector is considered (the slightly higher value for IXPE can be, however, affected by the fitted cross-calibration constants lower than 1). The parameters of the Comptonization model SIMPL were constrained well only from the NuSTAR spectra and therefore, we linked the values between the different detectors. The photon index is $\Gamma = 2.7 \pm 0.3$ and scattering fraction is $0.012^{+0.001}_{-0.002}$. Similarly, absorption was best constrained from the NICER data and we linked the absorption parameters for the different detectors to it.

In our preferred model, the black hole mass and inclination are initially fixed to the values from the dynamical measurements [Orosz et al., 2014]. Because in the IXPE observation of Cyg X-1 the inclination of the innermost accretion disk from the X-ray spectroscopy and polarimetry was found to be different from the value for the orbital inclination [Krawczynski et al., 2022], we also performed an alternative spectral fit with free inclination. The best-fit value of the inclination changed slightly to $i = 71.8^{+2.0}_{-1.2}$ deg, and corresponding inferred luminosity increased from $L = 0.43 L_{\text{Edd}}$ to $L = 0.48 L_{\text{Edd}}$. The goodness of the fit improved by $\Delta\chi^2 = 310 - 317 = -7$ compared to the initial fit. This improvement was only marginal and we conclude that the inclination of the accretion disk constrained from the X-ray spectra is consistent with the inclination of the binary system derived from the optical measurements.

7.4 Polarimetric analysis

We first included the IXPE Q and U spectra into our analysis by taking our best-fitting spectral model from Table 7.1 and assigning a constant PD and PA to it using the POLCONST model. For Q and U spectra, we applied the same gain as for I spectra, and we also kept the cross-normalization factors. The only free parameters were the PD and PA, noted as A and ψ in the polconst model. Considering the full IXPE bandpass yields a PD of $A = 3.2\% \pm 0.6\%$ and a PA $\psi = -42^\circ \pm 6^\circ$.

To test whether the polarization is increasing linearly with the energy, we replaced the POLCONST model by POLLIN and fitted the 2–8 keV I , Q , and U spectra. The polarization fraction in the POLLIN model is parametrized with the polarization fraction at 1 keV, A_1 , and the slope A_{slope} . We obtained a similarly good fit as with the

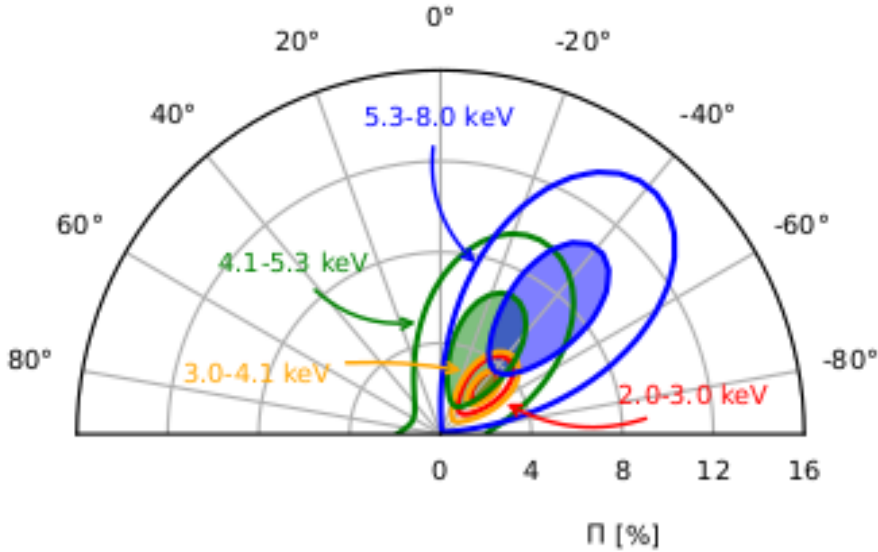


Figure 7.4: Polar plot of the polarization measured in different energy ranges with the spectral best-fit model. The filled contours correspond to the 68% (1σ) and the outer contours to the 99.9% confidence levels, respectively.

`polconst` model with $A_1 = 1_{-1}^{+2}\%$ and $A_{\text{slope}} = (6 \pm 6) \times 10^{-3}$, i.e. being consistent with constant polarization. The statistical improvement is only marginal with $\Delta\chi^2 \approx 2$ for 1 additional free parameter, giving the F-test probability ≈ 0.4 that the improvement is just coincidental.

To investigate any (other than linear) energy dependence, we performed the fit in four different energy bands spanning 2–8 keV and calculated contours using 50 steps in each parameter. We defined the energy bands as: 2–3, 3–4.1, 4.1–5.3, and 5.3–8 keV. Figure 7.4 shows the resulting contours in the polar plot of PD and PA. While there is an apparent trend of increasing PD with the energy as in Figure 7.2, the significance of the change is not high. The PD is consistent with being a constant below 5 keV, and increases with energy above 5 keV only at 1σ confidence level.

We then proceeded to fit physical models that self-consistently predict energy-dependent polarization properties. Since no polarized slim-disk model currently exists, we were limited to fitting standard thin-disk models. For simplicity, we neglected the contribution due to the Comptonization that is less than 1% in the 2–8 keV energy range. As in previous analysis, we employed the relativistic thin Novikov-Thorne disk model `KYNBBRR` [Taverna et al., 2020, Mikušincová et al., 2023]. A joint fit of the *IXPE* I , Q , and U spectra provided an acceptable fit with $\chi^2/\nu = 102/95$ using the model:

$$\text{CONST*TBFE0*KYNBBRR} \quad (7.3)$$

The parameters of the absorption, cross-normalization constants, and gain parameters were fixed to the values from the previous global spectral fit (see Tables 7.1 and 7.2). The only free values in the `kynbbrr` model were black hole spin, measured as $a_s = 0.1 \pm 0.1$, the accretion rate $\dot{M} = 0.45_{-0.04}^{+0.07} M_{\text{Edd}}$, the orientation of the disk rotation axis $\chi_0 = 47^\circ \pm 6^\circ$, and the normalization parameter $N_K = 0.042 \pm 0.005$. The accretion rate

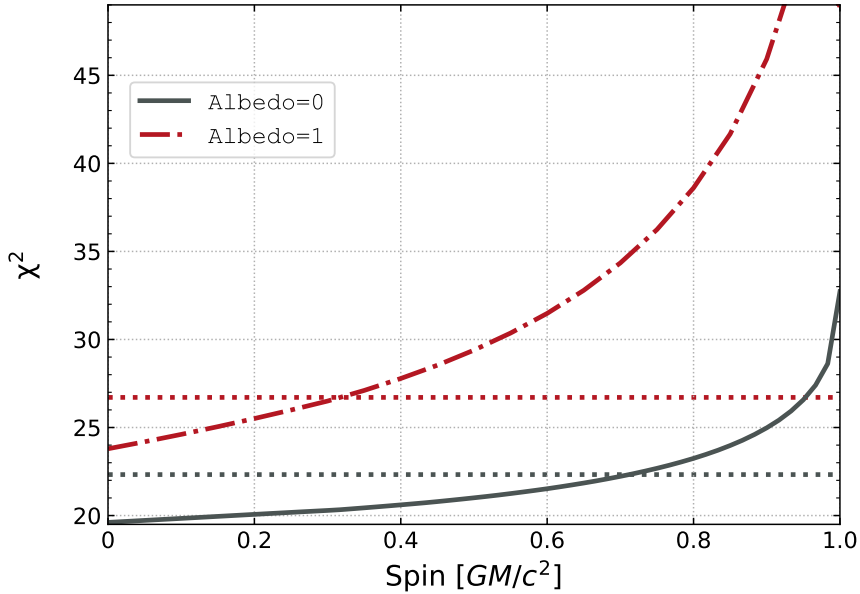


Figure 7.5: Polarimetry constraints of the black hole spin, expressed as goodness of the fit (as the χ^2 values) versus black-hole spin from Q/I and U/I fitting with the `kynbrr` model for two extreme values of albedo: 0 (black solid line) and 1 (red dot-dashed line). The dotted horizontal lines represent 90% confidence levels.

$\dot{M} \approx 0.45 M_{\text{Edd}}$ is consistent with the previous finding using the `KERRBB` and `SLIMBH` models. The normalization in the `KYNBRR` model would be 1 for a source at the distance of 10 kpc. The distance of LMC X-3 is ≈ 50 kpc and thus the normalization value is expected to be around $1/5^2 \approx 0.04$, consistent with the measurement.

For fitting the black-hole spin from the polarimetric measurements only, independently of the total spectrum, we employed the normalized Q/I and U/I spectra, to which we applied the `KYNBRR` model with the normalization fixed to 1. We fixed the accretion rate to $\dot{M} = 0.45 M_{\text{Edd}}$. We tested two cases of `albedo`, 0 and 1. While the `albedo = 0` means that no returning radiation is taken into account, `albedo = 1` corresponds to the 100% reflectivity of the gravitationally light-bended returning radiation. The `albedo` is important mainly for a highly spinning black hole when the ISCO extends closer to the black hole and more returning radiation is expected [Cunningham, 1976].

For the albedo equal to 0, we fitted the Q/I and U/I spectra with the black-hole spin a and χ_0 as free parameters. We obtained a perfectly acceptable fit with $\chi^2/\nu = 19.9/20 \approx 1.0$, $a_s < 0.66$ and $\chi_0 = 44^\circ.6 \pm 6^\circ.4$. For a non-zero value of the albedo, the model is currently calculated for 20 values of the spin and does not allow for a direct fitting of this parameter. We applied the `steppar` command in `XSPEC` to calculate the χ^2 values for the different values of the black-hole spin, and for the comparison, we performed the same procedure for albedo equal to 0.

Figure 7.5 shows the dependence of the fit goodness against the spin value for the two cases with `albedo` equal to 0 and 1, respectively. With the 90% confidence, the black-hole spin is required to be lower than 0.66 for `albedo = 0` and lower than 0.3 for `albedo = 1`. The case of `albedo = 0` is preferred by the fit with lower χ^2 values.

The results indicate that the sole polarimetry measurements are consistent with the low black-hole spin in LMC X-3, independently of the spectral fitting.

7.5 Discussion

The *IXPE* pointing of LMC X-3 observed a polarization degree of $3.2\% \pm 0.4\%$, with a polarization angle of $-45^\circ \pm 4^\circ$. This angle cannot be directly compared to the orientation of the system in the observer’s sky, as there are no known large-scale physical structures associated with this source. LMC X-3 is persistently in the high/soft state and no jet has been detected in the radio despite several efforts [Fender et al., 1998, Gallo et al., 2003, Lang et al., 2007]. There is also no evidence for ionization cones in the far-UV or the presence of any significant emission or absorption lines in soft X-rays [Page et al., 2003].

The level of the PD is consistent with expectations for the thermal disk emission around a black hole with a low spin and high inclination (see the case of $a_s = 0$ and $i = 70^\circ$ in Figure 4 in Mikušincová et al. [2023] with a constant PD just slightly below 3%). The Novikov-Thorne model, assumed in the KYNBBRR spectral model, provides a reasonably good fit to the X-ray polarimetry despite the best-fit spectral model employing a slim disk. This is most likely explained by the limited statistics of the X-ray polarimetry fit, while the spectral fit is sensitive to small differences between the KERRBB and SLIMBH models, which can possibly be attributed to the treatment of the spectral hardening in these models.

The black hole spin, solely constrained from the X-ray polarimetry using normalized Stokes parameters Q/I and U/I , is consistent with the results of determining the spin from the spectral fitting. The constraints on the spin are tighter if the reflection of the returning radiation is taken into account, but even for a model with no reflected returning radiation (`albedo=0`), the spin is constrained to be less than 0.7 (see Figure 7.5).

While there is a hint of an increase of PD with energy (see Figure 7.2, especially above 5 keV), it is not statistically significant and indeed the data are well described by a model with constant PD. However, taking the fact that an increase with energy of PD has been observed in other BHs in soft state (see Figure 8.1), we investigated this behavior more in detail. In particular, we used the model variant KYNEBBRR of KYNBBRR (introduced in the analysis of 4U 1630-47 as (Model C), see section 4.3). We employed this model using the same spectral parameters from the fit of the KERRBB model with only free parameters to be the optical depth τ and χ_0 . The spin was set to $a_s = 0.2$ because letting it free will lead to a tight degeneracy with τ . The accretion rate was fixed to $\dot{M} = 0.45\dot{M}_{\text{Edd}}$, the `albedo` to 0, and the normalization to 1. We obtained a very good fit with $\chi^2/\nu = 15/20 \approx 0.75$. The $\chi^2/\nu < 1$ indicates that the errors might be overestimated. The best-fit parameters are $\chi_0 = 45^\circ \pm 6^\circ$ and $\tau = 5_{-3}^{+4}$.

A similarly increasing trend of the polarization degree with energy has been observed also in 4U 1630-47 and 4U 1957+115 observations, presented in Chapter 4 and 5, respectively. Various explanations have been proposed, and different scenarios might be responsible for the observed trend in different sources. In the case of 4U 1630-47, the notable increase in PD with energy is statistically significant and could be linked to absorption in the accretion disk’s upper layer in combination with a relativistic bulk

motion. This explanation could also account for a PD higher than anticipated in an accretion disk atmosphere dominated by electron scattering [Ratheesh et al., 2024]. For 4U 1957+115 the increase can be explained by a combination of a high spin value and high albedo [Marra et al., 2024]. High albedo is, however, unlikely in the case of LMC X-3 given the low value of the black-hole spin. To perform a robust statistical test of the significance of the PD's increase with energy, a longer observation would be needed to obtain a significant measurement up to 8 keV.

Chapter 8

Conclusions

We now summarize the work presented in Chapters 3-7 of this thesis:

- In Chapter 3 we described the results obtained in our simulations of the spectral and polarization properties of the accretion disk emission. Following the procedure outlined by Taverna et al. [2021], to study the interaction of the radiation with the disk atmosphere we used the photoionization code CLOUDY [Ferland et al., 2017] to model the ionization profile of an optically thick layer located above the disk. We then studied the polarized radiative transfer of photons within this surface layer with the Monte-Carlo code STOKES [Marin, 2018], obtaining the Stokes parameters of the radiation as it emerges from the accretion disk. Our results show that photoelectric absorption and Compton scattering processes can have a strong impact on the emerging radiation polarization properties. Absorption processes, in particular, result in an increase in the radiation polarization degree, reducing the contribution of photons that are scattered multiple times inside the layer. On the other hand, if the plasma is completely ionized, we observe the polarization degree to be constant with energy, except for a bump, observed at high energies, likely caused by Compton down-scattering. A detailed analysis of the CIE and PIE regimes suggests that this high ionization configuration is more easily achieved if photoionization of the layer due to the underlying black body emission is taken into account. We furthermore explored the global accretion disk emission by assuming a temperature and density radial profile for the atmosphere. Our results agree with the findings of Taverna et al. [2021], suggesting that absorption processes are crucial in determining the polarization properties of non-rotating BHs. For maximally rotating objects, instead, the contribution of the absorption is limited by the larger ionization expected for the disk medium. Finally, we included in our computations the relativistic effects influencing the radiation spectro-polarimetric properties during its propagation toward the observed. For this purpose, we modified the KYNBBRR code [Dovčiak et al., 2008, Taverna et al., 2020], including the Stokes parameters of the emerging radiation as input for the ray-tracing code. Our final results show that, despite the depolarization induced by the general relativistic rotation of the polarization plane, the observed polarization degree of the accretion disk emission is larger than that predicted using the Chandrasekhar [1960]’s pure-scattering approximation (see Taverna et al. [2020]). The polarization degree at infinity recalls the one at the

emission, thus presenting a maximum in correspondence of the largest contribution of photoelectric absorption processes, which occur around 2 keV and 10 keV in the CIE case and around 9 keV in the PIE configuration. Also at infinity the polarization degree expected in the non-rotating case (max. $\sim 10\%$) exceeds the value expected for maximally rotating BHs (max. $\sim 3\%$). The GR rotation of the polarization plane also induces a rotation, at high energies, of the polarization angle, which was found to be perpendicular to the accretion disk axis for the emerging photons. A more detailed exploration, including the contribution of returning radiation, is in progress and will be presented in a future work.

- In Part II we described the results obtained by IXPE during its first two years of observation on accreting stellar-mass black holes in soft state. In particular:
 - In Chapter 4 we presented the result of the two observational campaigns conducted by *IXPE* on the transient source 4U 1630-47 [Ratheesh et al., 2024, Rodriguez Cavero et al., 2023]. During the first *IXPE* observation, which took place in August 2022, the source was found in soft state, with the spectrum being dominated by the thermal disk emission despite a small contribution from a Comptonized component. Prominent absorption lines were observed in NICER spectra, and attributed to the presence of a wind. The best spectral fit was obtained by implementing a slim disk model (SLIMBH) in place of a standard thin disk (KERRBB), for a large inclination value and intermediate BH spin ($a_s \approx 0.71$). The polarimetric data revealed a particularly large polarization degree ($8.3 \pm 0.2\%$), increasing with energy from $\sim 6\%$ at 2 keV up to $\sim 10\%$ at 8 keV. This unexpectedly large polarization degree cannot be reached in the standard thin disk scenario, assuming Chandrasekhar [1960] approximation for the disk emission polarization properties, without assuming important modifications. As such, we described several possible modelizations of these data, including our radiative transfer computations. We found that the model that best describes the data is the one assuming the disk emission to be reprocessed in an optically thick, highly ionized atmosphere outflowing toward the observer at relativistic speed. During the second observation, taking place in March 2023, 4U 1630-47 was found in a transition towards a steep powerlaw state, characterized by a larger flux and the hardening of the spectra. Despite the different spectral properties, this SPL state observation exhibited similar polarization properties to the first observation. The polarization degree was observed to be increasing with energy from $\sim 5\%$ at 2 keV up to $\sim 8\%$ at 8 keV, while the polarization angle was found to be consistent between the two observations. To explain these similarities we suggest that the geometry of the emitting region and the physical processes underlying both observations must be similar. In this hypothesis, the lower polarization degree observed in the SPL state observation could be attributed to an increased electron temperature in the disk atmosphere, provoking a transition from a Thomson scattering towards a Compton scattering scenario.
 - In Chapter 5 we described the *IXPE* observation of the LMXB source 4U 1957+115, which took place in May 2023 [Marra et al., 2024]. The

source was found in soft state, with the spectra being well-described by the standard thin disk model (KERRBB) for large values of the disk inclination and the BH spin ($a_s \approx 0.992$), plus a small contribution from a Comptonized component. The detected polarization degree ($1.9 \pm 0.6\%$) revealed an increasing trend with energy, while the polarization angle was found to be constant in the 2–8 keV band. In the spectro-polarimetric analysis, we obtained results in agreement with the spectral fit: the polarimetric data can be described in the standard thin disk scenario, but only assuming a substantial contribution from returning radiation. As this contribution depends on the BH spin and the disk inclination, we obtained a lower limit on both these parameters ($a > 0.96$, $i > 50^\circ$) by assuming a fiducial value of 10% for the corona emission polarization degree.

- In Chapter 6 we presented the *IXPE* observation of LMC X-1 [Podgorný et al., 2023b]. The observation took place in October 2022 and revealed a polarization degree below the MDP₉₉; as such, we consider the polarization degree an upper limit ($\lesssim 2.2\%$), while the polarization angle is by definition unconstrained. Nevertheless, the normalized Stokes parameters Q/I and U/I hint toward an alignment of the source polarization with the ionization cone observed in He II and O III line ratios. Our spectral analysis is in agreement with the source being in soft state, with a dominating thermal component and a minor corona contribution in the 2–8 keV band. The spectro-polarimetric analysis agrees with the standard Novikov and Thorne [1973] thin disk model, due to the low orbital inclination estimated for the source. By assuming a fixed corona polarization degree of 0%, 4%, and 10%, and assuming the two spectral components to be polarized perpendicularly to each other and the thermal component polarization vector to be perpendicular to the ionization cone, we obtained an upper limit of 2%, 0.9%, and 0.9% on the thermal component polarization degree
- In Chapter 7 we discussed the *IXPE* observation of LMC X-3, which took place in July 2023 [Svoboda et al., 2024b]. The source was observed in soft state, and the spectral analysis revealed the source spectra to be best described by a slim disk model (SLIMBH). This analysis was in agreement with the low BH spin value typically estimated for this source ($a_s \sim 0.19$), and revealed a negligible contribution from a Comptonized component in the 2–8 keV band. The measured polarization degree of $3.2 \pm 0.6\%$ hints at an increasing trend with energy, albeit with low statistical significance. This is confirmed by the spectro-polarimetric analysis, where we found the polarimetric data to be well described by a model with constant polarization degree. In particular, the polarization of the source can be described in the standard thin disk scenario. The relatively large polarization degree allowed us to infer a lower limit on the BH spin from the polarimetric data, as low as ~ 0.3 or ~ 0.7 considering or not the returning radiation.

Figure 8.1 illustrates the polarization degree’s dependence on energy across the four discussed sources. Except for LMC X-1, all sources exhibit an increasing PD trend with energy, albeit with different statistical significance. In particular, in

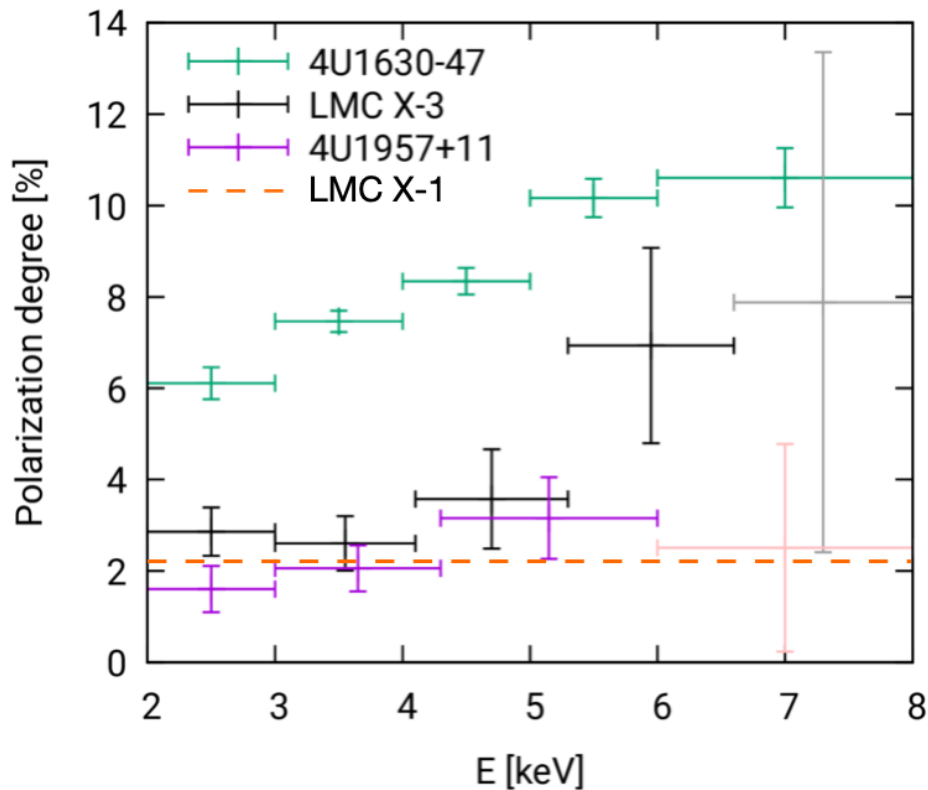


Figure 8.1: Comparison of the energy dependence of the PD in X-ray binaries in the high/soft state dominated by the thermal emission of the accretion disk.

the 4U 1957+115 observation, a model with an increasing PD is favored over a constant PD model with a confidence level of 99%. Given the high black hole spin derived from spectral analysis in this case, the PD rising trend can be attributed to the contribution of returning radiation, which starts dominating over the direct emission of the disk at high energies. However, this explanation doesn't hold for the other two sources with lower spin values. This discrepancy is particularly notable in the 4U 1630-47 observation, which also displays an unexpectedly high polarization degree. On the other hand, for LMC X-3, the low statistical significance of the measurement above 5 keV results in the polarimetric data being in good agreement with a model of constant PD, as expected in the standard thin disk scenario. For black holes with low spin values, a comprehensive model for the increasing PD trend is still lacking. A potential explanation could involve the transmission of emerging radiation through a highly ionized atmosphere, which can give rise to an increasing PD trend with energy in the *IXPE* band. Similarly, absorption processes in the disk atmosphere can provoke a substantial increase in the disk emission polarization degree. Therefore, refining models that describe the interactions between the disk plasma and emitted radiation becomes essential for interpreting both current and future *IXPE* data on accreting stellar-mass black holes in soft state.

Appendix A

Data Reduction

In this Appendix, we describe the details of the data reduction processes followed in the analysis of the BHB sources observed by *IXPE* and detailed in the second part of this thesis.

A.1 IXPE

The *IXPE* processed level-2 data of the observations presented in this thesis are publicly available from the HEASARC archive website ¹. The analysis of the *IXPE* data was performed using the `ixpeobssim` software [Baldini et al., 2022] based on the level-2 processed data. We used the combined data sample collected by the three identical detector units, with appropriate rotation to align them with the same reference system in sky coordinates. Subsequently, we proceeded with the selection of the source and background region using the SAOImage DS9 software [Joye and Mandel, 2003]. The source region was always chosen as a circular area centered at the region of maximum intensity within the field of view, consistent with the source location. The background region was defined as a concentric annulus centered on the source position as well. The `ixpeobssim` software version employed, as well as the source and background extraction regions selected for each source, are detailed in Table A.1. The `ixpeobssim` routine `xpselect` was used to create the source and background event files.

Two approaches were followed in computing the sources' polarization degree and angle. We used the `xpbin` routine of `ixpeobssim`, using the flag `--algorithm PCUBE`, to calculate the polarization degree and angle from the Stokes parameters without making any assumption on the emission spectrum, to obtain a model-independent estimate of the polarization properties of the source. The polarization cubes (PCUBEs) for both the source and background regions generated with `ixpeobssim` combine the observations from each detector unit (DU), and return the total polarization degree and angle as well as the minimum detectable polarization (MDP) at 99% confidence level. On the other hand, we used `ixpeobssim` with the PHA1, PHA1Q, PHA1U algorithms to create spectral files of Stokes *I*, *Q* and *U* parameters, respectively. These files are produced in the OGIP, type 1 PHA format, which is convenient for spectral, polarimetric, and joint analysis within `xspec`. The `xpselect` and `xpbin` routines were

¹<https://heasarc.gsfc.nasa.gov/docs/ixpe/archive/>

Source	ObsIDs	Exposure time [ks]	ixpeobssim	Source region	Background region
4U 1630-47 (HSS)	01250401	~ 463	v. 28.4.0	60''	I:150''; O:258''
4U 1630-47 (SPL)	02250601	~ 141	v. 28.4.0	60''	//
LMC X-1	02001901	~ 562	v. 28.4.0	90''	I:150''; O:240''
4U 1957+115	02006601	~ 571	v. 30.5.0	60''	I:180''; O:280''
LMC X-3	02006599	105.2 + 458.6	v. 30.5.0	60''	I:180''; O:280''

Table A.1: Details of *IXPE* data reduction process. The table lists the `ixpeobssim` version employed in the analysis, as well as the source and background extraction regions. The radius of the circular area used to extract the source is shown, as well as the inner and outer radii of the annular region selected for the background. In the SPL state observation of 4U 1630-47 we did not extract the background due to possible contamination of source photons [Di Marco et al., 2023], caused by its extremely high count-rate.

also used to generate event files for the analysis of variability over time.

A.2 NICER

NICER [Arzoumanian et al., 2014] is a soft X-ray spectral-timing instrument aboard the International Space Station, sensitive within ~ 0.2 –12 keV band. Its X-ray Timing Instrument (XTI) is composed of 56 co-aligned focal-plane modules (FPMs), 52 of which have been active since its launch in 2017, although in any given observation some detectors may be temporarily disabled. Each FPM houses a silicon drift detector and is paired with a single-bounce concentrator optic. The XTI is collimated to sample a field of view approximately $3'$ in radius. Because NICER is a non-imaging instrument, the background is modeled rather than sampled directly [Remillard et al., 2022]. Further details on the specific reduction process used for each observation, and on the empirical background model assumed, are as follows:

- **4U 1630-47 (HSS):** NICER carried out 11 observations of 4U 1630–47 during the *IXPE* campaign, from 2022 August 22 to 2022 September 1. A total of 64 Good Time Intervals (GTIs) have been used for our science analysis, for an aggregate time of ≈ 27 ks. NICER data were reduced and processed with version 9 of the NICER data analysis software `NICERDAS`. Data were filtered following standard practices, but allowing data from South Atlantic Anomaly passages. For each GTI, detectors 14, 34, and 54 data were excised owing to calibration problems among this subset. Additionally, the average rates of overshoot and undershoot events per GTI were assessed, which are generated by particle background and optical-loading events, respectively. Any detector with > 15 median absolute deviation was excluded for that GTI. All exposure times were corrected for the detector dead time ($< 1\%$). The background spectra were computed using the 3C 50 background model [Remillard et al., 2022]. Only GTIs of length $t > 60$ s and for which the background rate was 100 times below the source rate were used for the analysis. A total of 27 ks of simultaneous NICER observations were finally available for analysis. The spectral and light curve files were

extracted from the event files using XSELECT version 2.5b and the response files were generated using `nicerarf` and `nicerrmf`.

- **4U 1630-47 (SPL):** NICER observed the source from 2023 March 10 to March 13 for a total of ~ 32.81 ks of useful time among 6 ObsIDs. The data were reduced using `nicerdas v10` software and the xti20221001 release of NICER CALDB products. The SCORPEON background model² was adopted. Observations were filtered for hot detectors, corrected for detector dead-time, and screened to remove candidate good-time intervals with substantially elevated background or candidate intervals less than 100 s long.
- **LMC X-1:** NICER observed LMC X-1 during the course of the *IXPE* observational campaign, for a total of 13.5 ks useful time among 10 ObsIDs from 2022 October 19–28. NICER data were reduced using `nicer12` with unrestricted undershoot and overshoot rates. The background was computed using the 3C 50 model [Remillard et al., 2022]. Subsequently, the data were filtered to remove intervals with background count rates more than 1% of the source rate, and any short GTI intervals < 60 s were removed. For each observation, the detectors were screened for outliers in overshoot or undershoot event rates; for both fields, each detector was compared to the detector distribution, and those more than 10σ equivalent from the median were filtered out. NICER spectra were re-binned to over-sample the instrumental energy resolution by a factor ~ 3 .
- **4U 1957+115:** NICER observed 4U 1957+115 throughout the *IXPE* campaign, in continuous observations typically lasting ~ 10 min, up to 40 min. These observations were processed using `nicer12` with standard screening except for the undershoot and overshoot rate filters, which were left unrestricted during this initial stage of the processing. Data during South Atlantic Anomaly passages were reduced separately, but not automatically excluded from analysis. All resulting observations were separated into continuous GTIs. For each GTI, the per-FPM distributions of undershoot, overshoot and X-ray rates were compared across the detector ensemble, and any detector presenting a >10 robust standard deviation outlier for any of the rates was excised from the analysis. Between 1 and 7 detectors were screened out for each interval, owing to elevated undershoot rates associated with optical contamination. Detector 63 was particularly affected. Events from the remaining detectors were summed to produce spectra with associated response products. We adopt the SCORPEON background model² in our analysis. Any GTI < 100 s duration or exhibiting an elevated background (as screened by eye) was removed. Surviving the screening, in total we obtain approximately 58 ks of good NICER time, 96 GTIs, spread among 12 ObsIDs. Spectra and responses of all GTIs for a given ObsID were summed in a weighted combination for analysis.
- **LMC X-3:** NICER carried out two observations of LMC X-3 during the *IXPE* campaign, on 2023 July 8 and 17, corresponding to two ObsIDs. These observations were obtained after one of the detector thermal shields was damaged

²https://heasarc.gsfc.nasa.gov/docs/nicer/analysis_threads/scorpeon-xspec/

in May 2023, which resulted in a light leak during ISS daytime which resulted in optical loading of the detectors, producing an increase in noise and potential packet losses³. LMC X-3 could only be observed during ISS daytime, and as a result, we found it necessary to use nonstandard filtering to recover usable data. For both observations, 42 of NICER’s 52 detectors were turned on. We screened the active detectors for outlier behavior based on rates of X-ray, overshoot, and undershoot events, flagging > 10 -(robust) σ outliers from the detector ensemble. This resulted in discarding all data from between 1 and 7 detectors per continuous GTI interval. We obtain a useful exposure time of ≈ 2.2 ks and ≈ 160 s, for the two observations, respectively, and were initially extracted separately per continuous GTI segment. After checking their mutual consistency, we merged them for the spectral analysis. To avoid contamination from low-energy noise events which are exacerbated by the light leak, we restrict our analysis to an energy range > 0.5 keV. Response products were generated based on the number of active detectors, and rates were adjusted for $\gtrsim 1\%$ detector dead-time caused primarily by optical-loading events. We adopt the SCORPEON background model², normalized to the number of selected detectors.

A.3 NuSTAR

The *NuSTAR* (Nuclear Spectroscopic Telescope Array) satellite [Harrison et al., 2013] hosts the first orbiting telescopes to focus light in the high energy X-ray (3 - 79 keV) region of the electromagnetic spectrum. It has two detector units, named Focal Plane Module A and B (FMPA/FMPB), one at the focus of each of the two co-aligned optics units. In all observations, *NuSTAR* data have been processed with the *NuSTAR* Data Analysis Software (NuSTARDAS) package. Cleaned event files (level 2 data products) were produced and calibrated using standard filtering criteria with the `nupipeline` task and the most recent *NuSTAR* calibration files available in the CALDB database. As for *IXPE*, we selected the source and background region using the `ds9` package; the source region was selected as a circular area centered on the source location, while the background was extracted from the corner of the same quadrant in the source-free region. FTGROUUPPHA was used to re-bin the spectra implementing the Kaastra and Bleeker [2016] optimal binning scheme, with the additional request to have a signal-to-noise ratio greater than 3 in each spectral channel. The FPMA and FPMB spectra were fitted independently in the spectral analysis. Further details regarding the *NuSTAR* data reduction are detailed in Table A.2.

A.4 Other facilities

A.4.1 ART-XC

The Mikhail Pavlinsky ART-XC telescope is a grazing incidence focusing X-ray telescope [Pavlinsky et al., 2021] on board the *Spectrum-Rontgen-Gamma observatory* (*SRG*, Sunyaev et al. 2021). It observed LMC X-1 on 2022 Oct 27 with a total exposure

³https://heasarc.gsfc.nasa.gov/docs/nicer/analysis_threads/light-leak-overview/

Source	ObsIDs	Net exposure [ks]	Source region	Background region
4U 1630-47 (HSS)	80802313002	16.6	60''	60''
	80802313004	13.4	60''	60''
	80802313006	15.0	60''	60''
4U 1630-47 (SPL)	80902313002	10.8	60''	91''
	80902313004	7.9	60''	91''
	80902313006	9.6	60''	91''
LMC X-1	90801324002	19.0	67''	67''
4U 1957+115	30902042002	18.7	123''	60''
	30902042004	20.2	123''	60''
	30902042006	19.7	118''	60''
LMC X-3	309020041002	27.6	60''	90''
	309020041004	28.1	60''	90''
	309020041006	29.0	60''	90''

Table A.2: Details of *NuSTAR* data reduction process. The table lists the ObsIDs for all the analyzed sources, the net exposure time of each observation, and the source and background extraction regions' radii. For 4U 1957+115, the source extraction radius was selected following a procedure that maximizes the signal-to-noise ratio [Piconcelli et al., 2004].

of 84.4 ks, and observed 4U 1957+115 twice on May 13 and May 21, for 68 and 67 ks, respectively. The LMC X-1 observation has two short technical interruptions of ~ 100 s duration each. For both pointings, data were processed with the analysis software ARTPRODUCTSv1.0 and the CALDB version 20220908.

A.4.2 Neil Gehrels *Swift* Observatory

The Neil Gehrels *Swift* Observatory [Gehrels et al., 2004] observed LMC X-3 with exposure times of 1.3 ks (ObsID: 00089714001, 2023 July 09), 1.8 ks (ObsID: 00089714002, 14 July 2023), and 1.9 ks (ObsID: 00089714003, 2023 July 20), simultaneously with *NuSTAR*. Given the source brightness, *Swift* X-Ray Telescope (XRT; Burrows et al. [2005]) observations were performed in Windowed Timing mode (WT). Individual *Swift*/XRT spectra were extracted using the standard online tools provided by the UK Swift Science Data Centre [Evans et al., 2009] using a source region of 60'' radius centered at the source location.

Bibliography

- M. A. Abramowicz, B. Czerny, J. P. Lasota, and E. Szuszkiewicz. Slim Accretion Disks. *ApJ*, 332:646, September 1988. doi: 10.1086/166683.
- Md. Shah Alam, G. C. Dewangan, T. Belloni, D. Mukherjee, and S. Jhingan. Millihertz quasi-periodic oscillations and broad iron line from LMC X-1. *MNRAS*, 445(4):4259–4266, December 2014. doi: 10.1093/mnras/stu2048.
- Robert Antonucci. Unified models for active galactic nuclei and quasars. *ARA&A*, 31: 473–521, January 1993. doi: 10.1146/annurev.aa.31.090193.002353.
- K. A. Arnaud. XSPEC: The First Ten Years. In George H. Jacoby and Jeannette Barnes, editors, *Astronomical Data Analysis Software and Systems V*, volume 101 of *Astronomical Society of the Pacific Conference Series*, page 17, January 1996.
- Z. Arzoumanian, K. C. Gendreau, C. L. Baker, T. Cazeau, P. Hestnes, J. W. Kellogg, S. J. Kenyon, R. P. Kozon, K.-C. Liu, S. S. Manthripragada, C. B. Markwardt, A. L. Mitchell, J. W. Mitchell, C. A. Monroe, T. Okajima, S. E. Pollard, D. F. Powers, B. J. Savadkin, L. B. Winternitz, P. T. Chen, M. R. Wright, R. Foster, G. Prigozhin, R. Remillard, and J. Doty. The neutron star interior composition explorer (NICER): mission definition. In Tadayuki Takahashi, Jan-Willem A. den Herder, and Mark Bautz, editors, *Space Telescopes and Instrumentation 2014: Ultraviolet to Gamma Ray*, volume 9144, page 914420. International Society for Optics and Photonics, SPIE, 2014. doi: 10.1117/12.2056811. URL <https://doi.org/10.1117/12.2056811>.
- M. Asplund, N. Grevesse, and A. J. Sauval. The Solar Chemical Composition. In III Barnes, Thomas G. and Frank N. Bash, editors, *Cosmic Abundances as Records of Stellar Evolution and Nucleosynthesis*, volume 336 of *Astronomical Society of the Pacific Conference Series*, page 25, September 2005.
- Steven A. Balbus and John F. Hawley. A Powerful Local Shear Instability in Weakly Magnetized Disks. I. Linear Analysis. *ApJ*, 376:214, July 1991. doi: 10.1086/170270.
- Steven A. Balbus and John F. Hawley. Instability, turbulence, and enhanced transport in accretion disks. *Reviews of Modern Physics*, 70(1):1–53, January 1998. doi: 10.1103/RevModPhys.70.1.
- Luca Baldini, Niccolò Bucciantini, Niccolò Di Lalla, Steven Ehlert, Alberto Manfreda, Michela Negro, Nicola Omodei, Melissa Pesce-Rollins, Carmelo Sgrò, and Stefano Silvestri. ixpeobssim: A simulation and analysis framework for the imaging X-ray

- polarimetry explorer. *SoftwareX*, 19:101194, July 2022. doi: 10.1016/j.softx.2022.101194.
- James M. Bardeen, William H. Press, and Saul A. Teukolsky. Rotating Black Holes: Locally Nonrotating Frames, Energy Extraction, and Scalar Synchrotron Radiation. *ApJ*, 178:347–370, December 1972. doi: 10.1086/151796.
- Erin Barillier, Victoria Grinberg, David Horn, Michael A. Nowak, Ronald A. Remillard, James F. Steiner, Dominic J. Walton, and Jörn Wilms. NICER/NuSTAR Characterization of 4U 1957+11: A Near Maximally Spinning Black Hole Potentially in the Mass Gap. *ApJ*, 944(2):165, February 2023. doi: 10.3847/1538-4357/acaef.
- T. Bassi, M. Del Santo, A. D’A1, S. E. Motta, J. Malzac, A. Segreto, J. C. A. Miller-Jones, P. Atri, R. M. Plotkin, T. M. Belloni, T. Mineo, and A. K. Tzioumis. The long outburst of the black hole transient GRS 1716-249 observed in the X-ray and radio band. *MNRAS*, 482(2):1587–1601, January 2019. doi: 10.1093/mnras/sty2739.
- Amanda J. Bayless, Edward L. Robinson, Paul A. Mason, and Paul Robertson. The Optical Orbital Light Curve of the Low-mass X-ray Binary V1408 Aquilae (= 4U 1957+115). *ApJ*, 730(1):43, March 2011. doi: 10.1088/0004-637X/730/1/43.
- Kris Beckwith, John F. Hawley, and Julian H. Krolik. The Influence of Magnetic Field Geometry on the Evolution of Black Hole Accretion Flows: Similar Disks, Drastically Different Jets. *ApJ*, 678(2):1180–1199, May 2008. doi: 10.1086/533492.
- Mitchell C. Begelman, Roger D. Blandford, and Martin J. Rees. Theory of extragalactic radio sources. *Reviews of Modern Physics*, 56(2):255–351, April 1984. doi: 10.1103/RevModPhys.56.255.
- K. Belczynski, C. Done, and J. P. Lasota. All Apples: Comparing black holes in X-ray binaries and gravitational-wave sources. *arXiv e-prints*, art. arXiv:2111.09401, November 2021.
- T. Belloni, J. Homan, P. Casella, M. van der Klis, E. Nespoli, W. H. G. Lewin, J. M. Miller, and M. Méndez. The evolution of the timing properties of the black-hole transient GX 339-4 during its 2002/2003 outburst. *A&A*, 440(1):207–222, September 2005. doi: 10.1051/0004-6361:20042457.
- Tomaso M. Belloni and Sara E. Motta. Transient Black Hole Binaries. In Cosimo Bambi, editor, *Astrophysics of Black Holes: From Fundamental Aspects to Latest Developments*, volume 440 of *Astrophysics and Space Science Library*, page 61, January 2016. doi: 10.1007/978-3-662-52859-4_2.
- Anil Bhardwaj, Ronald F. Elsner, G. Randall Gladstone, Thomas E. Cravens, Carey M. Lisse, Konrad Dennerl, Graziella Branduardi-Raymont, Bradford J. Wargelin, J. Hunter Waite, Ina Robertson, Nikolai Østgaard, Peter Beiersdorfer, Steven L. Snowden, and Vasili Kharchenko. X-rays from solar system objects. *Planet. Space Sci.*, 55(9):1135–1189, June 2007. doi: 10.1016/j.pss.2006.11.009.

- G. R. Bhuvana, D. Radhika, V. K. Agrawal, S. Mandal, and A. Nandi. Broad-band 'spectro-temporal' features of extragalactic black hole binaries LMC X-1 and LMC X-3: an AstroSat perspective. *MNRAS*, 501(4):5457–5467, March 2021. doi: 10.1093/mnras/staa4012.
- G. R. Bhuvana, D. Radhika, and Anuj Nandi. Multi-mission view of extragalactic black hole X-ray binaries LMC X-1 and LMC X-3: Evolution of broadband spectral features. *Advances in Space Research*, 69(1):483–498, January 2022. doi: 10.1016/j.asr.2021.09.036.
- R. D. Blandford and D. G. Payne. Hydromagnetic flows from accretion disks and the production of radio jets. *MNRAS*, 199:883–903, June 1982. doi: 10.1093/mnras/199.4.883.
- R. D. Blandford and R. L. Znajek. Electromagnetic extraction of energy from Kerr black holes. *MNRAS*, 179:433–456, May 1977. doi: 10.1093/mnras/179.3.433.
- Roger D. Blandford and Mitchell C. Begelman. On the fate of gas accreting at a low rate on to a black hole. *MNRAS*, 303(1):L1–L5, February 1999. doi: 10.1046/j.1365-8711.1999.02358.x.
- G. Boella, R. C. Butler, G. C. Perola, L. Piro, L. Scarsi, and J. A. M. Bleeker. BeppoSAX, the wide band mission for X-ray astronomy. *A&AS*, 122:299–307, April 1997. doi: 10.1051/aas:1997136.
- C. T. Bolton. Identification of Cygnus X-1 with HDE 226868. *Nature*, 235(5336):271–273, February 1972. doi: 10.1038/235271b0.
- Robert H. Boyer and Richard W. Lindquist. Maximal Analytic Extension of the Kerr Metric. *Journal of Mathematical Physics*, 8(2):265–281, February 1967. doi: 10.1063/1.1705193.
- W. N. Brandt and G. Hasinger. Deep Extragalactic X-Ray Surveys. *ARA&A*, 43(1):827–859, September 2005. doi: 10.1146/annurev.astro.43.051804.102213.
- C. Brocksopp, R. M. Bandyopadhyay, and R. P. Fender. “Soft X-ray transient” outbursts which are not soft. *New A*, 9(4):249–264, May 2004. doi: 10.1016/j.newast.2003.11.002.
- C. Brocksopp, P. G. Jonker, D. Maitra, H. A. Krimm, G. G. Pooley, G. Ramsay, and C. Zurita. Disentangling jet and disc emission from the 2005 outburst of XTE J1118+480. *MNRAS*, 404(2):908–916, May 2010. doi: 10.1111/j.1365-2966.2010.16323.x.
- David N. Burrows, J. E. Hill, J. A. Nousek, J. A. Kennea, A. Wells, J. P. Osborne, A. F. Abbey, A. Beardmore, K. Mukerjee, A. D. T. Short, G. Chincarini, S. Campana, O. Citterio, A. Moretti, C. Pagani, G. Tagliaferri, P. Giommi, M. Capalbi, F. Tamburelli, L. Angelini, G. Cusumano, H. W. Bräuninger, W. Burkert, and G. D. Hartner. The Swift X-Ray Telescope. *Space Sci. Rev.*, 120(3-4):165–195, October 2005. doi: 10.1007/s11214-005-5097-2.

- Michal Bursa. Numerical implementation of equations for photon motion in Kerr spacetime. In *RAGtime 17-19: Workshops on Black Holes and Neutron Stars*, pages 7–21, December 2017.
- F. Capitanio, T. Belloni, M. Del Santo, and P. Ubertini. A failed outburst of H1743-322. *MNRAS*, 398(3):1194–1200, September 2009. doi: 10.1111/j.1365-2966.2009.15196.x.
- F. Capitanio, R. Campana, G. De Cesare, and C. Ferrigno. Missing hard states and regular outbursts: the puzzling case of the black hole candidate 4U 1630-472. *MNRAS*, 450(4):3840–3854, July 2015. doi: 10.1093/mnras/stv687.
- P. Casella, T. Belloni, J. Homan, and L. Stella. A study of the low-frequency quasi-periodic oscillations in the X-ray light curves of the black hole candidate *i*ASTROBJ_{*i*}XTE J1859+226/*i*ASTROBJ_{*i*}. *A&A*, 426:587–600, November 2004. doi: 10.1051/0004-6361:20041231.
- Sudip Chakraborty, Ajay Ratheesh, Sudip Bhattacharyya, John A. Tomsick, Francesco Tombesi, Keigo Fukumura, and Gaurava K. Jaisawal. NuSTAR monitoring of MAXI J1348-630: evidence of high density disc reflection. *MNRAS*, 508(1):475–488, November 2021. doi: 10.1093/mnras/stab2530.
- S. Chandrasekhar. The Maximum Mass of Ideal White Dwarfs. *ApJ*, 74:81, July 1931. doi: 10.1086/143324.
- S. Chandrasekhar. *The mathematical theory of black holes*. 1983.
- Subrahmanyan Chandrasekhar. *Radiative transfer*. 1960.
- P. A. Charles and M. J. Coe. Optical, ultraviolet and infrared observations of X-ray binaries. In *Compact stellar X-ray sources*, volume 39, pages 215–265. 2006.
- Kaushik Chatterjee, Dipak Debnath, Riya Bhowmick, Sujoy Kumar Nath, and Debjit Chatterjee. Anomalous nature of outbursts of black hole candidate 4U 1630-472. *MNRAS*, 510(1):1128–1135, February 2022. doi: 10.1093/mnras/stab3570.
- Geoffrey Compère and Roberto Oliveri. Self-similar accretion in thin discs around near-extremal black holes. *MNRAS*, 468(4):4351–4361, July 2017. doi: 10.1093/mnras/stx748.
- P. A. Connors and R. F. Stark. Observable gravitational effects on polarised radiation coming from near a black hole. *Nature*, 269(5624):128–129, September 1977. doi: 10.1038/269128a0.
- P. A. Connors, T. Piran, and R. F. Stark. Polarization features of X-ray radiation emitted near black holes. *ApJ*, 235:224–244, January 1980. doi: 10.1086/157627.
- Riley M. T. Connors, Javier A. García, Thomas Dauser, Victoria Grinberg, James F. Steiner, Navin Sridhar, Jörn Wilms, John Tomsick, Fiona Harrison, and Stefan Lickleder. Evidence for Returning Disk Radiation in the Black Hole X-Ray Binary XTE J1550-564. *ApJ*, 892(1):47, March 2020. doi: 10.3847/1538-4357/ab7afc.

- Riley M. T. Connors, Javier A. García, John Tomsick, Jeremy Hare, Thomas Dauser, Victoria Grinberg, James F. Steiner, Guglielmo Mastroserio, Navin Sridhar, Andrew C. Fabian, Jiachen Jiang, Michael L. Parker, Fiona Harrison, and Timothy R. Kallman. Reflection Modeling of the Black Hole Binary 4U 1630-47: The Disk Density and Returning Radiation. *ApJ*, 909(2):146, March 2021. doi: 10.3847/1538-4357/abdd2c.
- J. Contopoulos. Magnetically Driven Relativistic Jets and Winds: Exact Solutions. *ApJ*, 432:508, September 1994. doi: 10.1086/174590.
- R. Cooke, J. Bland-Hawthorn, R. Sharp, and Z. Kuncic. Ionization Cone in the X-Ray Binary LMC X-1. *ApJ*, 687(1):L29, November 2008. doi: 10.1086/593169.
- Ryan Cooke, Zdenka Kuncic, Rob Sharp, and Joss Bland-Hawthorn. Spectacular trailing streamers near lmc x-1: The first evidence of a jet? *ApJ*, 667(2):L163, sep 2007. doi: 10.1086/522517. URL <https://dx.doi.org/10.1086/522517>.
- P. S. Coppi. EQPAIR: A Hybrid Thermal/Non-Thermal Model for the Spectra of X-Ray Binaries. In *AAS/High Energy Astrophysics Division #5*, volume 5 of *AAS/High Energy Astrophysics Division*, page 23.11, October 2000.
- S. Corbel and R. P. Fender. Near-Infrared Synchrotron Emission from the Compact Jet of GX 339-4. *ApJ*, 573(1):L35–L39, July 2002. doi: 10.1086/341870.
- S. Corbel, R. P. Fender, A. K. Tzioumis, M. Nowak, V. McIntyre, P. Durouchoux, and R. Sood. Coupling of the X-ray and radio emission in the black hole candidate and compact jet source GX 339-4. *A&A*, 359:251–268, July 2000. doi: 10.48550/arXiv.astro-ph/0003460.
- S. Corbel, M. Coriat, C. Brocksopp, A. K. Tzioumis, R. P. Fender, J. A. Tomsick, M. M. Buxton, and C. D. Bailyn. The ‘universal’ radio/X-ray flux correlation: the case study of the black hole GX 339-4. *MNRAS*, 428(3):2500–2515, January 2013. doi: 10.1093/mnras/sts215.
- M. Coriat, S. Corbel, L. Prat, J. C. A. Miller-Jones, D. Cseh, A. K. Tzioumis, C. Brocksopp, J. Rodriguez, R. P. Fender, and G. R. Sivakoff. Accretion-outflow connection in the outliers of the “universal” radio/X-ray correlation. In Gustavo E. Romero, Rashid A. Sunyaev, and Tomaso Belloni, editors, *Jets at All Scales*, volume 275, pages 255–259, February 2011. doi: 10.1017/S174392131001611X.
- Enrico Costa. General History of X-Ray Polarimetry in Astrophysics. In *Handbook of X-ray and Gamma-ray Astrophysics*, page 36. 2022. doi: 10.1007/978-981-16-4544-0_140-1.
- Enrico Costa, Paolo Soffitta, Ronaldo Bellazzini, Alessandro Brez, Nicholas Lumb, and Gloria Spandre. An efficient photoelectric X-ray polarimeter for the study of black holes and neutron stars. *Nature*, 411(6838):662–665, June 2001. doi: 10.1038/35079508.

- C. Cunningham. Returning radiation in accretion disks around black holes. *ApJ*, 208: 534–549, September 1976. doi: 10.1086/154636.
- T. Dauser, J. A. García, A. Joyce, S. Lickleder, R. M. T. Connors, A. Ingram, C. S. Reynolds, and J. Wilms. The effect of returning radiation on relativistic reflection. *MNRAS*, 514(3):3965–3983, August 2022. doi: 10.1093/mnras/stac1593.
- Shane W. Davis and Samer El-Abd. Spectral Hardening in Black Hole Accretion: Giving Spectral Modelers an f. *ApJ*, 874(1):23, March 2019. doi: 10.3847/1538-4357/ab05c5.
- Shane W. Davis, Chris Done, and Omer M. Blaes. Testing Accretion Disk Theory in Black Hole X-Ray Binaries. *ApJ*, 647(1):525–538, August 2006. doi: 10.1086/505386.
- J. A. de Jong, J. van Paradijs, and T. Augusteijn. Reprocessing of X rays in low-mass X-ray binaries. *A&A*, 314:484–490, October 1996.
- M. Del Santo, J. Malzac, R. Belmont, L. Bouchet, and G. De Cesare. The magnetic field in the X-ray corona of Cygnus X-1. *MNRAS*, 430(1):209–220, March 2013. doi: 10.1093/mnras/sts574.
- M. Del Santo, T. M. Belloni, J. A. Tomsick, B. Sbarufatti, M. Cadolle Bel, P. Casella, A. Castro-Tirado, S. Corbel, V. Grinberg, J. Homan, E. Kalemci, S. Motta, T. Muñoz-Darias, K. Pottschmidt, J. Rodriguez, and J. Wilms. Spectral and timing evolution of the bright failed outburst of the transient black hole Swift J174510.8-262411. *MNRAS*, 456(4):3585–3595, March 2016. doi: 10.1093/mnras/stv2901.
- M. Del Santo, C. Pinto, A. Marino, A. D’Ai, P. O. Petrucci, J. Malzac, J. Ferreira, F. Pintore, S. E. Motta, T. D. Russell, A. Segreto, and A. Sanna. An ultrafast outflow in the black hole candidate MAXI J1810-222? *MNRAS*, 523(1):L15–L20, July 2023. doi: 10.1093/mnrasl/slاد048.
- Alessandro Di Marco, Paolo Soffitta, Enrico Costa, Riccardo Ferrazzoli, Fabio La Monaca, John Rankin, Ajay Ratheesh, Fei Xie, Luca Baldini, Ettore Del Monte, Steven R. Ehlert, Sergio Fabiani, Dawoon E. Kim, Fabio Muleri, Stephen L. O’Dell, Brian D. Ramsey, Alda Rubini, Carmelo Sgrò, Stefano Silvestri, Allyn F. Tennant, and Martin C. Weisskopf. Handling the Background in IXPE Polarimetric Data. *AJ*, 165(4):143, April 2023. doi: 10.3847/1538-3881/acba0f.
- T. Di Salvo, C. Done, P. T. Życki, L. Burderi, and N. R. Robba. Probing the Inner Region of Cygnus X-1 in the Low/Hard State through Its X-Ray Broadband Spectrum. *ApJ*, 547(2):1024–1033, February 2001. doi: 10.1086/318396.
- M. Díaz Trigo, S. Migliari, J. C. A. Miller-Jones, and M. Guainazzi. XMM-Newton observations reveal the disappearance of the wind in 4U 1630-47. *A&A*, 571:A76, November 2014a. doi: 10.1051/0004-6361/201424554.
- M. Díaz Trigo, S. Migliari, J. C. A. Miller-Jones, and M. Guainazzi. XMM-Newton observations reveal the disappearance of the wind in 4U 1630-47. *A&A*, 571:A76, November 2014b. doi: 10.1051/0004-6361/201424554.

- Chris Done. Observational characteristics of accretion onto black holes. *arXiv e-prints*, art. arXiv:1008.2287, August 2010. doi: 10.48550/arXiv.1008.2287.
- Chris Done and Marek Gierliński. Observing the effects of the event horizon in black holes. *MNRAS*, 342(4):1041–1055, July 2003. doi: 10.1046/j.1365-8711.2003.06614.x.
- Chris Done, Marek Gierliński, and Aya Kubota. Modelling the behaviour of accretion flows in X-ray binaries. Everything you always wanted to know about accretion but were afraid to ask. *A&A Rev.*, 15(1):1–66, December 2007. doi: 10.1007/s00159-007-0006-1.
- Chris Done, Ryota Tomaru, and Tadayuki Takahashi. Thermal winds in stellar mass black hole and neutron star binary systems. *MNRAS*, 473(1):838–848, January 2018. doi: 10.1093/mnras/stx2400.
- Michal Dovciak. *Radiation of Accretion Discs in Strong Gravity*. PhD thesis, Charles Univ., November 2004.
- M. Dovčiak, F. Muleri, R. W. Goosmann, V. Karas, and G. Matt. Thermal disc emission from a rotating black hole: X-ray polarization signatures. *MNRAS*, 391(1):32–38, November 2008. doi: 10.1111/j.1365-2966.2008.13872.x.
- Paul A. Draghis, Jon M. Miller, Abderahmen Zoghbi, Mark Reynolds, Elisa Costantini, Luigi C. Gallo, and John A. Tomsick. A Systematic View of Ten New Black Hole Spins. *ApJ*, 946(1):19, March 2023. doi: 10.3847/1538-4357/acafe7.
- Ken Ebisawa, Kazuhisa Mitsuda, and Hajime Inoue. Discovery of 0.08-Hz quasi-periodic oscillations from the black-hole candidate LMC X-1. *PASJ*, 41:519–530, January 1989.
- Ken Ebisawa, Fumiyoshi Makino, Kazuhisa Mitsuda, Tomaso Belloni, Anne P. Cowley, Paul C. Schmidtke, and Aldo Treves. Spectral Variations of LMC X-3 Observed with GINGA. *ApJ*, 403:684, February 1993. doi: 10.1086/172239.
- Ann A. Esin, Jeffrey E. McClintock, and Ramesh Narayan. Advection-Dominated Accretion and the Spectral States of Black Hole X-Ray Binaries: Application to Nova Muscae 1991. *ApJ*, 489(2):865–889, November 1997. doi: 10.1086/304829.
- P. A. Evans, A. P. Beardmore, K. L. Page, J. P. Osborne, P. T. O’Brien, R. Willingale, R. L. C. Starling, D. N. Burrows, O. Godet, L. Vetere, J. Racusin, M. R. Goad, K. Wiersema, L. Angelini, M. Capalbi, G. Chincarini, N. Gehrels, J. A. Kennea, R. Margutti, D. C. Morris, C. J. Mountford, C. Pagani, M. Perri, P. Romano, and N. Tanvir. Methods and results of an automatic analysis of a complete sample of Swift-XRT observations of GRBs. *MNRAS*, 397(3):1177–1201, August 2009. doi: 10.1111/j.1365-2966.2009.14913.x.
- A. C. Fabian, M. J. Rees, L. Stella, and N. E. White. X-ray fluorescence from the inner disc in Cygnus X-1. *MNRAS*, 238:729–736, May 1989. doi: 10.1093/mnras/238.3.729.
- Andrew C. Fabian and Anthony N. Lasenby. *Astrophysical Black Holes*. *arXiv e-prints*, art. arXiv:1911.04305, November 2019. doi: 10.48550/arXiv.1911.04305.

- S. Fabiani, E. Costa, E. Del Monte, F. Muleri, P. Soffitta, A. Rubini, R. Bellazzini, A. Brez, L. de Ruvo, M. Minuti, M. Pinchera, C. Sgró, G. Spandre, D. Spiga, G. Tagliaferri, G. Pareschi, S. Basso, O. Citterio, V. Burwitz, W. Burkert, B. Menz, and G. Hartner. The Imaging Properties of the Gas Pixel Detector as a Focal Plane Polarimeter. *ApJS*, 212(2):25, June 2014. doi: 10.1088/0067-0049/212/2/25.
- Sergio Fabiani and Fabio Muleri. *Astronomical X-Ray Polarimetry*. 2014.
- Will M. Farr, Niharika Sravan, Andrew Cantrell, Laura Kreidberg, Charles D. Bailyn, Ilya Mandel, and Vicky Kalogera. The Mass Distribution of Stellar-mass Black Holes. *ApJ*, 741(2):103, November 2011. doi: 10.1088/0004-637X/741/2/103.
- R. P. Fender, K. Southwell, and A. K. Tzioumis. A radio survey of supersoft, persistent and transient X-ray sources in the Magellanic Clouds. *MNRAS*, 298(3):692–696, August 1998. doi: 10.1046/j.1365-8711.1998.01680.x.
- R. P. Fender, G. G. Pooley, P. Durouchoux, R. P. J. Tilanus, and C. Brocksopp. The very flat radio-millimetre spectrum of Cygnus X-1. *MNRAS*, 312(4):853–858, March 2000. doi: 10.1046/j.1365-8711.2000.03219.x.
- R. P. Fender, T. M. Belloni, and E. Gallo. Towards a unified model for black hole X-ray binary jets. *MNRAS*, 355(4):1105–1118, December 2004. doi: 10.1111/j.1365-2966.2004.08384.x.
- R. P. Fender, J. Homan, and T. M. Belloni. Jets from black hole X-ray binaries: testing, refining and extending empirical models for the coupling to X-rays. *MNRAS*, 396(3):1370–1382, July 2009. doi: 10.1111/j.1365-2966.2009.14841.x.
- Rob Fender. Jets from X-ray binaries. In *Compact stellar X-ray sources*, volume 39, pages 381–419. 2006.
- Rob Fender, Tomaso Belloni, and Elena Gallo. A Unified Model for Black Hole X-Ray Binary Jets? *Ap&SS*, 300(1-3):1–13, November 2005. doi: 10.1007/s10509-005-1201-z.
- G. J. Ferland, M. Chatzikos, F. Guzmán, M. L. Lykins, P. A. M. van Hoof, R. J. R. Williams, N. P. Abel, N. R. Badnell, F. P. Keenan, R. L. Porter, and P. C. Stancil. The 2017 Release Cloudy. *Rev. Mexicana Astron. Astrofis.*, 53:385–438, October 2017.
- J. E. Fernández, J. H. Hubbell, A. L. Hanson, and L. V. Spencer. Polarization effects on multiple scattering gamma transport. *Radiation Physics and Chemistry*, 41(4-5): 579–630, April 1993. doi: 10.1016/0969-806X(93)90316-M.
- C. Ferrigno, E. Bozzo, M. Del Santo, and F. Capitanio. The first outburst of the black-hole candidate MAXI J1836-194 observed by INTEGRAL, Swift, and RXTE. *A&A*, 537:L7, January 2012. doi: 10.1051/0004-6361/201118474.
- Richard P. Feynman, Robert B. Leighton, Matthew Sands, and E. M. Hafner. The Feynman Lectures on Physics; Vol. I. *American Journal of Physics*, 33(9):750–752, September 1965. doi: 10.1119/1.1972241.

- Maya Fishbach and Vicky Kalogera. Apples and Oranges: Comparing Black Holes in X-Ray Binaries and Gravitational-wave Sources. *ApJ*, 929(2):L26, April 2022. doi: 10.3847/2041-8213/ac64a5.
- Chris L. Fryer, Krzysztof Belczynski, Grzegorz Wiktorowicz, Michal Dominik, Vicky Kalogera, and Daniel E. Holz. Compact Remnant Mass Function: Dependence on the Explosion Mechanism and Metallicity. *ApJ*, 749(1):91, April 2012. doi: 10.1088/0004-637X/749/1/91.
- Keigo Fukumura, Demosthenes Kazanas, Ioannis Contopoulos, and Ehud Behar. Magnetohydrodynamic Accretion Disk Winds as X-ray Absorbers in Active Galactic Nuclei. *ApJ*, 715(1):636–650, May 2010. doi: 10.1088/0004-637X/715/1/636.
- Keigo Fukumura, Demosthenes Kazanas, Chris Shrader, Francesco Tombesi, Constantinos Kalapotharakos, and Ehud Behar. Modeling Magnetic Disk Wind State Transitions in Black Hole X-Ray Binaries. *ApJ*, 912(2):86, May 2021. doi: 10.3847/1538-4357/abedaf.
- Keigo Fukumura, Francesco Tombesi, Sudip Chakraborty, and Ajay Ratheesh. Probing Accretion Disks in BH XRBs with Reflection and Wind Spectroscopy. In *44th COSPAR Scientific Assembly. Held 16-24 July*, volume 44, page 1766, July 2022.
- Gaia Collaboration, A. G. A. Brown, A. Vallenari, T. Prusti, J. H. J. de Bruijne, C. Babusiaux, M. Biermann, O. L. Creevey, D. W. Evans, L. Eyer, A. Hutton, F. Jansen, C. Jordi, S. A. Klioner, U. Lammers, L. Lindegren, X. Luri, F. Mignard, C. Panem, D. Pourbaix, S. Randich, P. Sartoretti, C. Soubiran, N. A. Walton, F. Arenou, C. A. L. Bailer-Jones, U. Bastian, M. Cropper, R. Drimmel, D. Katz, M. G. Lattanzi, F. van Leeuwen, J. Bakker, C. Cacciari, J. Castañeda, F. De Angeli, C. Ducourant, C. Fabricius, M. Fouesneau, Y. Frémat, R. Guerra, A. Guerrier, J. Guiraud, A. Jean-Antoine Piccolo, E. Masana, R. Messineo, N. Mowlavi, C. Nicolas, K. Nienartowicz, F. Pailler, P. Panuzzo, F. Riclet, W. Roux, G. M. Seabroke, R. Sordo, P. Tanga, F. Thévenin, G. Gracia-Abril, J. Portell, D. Teyssier, M. Altmann, R. Andrae, I. Bellas-Velidis, K. Benson, J. Berthier, R. Blomme, E. Brugaletta, P. W. Burgess, G. Busso, B. Carry, A. Cellino, N. Cheek, G. Clementini, Y. Damerджи, M. Davidson, L. Delchambre, A. Dell’Oro, J. Fernández-Hernández, L. Galluccio, P. García-Lario, M. Garcia-Reinaldos, J. González-Núñez, E. Gosset, R. Haigron, J. L. Halbwegs, N. C. Hambly, D. L. Harrison, D. Hatzidimitriou, U. Heiter, J. Hernández, D. Hestroffer, S. T. Hodgkin, B. Holl, K. Janßen, G. Jevardat de Fombelle, S. Jordan, A. Krone-Martins, A. C. Lanzafame, W. Löffler, A. Lorca, M. Manteiga, O. Marchal, P. M. Marrese, A. Moitinho, A. Mora, K. Muinonen, P. Osborne, E. Pancino, T. Pauwels, J. M. Petit, A. Recio-Blanco, P. J. Richards, M. Riello, L. Rimoldini, A. C. Robin, T. Roegiers, J. Rybizki, L. M. Sarro, C. Siopis, M. Smith, A. Sozzetti, A. Ulla, E. Utrilla, M. van Leeuwen, W. van Reeve, U. Abbas, A. Abreu Aramburu, S. Accart, C. Aerts, J. J. Aguado, M. Ajaj, G. Altavilla, M. A. Álvarez, J. Álvarez Cid-Fuentes, J. Alves, R. I. Anderson, E. Anglada Varela, T. Antoja, M. Audard, D. Baines, S. G. Baker, L. Balaguer-Núñez, E. Balbinot, Z. Balog, C. Barache, D. Barbato, M. Barros, M. A. Barstow,

S. Bartolomé, J. L. Bassilana, N. Bauchet, A. Baudesson-Stella, U. Becciani, M. Bellazzini, M. Bernet, S. Bertone, L. Bianchi, S. Blanco-Cuaresma, T. Boch, A. Bombrun, D. Bossini, S. Bouquillon, A. Bragaglia, L. Bramante, E. Breedt, A. Bressan, N. Brouillet, B. Bucciarelli, A. Burlacu, D. Busonero, A. G. Butkevich, R. Buzzi, E. Caffau, R. Cancelliere, H. Cánovas, T. Cantat-Gaudin, R. Carballo, T. Carlucci, M. I. Carnerero, J. M. Carrasco, L. Casamiquela, M. Castellani, A. Castro-Ginard, P. Castro Sampol, L. Chaoul, P. Charlot, L. Chemin, A. Chiavassa, M. R. L. Cioni, G. Comoretto, W. J. Cooper, T. Cornez, S. Cowell, F. Crifo, M. Crosta, C. Crowley, C. Dafonte, A. Dapergolas, M. David, P. David, P. de Laverny, F. De Luise, R. De March, J. De Ridder, R. de Souza, P. de Teodoro, A. de Torres, E. F. del Peloso, E. del Pozo, M. Delbo, A. Delgado, H. E. Delgado, J. B. Delisle, P. Di Matteo, S. Diakite, C. Diener, E. Distefano, C. Dolding, D. Eappachen, B. Edvardsson, H. Enke, P. Esquej, C. Fabre, M. Fabrizio, S. Faigler, G. Fedorets, P. Fernique, A. Fienga, F. Figueras, C. Fouron, F. Fragkoudi, E. Fraile, F. Franke, M. Gai, D. Garabato, A. Garcia-Gutierrez, M. García-Torres, A. Garofalo, P. Gavras, E. Gerlach, R. Geyer, P. Giacobbe, G. Gilmore, S. Girona, G. Giuffrida, R. Gomel, A. Gomez, I. Gonzalez-Santamaria, J. J. González-Vidal, M. Granvik, R. Gutiérrez-Sánchez, L. P. Guy, M. Hauser, M. Haywood, A. Helmi, S. L. Hidalgo, T. Hilger, N. Hładczuk, D. Hobbs, G. Holland, H. E. Huckle, G. Jasiewicz, P. G. Jonker, J. Juaristi Campillo, F. Julbe, L. Karbevská, P. Kervella, S. Khanna, A. Kochoska, M. Kontizas, G. Kordopatis, A. J. Korn, Z. Kostrzewa-Rutkowska, K. Kruszyńska, S. Lambert, A. F. Lanza, Y. Lasne, J. F. Le Campion, Y. Le Fustec, Y. Lebreton, T. Lebzelter, S. Leccia, N. Leclerc, I. Lecoœur-Taïbi, S. Liao, E. Licata, E. P. Lindstrøm, T. A. Lister, E. Livanou, A. Lobel, P. Madrero Pardo, S. Managau, R. G. Mann, J. M. Marchant, M. Marconi, M. M. S. Marcos Santos, S. Marinoni, F. Marocco, D. J. Marshall, L. Martin Polo, J. M. Martín-Fleitas, A. Masip, D. Massari, A. Mastrobuono-Battisti, T. Mazeh, P. J. McMillan, S. Messina, D. Michalik, N. R. Millar, A. Mints, D. Molina, R. Molinaro, L. Molnár, P. Montegriffo, R. Mor, R. Morbidelli, T. Morel, D. Morris, A. F. Mulone, D. Munoz, T. Muraveva, C. P. Murphy, I. Musella, L. Noval, C. Ordénovic, G. Orrù, J. Osinde, C. Pagani, I. Pagano, L. Palaversa, P. A. Palicio, A. Panahi, M. Pawlak, X. Peñalosa Esteller, A. Penttilä, A. M. Piersimoni, F. X. Pineau, E. Plachy, G. Plum, E. Poggio, E. Poretti, E. Poujoulet, A. Prša, L. Pulone, E. Racero, S. Ragaini, M. Rainer, C. M. Raiteri, N. Rambaux, P. Ramos, M. Ramos-Lerate, P. Re Fiorentin, S. Regibo, C. Reylé, V. Ripepi, A. Riva, G. Rixon, N. Robichon, C. Robin, M. Roelens, L. Rohrbasser, M. Romero-Gómez, N. Rowell, F. Royer, K. A. Rybicki, G. Sadowski, A. Sagristà Sellés, J. Sahlmann, J. Salgado, E. Salguero, N. Samaras, V. Sanchez Gimenez, N. Sanna, R. Santoveña, M. Sarasso, M. Schultheis, E. Sciacca, M. Segol, J. C. Segovia, D. Ségransan, D. Semeux, S. Shahaf, H. I. Siddiqui, A. Siebert, L. Siltala, E. Slezak, R. L. Smart, E. Solano, F. Solitro, D. Souami, J. Souchay, A. Spagna, F. Spoto, I. A. Steele, H. Steidelmüller, C. A. Stephenson, M. Süveges, L. Szabados, E. Szegedi-Elek, F. Taris, G. Tauran, M. B. Taylor, R. Teixeira, W. Thuillot, N. Tonello, F. Torra, J. Torra, C. Turon, N. Unger, M. Vaillant, E. van Dillen, O. Vanel, A. Vecchiato, Y. Viala, D. Vicente, S. Voutsinas, M. Weiler, T. Wevers, Ł. Wyrzykowski, A. Yoldas, P. Yvard, H. Zhao, J. Zorec, S. Zucker, C. Zurbach, and T. Zwitter. Gaia Early Data Release 3. Summary of the contents and survey

- properties. *A&A*, 649:A1, May 2021. doi: 10.1051/0004-6361/202039657.
- E. Gallo, R. P. Fender, and G. G. Pooley. A universal radio-X-ray correlation in low/hard state black hole binaries. *MNRAS*, 344(1):60–72, September 2003. doi: 10.1046/j.1365-8711.2003.06791.x.
- E. Gatuzz, M. Díaz Trigo, J. C. A. Miller-Jones, and S. Migliari. Chandra high-resolution spectra of 4U 1630-47: the disappearance of the wind. *MNRAS*, 482(2): 2597–2611, January 2019. doi: 10.1093/mnras/sty2850.
- N. Gehrels, G. Chincarini, P. Giommi, K. O. Mason, J. A. Nousek, A. A. Wells, N. E. White, S. D. Barthelmy, D. N. Burrows, L. R. Cominsky, K. C. Hurley, F. E. Marshall, P. Mészáros, P. W. A. Roming, L. Angelini, L. M. Barbier, T. Belloni, S. Campana, P. A. Caraveo, M. M. Chester, O. Citterio, T. L. Cline, M. S. Cropper, J. R. Cummings, A. J. Dean, E. D. Feigelson, E. E. Fenimore, D. A. Frail, A. S. Fruchter, G. P. Garmire, K. Gendreau, G. Ghisellini, J. Greiner, J. E. Hill, S. D. Hunsberger, H. A. Krimm, S. R. Kulkarni, P. Kumar, F. Lebrun, N. M. Lloyd-Ronning, C. B. Markwardt, B. J. Mattson, R. F. Mushotzky, J. P. Norris, J. Osborne, B. Paczynski, D. M. Palmer, H. S. Park, A. M. Parsons, J. Paul, M. J. Rees, C. S. Reynolds, J. E. Rhoads, T. P. Sasseen, B. E. Schaefer, A. T. Short, A. P. Smale, I. A. Smith, L. Stella, G. Tagliaferri, T. Takahashi, M. Tashiro, L. K. Townsley, J. Tueller, M. J. L. Turner, M. Vietri, W. Voges, M. J. Ward, R. Willingale, F. M. Zerbi, and W. W. Zhang. The Swift Gamma-Ray Burst Mission. *ApJ*, 611(2): 1005–1020, August 2004. doi: 10.1086/422091.
- Gabriele Ghisellini. *Radiative Processes in High Energy Astrophysics*, volume 873. 2013. doi: 10.1007/978-3-319-00612-3.
- R. Giacconi, S. Murray, H. Gursky, E. Kellogg, E. Schreier, and H. Tananbaum. The Uhuru catalog of X-ray sources. *ApJ*, 178:281–308, December 1972. doi: 10.1086/151790.
- R. Giacconi, S. Murray, H. Gursky, E. Kellogg, E. Schreier, T. Matilsky, D. Koch, and H. Tananbaum. The Third UHURU Catalog of X-Ray Sources. *ApJS*, 27:37, February 1974. doi: 10.1086/190288.
- R. Giacconi, G. Branduardi, U. Briel, A. Epstein, D. Fabricant, E. Feigelson, W. Forman, P. Gorenstein, J. Grindlay, H. Gursky, F. R. Harnden, J. P. Henry, C. Jones, E. Kellogg, D. Koch, S. Murray, E. Schreier, F. Seward, H. Tananbaum, K. Topka, L. Van Speybroeck, S. S. Holt, R. H. Becker, E. A. Boldt, P. J. Serlemitsos, G. Clark, C. Canizares, T. Markert, R. Novick, D. Helfand, and K. Long. The Einstein (HEAO 2) X-ray Observatory. *ApJ*, 230:540–550, June 1979. doi: 10.1086/157110.
- Riccardo Giacconi, Herbert Gursky, Frank R. Paolini, and Bruno B. Rossi. Evidence for x Rays From Sources Outside the Solar System. *Phys. Rev. Lett.*, 9(11):439–443, December 1962. doi: 10.1103/PhysRevLett.9.439.
- Marek Gierliński, Andrzej A. Zdziarski, Juri Poutanen, Paolo S. Coppi, Ken Ebisawa, and W. Neil Johnson. Radiation mechanisms and geometry of Cygnus X-1 in the

- soft state. *MNRAS*, 309(2):496–512, October 1999. doi: 10.1046/j.1365-8711.1999.02875.x.
- Marek Gierliński, Andrzej Maciołek-Niedźwiecki, and Ken Ebisawa. Application of a relativistic accretion disc model to X-ray spectra of LMC X-1 and GRO J1655-40. *MNRAS*, 325(3):1253–1265, August 2001. doi: 10.1046/j.1365-8711.2001.04540.x.
- Sebastian Gomez, Paul A. Mason, and Edward L. Robinson. The Case for a Low Mass Black Hole in the Low Mass X-Ray Binary V1408 Aquilae (= 4U 1957+115). *ApJ*, 809(1):9, August 2015. doi: 10.1088/0004-637X/809/1/9.
- R. W. Goosmann and C. M. Gaskell. Modeling optical and UV polarization of AGNs. I. Imprints of individual scattering regions. *A&A*, 465(1):129–145, April 2007. doi: 10.1051/0004-6361:20053555.
- Lijun Gou, Jeffrey E. McClintock, Jifeng Liu, Ramesh Narayan, James F. Steiner, Ronald A. Remillard, Jerome A. Orosz, Shane W. Davis, Ken Ebisawa, and Eric M. Schlegel. A determination of the spin of the black hole primary in lmc x-1. *ApJ*, 701(2):1076, jul 2009. doi: 10.1088/0004-637X/701/2/1076. URL <https://dx.doi.org/10.1088/0004-637X/701/2/1076>.
- Manuel Güdel and Yaël Nazé. X-ray spectroscopy of stars. *A&A Rev.*, 17(3):309–408, September 2009. doi: 10.1007/s00159-009-0022-4.
- P. J. Hakala, P. Muhli, and G. Dubus. Evidence for evolving accretion disc structure in 4U1957+115. *MNRAS*, 306(3):701–707, July 1999. doi: 10.1046/j.1365-8711.1999.02571.x.
- Pasi Hakala, Panu Muhli, and Phil Charles. Simultaneous optical and near-IR photometry of 4U1957+115 - a missing secondary star. *MNRAS*, 444(4):3802–3808, November 2014. doi: 10.1093/mnras/stu1687.
- M. Hanke, J. Wilms, M. A. Nowak, L. Barragán, and N. S. Schulz. The column density towards LMC X-1. *A&A*, 509:L8, January 2010. doi: 10.1051/0004-6361/200913583.
- Fiona A. Harrison, William W. Craig, Finn E. Christensen, Charles J. Hailey, William W. Zhang, Steven E. Boggs, Daniel Stern, W. Rick Cook, Karl Forster, Paolo Giommi, Brian W. Grefenstette, Yunjin Kim, Takao Kitaguchi, Jason E. Koglin, Kristin K. Madsen, Peter H. Mao, Hiromasa Miyasaka, Kaya Mori, Matteo Perri, Michael J. Pivovarov, Simonetta Puccetti, Vikram R. Rana, Niels J. Westergaard, Jason Willis, Andreas Zoglauer, Hongjun An, Matteo Bachetti, Nicolas M. Barrière, Eric C. Bellm, Varun Bhalerao, Nicolai F. Brejnholt, Felix Fuerst, Carl C. Liebe, Craig B. Markwardt, Melania Nynka, Julia K. Vogel, Dominic J. Walton, Daniel R. Wik, David M. Alexander, Lynn R. Cominsky, Ann E. Hornschemeier, Allan Hornstrup, Victoria M. Kaspi, Greg M. Madejski, Giorgio Matt, Silvano Molendi, David M. Smith, John A. Tomsick, Marco Ajello, David R. Ballantyne, Mislav Baloković, Didier Barret, Franz E. Bauer, Roger D. Blandford, W. Niel Brandt, Laura W. Brenneman, James Chiang, Deepto Chakrabarty, Jerome Chenevez, Andrea Comastri, Francois Dufour, Martin Elvis, Andrew C. Fabian, Duncan

- Farrah, Chris L. Fryer, Eric V. Gotthelf, Jonathan E. Grindlay, David J. Helfand, Roman Krivonos, David L. Meier, Jon M. Miller, Lorenzo Natalucci, Patrick Ogle, Eran O. Ofek, Andrew Ptak, Stephen P. Reynolds, Jane R. Rigby, Gianpiero Tagliaferri, Stephen E. Thorsett, Ezequiel Treister, and C. Megan Urry. The Nuclear Spectroscopic Telescope Array (NuSTAR) High-energy X-Ray Mission. *ApJ*, 770(2): 103, June 2013. doi: 10.1088/0004-637X/770/2/103.
- Lee Hartmann, Nuria Calvet, Erik Gullbring, and Paola D'Alessio. Accretion and the Evolution of T Tauri Disks. *ApJ*, 495(1):385–400, March 1998. doi: 10.1086/305277.
- Stephen W. Hawking. *A brief history of time. From the Big Bang to Black Holes*. 1988.
- W. Heitler. *Quantum theory of radiation*. 1954.
- HI4PI Collaboration, N. Ben Bekhti, L. Flöer, R. Keller, J. Kerp, D. Lenz, B. Winkel, J. Bailin, M. R. Calabretta, L. Dedes, H. A. Ford, B. K. Gibson, U. Haud, S. Janowiecki, P. M. W. Kalberla, F. J. Lockman, N. M. McClure-Griffiths, T. Murphy, H. Nakanishi, D. J. Pisano, and L. Staveley-Smith. HI4PI: A full-sky H I survey based on EBHIS and GASS. *A&A*, 594:A116, October 2016. doi: 10.1051/0004-6361/201629178.
- L. Hjalmarsson, A. A. Zdziarski, A. Szostek, and D. C. Hannikainen. Spectral variability in Cygnus X-3. *MNRAS*, 392(1):251–263, January 2009. doi: 10.1111/j.1365-2966.2008.14036.x.
- R. M. Hjellming, M. P. Rupen, R. W. Hunstead, D. Campbell-Wilson, A. J. Mioduszewski, B. M. Gaensler, D. A. Smith, R. J. Sault, R. P. Fender, R. E. Spencer, C. J. de la Force, A. M. S. Richards, S. T. Garrington, S. A. Trushkin, F. D. Ghigo, E. B. Waltman, and M. McCollough. Light Curves and Radio Structure of the 1999 September Transient Event in V4641 Sagittarii (=XTE J1819-254=SAX J1819.3-2525). *ApJ*, 544(2):977–992, December 2000. doi: 10.1086/317255.
- Takafumi Hori, Yoshihiro Ueda, Megumi Shidatsu, Taiki Kawamuro, Aya Kubota, Chris Done, Satoshi Nakahira, Kohji Tsumura, Mai Shirahata, and Takahiro Nagayama. SUZAKU Observation of the Black Hole Binary 4U 1630-47 in the Very High State. *ApJ*, 790(1):20, July 2014. doi: 10.1088/0004-637X/790/1/20.
- Min Huang and J. Craig Wheeler. Thermal Instability Accretion Disk Model for the X-Ray Transient A0620-00. *ApJ*, 343:229, August 1989. doi: 10.1086/167700.
- I. Hubeny and T. Lanz. Non-LTE Line-blanketed Model Atmospheres of Hot Stars. I. Hybrid Complete Linearization/Accelerated Lambda Iteration Method. *ApJ*, 439: 875, February 1995. doi: 10.1086/175226.
- Ivan Hubeny and Veronika Hubeny. Non-LTE Models and Theoretical Spectra of Accretion Disks in Active Galactic Nuclei. II. Vertical Structure of the Disk. *ApJ*, 505(2):558–576, October 1998. doi: 10.1086/306207.

- A. Hughes, L. Staveley-Smith, S. Kim, M. Wolleben, and M. Filipović. An Australia Telescope Compact Array 20-cm radio continuum study of the Large Magellanic Cloud. *MNRAS*, 382(2):543–552, December 2007. doi: 10.1111/j.1365-2966.2007.12466.x.
- E. A. Hyde, D. M. Russell, A. Ritter, M. D. Filipović, L. Kaper, K. Grieve, and A. N. O’Brien. LMC X-1: A New Spectral Analysis of the O-star in the Binary and Surrounding Nebula. *PASP*, 129(979):094201, September 2017. doi: 10.1088/1538-3873/aa7407.
- Adam Ingram, Niek Bollemeijer, Alexandra Veledina, Michal Dovciak, Juri Poutanen, Elise Egron, Thomas D. Russell, Sergei A. Trushkin, Michela Negro, Ajay Ratheesh, Fiamma Capitanio, Riley Connors, Joseph Neilsen, Alexander Kraus, Maria Noemi Iacolina, Alberto Pellizzoni, Maura Pilia, Francesco Carotenuto, Giorgio Matt, Guglielmo Mastroserio, Philip Kaaret, Stefano Bianchi, Javier A. Garcia, Matteo Bachetti, Kinwah Wu, Enrico Costa, Melissa Ewing, Vadim Kravtsov, Henric Krawczynski, Vladislav Loktev, Andrea Marinucci, Lorenzo Marra, Romana Mikušincová, Edward Nathan, Maxime Parra, Pierre-Olivier Petrucci, Simona Righini, Paolo Soffitta, James F. Steiner, Jiri Svoboda, Francesco Tombesi, Stefano Tugliani, Francesco Ursini, Yi-Jung Yang, Silvia Zane, Wenda Zhang, Ivan Agudo, Lucio A. Antonelli, Luca Baldini, Wayne H. Baumgartner, Ronaldo Bellazzini, Stephen D. Bongiorno, Raffaella Bonino, Alessandro Brez, Niccolo Bucciantini, Simone Castellano, Elisabetta Cavazzuti, Chien-Ting Chen, Stefano Ciprini, Alessandra De Rosa, Ettore Del Monte, Laura Di Gesu, Niccolo Di Lalla, Alessandro Di Marco, Immacolata Donnarumma, Victor Doroshenko, Steven R. Ehlert, Teruaki Enoto, Yuri Evangelista, Sergio Fabiani, Riccardo Ferrazzoli, Shuichi Gunji, Kiyoshi Hayashida, Jeremy Heyl, Wataru Iwakiri, Svetlana G. Jorstad, Vladimir Karas, Fabian Kislak, Takao Kitaguchi, Jeffery J. Kolodziejczak, Fabio La Monaca, Luca Latronico, Ioannis Liodakis, Simone Maldera, Alberto Manfreda, Frederic Marin, Alan P. Marscher, Herman L. Marshall, Francesco Massaro, Ikuyuki Mitsuishi, Tsunefumi Mizuno, Fabio Muleri, Chi-Yung Ng, Stephen L. O’Dell, Nicola Omodei, Chiara Oppedisano, Alessandro Papitto, George G. Pavlov, Abel L. Peirson, Matteo Perri, Melissa Pesce-Rollins, Andrea Possenti, Simonetta Puccetti, Brian D. Ramsey, John Rankin, Oliver J. Roberts, Roger W. Romani, Carmelo Sgro, Patrick Slane, Gloria Spandre, Douglas A. Swartz, Toru Tamagawa, Fabrizio Tavecchio, Roberto Taverna, Yuzuru Tawara, Allyn F. Tennant, Nicholas E. Thomas, Alessio Trois, Sergey S. Tsygankov, Roberto Turolla, Jacco Vink, Martin C. Weisskopf, and Fei Xie. Tracking the X-ray Polarization of the Black Hole Transient Swift J1727.8-1613 during a State Transition. *arXiv e-prints*, art. arXiv:2311.05497, November 2023. doi: 10.48550/arXiv.2311.05497.
- Adam R. Ingram and Sara E. Motta. A review of quasi-periodic oscillations from black hole X-ray binaries: Observation and theory. *New A Rev.*, 85:101524, September 2019. doi: 10.1016/j.newar.2020.101524.
- Arghajit Jana, Sachindra Naik, Debjit Chatterjee, and Gaurava K. Jaisawal. NuSTAR and Swift observations of the extragalactic black hole X-ray binaries. *MNRAS*, 507(4):4779–4787, November 2021. doi: 10.1093/mnras/stab2448.

- Jiachen Jiang, John Tomsick, Honghui Liu, Andrew Fabian, Riley Connors, Javier Garcia, and Jeremy Hare. Swift Follow-up of 4U 1630-47 in Outburst. *The Astronomer's Telegram*, 15575:1, August 2022.
- F. Jiménez-Ibarra, T. Muñoz-Darias, J. Casares, M. Armas Padilla, and J. M. Corral-Santana. An equatorial outflow in the black hole optical dipper Swift J1357.2-0933. *MNRAS*, 489(3):3420–3426, November 2019. doi: 10.1093/mnras/stz2393.
- P. G. Jonker and G. Nelemans. The distances to Galactic low-mass X-ray binaries: consequences for black hole luminosities and kicks. *MNRAS*, 354(2):355–366, October 2004. doi: 10.1111/j.1365-2966.2004.08193.x.
- W. A. Joye and E. Mandel. New Features of SAOImage DS9. In H. E. Payne, R. I. Jedrzejewski, and R. N. Hook, editors, *Astronomical Data Analysis Software and Systems XII*, volume 295 of *Astronomical Society of the Pacific Conference Series*, page 489, January 2003.
- Philip Kaaret. X-Ray Polarimetry. *arXiv e-prints*, art. arXiv:1408.5899, August 2014. doi: 10.48550/arXiv.1408.5899.
- J. S. Kaastra and J. A. M. Bleeker. Optimal binning of X-ray spectra and response matrix design. *A&A*, 587:A151, March 2016. doi: 10.1051/0004-6361/201527395.
- E. Kalemci, T. J. Maccarone, and J. A. Tomsick. A Dust-scattering Halo of 4U 1630-47 Observed with Chandra and Swift: New Constraints on the Source Distance. *ApJ*, 859(2):88, June 2018. doi: 10.3847/1538-4357/aabcd3.
- Roy P. Kerr. Gravitational Field of a Spinning Mass as an Example of Algebraically Special Metrics. *Phys. Rev. Lett.*, 11(5):237–238, September 1963. doi: 10.1103/PhysRevLett.11.237.
- Brooks E. Kinch, Jeremy D. Schnittman, Scott C. Noble, Timothy R. Kallman, and Julian H. Krolik. Spin and Accretion Rate Dependence of Black Hole X-Ray Spectra. *ApJ*, 922(2):270, December 2021. doi: 10.3847/1538-4357/ac2b9a.
- A. L. King, J. M. Miller, J. Raymond, A. C. Fabian, C. S. Reynolds, T. R. Kallman, D. Maitra, E. M. Cackett, and M. P. Rupen. An Extreme X-Ray Disk Wind in the Black Hole Candidate IGR J17091-3624. *ApJ*, 746(2):L20, February 2012. doi: 10.1088/2041-8205/746/2/L20.
- Ashley L. King, Dominic J. Walton, Jon M. Miller, Didier Barret, Steven E. Boggs, Finn E. Christensen, William W. Craig, Andy C. Fabian, Felix Fürst, Charles J. Hailey, Fiona A. Harrison, Roman Krivonos, Kaya Mori, Lorenzo Natalucci, Daniel Stern, John A. Tomsick, and William W. Zhang. The Disk Wind in the Rapidly Spinning Stellar-mass Black Hole 4U 1630-472 Observed with NuSTAR. *ApJ*, 784(1):L2, March 2014. doi: 10.1088/2041-8205/784/1/L2.
- Ashley L. King, Jon M. Miller, John Raymond, Mark T. Reynolds, and Warren Morningstar. High-resolution Chandra HETG Spectroscopy of V404 Cygni in Outburst. *ApJ*, 813(2):L37, November 2015. doi: 10.1088/2041-8205/813/2/L37.

- F. Kislak, B. Clark, M. Beilicke, and H. Krawczynski. Analyzing the data from X-ray polarimeters with Stokes parameters. *Astroparticle Physics*, 68:45–51, August 2015. doi: 10.1016/j.astropartphys.2015.02.007.
- Shu Koyama, Shin'ya Yamada, Aya Kubota, Makoto S. Tashiro, Yukikatsu Terada, and Kazuo Makishima. Suzaku observation of X-ray variability in soft state LMC X-1. *PASJ*, 67(3):46, June 2015. doi: 10.1093/pasj/psv017.
- H. Krawczynski and B. Beheshtipour. New Constraints on the Spin of the Black Hole Cygnus X-1 and the Physical Properties of its Accretion Disk Corona. *ApJ*, 934(1): 4, July 2022. doi: 10.3847/1538-4357/ac7725.
- Henric Krawczynski, Fabio Muleri, Michal Dovčiak, Alexandra Veledina, Nicole Rodriguez Cavero, Jiri Svoboda, Adam Ingram, Giorgio Matt, Javier A. Garcia, Vladislav Loktev, Michela Negro, Juri Poutanen, Takao Kitaguchi, Jakub Podgorný, John Rankin, Wenda Zhang, Andrei Berdyugin, Svetlana V. Berdyugina, Stefano Bianchi, Dmitry Blinov, Fiamma Capitanio, Niccolò Di Lalla, Paul Draghis, Sergio Fabiani, Masato Kagitani, Vadim Kravtsov, Sebastian Kiehlmann, Luca Latronico, Alexander A. Lutovinov, Nikos Mandarakas, Frédéric Marin, Andrea Marinucci, Jon M. Miller, Tsunefumi Mizuno, Sergey V. Molkov, Nicola Omodei, Pierre-Olivier Petrucci, Ajay Ratheesh, Takeshi Sakanoi, Andrei N. Semena, Raphael Skalidis, Paolo Soffitta, Allyn F. Tennant, Phillipp Thalhammer, Francesco Tombesi, Martin C. Weisskopf, Joern Wilms, Sixuan Zhang, Iván Agudo, Lucio A. Antonelli, Matteo Bachetti, Luca Baldini, Wayne H. Baumgartner, Ronaldo Bellazzini, Stephen D. Bongiorno, Raffaella Bonino, Alessandro Brez, Niccolò Bucciantini, Simone Castellano, Elisabetta Cavazzuti, Stefano Ciprini, Enrico Costa, Alessandra De Rosa, Ettore Del Monte, Laura Di Gesu, Alessandro Di Marco, Immacolata Donnarumma, Victor Doroshenko, Steven R. Ehlert, Teruaki Enoto, Yuri Evangelista, Riccardo Ferrazzoli, Shuichi Gunji, Kiyoshi Hayashida, Jeremy Heyl, Wataru Iwakiri, Svetlana G. Jorstad, Vladimir Karas, Jeffery J. Kolodziejczak, Fabio La Monaca, Ioannis Liodakis, Simone Maldera, Alberto Manfreda, Alan P. Marscher, Herman L. Marshall, Ikuyuki Mitsuishi, Chi-Yung Ng, Stephen L. O'Dell, Chiara Oppedisano, Alessandro Papitto, George G. Pavlov, Abel L. Peirson, Matteo Perri, Melissa Pesce-Rollins, Maura Pilia, Andrea Possenti, Simonetta Puccetti, Brian D. Ramsey, Roger W. Romani, Carmelo Sgrò, Patrick Slane, Gloria Spandre, Toru Tamagawa, Fabrizio Tavecchio, Roberto Taverna, Yuzuru Tawara, Nicholas E. Thomas, Alessio Trois, Sergey Tsygankov, Roberto Turolla, Jacco Vink, Kinwah Wu, Fei Xie, and Silvia Zane. Polarized x-rays constrain the disk-jet geometry in the black hole x-ray binary Cygnus X-1. *Science*, 378(6620):650–654, November 2022. doi: 10.1126/science.add5399.
- Laura Kreidberg, Charles D. Bailyn, Will M. Farr, and Vicky Kalogera. Mass Measurements of Black Holes in X-Ray Transients: Is There a Mass Gap? *ApJ*, 757(1): 36, September 2012. doi: 10.1088/0004-637X/757/1/36.
- Aya Kubota, Ken Ebisawa, Kazuo Makishima, and Kazuhiro Nakazawa. On the Temperature Profile of Radiatively Efficient Geometrically Thin Disks in Black Hole Binaries with the ASCA GIS. *ApJ*, 631(2):1062–1071, October 2005. doi: 10.1086/432900.

- Erik Kuulkers, Rudy Wijnands, Tomaso Belloni, Mariano Méndez, Michiel van der Klis, and Jan van Paradijs. Absorption Dips in the Light Curves of GRO J1655-40 and 4U 1630-47 during Outburst. *ApJ*, 494(2):753–758, February 1998. doi: 10.1086/305248.
- G. Lamer, A. D. Schwope, P. Predehl, I. Traulsen, J. Wilms, and M. Freyberg. A giant X-ray dust scattering ring discovered with SRG/eROSITA around the black hole transient MAXI J1348-630. *A&A*, 647:A7, March 2021. doi: 10.1051/0004-6361/202039757.
- L. D. Landau and E. M. Lifshitz. *Fluid Mechanics*. 1987.
- Cornelia C. Lang, Philip Kaaret, Stéphane Corbel, and Allison Mercer. A Radio Nebula Surrounding the Ultraluminous X-Ray Source in NGC 5408. *ApJ*, 666(1):79–85, September 2007. doi: 10.1086/519553.
- Jean-Pierre Lasota. The disc instability model of dwarf novae and low-mass X-ray binary transients. *New A Rev.*, 45(7):449–508, June 2001. doi: 10.1016/S1387-6473(01)00112-9.
- Josef Lense and Hans Thirring. Über den Einfluß der Eigenrotation der Zentralkörper auf die Bewegung der Planeten und Monde nach der Einsteinschen Gravitationstheorie. *Physikalische Zeitschrift*, 19:156, January 1918.
- C. Leong, E. Kellogg, H. Gursky, H. Tananbaum, and R. Giacconi. X-Ray Emission from the Magellanic Clouds Observed by UHURU. *ApJ*, 170:L67, December 1971. doi: 10.1086/180842.
- Alan M. Levine, Hale Bradt, Wei Cui, J. G. Jernigan, Edward H. Morgan, Ronald Remillard, Robert E. Shirey, and Donald A. Smith. First Results from the All-Sky Monitor on the Rossi X-Ray Timing Explorer. *ApJ*, 469:L33, September 1996. doi: 10.1086/310260.
- Alan M. Levine, Hale V. Bradt, Deepto Chakrabarty, Robin H. D. Corbet, and Robert J. Harris. An Extended and More Sensitive Search for Periodicities in Rossi X-Ray Timing Explorer/All-Sky Monitor X-Ray Light Curves. *ApJS*, 196(1):6, September 2011. doi: 10.1088/0067-0049/196/1/6.
- Li-Xin Li, Erik R. Zimmerman, Ramesh Narayan, and Jeffrey E. McClintock. Multitemperature Blackbody Spectrum of a Thin Accretion Disk around a Kerr Black Hole: Model Computations and Comparison with Observations. *ApJS*, 157(2):335–370, April 2005. doi: 10.1086/428089.
- K. S. Long, G. A. Chanan, W. H. M. Ku, and R. Novick. The linear X-ray polarization of Scorpius X-1. *ApJ*, 232:L107–L110, September 1979. doi: 10.1086/183045.
- Penélope Longa-Peña. PhD thesis, University of Warwick, 2015.
- Malcolm S. Longair. *High Energy Astrophysics*. 2011.

- Thomas J. Maccarone. Observational Tests of the Picture of Disk Accretion. *Space Sci. Rev.*, 183(1-4):101–120, September 2014. doi: 10.1007/s11214-013-0032-4.
- Thomas J. Maccarone, Arlo Osler, James C. A. Miller-Jones, P. Atri, David M. Russell, David L. Meier, Ian M. McHardy, and Penelope A. Longa-Peña. The stringent upper limit on jet power in the persistent soft-state source 4U 1957+11. *MNRAS*, 498(1): L40–L45, October 2020. doi: 10.1093/mnrasl/slaa120.
- Kristin K. Madsen, Karl Forster, Brian Grefenstette, Fiona A. Harrison, and Hiromasa Miyasaka. Effective area calibration of the Nuclear Spectroscopic Telescope Array. *Journal of Astronomical Telescopes, Instruments, and Systems*, 8:034003, July 2022. doi: 10.1117/1.JATIS.8.3.034003.
- Dipankar Maitra, Jon M. Miller, Mark T. Reynolds, Rubens Reis, and Mike Nowak. Results of the Swift Monitoring Campaign of the X-Ray Binary 4U 1957+11: Constraints on Binary Parameters. *ApJ*, 794(1):85, October 2014. doi: 10.1088/0004-637X/794/1/85.
- Ben Margalit and Brian D. Metzger. Constraining the Maximum Mass of Neutron Stars from Multi-messenger Observations of GW170817. *ApJ*, 850(2):L19, December 2017. doi: 10.3847/2041-8213/aa991c.
- B. Margon, J. R. Thorstensen, and S. Bowyer. The optical counterpart of 3U 1956+11. *ApJ*, 221:907–911, May 1978. doi: 10.1086/156093.
- F. Marin. Modeling optical and UV polarization of AGNs. V. Dilution by interstellar polarization and the host galaxy. *A&A*, 615:A171, July 2018. doi: 10.1051/0004-6361/201833225.
- F. Marin, R. W. Goosmann, C. M. Gaskell, D. Porquet, and M. Dovčiak. Modeling optical and UV polarization of AGNs. II. Polarization imaging and complex reprocessing. *A&A*, 548:A121, December 2012. doi: 10.1051/0004-6361/201219751.
- Hans Mark, R. Price, R. Rodrigues, F. D. Seward, and C. D. Swift. Detection of X-Rays from the Large Magellanic Cloud. *ApJ*, 155:L143, March 1969. doi: 10.1086/180322.
- L. Marra, M. Brigitte, N. Rodriguez Cavero, S. Chun, J. F. Steiner, M. Dovčiak, M. Nowak, S. Bianchi, F. Capitanio, A. Ingram, G. Matt, F. Muleri, J. Podgorný, J. Poutanen, J. Svoboda, R. Taverna, F. Ursini, A. Veledina, A. De Rosa, J. A. García, A. A. Lutovinov, I. A. Mereminskiy, R. Farinelli, S. Gunji, P. Kaaret, T. Kallman, H. Krawczynski, Y. Kan, K. Hu, A. Marinucci, G. Mastroserio, R. Mikušincová, M. Parra, P. O. Petrucci, A. Ratheesh, P. Soffitta, F. Tombesi, S. Zane, I. Agudo, L. A. Antonelli, M. Bachetti, L. Baldini, W. H. Baumgartner, R. Bellazzini, S. D. Bongiorno, R. Bonino, A. Brez, N. Bucciantini, S. Castellano, E. Cavazzuti, C. Chen, S. Ciprini, E. Costa, E. Del Monte, L. Di Gesu, N. Di Lalla, A. Di Marco, I. Donnarumma, V. Doroshenko, S. R. Ehlert, T. Enoto, Y. Evangelista, S. Fabiani, R. Ferrazzoli, K. Hayashida, J. Heyl, W. Iwakiri, S. G. Jorstad, V. Karas, F. Kislat, T. Kitaguchi, J. J. Kolodziejczak, F. La Monaca, L. Latronico, I. Liodakis, S. Maldera, A. Manfreda, F. Marin, A. P. Marscher, H. L. Marshall,

- F. Massaro, I. Mitsuishi, T. Mizuno, M. Negro, C. Y. Ng, S. L. O'Dell, N. Omodei, C. Oppedisano, A. Papitto, G. G. Pavlov, A. L. Peirson, M. Perri, M. Pesce-Rollins, M. Pilia, A. Possenti, S. Puccetti, B. D. Ramsey, J. Rankin, O. J. Roberts, R. W. Romani, C. Sgrò, P. Slane, G. Spandre, D. A. Swartz, T. Tamagawa, F. Tavecchio, Y. Tawara, A. F. Tennant, N. E. Thomas, A. Trois, S. S. Tsygankov, R. Turolla, J. Vink, M. C. Weisskopf, K. Wu, and F. Xie. IXPE observation confirms a high spin in the accreting black hole 4U 1957+115. *A&A*, 684:A95, April 2024. doi: 10.1051/0004-6361/202348277.
- A. Martocchia, V. Karas, and G. Matt. Effects of Kerr space-time on spectral features from X-ray illuminated accretion discs. *MNRAS*, 312(4):817–826, March 2000. doi: 10.1046/j.1365-8711.2000.03205.x.
- Paul A. Mason, Edward L. Robinson, Amanda J. Bayless, and Pasi J. Hakala. Long-term Optical Observations of Two LMXBS: UW CrB (=MS 1603+260) and V1408 Aql (=4U 1957+115). *AJ*, 144(4):108, October 2012. doi: 10.1088/0004-6256/144/4/108.
- Masaru Matsuoka, Kazuyoshi Kawasaki, Shiro Ueno, Hiroshi Tomida, Mitsuhiro Kohama, Motoko Suzuki, Yasuki Adachi, Masaki Ishikawa, Tatehiro Mihara, Mutsumi Sugizaki, Naoki Isobe, Yujin Nakagawa, Hiroshi Tsunemi, Emi Miyata, Nobuyuki Kawai, Jun Kataoka, Mikio Morii, Atsumasa Yoshida, Hitoshi Negoro, Motoki Nakajima, Yoshihiro Ueda, Hirotaka Chujo, Kazutaka Yamaoka, Osamu Yamazaki, Satoshi Nakahira, Tetsuya You, Ryoji Ishiwata, Sho Miyoshi, Satoshi Eguchi, Kazuo Hiroi, Haruyoshi Katayama, and Ken Ebisawa. The MAXI Mission on the ISS: Science and Instruments for Monitoring All-Sky X-Ray Images. *PASJ*, 61:999, October 2009. doi: 10.1093/pasj/61.5.999.
- G. Matt. General Relativity effects and line emission. *Astronomische Nachrichten*, 327(10):949, December 2006. doi: 10.1002/asna.200610670.
- G. Matt, A. C. Fabian, and R. R. Ross. X-ray photoionized accretion discs : UV and X-ray continuum spectra and polarization. *MNRAS*, 264:839–852, October 1993. doi: 10.1093/mnras/264.4.839.
- G. Matt, A. C. Fabian, and C. S. Reynolds. Geometrical and chemical dependence of K-shell X-ray features. *MNRAS*, 289(1):175–184, July 1997. doi: 10.1093/mnras/289.1.175.
- Giorgio Matt, Marco Feroci, Massimo Rapisarda, and Enrico Costa. Treatment of Compton scattering of linearly polarized photons in Monte Carlo codes. *Radiation Physics and Chemistry*, 48(4):403–411, October 1996. doi: 10.1016/0969-806X(95)00472-A.
- Jeffrey E. McClintock and Ronald A. Remillard. Black hole binaries. In *Compact stellar X-ray sources*, volume 39, pages 157–213. 2006. doi: 10.48550/arXiv.astro-ph/0306213.
- William H. McMaster. Matrix Representation of Polarization. *Reviews of Modern Physics*, 33(1):8–27, January 1961. doi: 10.1103/RevModPhys.33.8.

- Viraf M. Mehta, Mehmet Demirtas, Cody Long, David J. E. Marsh, Liam McAllister, and Matthew J. Stott. Superradiance in string theory. *J. Cosmology Astropart. Phys.*, 2021(7):033, July 2021. doi: 10.1088/1475-7516/2021/07/033.
- F. Meyer and E. Meyer-Hofmeister. On the elusive cause of cataclysmic variable outbursts. *A&A*, 104:L10–L12, January 1981.
- F. Meyer and E. Meyer-Hofmeister. Accretion disk evaporation by a coronal siphon flow. *A&A*, 288:175–182, August 1994.
- John Michell. On the Means of Discovering the Distance, Magnitude, &c. of the Fixed Stars, in Consequence of the Diminution of the Velocity of Their Light, in Case Such a Diminution Should be Found to Take Place in any of Them, and Such Other Data Should be Procured from Observations, as Would be Farther Necessary for That Purpose. By the Rev. John Michell, B. D. F. R. S. In a Letter to Henry Cavendish, Esq. F. R. S. and A. S. *Philosophical Transactions of the Royal Society of London Series I*, 74:35–57, January 1784.
- Romana Mikušincová, Michal Dovciak, Michal Bursa, Niccolo Di Lalla, Giorgio Matt, Jiri Svoboda, Roberto Taverna, and Wenda Zhang. X-ray polarimetry as a tool to measure the black hole spin in microquasars: simulations of IXPE capabilities. *MNRAS*, 519(4):6138–6148, March 2023. doi: 10.1093/mnras/stad077.
- J. M. Miller, C. S. Reynolds, A. C. Fabian, G. Miniutti, and L. C. Gallo. Stellar-Mass Black Hole Spin Constraints from Disk Reflection and Continuum Modeling. *ApJ*, 697(1):900–912, May 2009. doi: 10.1088/0004-637X/697/1/900.
- J. M. Miller, A. C. Fabian, J. Kaastra, T. Kallman, A. L. King, D. Proga, J. Raymond, and C. S. Reynolds. Powerful, Rotating Disk Winds from Stellar-mass Black Holes. *ApJ*, 814(2):87, December 2015. doi: 10.1088/0004-637X/814/2/87.
- J. M. Miller, J. Raymond, A. C. Fabian, E. Gallo, J. Kaastra, T. Kallman, A. L. King, D. Proga, C. S. Reynolds, and A. Zoghbi. The Accretion Disk Wind in the Black Hole GRS 1915+105. *ApJ*, 821(1):L9, April 2016. doi: 10.3847/2041-8205/821/1/L9.
- J. C. A. Miller-Jones, P. G. Jonker, V. Dhawan, W. Brisken, M. P. Rupen, G. Nelemans, and E. Gallo. The First Accurate Parallax Distance to a Black Hole. *ApJ*, 706(2):L230–L234, December 2009. doi: 10.1088/0004-637X/706/2/L230.
- James C. A. Miller-Jones, Arash Bahramian, Jerome A. Orosz, Ilya Mandel, Lijun Gou, Thomas J. Maccarone, Coenraad J. Neijssel, Xueshan Zhao, Janusz Ziółkowski, Mark J. Reid, Phil Uttley, Xueying Zheng, Do-Young Byun, Richard Dodson, Victoria Grinberg, Taehyun Jung, Jeong-Sook Kim, Benito Marcote, Sera Markoff, María J. Rioja, Anthony P. Rushton, David M. Russell, Gregory R. Sivakoff, Alexandra J. Tetarenko, Valeriu Tudose, and Joern Wilms. Cygnus X-1 contains a 21-solar mass black hole—Implications for massive star winds. *Science*, 371(6533):1046–1049, March 2021. doi: 10.1126/science.abb3363.
- I. F. Mirabel and L. F. Rodríguez. Sources of Relativistic Jets in the Galaxy. *ARA&A*, 37:409–443, January 1999. doi: 10.1146/annurev.astro.37.1.409.

- I. F. Mirabel, L. F. Rodriguez, B. Cordier, J. Paul, and F. Lebrun. A double-sided radio jet from the compact Galactic Centre annihilator 1E1740.7-2942. *Nature*, 358 (6383):215–217, July 1992. doi: 10.1038/358215a0.
- Charles W. Misner, Kip S. Thorne, and John Archibald Wheeler. *Gravitation*. 1973.
- K. Mitsuda, H. Inoue, K. Koyama, K. Makishima, M. Matsuoka, Y. Ogawara, N. Shibasaki, K. Suzuki, Y. Tanaka, and T. Hirano. Energy spectra of low-mass binary X-ray sources observed from Tenma. *PASJ*, 36:741–759, January 1984.
- S. Motta, T. Muñoz-Darias, P. Casella, T. Belloni, and J. Homan. Low-frequency oscillations in black holes: a spectral-timing approach to the case of GX 339-4. *MNRAS*, 418(4):2292–2307, December 2011. doi: 10.1111/j.1365-2966.2011.19566.x.
- S. E. Motta, T. M. Belloni, L. Stella, T. Muñoz-Darias, and R. Fender. Precise mass and spin measurements for a stellar-mass black hole through X-ray timing: the case of GRO J1655-40. *MNRAS*, 437(3):2554–2565, January 2014. doi: 10.1093/mnras/stt2068.
- S. E. Motta, P. Casella, M. Henze, T. Muñoz-Darias, A. Sanna, R. Fender, and T. Belloni. Geometrical constraints on the origin of timing signals from black holes. *MNRAS*, 447(2):2059–2072, February 2015. doi: 10.1093/mnras/stu2579.
- T. Muñoz-Darias, J. Casares, D. Mata Sánchez, R. P. Fender, M. Armas Padilla, M. Linares, G. Ponti, P. A. Charles, K. P. Mooley, and J. Rodriguez. Regulation of black-hole accretion by a disk wind during a violent outburst of V404 Cygni. *Nature*, 534(7605):75–78, June 2016. doi: 10.1038/nature17446.
- Sneha Prakash Mudambi, A Rao, S B Gudennavar, R Misra, and S G Bubbly. Estimation of the black hole spin in LMC X-1 using AstroSat. *MNRAS*, 498 (3):4404–4410, 09 2020. ISSN 0035-8711. doi: 10.1093/mnras/staa2656. URL <https://doi.org/10.1093/mnras/staa2656>.
- Joseph Neilsen and Julia C. Lee. Accretion disk winds as the jet suppression mechanism in the microquasar GRS 1915+105. *Nature*, 458(7237):481–484, March 2009. doi: 10.1038/nature07680.
- I. D. Novikov and K. S. Thorne. Astrophysics of black holes. In *Black Holes (Les Astres Occlus)*, pages 343–450, January 1973.
- M. A. Nowak, J. Wilms, W. A. Heindl, K. Pottschmidt, J. B. Dove, and M. C. Begelman. A good long look at the black hole candidates LMC X-1 and LMC X-3. *MNRAS*, 320(3):316–326, January 2001. doi: 10.1046/j.1365-8711.2001.03984.x.
- Michael A. Nowak and Jörn Wilms. On the Enigmatic X-Ray Source V1408 Aquilae (=4U 1957+11). *ApJ*, 522(1):476–486, September 1999. doi: 10.1086/307633.
- Michael A. Nowak, Adrienne Juett, Jeroen Homan, Yangsen Yao, Jörn Wilms, Norbert S. Schulz, and Claude R. Canizares. Disk-dominated States of 4U 1957+11: Chandra, XMM-Newton, and RXTE Observations of Ostensibly the Most Rapidly

- Spinning Galactic Black Hole. *ApJ*, 689(2):1199–1214, December 2008. doi: 10.1086/592227.
- Michael A. Nowak, Jörn Wilms, Katja Pottschmidt, Norbert Schulz, Dipankar Maitra, and Jon Miller. Suzaku Observations of 4U 1957+11: Potentially the Most Rapidly Spinning Black Hole in (the Halo of) the Galaxy. *ApJ*, 744(2):107, January 2012. doi: 10.1088/0004-637X/744/2/107.
- J. R. Oppenheimer and G. M. Volkoff. On Massive Neutron Cores. *Physical Review*, 55(4):374–381, February 1939. doi: 10.1103/PhysRev.55.374.
- Jerome A. Orosz, Danny Steeghs, Jeffrey E. McClintock, Manuel A. P. Torres, Ivan Bochkov, Lijun Gou, Ramesh Narayan, Michael Blaschak, Alan M. Levine, Ronald A. Remillard, Charles D. Bailyn, Morgan M. Dwyer, and Michelle Buxton. A New Dynamical Model for the Black Hole Binary LMC X-1. *ApJ*, 697(1):573–591, May 2009. doi: 10.1088/0004-637X/697/1/573.
- Jerome A. Orosz, James F. Steiner, Jeffrey E. McClintock, Michelle M. Buxton, Charles D. Bailyn, Danny Steeghs, Alec Guberman, and Manuel A. P. Torres. The Mass of the Black Hole in LMC X-3. *ApJ*, 794(2):154, October 2014. doi: 10.1088/0004-637X/794/2/154.
- Feryal Özel, Dimitrios Psaltis, Ramesh Narayan, and Jeffrey E. McClintock. The Black Hole Mass Distribution in the Galaxy. *ApJ*, 725(2):1918–1927, December 2010. doi: 10.1088/0004-637X/725/2/1918.
- Don N. Page and Kip S. Thorne. Disk-Accretion onto a Black Hole. Time-Averaged Structure of Accretion Disk. *ApJ*, 191:499–506, July 1974. doi: 10.1086/152990.
- M. J. Page, R. Soria, K. Wu, K. O. Mason, F. A. Cordova, and W. C. Priedhorsky. XMM-Newton RGS spectroscopy of LMC X-3. *MNRAS*, 345(2):639–649, October 2003. doi: 10.1046/j.1365-8711.2003.06967.x.
- Mayukh Pahari, Sudip Bhattacharyya, A. R. Rao, Dipankar Bhattacharya, Santosh V. Vadawale, Gulab C. Dewangan, I. M. McHardy, Poshak Gandhi, Stéphane Corbel, Norbert S. Schulz, and Diego Altamirano. AstroSat and Chandra View of the High Soft State of 4U 1630-47 (4U 1630-472): Evidence of the Disk Wind and a Rapidly Spinning Black Hole. *ApJ*, 867(2):86, November 2018. doi: 10.3847/1538-4357/aae53b.
- M. W. Pakull and L. P. Angebault. Detection of an X-ray-ionized nebula around the black hole candidate binary LMC X-1. *Nature*, 322(6079):511–517, August 1986. doi: 10.1038/322511a0.
- A. N. Parmar, L. Stella, and N. E. White. The Evolution of the 1984 Outburst of the Transient X-Ray Source 4U 1630-47. *ApJ*, 304:664, May 1986. doi: 10.1086/164204.
- M. Parra, P. O. Petrucci, S. Bianchi, V. E. Gianolli, F. Ursini, and G. Ponti. The current state of disk wind observations in BHLMBs through X-ray absorption lines in the iron band. *arXiv e-prints*, art. arXiv:2308.00691, August 2023. doi: 10.48550/arXiv.2308.00691.

- M. Pavlinsky, A. Tkachenko, V. Levin, N. Alexandrovich, V. Arefiev, V. Babyshkin, O. Batanov, Yu. Bodnar, A. Bogomolov, A. Bubnov, M. Buntov, R. Burenin, I. Chelovekov, C. T. Chen, T. Drozdova, S. Ehlert, E. Filippova, S. Frolov, D. Gamkov, S. Garanin, M. Garin, A. Glushenko, A. Gorelov, S. Grebenev, S. Grigorovich, P. Gureev, E. Gurova, R. Ilkaev, I. Katasonov, A. Krivchenko, R. Krivonos, F. Korotkov, M. Kudelin, M. Kuznetsova, V. Lazarchuk, I. Lomakin, I. Lapshov, V. Lipilin, A. Lutovinov, I. Mereminskiy, S. Molkov, V. Nazarov, V. Oleinikov, E. Pikalov, B. D. Ramsey, I. Roiz, A. Rotin, A. Ryadov, E. Sankin, S. Sazonov, D. Sedov, A. Semena, N. Semena, D. Serbinov, A. Shirshakov, A. Shtykovsky, A. Shvetsov, R. Sunyaev, D. A. Swartz, V. Tambov, V. Voron, and A. Yaskovich. The ART-XC telescope on board the SRG observatory. *A&A*, 650:A42, June 2021. doi: 10.1051/0004-6361/202040265.
- Roger Penrose. Gravitational Collapse: the Role of General Relativity. *Nuovo Cimento Rivista Serie*, 1:252, January 1969.
- E. Piconcelli, E. Jimenez-Bailón, M. Guainazzi, N. Schartel, P. M. Rodríguez-Pascual, and M. Santos-Lleó. Evidence for a multizone warm absorber in the XMM-Newton spectrum of Markarian 304. *MNRAS*, 351(1):161–168, June 2004. doi: 10.1111/j.1365-2966.2004.07764.x.
- G. Pietrzyński, D. Graczyk, W. Gieren, I. B. Thompson, B. Pilecki, A. Udalski, I. Soszyński, S. Kozłowski, P. Konorski, K. Suchomska, G. Bono, P. G. Prada Moroni, S. Villanova, N. Nardetto, F. Bresolin, R. P. Kudritzki, J. Storm, A. Gallenne, R. Smolec, D. Minniti, M. Kubiak, M. K. Szymański, R. Poleski, Ł. Wyrzykowski, K. Ulaczyk, P. Pietrukowicz, M. Górski, and P. Karczmarek. An eclipsing-binary distance to the Large Magellanic Cloud accurate to two per cent. *Nature*, 495(7439):76–79, March 2013. doi: 10.1038/nature11878.
- G. Pietrzyński, D. Graczyk, A. Gallenne, W. Gieren, I. B. Thompson, B. Pilecki, P. Karczmarek, M. Górski, K. Suchomska, M. Taormina, B. Zgirski, P. Wielgórski, Z. Kołaczkowski, P. Konorski, S. Villanova, N. Nardetto, P. Kervella, F. Bresolin, R. P. Kudritzki, J. Storm, R. Smolec, and W. Narloch. A distance to the Large Magellanic Cloud that is precise to one per cent. *Nature*, 567(7747):200–203, March 2019. doi: 10.1038/s41586-019-0999-4.
- Richard M. Plotkin, Elena Gallo, Sera Markoff, Jeroen Homan, Peter G. Jonker, James C. A. Miller-Jones, David M. Russell, and Samia Drappeau. Constraints on relativistic jets in quiescent black hole X-ray binaries from broad-band spectral modelling. *MNRAS*, 446(4):4098–4111, February 2015. doi: 10.1093/mnras/stu2385.
- J. Podgorný, M. Dovčiak, R. Goosmann, F. Marin, G. Matt, A. Róžańska, and V. Karas. Spectral and polarization properties of reflected X-ray emission from black-hole accretion discs for a distant observer: the lamp-post model. *MNRAS*, 524(3):3853–3876, September 2023a. doi: 10.1093/mnras/stad2169.
- J. Podgorný, L. Marra, F. Muleri, N. Rodriguez Cavero, A. Ratheesh, M. Dovčiak, R. Mikušincová, M. Brigitte, J. F. Steiner, A. Veledina, S. Bianchi, H. Krawczynski, J. Svoboda, P. Kaaret, G. Matt, J. A. García, P. O. Petrucci, A. Lutovinov,

- A. Semena, A. Di Marco, M. Negro, M. C. Weisskopf, A. Ingram, J. Poutanen, B. Beheshtipour, S. Chun, K. Hu, T. Mizuno, Z. Sixuan, F. Tombesi, S. Zane, I. Agudo, L. A. Antonelli, M. Bachetti, L. Baldini, W. H. Baumgartner, R. Bellazzini, S. D. Bongiorno, R. Bonino, A. Brez, N. Bucciantini, F. Capitanio, S. Castellano, E. Cavazzuti, C. Chen, S. Ciprini, E. Costa, A. De Rosa, E. Del Monte, L. Di Gesu, N. Di Lalla, I. Donnarumma, V. Doroshenko, S. R. Ehlert, T. Enoto, Y. Evangelista, S. Fabiani, R. Ferrazzoli, S. Gunji, K. Hayashida, J. Heyl, W. Iwakiri, S. G. Jorstad, V. Karas, F. Kislak, T. Kitaguchi, J. J. Kolodziejczak, F. La Monaca, L. Latronico, I. Lioudakis, S. Maldera, A. Manfreda, F. Marin, A. Marinucci, A. P. Marscher, H. L. Marshall, F. Massaro, I. Mitsuishi, C. Y. Ng, S. L. O'Dell, N. Omodei, C. Oppedisano, A. Papitto, G. G. Pavlov, A. L. Peirson, M. Perri, M. Pesce-Rollins, M. Pilia, A. Possenti, S. Puccetti, B. D. Ramsey, J. Rankin, O. J. Roberts, R. W. Romani, C. Sgrò, P. Slane, P. Soffitta, G. Spandre, D. A. Swartz, T. Tamagawa, F. Tavecchio, R. Taverna, Y. Tawara, A. F. Tennant, N. E. Thomas, A. Trois, S. S. Tsygankov, R. Turolla, J. Vink, K. Wu, and F. Xie. The first X-ray polarimetric observation of the black hole binary LMC X-1. *MNRAS*, 526(4):5964–5975, December 2023b. doi: 10.1093/mnras/stad3103.
- Ph. Podsiadlowski, S. Rappaport, and Z. Han. On the formation and evolution of black hole binaries. *MNRAS*, 341(2):385–404, May 2003. doi: 10.1046/j.1365-8711.2003.06464.x.
- G. Ponti, R. P. Fender, M. C. Begelman, R. J. H. Dunn, J. Neilsen, and M. Coriat. Ubiquitous equatorial accretion disc winds in black hole soft states. *MNRAS*, 422(1):L11–L15, May 2012. doi: 10.1111/j.1745-3933.2012.01224.x.
- G. Ponti, S. Bianchi, T. Muñoz-Darias, K. De, R. Fender, and A. Merloni. High ionisation absorption in low mass X-ray binaries. *Astronomische Nachrichten*, 337(4-5):512–517, May 2016. doi: 10.1002/asna.201612339.
- J. Poutanen and P. S. Coppi. Unification of Spectral States of Accreting Black Holes. *Physica Scripta Volume T*, 77:57, January 1998. doi: 10.48550/arXiv.astro-ph/9711316.
- J. Poutanen and O. Vilhu. Compton scattering of polarized light in two-phase accretion discs. *A&A*, 275:337, August 1993.
- Juri Poutanen. Relativistic Jets in Blazars: Polarization of Radiation. *ApJS*, 92:607, June 1994. doi: 10.1086/192024.
- Juri Poutanen and Roland Svensson. The Two-Phase Pair Corona Model for Active Galactic Nuclei and X-Ray Binaries: How to Obtain Exact Solutions. *ApJ*, 470:249, October 1996. doi: 10.1086/177865.
- Juri Poutanen, Alexandra Veledina, and Andrei M. Beloborodov. Polarized X-Rays from Windy Accretion in Cygnus X-1. *ApJ*, 949(1):L10, May 2023. doi: 10.3847/2041-8213/acd33e.

- W. Priedhorsky. Recurrent Population II X-ray transients — similarities to SU UMa cataclysmic variables. *Ap&SS*, 126(1):89–98, October 1986. doi: 10.1007/BF00644177.
- Ying Qin, Pablo Marchant, Tassos Fragos, Georges Meynet, and Vicky Kalogera. On the Origin of Black Hole Spin in High-mass X-Ray Binaries. *ApJ*, 870(2):L18, January 2019. doi: 10.3847/2041-8213/aaf97b.
- John Rankin, Vadim Kravtsov, Fabio Muleri, Juri Poutanen, Frédéric Marin, Fiamma Capitanio, Giorgio Matt, Enrico Costa, Alessandro Di Marco, Sergio Fabiani, Fabio La Monaca, Lorenzo Marra, and Paolo Soffitta. X-Ray Polarimetry as a Tool to Constrain Orbital Parameters in X-Ray Binaries. *ApJ*, 962(1):34, February 2024. doi: 10.3847/1538-4357/ad1991.
- A. Ratheesh, G. Matt, F. Tombesi, P. Soffitta, M. Pesce-Rollins, and A. Di Marco. Exploring the accretion-ejection geometry of GRS 1915+105 in the obscured state with future X-ray spectro-polarimetry. *A&A*, 655:A96, November 2021. doi: 10.1051/0004-6361/202140701.
- Ajay Ratheesh, Michal Dovčiak, Henric Krawczynski, Jakub Podgorný, Lorenzo Marra, Alexandra Veledina, Valery F. Suleimanov, Nicole Rodriguez Cavero, James F. Steiner, Jiří Svoboda, Andrea Marinucci, Stefano Bianchi, Michela Negro, Giorgio Matt, Francesco Tombesi, Juri Poutanen, Adam Ingram, Roberto Taverna, Andrew West, Vladimir Karas, Francesco Ursini, Paolo Soffitta, Fiamma Capitanio, Domenico Viscolo, Alberto Manfreda, Fabio Muleri, Maxime Parra, Banafsheh Beheshtipour, Sohee Chun, Nicolò Cibrario, Niccolò Di Lalla, Sergio Fabiani, Kun Hu, Philip Kaaret, Vladislav Loktev, Romana Mikušincová, Tsunefumi Mizuno, Nicola Omodei, Pierre-Olivier Petrucci, Simonetta Puccetti, John Rankin, Silvia Zane, Sixuan Zhang, Iván Agudo, Lucio A. Antonelli, Matteo Bachetti, Luca Baldini, Wayne H. Baumgartner, Ronaldo Bellazzini, Stephen D. Bongiorno, Raffaella Bonino, Alessandro Brez, Niccolò Bucciantini, Simone Castellano, Elisabetta Cavazzuti, Chien-Ting Chen, Stefano Ciprini, Enrico Costa, Alessandra De Rosa, Ettore Del Monte, Laura Di Gesu, Alessandro Di Marco, Immacolata Donnarumma, Victor Doroshenko, Steven R. Ehlert, Teruaki Enoto, Yuri Evangelista, Riccardo Ferrazzoli, Javier A. Garcia, Shuichi Gunji, Kiyoshi Hayashida, Jeremy Heyl, Wataru Iwakiri, Svetlana G. Jorstad, Fabian Kislak, Takao Kitaguchi, Jeffery J. Kolodziejczak, Fabio La Monaca, Luca Latronico, Ioannis Liodakis, Simone Maldera, Frédéric Marin, Alan P. Marscher, Herman L. Marshall, Francesco Massaro, Ikuyuki Mitsuishi, Stephen C. Y. Ng, Stephen L. O’Dell, Chiara Oppedisano, Alessandro Papitto, George G. Pavlov, Abel L. Peirson, Matteo Perri, Melissa Pesce-Rollins, Maura Pilia, Andrea Possenti, Brian D. Ramsey, Oliver J. Roberts, Roger W. Romani, Carmelo Sgrò, Patrick Slane, Gloria Spandre, Douglas A. Swartz, Toru Tamagawa, Fabrizio Tavecchio, Yuzuru Tawara, Allyn F. Tennant, Nicholas E. Thomas, Alessio Trois, Sergey S. Tsygankov, Roberto Turolla, Jacco Vink, Martin C. Weisskopf, Kinwah Wu, and Fei Xie. X-Ray Polarization of the Black Hole X-Ray Binary 4U 1630–47 Challenges the Standard Thin Accretion Disk Scenario. *ApJ*, 964(1):77, March 2024. doi: 10.3847/1538-4357/ad226e.

- C. A. Reid, M. D. Johnston, H. V. Bradt, R. E. Doxsey, R. E. Griffiths, and D. A. Schwartz. Unidentified galactic X-ray sources positioned with the HEAO-1 scanning modulation collimator. *AJ*, 85:1062–1070, August 1980. doi: 10.1086/112768.
- Ronald A. Remillard and Jeffrey E. McClintock. X-Ray Properties of Black-Hole Binaries. *ARA&A*, 44(1):49–92, September 2006. doi: 10.1146/annurev.astro.44.051905.092532.
- Ronald A. Remillard, Michael Loewenstein, James F. Steiner, Gregory Y. Prigozhin, Beverly LaMarr, Teruaki Enoto, Keith C. Gendreau, Zaven Arzoumanian, Craig Markwardt, Arkadip Basak, Abigail L. Stevens, Paul S. Ray, Diego Altamirano, and Douglas J. K. Buisson. An Empirical Background Model for the NICER X-Ray Timing Instrument. *AJ*, 163(3):130, March 2022. doi: 10.3847/1538-3881/ac4ae6.
- M. Revnivtsev, S. Sazonov, E. Churazov, W. Forman, A. Vikhlinin, and R. Sunyaev. Discrete sources as the origin of the Galactic X-ray ridge emission. *Nature*, 458(7242):1142–1144, April 2009. doi: 10.1038/nature07946.
- Christopher S. Reynolds. Observational Constraints on Black Hole Spin. *ARA&A*, 59:117–154, September 2021. doi: 10.1146/annurev-astro-112420-035022.
- Clifford E. Rhoades and Remo Ruffini. Maximum Mass of a Neutron Star. *Phys. Rev. Lett.*, 32(6):324–327, February 1974. doi: 10.1103/PhysRevLett.32.324.
- D. Ricci, G. L. Israel, and L. Stella. EXOSAT observations of the ultra-soft X-ray binary 4U 1957+11. *A&A*, 299:731, July 1995. doi: 10.48550/arXiv.astro-ph/9501098.
- Nicole Rodriguez Cavero, Lorenzo Marra, Henric Krawczynski, Michal Dovčiak, Stefano Bianchi, James F. Steiner, Jiri Svoboda, Fiamma Capitanio, Giorgio Matt, Michela Negro, Adam Ingram, Alexandra Veledina, Roberto Taverna, Vladimir Karas, Francesco Ursini, Jakub Podgorný, Ajay Ratheesh, Valery Suleimanov, Romana Mikušincová, Silvia Zane, Philip Kaaret, Fabio Muleri, Juri Poutanen, Christian Malacaria, Pierre-Olivier Petrucci, Ephraim Gau, Kun Hu, Sohee Chun, Iván Agudo, Lucio A. Antonelli, Matteo Bachetti, Luca Baldini, Wayne H. Baumgartner, Ronaldo Bellazzini, Stephen D. Bongiorno, Raffaella Bonino, Alessandro Brez, Niccolò Bucciantini, Simone Castellano, Elisabetta Cavazzuti, Chien-Ting Chen, Stefano Ciprini, Enrico Costa, Alessandra De Rosa, Ettore Del Monte, Laura Di Gesu, Niccolò Di Lalla, Alessandro Di Marco, Immacolata Donnarumma, Victor Doroshenko, Steven R. Ehlert, Teruaki Enoto, Yuri Evangelista, Sergio Fabiani, Riccardo Ferrazzoli, Javier A. García, Shuichi Gunji, Kiyoshi Hayashida, Jeremy Heyl, Wataru Iwakiri, Svetlana G. Jorstad, Fabian Kislat, Takao Kitaguchi, Jeffery J. Kolodziejczak, Fabio La Monaca, Luca Latronico, Ioannis Lioudakis, Simone Maldera, Alberto Manfreda, Frédéric Marin, Andrea Marinucci, Alan P. Marscher, Herman L. Marshall, Francesco Massaro, Ikuyuki Mitsuishi, Tsunefumi Mizuno, Chi-Yung Ng, Stephen L. O’Dell, Nicola Omodei, Chiara Oppedisano, Alessandro Papitto, George G. Pavlov, Abel L. Peirson, Matteo Perri, Melissa Pesce-Rollins, Maura Pilia, Andrea Possenti, Simonetta Puccetti, Brian D. Ramsey, John Rankin, Oliver J. Roberts, Roger W. Romani, Carmelo Sgrò, Patrick Slane, Gloria Spandre, Paolo Soffitta, Douglas A. Swartz, Toru Tamagawa, Fabrizio Tavecchio, Yuzuru

- Tawara, Allyn F. Tennant, Nicholas E. Thomas, Francesco Tombesi, Alessio Trois, Sergey S. Tsygankov, Roberto Turolla, Jacco Vink, Martin C. Weisskopf, Kinwah Wu, and Fei Xie. The First X-Ray Polarization Observation of the Black Hole X-Ray Binary 4U 1630-47 in the Steep Power-law State. *ApJ*, 958(1):L8, November 2023. doi: 10.3847/2041-8213/acfd2c.
- A. Rózańska, A. M. Dumont, B. Czerny, and S. Collin. The structure and radiation spectra of illuminated accretion discs in active galactic nuclei - I. Moderate illumination. *MNRAS*, 332(4):799–813, June 2002. doi: 10.1046/j.1365-8711.2002.05338.x.
- D. M. Russell, J. C. A. Miller-Jones, T. J. Maccarone, Y. J. Yang, R. P. Fender, and F. Lewis. Testing the Jet Quenching Paradigm with an Ultradeep Observation of a Steadily Soft State Black Hole. *ApJ*, 739(1):L19, September 2011a. doi: 10.1088/2041-8205/739/1/L19.
- D. M. Russell, J. C. A. Miller-Jones, T. J. Maccarone, Y. J. Yang, R. P. Fender, and F. Lewis. Testing the Jet Quenching Paradigm with an Ultradeep Observation of a Steadily Soft State Black Hole. *ApJ*, 739(1):L19, September 2011b. doi: 10.1088/2041-8205/739/1/L19.
- George B. Rybicki and Alan P. Lightman. *Radiative Processes in Astrophysics*. 1986.
- A. Sądowski. Slim accretion disks around black holes. *arXiv e-prints*, art. arXiv:1108.0396, August 2011. doi: 10.48550/arXiv.1108.0396.
- Simon Schaffer. John Michell and Black Holes. *Journal for the History of Astronomy*, 10:42, January 1979. doi: 10.1177/002182867901000104.
- M. Schmidt. 3C 273 : A Star-Like Object with Large Red-Shift. *Nature*, 197(4872):1040, March 1963. doi: 10.1038/1971040a0.
- P. C. Schmidtke, A. L. Ponder, and A. P. Cowley. ROSSI X-RAY TIMING EXPLORER Observations of LMC X-1. *AJ*, 117(3):1292–1296, March 1999. doi: 10.1086/300793.
- Jeremy D. Schnittman and Julian H. Krolik. X-ray Polarization from Accreting Black Holes: The Thermal State. *ApJ*, 701(2):1175–1187, August 2009. doi: 10.1088/0004-637X/701/2/1175.
- Jeremy D. Schnittman and Julian H. Krolik. X-ray Polarization from Accreting Black Holes: Coronal Emission. *ApJ*, 712(2):908–924, April 2010. doi: 10.1088/0004-637X/712/2/908.
- H. W. Schnopper and K. Kalata. Polarimeter for Celestial X Rays. *AJ*, 74:854, September 1969. doi: 10.1086/110873.
- Karl Schwarzschild. Über das Gravitationsfeld eines Massenpunktes nach der Einsteinschen Theorie. *Sitzungsberichte der Königlich Preussischen Akademie der Wissenschaften*, pages 189–196, January 1916.

- Elena Seifina, Lev Titarchuk, and Nikolai Shaposhnikov. Black Hole Mass Determination in the X-Ray Binary 4U 1630-47: Scaling of Spectral and Variability Characteristics. *ApJ*, 789(1):57, July 2014. doi: 10.1088/0004-637X/789/1/57.
- Carl K. Seyfert. Nuclear Emission in Spiral Nebulae. *ApJ*, 97:28, January 1943. doi: 10.1086/144488.
- N. I. Shakura and R. A. Sunyaev. Black holes in binary systems. Observational appearance. *A&A*, 24:337–355, January 1973.
- Yong Shao and Xiang-Dong Li. Stable Mass Transfer Can Explain Massive Binary Black Hole Mergers with a High-spin Component. *ApJ*, 930(1):26, May 2022. doi: 10.3847/1538-4357/ac61da.
- Prince Sharma, Rahul Sharma, Chetana Jain, Gulab C. Dewangan, and Anjan Dutta. Broad-band spectral study of LMXB black hole candidate 4U 1957+11 with NuSTAR. *Research in Astronomy and Astrophysics*, 21(9):214, November 2021. doi: 10.1088/1674-4527/21/9/214.
- Toshiya Shimura and Fumio Takahara. On the Spectral Hardening Factor of the X-Ray Emission from Accretion Disks in Black Hole Candidates. *ApJ*, 445:780, June 1995. doi: 10.1086/175740.
- Alan P. Smale and Patricia T. Boyd. Anomalous Low States and Long-term Variability in the Black Hole Binary LMC X-3. *ApJ*, 756(2):146, September 2012. doi: 10.1088/0004-637X/756/2/146.
- Viktor Viktorovich Sobolev. *A treatise on radiative transfer*. 1963.
- Paolo Soffitta, Enrico Costa, Ennio Morelli, Ronaldo Bellazzini, Alessandro Brez, and R. Raffo. Sensitivity to x-ray polarization of a microgap gas proportional counter. In Silvano Fineschi, editor, *X-Ray and EUV/FUV Spectroscopy and Polarimetry*, volume 2517 of *Society of Photo-Optical Instrumentation Engineers (SPIE) Conference Series*, pages 156–163, October 1995. doi: 10.1117/12.224922.
- Paolo Soffitta, Fabio Muleri, Sergio Fabiani, Enrico Costa, Ronaldo Bellazzini, Alessandro Brez, Massimo Minuti, Michele Pinchera, and Gloria Spandre. Measurement of the position resolution of the Gas Pixel Detector. *Nuclear Instruments and Methods in Physics Research A*, 700:99–105, February 2013. doi: 10.1016/j.nima.2012.09.055.
- Paolo Soffitta, Luca Baldini, Ronaldo Bellazzini, Enrico Costa, Luca Latronico, Fabio Muleri, Ettore Del Monte, Sergio Fabiani, Massimo Minuti, Michele Pinchera, Carmelo Sgro', Gloria Spandre, Alessio Trois, Fabrizio Amici, Hans Andersson, Primo Attina', Matteo Bachetti, Mattia Barbanera, Fabio Borotto, Alessandro Brez, Daniele Brienza, Ciro Caporale, Claudia Cardelli, Rita Carpentiero, Simone Castellano, Marco Castronuovo, Luca Cavalli, Elisabetta Cavazzuti, Marco Ceccanti, Mauro Centrone, Stefano Ciprini, Saverio Citraro, Fabio D'Amico, Elisa D'Alba, Sergio Di Cosimo, Niccolo' Di Lalla, Alessandro Di Marco, Giuseppe Di Persio, Immacolata Donnarumma, Yuri Evangelista, Riccardo Ferrazzoli, Asami Hayato, Takao

- Kitaguchi, Fabio La Monaca, Carlo Lefevre, Pasqualino Loffredo, Paolo Lorenzi, Leonardo Lucchesi, Carlo Magazzu, Simone Maldera, Alberto Manfreda, Elio Mangraviti, Marco Marengo, Giorgio Matt, Paolo Mereu, Alfredo Morbidini, Federico Mosti, Toshio Nakano, Hikmat Nasimi, Barbara Negri, Seppo Nenonen, Alessio Nuti, Leonardo Orsini, Matteo Perri, Melissa Pesce-Rollins, Raffaele Piazzolla, Maura Pilia, Alessandro Profeti, Simonetta Puccetti, John Rankin, Ajay Ratheesh, Alda Rubini, Francesco Santoli, Paolo Sarra, Emanuele Scalise, Andrea Sciortino, Toru Tamagawa, Marcello Tardiola, Antonino Tobia, Marco Vimercati, and Fei Xie. The Instrument of the Imaging X-Ray Polarimetry Explorer. *AJ*, 162(5):208, November 2021. doi: 10.3847/1538-3881/ac19b0.
- P. Soleri, T. Muñoz-Darias, S. Motta, T. Belloni, P. Casella, M. Méndez, D. Altamirano, M. Linares, R. Wijnands, R. Fender, and M. van der Klis. A complex state transition from the black hole candidate Swift J1753.5-0127. *MNRAS*, 429(2):1244–1257, February 2013. doi: 10.1093/mnras/sts405.
- R. F. Stark and P. A. Connors. Observational test for the existence of a rotating black hole in Cyg X-1. *Nature*, 266(5601):429–430, March 1977. doi: 10.1038/266429a0.
- James F. Steiner, Ramesh Narayan, Jeffrey E. McClintock, and Ken Ebisawa. A Simple Comptonization Model. *PASP*, 121(885):1279, November 2009. doi: 10.1086/648535.
- James F. Steiner, Jeffrey E. McClintock, Ronald A. Remillard, Lijun Gou, Shin'ya Yamada, and Ramesh Narayan. The Constant Inner-disk Radius of LMC X-3: A Basis for Measuring Black Hole Spin. *ApJ*, 718(2):L117–L121, August 2010. doi: 10.1088/2041-8205/718/2/L117.
- James F. Steiner, Rubens C. Reis, Andrew C. Fabian, Ronald A. Remillard, Jeffrey E. McClintock, Lijun Gou, Ryan Cooke, Laura W. Brenneman, and Jeremy S. Sanders. A broad iron line in LMC X-1. *MNRAS*, 427(3):2552–2561, 12 2012. ISSN 0035-8711. doi: 10.1111/j.1365-2966.2012.22128.x. URL <https://doi.org/10.1111/j.1365-2966.2012.22128.x>.
- James F. Steiner, Jeffrey E. McClintock, Jerome A. Orosz, Ronald A. Remillard, Charles D. Bailyn, Mari Kolehmainen, and Odele Straub. The Low-spin Black Hole in LMC X-3. *ApJ*, 793(2):L29, October 2014. doi: 10.1088/2041-8205/793/2/L29.
- Luigi Stella, Mario Vietri, and Sharon M. Morsink. Correlations in the Quasi-periodic Oscillation Frequencies of Low-Mass X-Ray Binaries and the Relativistic Precession Model. *ApJ*, 524(1):L63–L66, October 1999. doi: 10.1086/312291.
- A. M. Stirling, R. E. Spencer, C. J. de la Force, M. A. Garrett, R. P. Fender, and R. N. Ogle. A relativistic jet from Cygnus X-1 in the low/hard X-ray state. *MNRAS*, 327(4):1273–1278, November 2001. doi: 10.1046/j.1365-8711.2001.04821.x.
- G. G. Stokes. On the Change of Refrangibility of Light. *Philosophical Transactions of the Royal Society of London Series I*, 142:463–562, January 1852.

- O. Straub, M. Bursa, A. Sądowski, J. F. Steiner, M. A. Abramowicz, W. Kluźniak, J. E. McClintock, R. Narayan, and R. A. Remillard. Testing slim-disk models on the thermal spectra of LMC X-3. *A&A*, 533:A67, September 2011. doi: 10.1051/0004-6361/201117385.
- R. Sunyaev, V. Arefiev, V. Babushkin, A. Bogomolov, K. Borisov, M. Buntov, H. Brunner, R. Burenin, E. Churazov, D. Coutinho, J. Eder, N. Eismont, M. Freyberg, M. Gilfanov, P. Gureyev, G. Hasinger, I. Khabibullin, V. Kolmykov, S. Komovkin, R. Krivonos, I. Lapshov, V. Levin, I. Lomakin, A. Lutovinov, P. Medvedev, A. Merloni, T. Mernik, E. Mikhailov, V. Molodtsov, P. Mzhelsky, S. Müller, K. Nandra, V. Nazarov, M. Pavlinsky, A. Poghodin, P. Predehl, J. Robrade, S. Sazonov, H. Scheuerle, A. Shirshakov, A. Tkachenko, and V. Voron. SRG X-ray orbital observatory. Its telescopes and first scientific results. *A&A*, 656:A132, December 2021. doi: 10.1051/0004-6361/202141179.
- R. A. Sunyaev and L. G. Titarchuk. Comptonization of X-rays in plasma clouds - Typical radiation spectra. *A&A*, 86:121–138, June 1980.
- Jiří Svoboda, Michal Dovčiak, James F. Steiner, Philip Kaaret, Jakub Podgorný, Juri Poutanen, Alexandra Veledina, Fabio Muleri, Roberto Taverna, Henric Krawczynski, Maïmouna Brigitte, Sudeb Ranjan Datta, Stefano Bianchi, Noel Castro Segura, Javier A. García, Adam Ingram, Giorgio Matt, Teo Muñoz-Darias, Edward Nathan, Martin C. Weisskopf, Diego Altamirano, Luca Baldini, Niek Bollemeijer, Fiamma Capitanio, Elise Egron, Razieh Emami, Kun Hu, Lorenzo Marra, Guglielmo Mastroserio, Michela Negro, Pierre-Olivier Petrucci, Ajay Ratheesh, Nicole Rodriguez Cavero, Paolo Soffitta, Francesco Tombesi, Yi-Jung Yang, and Yuexin Zhang. Dramatic Drop in the X-Ray Polarization of Swift J1727.8–1613 in the Soft Spectral State. *arXiv e-prints*, art. arXiv:2403.04689, March 2024a. doi: 10.48550/arXiv.2403.04689.
- Jiří Svoboda, Michal Dovčiak, James F. Steiner, Fabio Muleri, Adam Ingram, Anastasiya Yilmaz, Nicole Rodriguez Cavero, Lorenzo Marra, Juri Poutanen, Alexandra Veledina, Mehrnoosh Rahbardar Mojaver, Stefano Bianchi, Javier A. García, Philip Kaaret, Henric Krawczynski, Giorgio Matt, Jakub Podgorný, Martin C. Weisskopf, Fabian Kislak, Pierre-Olivier Petrucci, Maimouna Brigitte, Michal Bursa, Sergio Fabiani, Kun Hu, Sohee Chun, Guglielmo Mastroserio, Romana Mikušincová, Ajay Ratheesh, Roger W. Romani, Paolo Soffitta, Francesco Ursini, Silvia Zane, Iván Agudo, Lucio A. Antonelli, Matteo Bachetti, Luca Baldini, Wayne H. Baumgartner, Ronaldo Bellazzini, Stephen D. Bongiorno, Raffaella Bonino, Alessandro Brez, Niccolò Bucciantini, Fiamma Capitanio, Simone Castellano, Elisabetta Cavazzuti, Chien-Ting Chen, Stefano Ciprini, Enrico Costa, Alessandra De Rosa, Ettore Del Monte, Laura Di Gesu, Niccolò Di Lalla, Alessandro Di Marco, Immacolata Donnarumma, Victor Doroshenko, Steven R. Ehlert, Teruaki Enoto, Yuri Evangelista, Riccardo Ferrazzoli, Shuichi Gunji, Kiyoshi Hayashida, Jeremy Heyl, Wataru Iwakiri, Svetlana G. Jorstad, Vladimír Karas, Takao Kitaguchi, Jeffery J. Kolodziejczak, Fabio La Monaca, Luca Latronico, Ioannis Liodakis, Simone Maldera, Alberto Manfreda, Frédéric Marin, Andrea Marinucci, Alan P. Marscher, Herman L. Marshall, Francesco Massaro, Ikuyuki Mitsuishi, Tsunefumi Mizuno, Michela Negro, Chi-Yung

- Ng, Stephen L. O'Dell, Nicola Omodei, Chiara Oppedisano, Alessandro Papitto, George G. Pavlov, Abel L. Peirson, Matteo Perri, Melissa Pesce-Rollins, Maura Pilia, Andrea Possenti, Simonetta Puccetti, Brian D. Ramsey, John Rankin, Oliver J. Roberts, Carmelo Sgrò, Patrick Slane, Gloria Spandre, Douglas A. Swartz, Toru Tamagawa, Fabrizio Tavecchio, Roberto Taverna, Yuzuru Tawara, Allyn F. Tennant, Nicholas E. Thomas, Francesco Tombesi, Alessio Trois, Sergey S. Tsygankov, Roberto Turolla, Jacco Vink, Kinwah Wu, and Fei Xie. First X-Ray Polarization Measurement Confirms the Low Black Hole Spin in LMC X-3. *ApJ*, 960(1):3, January 2024b. doi: 10.3847/1538-4357/ad0842.
- J. H. Swank. The Rossi X-Ray Timing Explorer. *Nuclear Physics B Proceedings Supplements*, 69(1-3):12–19, January 1999. doi: 10.1016/S0920-5632(98)00175-3.
- A. Szostek and A. A. Zdziarski. A study of RXTE and BeppoSAX observations of Cyg X-3. *arXiv e-prints*, art. astro-ph/0401265, January 2004. doi: 10.48550/arXiv.astro-ph/0401265.
- Francesco Tamborra, Giorgio Matt, Stefano Bianchi, and Michal Dovčiak. MoCA: A Monte Carlo code for Comptonisation in Astrophysics. I. Description of the code and first results. *A&A*, 619:A105, November 2018. doi: 10.1051/0004-6361/201732023.
- Y. Tanaka and W. H. G. Lewin. Black hole binaries. In *X-ray Binaries*, pages 126–174, January 1995.
- H. Tananbaum, H. Gursky, E. Kellogg, R. Giacconi, and C. Jones. Observation of a Correlated X-Ray Transition in Cygnus X-1. *ApJ*, 177:L5, October 1972. doi: 10.1086/181042.
- R. Taverna, W. Zhang, M. Dovčiak, S. Bianchi, M. Bursa, V. Karas, and G. Matt. Towards a complete description of spectra and polarization of black hole accretion discs: albedo profiles and returning radiation. *MNRAS*, 493(4):4960–4977, April 2020. doi: 10.1093/mnras/staa598.
- R. Taverna, L. Marra, S. Bianchi, M. Dovčiak, R. Goosmann, F. Marin, G. Matt, and W. Zhang. Spectral and polarization properties of black hole accretion disc emission: including absorption effects. *MNRAS*, 501(3):3393–3405, March 2021. doi: 10.1093/mnras/staa3859.
- B. E. Tetarenko, G. R. Sivakoff, C. O. Heinke, and J. C. Gladstone. WATCHDOG: A Comprehensive All-sky Database of Galactic Black Hole X-ray Binaries. *ApJS*, 222(2):15, February 2016. doi: 10.3847/0067-0049/222/2/15.
- Kip S. Thorne. Disk-Accretion onto a Black Hole. II. Evolution of the Hole. *ApJ*, 191: 507–520, July 1974. doi: 10.1086/152991.
- John R. Thorstensen. A 9.3 Hour Orbital Period in the Potential Black Hole Binary 4U 1957+11. *ApJ*, 312:739, January 1987. doi: 10.1086/164917.

- A. Tiengo, G. Vianello, P. Esposito, S. Mereghetti, A. Giuliani, E. Costantini, G. L. Israel, L. Stella, R. Turolla, S. Zane, N. Rea, D. Götz, F. Bernardini, A. Moretti, P. Romano, M. Ehle, and N. Gehrels. The Dust-scattering X-ray Rings of the Anomalous X-ray Pulsar 1E 1547.0-5408. *ApJ*, 710(1):227–235, February 2010. doi: 10.1088/0004-637X/710/1/227.
- Ryota Tomaru, Chris Done, and Junjie Mao. What powers the wind from the black hole accretion disc in GRO J1655-40? *MNRAS*, 518(2):1789–1801, January 2023. doi: 10.1093/mnras/stac3210.
- J. A. Tomsick, I. Lapshov, and P. Kaaret. An X-Ray Dip in the X-Ray Transient 4U 1630-47. *ApJ*, 494(2):747–752, February 1998. doi: 10.1086/305240.
- John A. Tomsick, Stéphane Corbel, Andrea Goldwurm, and Philip Kaaret. X-Ray Observations of the Black Hole Transient 4U 1630-47 during 2 Years of X-Ray Activity. *ApJ*, 630(1):413–429, September 2005. doi: 10.1086/431896.
- John A. Tomsick, Kazutaka Yamaoka, Stephane Corbel, Emrah Kalemci, Simone Migliari, and Philip Kaaret. A Delayed Transition to the Hard State for 4U 1630-47 at the End of its 2010 Outburst. *ApJ*, 791(1):70, August 2014. doi: 10.1088/0004-637X/791/1/70.
- Trevor J. Torpin, Patricia T. Boyd, Alan P. Smale, and Lynne A. Valencic. Unusual Black Hole Binary LMC X-3: A Transient High-mass X-Ray Binary That Is Almost Always On? *ApJ*, 849(1):32, November 2017. doi: 10.3847/1538-4357/aa8f96.
- A. Treves, T. Belloni, L. Chiappetti, L. Maraschi, L. Stella, E. G. Tanzi, and M. van der Klis. X-Ray Spectrum and Variability of the Black Hole Candidate LMC X-3. *ApJ*, 325:119, February 1988. doi: 10.1086/165987.
- Ashutosh Tripathi, Menglei Zhou, Askar B. Abdikamalov, Dimitry Ayzenberg, Cosimo Bambi, Lijun Gou, Victoria Grinberg, Honghui Liu, and James F. Steiner. Testing General Relativity with the Stellar-mass Black Hole in LMC X-1 Using the Continuum-fitting Method. *ApJ*, 897(1):84, July 2020. doi: 10.3847/1538-4357/ab9600.
- T. J. Turner and L. Miller. X-ray absorption and reflection in active galactic nuclei. *A&A Rev.*, 17(1):47–104, March 2009. doi: 10.1007/s00159-009-0017-1.
- M. van der Klis. Quasi-periodic oscillations and noise in low-mass X-ray binaries. *ARA&A*, 27:517–553, January 1989. doi: 10.1146/annurev.aa.27.090189.002505.
- Alexandra Veledina and Juri Poutanen. Polarization of Comptonized emission in slab geometry, September 2022.
- Alexandra Veledina, Fabio Muleri, Michal Dovčiak, Juri Poutanen, Ajay Ratheesh, Fiamma Capitanio, Giorgio Matt, Paolo Soffitta, Allyn F. Tennant, Michela Negro, Philip Kaaret, Enrico Costa, Adam Ingram, Jiří Svoboda, Henric Krawczynski, Stefano Bianchi, James F. Steiner, Javier A. García, Vadim Kravtsov, Anagha P. Nitindala, Melissa Ewing, Guglielmo Mastroserio, Andrea Marinucci, Francesco Ursini,

Francesco Tombesi, Sergey S. Tsygankov, Yi-Jung Yang, Martin C. Weisskopf, Sergei A. Trushkin, Elise Egron, Maria Noemi Iacolina, Maura Pilia, Lorenzo Marra, Romana Mikušincová, Edward Nathan, Maxime Parra, Pierre-Olivier Petrucci, Jakub Podgorný, Stefano Tugliani, Silvia Zane, Wenda Zhang, Iván Agudo, Lucio A. Antonelli, Matteo Bachetti, Luca Baldini, Wayne H. Baumgartner, Ronaldo Bellazzini, Stephen D. Bongiorno, Raffaella Bonino, Alessandro Brez, Niccolò Bucciantini, Simone Castellano, Elisabetta Cavazzuti, Chien-Ting Chen, Stefano Ciprini, Alessandra De Rosa, Ettore Del Monte, Laura Di Gesu, Niccolò Di Lalla, Alessandro Di Marco, Immacolata Donnarumma, Victor Doroshenko, Steven R. Ehlert, Teruaki Enoto, Yuri Evangelista, Sergio Fabiani, Riccardo Ferrazzoli, Shuichi Gunji, Kiyoshi Hayashida, Jeremy Heyl, Wataru Iwakiri, Svetlana G. Jorstad, Vladimir Karas, Fabian Kislak, Takao Kitaguchi, Jeffery J. Kolodziejczak, Fabio La Monaca, Luca Latronico, Ioannis Liodakis, Simone Maldera, Alberto Manfreda, Frédéric Marin, Alan P. Marscher, Herman L. Marshall, Francesco Massaro, Ikuyuki Mitsuishi, Tsunefumi Mizuno, Chi-Yung Ng, Stephen L. O'Dell, Nicola Omodei, Chiara Oppedisano, Alessandro Papitto, George G. Pavlov, Abel L. Peirson, Matteo Perri, Melissa Pesce-Rollins, Andrea Possenti, Simonetta Puccetti, Brian D. Ramsey, John Rankin, Oliver J. Roberts, Roger W. Romani, Carmelo Sgrò, Patrick Slane, Gloria Spandre, Douglas A. Swartz, Toru Tamagawa, Fabrizio Tavecchio, Roberto Taverna, Yuzuru Tawara, Nicholas E. Thomas, Alessio Trois, Roberto Turolla, Jacco Vink, Kinwah Wu, and Fei Xie. Discovery of X-Ray Polarization from the Black Hole Transient Swift J1727.8-1613. *ApJ*, 958(1):L16, November 2023a. doi: 10.3847/2041-8213/ad0781.

Alexandra Veledina, Fabio Muleri, Juri Poutanen, Jakub Podgorný, Michal Dovčiak, Fiamma Capitano, Eugene Churazov, Alessandra De Rosa, Alessandro Di Marco, Sofia Forsblom, Philip Kaaret, Henric Krawczynski, Fabio La Monaca, Vladislav Loktev, Alexander A. Lutovinov, Sergey V. Molkov, Alexander A. Mushtukov, Ajay Ratheesh, Nicole Rodriguez Caverio, James F. Steiner, Rashid A. Sunyaev, Sergey S. Tsygankov, Andrzej A. Zdziarski, Stefano Bianchi, Joe S. Bright, Nikolaj Bursov, Enrico Costa, Elise Egron, Javier A. Garcia, David A. Green, Mark Gurwell, Adam Ingram, Jari J. E. Kajava, Ruta Kale, Alex Kraus, Denys Malyshev, Frédéric Marin, Giorgio Matt, Michael McCollough, Ilia A. Mereminskiy, Nikolaj Nizhelsky, Giovanni Piano, Maura Pilia, Carlotta Pittori, Ramprasad Rao, Simona Righini, Paolo Soffitta, Anton Shevchenko, Jiri Svoboda, Francesco Tombesi, Sergei Trushkin, Peter Tsybulev, Francesco Ursini, Martin C. Weisskopf, Kinwah Wu, Iván Agudo, Lucio A. Antonelli, Matteo Bachetti, Luca Baldini, Wayne H. Baumgartner, Ronaldo Bellazzini, Stephen D. Bongiorno, Raffaella Bonino, Alessandro Brez, Niccolò Bucciantini, Simone Castellano, Elisabetta Cavazzuti, Chien-Ting Chen, Stefano Ciprini, Ettore Del Monte, Laura Di Gesu, Niccolò Di Lalla, Immacolata Donnarumma, Victor Doroshenko, Steven R. Ehlert, Teruaki Enoto, Yuri Evangelista, Sergio Fabiani, Riccardo Ferrazzoli, Shuichi Gunji, Kiyoshi Hayashida, Jeremy Heyl, Wataru Iwakiri, Svetlana G. Jorstad, Vladimir Karas, Fabian Kislak, Takao Kitaguchi, Jeffery J. Kolodziejczak, Luca Latronico, Ioannis Liodakis, Simone Maldera, Alberto Manfreda, Andrea Marinucci, Alan P. Marscher, Herman L. Marshall, Francesco Massaro, Ikuyuki Mitsuishi, Tsunefumi Mizuno, Michela Negro, Chi-Yung Ng, Stephen L. O'Dell, Nicola Omodei, Chiara Oppedisano, Alessandro Papitto, George G. Pavlov,

- Abel L. Peirson, Matteo Perri, Melissa Pesce-Rollins, Pierre-Olivier Petrucci, Andrea Possenti, Simonetta Puccetti, Brian D. Ramsey, John Rankin, Oliver Roberts, Roger W. Romani, Carmelo Sgrò, Patrick Slane, Gloria Spandre, Doug Swartz, Toru Tamagawa, Fabrizio Tavecchio, Roberto Taverna, Yuzuru Tawara, Allyn F. Tennant, Nicholas E. Thomas, Alessio Trois, Roberto Turolla, Jacco Vink, Fei Xie, and Silvia Zane. Astronomical puzzle Cyg X-3 is a hidden Galactic ultraluminous X-ray source. *arXiv e-prints*, art. arXiv:2303.01174, March 2023b. doi: 10.48550/arXiv.2303.01174.
- W. Voges, B. Aschenbach, Th. Boller, H. Bräuninger, U. Briel, W. Burkert, K. Dennerl, J. Englhauser, R. Gruber, F. Haberl, G. Hartner, G. Hasinger, M. Kürster, E. Pfeffermann, W. Pietsch, P. Predehl, C. Rosso, J. H. M. M. Schmitt, J. Trümper, and H. U. Zimmermann. The ROSAT all-sky survey bright source catalogue. *A&A*, 349:389–405, September 1999. doi: 10.48550/arXiv.astro-ph/9909315.
- Martin Walker and Roger Penrose. On quadratic first integrals of the geodesic equations for type $\{2,2\}$ spacetimes. *Communications in Mathematical Physics*, 18(4):265–274, December 1970. doi: 10.1007/BF01649445.
- Ding-xiong Wang. The radial temperature profile in the inner region of a black-hole accretion disk. *Chinese Astron. Astrophys.*, 24(1):13–22, January 2000. doi: 10.1016/S0275-1062(00)00021-7.
- Jingyi Wang, Guglielmo Mastroserio, Erin Kara, Javier A. García, Adam Ingram, Riley Connors, Michiel van der Klis, Thomas Dauser, James F. Steiner, Douglas J. K. Buisson, Jeroen Homan, Matteo Lucchini, Andrew C. Fabian, Joe Bright, Rob Fender, Edward M. Cackett, and Ron A. Remillard. Disk, Corona, Jet Connection in the Intermediate State of MAXI J1820+070 Revealed by NICER Spectral-timing Analysis. *ApJ*, 910(1):L3, March 2021a. doi: 10.3847/2041-8213/abec79.
- Yanan Wang, Long Ji, Javier A. García, Thomas Dauser, Mariano Méndez, Junjie Mao, L. Tao, Diego Altamirano, Pierre Maggi, S. N. Zhang, M. Y. Ge, L. Zhang, J. L. Qu, S. Zhang, X. Ma, F. J. Lu, T. P. Li, Y. Huang, S. J. Zheng, Z. Chang, Y. L. Tuo, L. M. Song, Y. P. Xu, Y. Chen, C. Z. Liu, Q. C. Bu, C. Cai, X. L. Cao, L. Chen, T. X. Chen, Y. P. Chen, W. W. Cui, Y. Y. Du, G. H. Gao, Y. D. Gu, J. Guan, C. C. Guo, D. W. Han, J. Huo, S. M. Jia, W. C. Jiang, J. Jin, L. D. Kong, B. Li, C. K. Li, G. Li, W. Li, X. Li, X. B. Li, X. F. Li, Z. W. Li, X. H. Liang, J. Y. Liao, H. W. Liu, X. J. Liu, X. F. Lu, Q. Luo, T. Luo, B. Meng, Y. Nang, J. Y. Nie, G. Ou, N. Sai, R. C. Shang, X. Y. Song, L. Sun, Y. Tan, W. S. Wang, Y. D. Wang, Y. S. Wang, X. Y. Wen, B. B. Wu, B. Y. Wu, M. Wu, G. C. Xiao, S. Xiao, S. L. Xiong, S. Yang, Y. J. Yang, Q. B. Yi, Q. Q. Yin, Y. You, F. Zhang, H. M. Zhang, J. Zhang, W. C. Zhang, W. Zhang, Y. F. Zhang, H. S. Zhao, X. F. Zhao, and D. K. Zhou. A Variable Ionized Disk Wind in the Black Hole Candidate EXO 1846-031. *ApJ*, 906(1):11, January 2021b. doi: 10.3847/1538-4357/abc55e.
- M. C. Weisskopf, G. G. Cohen, H. L. Kestenbaum, K. S. Long, R. Novick, and R. S. Wolff. Measurement of the X-ray polarization of the Crab nebula. *ApJ*, 208:L125–L128, September 1976. doi: 10.1086/182247.

- Martin C. Weisskopf, Ronald F. Elsner, and Stephen L. O'Dell. On understanding the figures of merit for detection and measurement of x-ray polarization. In Monique Arnaud, Stephen S. Murray, and Tadayuki Takahashi, editors, *Space Telescopes and Instrumentation 2010: Ultraviolet to Gamma Ray*, volume 7732 of *Society of Photo-Optical Instrumentation Engineers (SPIE) Conference Series*, page 77320E, July 2010. doi: 10.1117/12.857357.
- Martin C. Weisskopf, Brian Ramsey, Stephen O'Dell, Allyn Tennant, Ronald Elsner, Paolo Soffitta, Ronaldo Bellazzini, Enrico Costa, Jeffrey Kolodziejczak, Victoria Kaspi, Fabio Muleri, Herman Marshall, Giorgio Matt, and Roger Romani. The Imaging X-ray Polarimetry Explorer (IXPE). In Jan-Willem A. den Herder, Tadayuki Takahashi, and Marshall Bautz, editors, *Space Telescopes and Instrumentation 2016: Ultraviolet to Gamma Ray*, volume 9905 of *Society of Photo-Optical Instrumentation Engineers (SPIE) Conference Series*, page 990517, July 2016. doi: 10.1117/12.2235240.
- Martin C. Weisskopf, Paolo Soffitta, Luca Baldini, Brian D. Ramsey, Stephen L. O'Dell, Roger W. Romani, Giorgio Matt, William D. Deininger, Wayne H. Baumgartner, Ronaldo Bellazzini, Enrico Costa, Jeffery J. Kolodziejczak, Luca Latronico, Herman L. Marshall, Fabio Muleri, Stephen D. Bongiorno, Allyn Tennant, Niccolo Bucciantini, Michal Dovciak, Frederic Marin, Alan Marscher, Juri Poutanen, Pat Slane, Roberto Turolla, William Kalinowski, Alessandro Di Marco, Sergio Fabiani, Massimo Minuti, Fabio La Monaca, Michele Pinchera, John Rankin, Carmelo Sgro', Alessio Trois, Fei Xie, Cheryl Alexander, D. Zachery Allen, Fabrizio Amici, Jason Andersen, Angelo Antonelli, Spencer Antoniak, Primo Attinà, Mattia Barbanera, Matteo Bachetti, Randy M. Baggett, Jeff Blatt, Alessandro Brez, Raffaella Bonino, Christopher Boree, Fabio Borotto, Shawn Breeding, Daniele Brienza, H. Kyle Bygott, Ciro Caporale, Claudia Cardelli, Rita Carpentiero, Simone Castellano, Marco Castronuovo, Luca Cavalli, Elisabetta Cavazzuti, Marco Ceccanti, Mauro Centrone, Saverio Citraro, Fabio D'Amico, Elisa D'Alba, Laura Di Gesu, Ettore Del Monte, Kurtis L. Dietz, Niccolo' Di Lalla, Giuseppe Di Persio, David Dolan, Immacolata Donnarumma, Yuri Evangelista, Kevin Ferrant, Riccardo Ferrazzoli, MacKenzie Ferrie, Joseph Footdale, Brent Forsyth, Michelle Foster, Benjamin Garelick, Shuichi Gunji, Eli Gurnee, Michael Head, Grant Hibbard, Samantha Johnson, Erik Kelly, Kiranmayee Kilaru, Carlo Lefevre, Shelley Le Roy, Pasqualino Loffredo, Paolo Lorenzi, Leonardo Lucchesi, Tyler Maddox, Guido Magazzu, Simone Maldera, Alberto Manfreda, Elio Mangraviti, Marco Marengo, Alessandra Marrocchesi, Francesco Massaro, David Mauger, Jeffrey McCracken, Michael McEachen, Rondal Mize, Paolo Mereu, Scott Mitchell, Ikuyuki Mitsuishi, Alfredo Morbidini, Federico Mosti, Hikmat Nasimi, Barbara Negri, Michela Negro, Toan Nguyen, Isaac Nitschke, Alessio Nuti, Mitch Onizuka, Chiara Oppedisano, Leonardo Orsini, Darren Osborne, Richard Pacheco, Alessandro Paggi, Will Painter, Steven D. Pavelitz, Christina Pentz, Raffaele Piazzolla, Matteo Perri, Melissa Pesce-Rollins, Colin Peterson, Maura Pilia, Alessandro Profeti, Simonetta Puccetti, Jaganathan Ranganathan, Ajay Ratheesh, Lee Reedy, Noah Root, Alda Rubini, Stephanie Ruswick, Javier Sanchez, Paolo Sarra, Francesco Santoli, Emanuele Scalise, Andrea Sciortino, Christopher Schroeder, Tim Seek, Kalie Sossdian, Gloria Spandre, Chet O. Speegle, Toru Tamagawa, Marcello Tardiola,

- Antonino Tobia, Nicholas E. Thomas, Robert Valerie, Marco Vimercati, Amy L. Walden, Bruce Weddendorf, Jeffrey Wedmore, David Welch, Davide Zanetti, and Francesco Zanetti. The Imaging X-Ray Polarimetry Explorer (IXPE): Pre-Launch. *Journal of Astronomical Telescopes, Instruments, and Systems*, 8(2):026002, April 2022. doi: 10.1117/1.JATIS.8.2.026002.
- Maciek Wielgus, Debora Lančová, Odele Straub, Włoddek Kluźniak, Ramesh Narayan, David Abarca, Agata Róžańska, Frederic Vincent, Gabriel Török, and Marek Abramowicz. Observational properties of puffy discs: radiative GRMHD spectra of mildly sub-Eddington accretion. *MNRAS*, 514(1):780–789, July 2022. doi: 10.1093/mnras/stac1317.
- Rudy Wijnands, Jon M. Miller, and Michiel van der Klis. 4U 1957+11: a persistent low-mass X-ray binary and black hole candidate in the high state? *MNRAS*, 331(1): 60–70, March 2002. doi: 10.1046/j.1365-8711.2002.05137.x.
- Reva Kay Williams. Extracting x rays, γ rays, and relativistic e^-e^+ pairs from supermassive Kerr black holes using the Penrose mechanism. *Phys. Rev. D*, 51(10): 5387–5427, May 1995. doi: 10.1103/PhysRevD.51.5387.
- J. Wilms, A. Allen, and R. McCray. On the Absorption of X-Rays in the Interstellar Medium. *ApJ*, 542(2):914–924, October 2000. doi: 10.1086/317016.
- J. Wilms, M. A. Nowak, K. Pottschmidt, W. A. Heindl, J. B. Dove, and M. C. Begelman. Discovery of recurring soft-to-hard state transitions in LMC X-3. *MNRAS*, 320(3):327–340, 01 2001. ISSN 0035-8711. doi: 10.1046/j.1365-8711.2001.03983.x. URL <https://doi.org/10.1046/j.1365-8711.2001.03983.x>.
- S. J. Wolk, Jr. Harnden, F. R., E. Flaccomio, G. Micela, F. Favata, H. Shang, and E. D. Feigelson. Stellar Activity on the Young Suns of Orion: COUP Observations of K5-7 Pre-Main-Sequence Stars. *ApJS*, 160(2):423–449, October 2005. doi: 10.1086/432099.
- K. Wu, R. Soria, M. J. Page, I. Sakelliou, S. M. Kahn, and C. P. de Vries. XMM-Newton EPIC and RGS observations of LMC X-3. *A&A*, 365:L267–L272, January 2001. doi: 10.1051/0004-6361:20000229.
- Y. Yao, M. A. Nowak, Q. D. Wang, N. S. Schulz, and C. R. Canizares. Limits on Hot Galactic Halo Gas from X-Ray Absorption Lines. *ApJ*, 672(1):L21, January 2008. doi: 10.1086/526767.
- T. Yaqoob, K. Ebisawa, and K. Mitsuda. Is X1957+11 a black hole candidate ? *MNRAS*, 264:411–420, September 1993. doi: 10.1093/mnras/264.2.411.
- Anastasiya Yilmaz, Jiří Svoboda, Victoria Grinberg, Peter G. Boorman, Michal Bursa, and Michal Dovčiak. Accretion disc evolution in GRO J1655-40 and LMC X-3 with relativistic and non-relativistic disc models. *MNRAS*, August 2023. doi: 10.1093/mnras/stad2339.

- A. A. Zdziarski and M. Gierliński. Radiative Processes, Spectral States and Variability of Black-Hole Binaries. *Progr. Theor. Phys. Suppl.*, 155:99–119, 2004. doi: 10.1143/PTPS.155.99.
- A. A. Zdziarski, W. N. Johnson, and P. Magdziarz. Broad-band γ -ray and X-ray spectra of NGC 4151 and their implications for physical processes and geometry. *MNRAS*, 283(1):193–206, November 1996. doi: 10.1093/mnras/283.1.193.
- Andrzej A. Zdziarski, J. Eric Grove, Juri Poutanen, A. R. Rao, and S. V. Vadawale. OSSE and RXTE Observations of GRS 1915+105: Evidence for Nonthermal Comptonization. *ApJ*, 554(1):L45–L48, June 2001. doi: 10.1086/320932.
- Andrzej A. Zdziarski, Juri Poutanen, William S. Paciesas, and Linqing Wen. Understanding the Long-Term Spectral Variability of Cygnus X-1 with Burst and Transient Source Experiment and All-Sky Monitor Observations. *ApJ*, 578(1):357–373, October 2002. doi: 10.1086/342402.
- Andrzej A. Zdziarski, Marek Gierliński, Joanna Mikołajewska, Grzegorz Wardziński, David M. Smith, B. Alan Harmon, and Shunji Kitamoto. GX 339-4: the distance, state transitions, hysteresis and spectral correlations. *MNRAS*, 351(3):791–807, July 2004. doi: 10.1111/j.1365-2966.2004.07830.x.
- Andrzej A. Zdziarski, Srimanta Banerjee, Swadesh Chand, Gulab Dewangan, Ranjeev Misra, Michal Szaneci, and Andrzej Niedzwiecki. Black hole spin measurements in LMC X-1 are highly model-dependent. *arXiv e-prints*, art. arXiv:2308.06167, August 2023. doi: 10.48550/arXiv.2308.06167.
- Wenda Zhang, Michal Dovčiak, and Michal Bursa. Constraining the Size of the Corona with Fully Relativistic Calculations of Spectra of Extended Coronae. I. The Monte Carlo Radiative Transfer Code. *ApJ*, 875(2):148, April 2019. doi: 10.3847/1538-4357/ab1261.
- Wenda Zhang, Michal Dovčiak, Michal Bursa, Vladimír Karas, Giorgio Matt, and Francesco Ursini. Investigating the X-ray polarization of lamp-post coronae in BHXRBs. *MNRAS*, 515(2):2882–2889, September 2022. doi: 10.1093/mnras/stac1937.
- Piotr T. Życki, Chris Done, and David A. Smith. The 1989 May outburst of the soft X-ray transient GS 2023+338 (V404 Cyg). *MNRAS*, 309(3):561–575, November 1999. doi: 10.1046/j.1365-8711.1999.02885.x.
- Piotr T. Życki, Chris Done, and David A. Smith. On the complex disc-corona interactions in the soft spectral states of soft X-ray transients. *MNRAS*, 326(4):1367–1380, October 2001. doi: 10.1111/j.1365-2966.2001.04698.x.